UNCLASSIFIED

AD 210239

Armed Services Technical Information Agency

ARLINGTON HALL STATION
ARLINGTON 12 VIRGINIA

FOR
MICRO-CARD
CONTROL ONLY

1 OF 6

NOTICE: WHEN GOVERNMENT OR OTHER DRAWINGS, SPECIFICATIONS OR OTHER DATA ARE USED FOR ANY PURPOSE OTHER THAN IN CONNECTION WITH A DEFINITELY RELATED GOVERNMENT PROCUREMENT OPERATION, THE U. S. GOVERNMENT THEREBY INCURS NO RESPONSIBILITY, NOR ANY OBLIGATION WHATSOEVER; AND THE FACT THAT THE GOVERNMENT MAY HAVE FORMULATED, FURNISHED, OR IN ANY WAY SUPPLIED THE SAID DRAWINGS, SPECIFICATIONS, OR OTHER DATA IS NOT TO BE REGARDED BY IMPLICATION OR OTHERWISE AS IN ANY MANNER LICENSING THE HOLDER OR ANY OTHER PERSON OR CORPORATION, OR CONVEYING ANY RIGHTS OR PERMISSION TO MANUFACTURE, USE OR SELL ANY PATENTED INVENTION THAT MAY IN ANY WAY BE RELATED THERETO.

UNCLASSIFIED

SWR-TM-58-3

/0

SWR
TM
58-3

211239
AD NO.
ASTIA FILE COPY

HEADQUARTERS

AIR FORCE SPECIAL WEAPONS CENTER

AIR RESEARCH AND DEVELOPMENT COMMAND

KIRTLAND AIR FORCE BASE, NEW MEXICO

FILE COPY

Return to
ASTIA
ARLINGTON HALL STATION
ARLINGTON 12, VIRGINIA

Attn: TISSS

FC

PROCEEDINGS

of

SECOND SHOCK TUBE SYMPOSIUM

5 - 6 March 1958

Sponsored by
Air Force Special Weapons Center

ASTIA
RECEIVED
FEB 16 1959
TIPDR

SWR-TM-58-3

PROCEEDINGS
OF
SECOND SHOCK TUBE SYMPOSIUM

5 - 6 March 1958

Research Directorate
AIR FORCE SPECIAL WEAPONS CENTER
Air Research and Development Command
Kirtland Air Force Base
New Mexico

Approved:

Leonard A Eddy
LEONARD A. EDDY
Colonel USAF
Acting Director

Project No. 1080

Wednesday & Thursday, 5 & 6 March, 1958
Palo Alto, California

PROGRAM OF SECOND SHOCK TUBE SYMPOSIUM

Sponsored by
Air Force Special Weapons Center

AGENDA

5th March - Moderator: Eric H. Wang, AFSWC

Official Welcome - Col. L. A. Eddy, AFSWC, Deputy Director of Research

AFSWP Interest in Shock Tube Research:
Jack Kelso, Armed Forces Special Weapons Project
Shock Tube Wind Tunnel Research at the Naval Ordnance Laboratory:
P. Aronson and T. Marshal, Naval Ordnance Laboratory

Shock Tube Studies of Blast Pressures Behind Frangible Wall Panels:
T. A. Zaker Armour Research Foundation
Comparison of Shock Tube and Field Test Data on the Pressure Build-up Behind Frangible Walls:
E. Sevin, Armour Research Foundation

LUNCH

Trip to Lockheed Research Center

Some Results from Use of a Shock Tube for Biomedical Investigation:
Dr. D. R. Richmond; R. V. Taborelli, Lovelace Clinic, Albuquerque, New Mexico
Experimentation with General Electric Six-Inch Shock Tunnel:
E. M. Kaegi, General Electric
Pressure-Time History in a Chamber Subjected to Shock Wave Filling Through an Orifice:
R. Clark, Ballistics Research Laboratories
Determination of the Time History of the Flow Field about a Blunt Body in a Shock Tube:
Edward Offenhartz; Herbert Weisblatt, AVCO Research Laboratory

6th March - Moderator: Jack Kelso, AFSWP

Some Experiments with Periodic Shocks:
Dr. Jack Kotik, Cambridge Research Center
On the Effect of Attenuation on Gas Dynamic Measurements Made in Shock Tubes:
P. H. Rose; W. Nelson, AVCO Research Laboratory

A Method of Generating Various Desired Pressure Pulses in a Shock Tube:
Dr. T. H. Schiffman; D. Anderson, G. Tzantzos, Armour Research Foundation

Problems in the Use of Piezogauges for Shock Tube Instrumentation:
G. Coulter, Ballistic Research Laboratories

Determination of the Dynamic Response Characteristics of Pressure Measuring Systems Utilizing Shock Tube Testing Techniques:
1/Lt. William Russell, WADC, U.S. Air Forces (WCLSS-3)

LUNCH

High Temperature Effects in Shock Structure:
Hari K. Sen, Air Force Cambridge Research Center

Shock Wave Calculations for High Temperature Gases:
J. D. Teare, AVCO Research Laboratories

Laminar and Turbulent Heat Transfer Measurements on a Hemispherical Cylinder in the Lockheed 3-Inch Shock Tube:
R. Rutowski, Lockheed Aircraft Corporation

A Particular Application of the Conventional Shock Tube for the Study of Ignition and Combustion in Subsonic Flow:
Dr. D. Bitondo, Aerophysics Development Corporation, Curtis Wright Corporation

One Dimensional Blast Waves from an Axially Symmetric Electrical Discharge:
J. Gauger, Lockheed Aircraft Corporation

Closing Remarks:
Roman R. Birukoff, AFSWC

Attendance at the

SECOND SHOCK TUBE SYMPOSIUM

sponsored by the

AIR FORCE SPECIAL WEAPONS CENTER

5 - 6 March 1958
Palo Alto, California

Jay R. Allgood
Naval Civil Engineering Research
& Evaluation Lab.
Port Hueneme, California

O. R. Anderson
Allied Research Associates, Inc.
Boston, Mass.

Olof Anderson
United Aircraft Corp.
East Hartford, Connecticut

P. M. Aronson
Naval Ordnance Laboratory
White Oak, Silver Spring, Md.

George R. Barber, Jr.
Physical Vulnerability Div.
Hq. USAF, Washington, D. C.

William P. Barnes
Atlantic Research Corp.
Alexandria, Virginia

John C. Beckman
Beckman & Whitley
San Carlos, California

Daniel Bershader
Lockheed MSD & Stanford Univ.
Palo Alto, Cal. Stanford, Cal.

R. R. Birukoff
AFSWC
Kirtland Air Force Base,
New Mexico

Domenic Bitondo
Aerophysics Dev. Corp.
Santa Barbara, California

J. Christopher Boison
ARO, Inc.
Tullahoma, Tenn.

James E. Broadwell
Dept. of Aero. Engr.
Univ. of Michigan
Ann Arbor, Michigan

Fred R. Brown
Waterways Experiment Station
Corps of Engineers
Vicksburg, Miss.

K. K. Chan
Lockheed, Palo Alto, Calif.

Robert O. Clark
Ballistics Research Laboratory
Aberdeen Proving Ground, Md.

R. P. Clifford
Dresser Dynamics Inc.
Northridge, California

Charles W. Coale
Stanford Research Institute
Menlo Park, California

George A. Coulter
Ballistics Research Laboratory
Aberdeen Proving Ground, Md.

J. A. Crumley, Jr.
Douglas Aircraft Company
Santa Monica, California

Theodore Davis
United Aircraft Corp.
East Hartford, Conn.

Ralph E. Deem
Douglas Aircraft
Long Beach, California

Richard A. Early
NACA, Ames Aero. Lab.
Moffett Field, California

Col. L. Eddy
Deputy Director of Research
AFSWC
Kirtland Air Force Base,
New Mexico

John M. Edgar
Beech Aircraft Corporation
Boulder, Colorado

Wayne Ehler
Douglas Aircraft
Santa Monica, California

John B. Elliott
Lockheed MSD
Palo Alto, California

Daryl D. Errett
Santa Barbara Res. Center
Santa Barbara, California

Galen Etamad
Lockheed
Sunnyvale, California

James E. Francis
Calif. Advanced Propulsion
Systems Oper.
General Electric Co., Box 336
Danville, California

Edward V. Gallagher
Armour Research Foundation
Chicago, Illinois

J. Ganger
Lockheed MSD
Palo Alto, California

Victor M. Ganzer
University of Washington
Seattle, Washington

M. F. Gates
Hiller Helicopter
Palo Alto, California

Stanley A. Greene
Rocketdyne
Canoga Park, California

William G. Griffin
Air Force Cambridge Research
Center, Hanscom Field,
Bedford, Massachusetts

N. N. Hankin
Convair San Diego
San Diego, California

William G. Harris
Boeing Airplane Company
Seattle, Washington

H. Harrison
Chem. Department
Stanford University
Palo Alto, California

Dr. G. Hecht
Detonation Research Bldg. #128
Engrg. Field Sta., U. of Calif.
Richmond, Calif.

Neil C. Heslin
Sikorsky Aircraft Div.
United Aircraft Corporation
Stratford, Conn.

William W. Higbee, Major, USAF
Hq. Arnold Engineering Dev.
Center
Tullahoma, Tenn.

Harold B. Hopkins, Jr.
Grumman Aircraft Engrg. Corp.
Bethpage, New York

Roger F. Hoppmann
Ryan Aero. Co.
San Diego, California

John W. Jameson
Biophysics Div., Chem. Warfare Labs.
Army Chemical Center, Maryland

Lt. Col. M. McD. Jones Jr.
Hq. AFSWP
Washington 25, D. C.

Robert G. Joppa
University of Washington
Seattle, Washington

Emil M. Kaegi
MOSD General Electric Co.

Kenneth Kaplan
Broadview Research Corp.
Burlingame, California

Milton C. Kells
Stanford Research Institute
Menlo Park, California

Jack M. Kelso
HQ. AFSWP
Washington, D. C.

Gordon Kino
Microwave Lab., Stanford Univ.
Stanford, California

Bernard Kornhauser
Physical Vulnerability Div.
Hq. USAF, Washington, D. C.

Dr. Jack Kotik
TRG, Inc.
New York, New York

Anthony R. Kriebel
Stanford Research Institute
Menlo Park, California

Milton C. Kurtz
Beckman & Whitley, Inc.
San Carlos, California

C. R. Leef
North American Aviation
Los Angeles, California

R. C. Ling
Picatinny Arsenal
Dover, New Jersey

Raymond M. Lockwood
Hiller Helicopters
Palo Alto, California

Joseph G. Logan
Ramo-Wooldridge
Los Angeles, California

R. C. McWherter
Chance Vought Aircraft
Dallas, Texas

Theodore Marshall
Naval Ordnance Laboratory
White Oak, Silver Spring, Md.

Herman Medwin
U. S. Naval Postgraduate School
Monterey, California

Lt. B. S. Merril Jr.
Hq. AFSWP
Washington, D. C. (25)

Carlyle W. Miller
Westinghouse Electric Corp
San Francisco, California

James Mills
Broadview Research Corporation
Burlingame, California

Byron F. Murphey
Minn. Mining & Mfg. Co.
St. Paul, Minn.

George Nagumo
Armour Research Foundation
Chicago, Illinois

Dr. Floyd A. Odell
U. S. Army Medical Research Lab.
Ft. Knox, Kentucky

E. Offenhartz
Research & Advanced Development
Division, AVCO Mfg. Corp.
Lawrence, Mass.

Prof. A. K. Oppenheim, Mech. Engr.
Berkeley 4, California

Howard T. Orville
Beckman & Whitley, Inc.
San Carlos, California

Jack M. Patterson
Beckman & Whitley
San Carlos, California

H. F. Poppendiek
Convair
San Diego, California

Boris Ragent
Broadview Research Corporation
Burlingame, California

D. Richmond
Lovelace Foundation
Albuquerque, New Mexico

Harold S. Robinson
Westinghouse Electric Corp.
410 Bush St.,
San Francisco, California

Robert E. Rohtert
McDonnel Aircraft Corporation
St. Louis, Missouri

Peter H. Rose
AVCO Research Laboratory
Everett, Mass.

Vernon J. Rossow
Ames Aero. Laboratory
Moffett Field, California

Lt. William A. Russell, Jr.
Wright Air Development Center
Dayton, Ohio

R. W. Rutowski
Gas Dynamics Dept. Lockheed MSD
Palo Alto, California

P. R. Ryason
California Research Corp.
Richmond, California

LCDR Edward M. Saunders
U. S. Naval School, Civil Engineer
Port Hueneme, California

Theodore M. Schiffman
Armour Research Foundation
Chicago, Illinois

Hari K. Sen
Geophysics Research Directorate
AF Cambridge Research Center
Hanscom Field, Bedford, Mass.

E. Sevin
Armour Research Foundation
Chicago, Illinois

R. V. Taborelli
Lovelace Foundation
Albuquerque, New Mexico

William J. Taylor
Ballistics Research Laboratory
Aberdeen Proving Ground, Md.

J. Derek Teare
AVCO Research Laboratory
Everett, Mass.

J. R. Thompson
Lockheed, California Division
Burbank, California

George H. Tweney
Pilotless Aircraft Division
Boeing Airplane Company
Seattle, Washington

Eugene B. Turner
Ramo-Wooldridge
Los Angeles, California

Victor Vali
Lockheed MSD
Palo Alto, California

Eric Wang
Air Force Special Weapons Proj
Kirtland Air Force Base,
New Mexico

John A. Weeks
A. F. Cambridge Research Center,
Hanscom Field, Bedford, Mass.

David Weimer
Lockheed Aircraft
Palo Alto, California

Herbert Weisblatt
Research & Advanced Development
Division, AVCO Mfg. Corp
Lawrence, Mass.

Marcus L. Whitfield, Capt.
Hg., AFSWP
Washington, D. C.

James H. Wiegand
Aerojet General Corporation
Sacramento, California

A. B. Willoughby
Broadview Research Corp.
1127 Chula Vista Ave.
Burlingame, Calif.

Thomas A. Zaker
Armour Research Foundation
Chicago, Illinois

Richard Ziemer
Ramo-Wooldridge
Los Angeles, California

TABLE OF CONTENTS

	Page
Welcoming Address.	xiii
AFSWP Interest in Shock Tube Research	1
Shock Tube Wind Tunnel Research at the U. S. Naval Ordnance Laboratory	4
Shock Tube Studies of Blast Pressures behind Frangible Wall Panels	28
A Comparison of Shock Tube and Field Test Data on the Pressure Buildup behind Frangible Walls	44
Some Results of a Shock Tube for Biomedical Investigation . . .	56
Experimentation with the General Electric Six-Inch Shock Tunnel	70
Pressure-Time History in a Chamber Subjected to Shock Wave Filling through an Orifice	101
Determination of the Time History of the Flow Field about Blunt Bodies in a Shock Tube	119
Some Experiments with Periodic Shocks	131
On the Effect of Attenuation on Gas Dynamic Measurements Made in Shock Tubes	133
Generation of Pressure Wave Forms through the Detonation of Explosive Charges	161
Problems in the Use of Piezo-Gages for Shock Tube Instrumentation	191
Determination of the Dynamic Response Characteristics of Pressure Measuring Systems Utilizing Shock Tube Testing Techniques	204
High Temperature Effects in Shock Structure	216
Shock Wave Calculations for High Temperature Gases	237
Heat Transfer Measurements on a Hemisphere-Cylinder in the Lockheed Three-Inch Shock Tube	249
A Particular Application of a Conventional Shock Tube for the Study of Transient Ignition and Combustion in Subsonic Flow	264
One-Dimensional Shock Waves from an Axially Symmetric Electrical Discharge	283

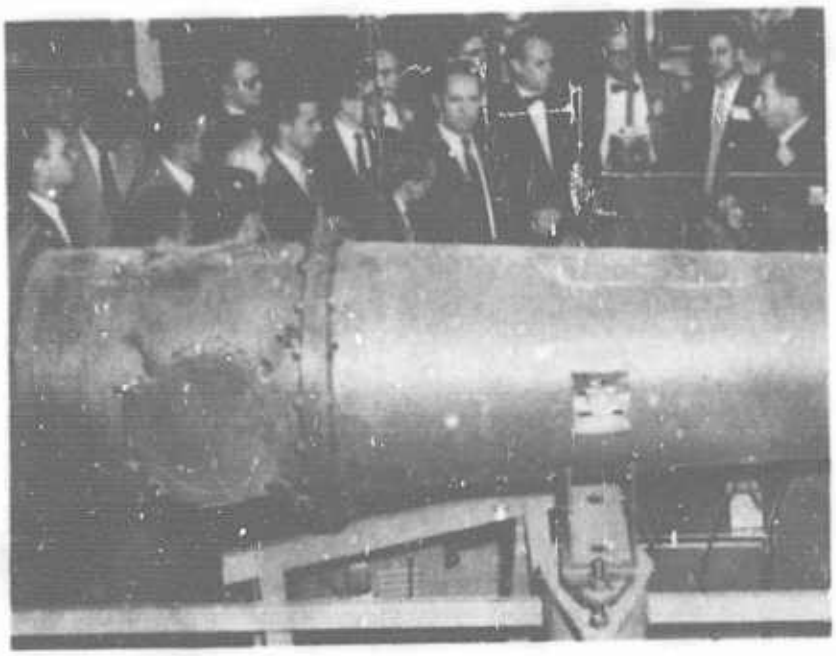

Dr. Bershader (far right) explaining the operation of the spark-heated tunnel.

Dr. Kash (with paper) describing spectroscopic measurements of high temperature plasmas.

A tour was conducted at the Lockheed Missile Systems Division on the first day of the conference, March 5, 1958.

WELCOMING ADDRESS

Colonel Leonard A. Eddy - USAF
Deputy Director
Research Directorate
Air Force Special Weapons Center
Kirtland Air Force Base, New Mexico

On behalf of the Air Force Special Weapons Center, Colonel Eddy welcomed the assembled group. He clarified the reason for the Air Force Special Weapons Center in sponsoring the Shock Tube Symposium by indicating that the Air Force Shock Tube Laboratory at Gary, Indiana is the AFSWC facility. and described its physical characteristics and capability. This laboratory consists of 6 ft, 2 ft and 4 in. diameter shock tubes.

Next, Colonel Eddy emphasized the primary concern of this symposium in keeping abreast with the modern development, techniques, operation and instrumentation of shock tubes, wished a success, and turned the meeting to Mr. Eric H. Wang of AFSWC, who was the moderator th first day of the symposium.

AFSWP INTEREST IN SHOCK TUBE RESEARCH

Jack R. Kelso
Armed Forces Special Weapons Project

It is again a privilege for me to speak before this group concerning the interest of the Armed Forces Special Weapons Project in shock tube research. As many of you are aware, our headquarters is a tri-Service organization which supports various research and development projects in the weapons effects field. The specific objectives of such studies are concerned with problems common to the three Services. Consequently, these projects are usually administered for us by different service groups. Our interest is largely concerned with providing as many answers as possible to these various problems through shock tube research.

I should therefore like to discuss the use of shock tubes in terms of the application of the information which is obtained rather than from the operational viewpoint. In particular, I would like to consider current trends in shock tube research with some attention to a recent change of philosophy which is quite significant. Many of you were present last year at the First Annual Shock Tube Symposium held in Boston. At that time, I listed the three types of investigations which are usually carried out in the shock tube; namely,

(1) Studies of basic phenomena,
(2) Loading of objects,
(3) Response of objects.

Further, I stated that most of the effort in the weapon effects field up to that time was concerned with the first two items; namely, basic phenomena and loading of objects. It appeared then that only limited response tests were feasible in the shock tube because of size and other considerations, such as modeling, which could not always account for mass and gravity effects. Consequently, response tests as such were usually confined to proof tests of small components to determine damage and translation.

However, it now appears that response tests can be successfully designed for the shock tube which will give information on the mode of failure of a particular item. Such information, when coupled with loading data on a non-responding model, can be used to calculate the response of a much larger structure. An example of this procedure might be a recent program conducted by the Armour Research Foundation in the six-foot shock tube at Gary, Indiana to determine the blast loading and response of floating roof oil storage tanks. Very heavy lead models were used to obtain air blast loading information for various shock strengths and degrees of filling. Scaled models containing water and mercury were also tested to find modes of response. The results of these tests were used to develop a generalized blast loading procedure which is now being applied in an extensive analytical program. When this program is completed, reliable predictions of damage to such structures can be made under a variety of conditions.

Other examples of response testing are equipment checkout and aircraft components. The tests of various aircraft components were described by Dr. Schiffman of Armour Research Foundation last year. Equipment checkout includes tests of miniature gages for shock tube use as well as large field gages such as dynamic pressure and total force gages and also, complex recording and telemetering equipment. Incidently, such field instrumentation as well as models can further be tested under simulated environmental conditions when particulate matter such as water or dust is introduced into a shock tube. The shock wave passes through such material and the loading and response of particular items are then compared to similar data involving only clean air.

Due to the successful results obtained during these various response tests in the past year, the interest of the AFSWP has turned more to the loading and response of objects and less to the basic phenomena. It is felt that in many area detailed information can be obtained by a shock tube program at a very reasonable cost while a similar amount of data could not be obtained in the field during an atomic test because of economic or practical reasons. A particular model can be investigated in the shock tube under as many different conditions as you may wish to impose, that is, an almost infinite variation of parameters. And of course, reproducibility can be easily determined while a full-scale structure is usually tested on a one-time basis only. Therefore, we feel that the shock tube is the best place to conduct fundamental studies and thus narrow the limits of uncertainty.

A properly designed shock tube program enables one to determine the relation between free field blast phenomena and the loading of representative targets which can then be extended to full-scale conditions through the proper scaling. In many cases the requirement for exposure to an atomic blast wave can be reduced or eliminated through shock tube research. In other cases information can be obtained which will assist in planning or analyzing the results of a full-scale test. The ultimate use of all such information is in its application to structural response and damage; for example, data of this nature is contained in the unclassified AEC-DOD publications, "Effects of Nuclear Weapons" (1957), which supercedes the "Effect of Atomic Weapons" (1950) I mentioned last year.

At that time I also mentioned a number of areas in which further work seemed necessary. These concerned the development of shock tube capability to provide higher shock strengths and longer durations as well as more direct methods for measuring particle velocity and dynamic pressure. A large amount of work has been carried out in these areas which, in fact, are becoming more important each day, particularly with respect to the protective construction field. For example, reliable data has been obtained for shock strengths up to ten in the 6-foot shock tube by evaucating the expansion section. Higher shock strengths up to 35 have been observed, but the gages broke down quickly so that it was not possible to obtain loading information. Also during this period the Ballistic Research Laboratories began the construction of a high pressure shock tube so that tests can be carried out at ambient atmospheric pressure for overpressures up to 300 psi while the normal relations between shock parameters can be obtained.

Other effort has been concerned with developing a miniature dynamic pressure gage or q-gage at both of these agencies. Some progress has been made but neither gage is currently available in operational status. The Ballistic Research Laboratories has been successful in developing a transient force balance which has given drag coefficients which are in general agreement with those derived from wind tunnel and full-scale tests. However, in the 6-foot shock tube a full-scale q-gage will be used to obtain some knowledge of the actual flow field in order to obtain more reliable drag coefficients.

In addition to those tasks I have already mentioned, other current AFSWP projects involve the blast loading of ship superstructures, pickup of water by shock waves, loading and response of arches and domes in the high pressure region as well as tests of entranceways and ventilation systems, and also terrain effects and shielding and biomedical experiments.

In conclusion, I would like to mention that the interest of the AFSWP in future shock tube work lies in the utilization of higher pressures to obtain blast loading information on other structural configurations as well as additional gage calibration. It is hoped that the miniature q-gage development can be successfully accomplished in the near future. At the same time, longer durations are desired to provide further information on transient drag coefficients. However, the progress of work presently being done in these areas leads one to believe that the shock tube will continue to be an efficient and economical means to obtain a large amount of useful information that can be readily applied to military problems in the weapons effects field.

SHOCK TUBE WIND TUNNEL RESEARCH

AT THE U. S. NAVAL ORDNANCE LABORATORY

P. M. Aronson, T. Marshall, A. E. Seigel,
Z. I. Slawsky and E. F. Smiley

I. Description of Facilities

The U. S. Naval Ordnance Laboratory has been pioneering the use of hypersonic shock tunnel as aerodynamic tools since 1951 when Dr. Ernst H. Winkler conceived and constructed at NOL a simple model utilizing a 0.50 caliber gun barrel as the low-pressure chamber with a hydgrogen-oxygen driver. At that time a conical nozzle was fastened to the end of the 0.50 caliber gun barrel, transforming the shock tube into a shock tube wind tunnel (shock tunnel) capable of producing a flow of argon at a velocity of Mach 5 at one atmosphere free stream pressure. The 0.50 caliber shock tunnel provided too short a blowing time to be of much use aerodynamically so that interest was soon shifted to larger facilities.

A table listing the shock tunnel facilities at the Naval Ordnance Laboratory is shown in Figure 1. Each facility is identified by the inside diameter of its low-pressure chamber. A 20mm, a 40mm, a 1-3/4-inch, and a 4-inch shock tunnel comprise the list of shock tunnel facilities. All but the 4-inch shock tunnel are presently in use at the Laboratory. Installation of the 4-inch shock tunnel is now taking place, and this facility is expected to be in operation 15 May 1958.

The table shown in Figure 1 compares the various dimensions of the four shock tunnels. The lengths of the low-pressure chambers are given in calibers; that is, length divided by diameter. The 61-foot-long, low-pressure chamber of the 4-inch shock tunnel is expected to provide a blowing time in the millisecond range, which is twice as long as the blowing time obtained with the 40mm shock tunnel. Because the 4-inch shock tunnel is so constructed as to permit lengthening of the low-pressure chamber, the blowing time of this tunnel can be varied correspondingly.

In order to increase driver efficiency, each shock tunnel makes use of chambrage; that is, each utilizes a high-pressure chamber having an inside diameter larger than the inside diameter of the low-pressure chamber. If chambrage is a number representing the ratio between inside diameters of the high and low-pressure chambers, then (see Table I), the amount of chambrage used in the 20mm, 1-3/4-inch, and 4-inch shock tunnels is about the same, approximately 2.5. The chambrage on the 40mm shock tunnel is less, about 1.75.

The high-pressure chambers of the 20mm, 1-3/4-inch and 4-inch shock tunnels have been designed to withstand internal pressures in excess of 60,000 psi. The high-pressure chamber of the 4-inch facility is actually an 8-inch Naval gun bored out to 10 inches. The 40mm shock tunnel has also a gun-like high-pressure chamber which is capable of withstanding combustion pressures of 110,000 psi. High-pressure chambers designed to withstand such high internal pressures are required in shock tunnels to produce very strong shock waves in air which is considerably above sea-level density.

The ratio of low to high-pressure chamber lengths for each facility is listed in the table. Proportional to its length, the 4-inch shock tunnel has the longest high-pressure chamber, it being 13 feet long and having an internal volume of 7.3 cubic feet.

Both the 20mm and 1-3/4-inch shock tunnels have 30 degree, total angle, conical nozzles located at the end of the low-pressure chamber. However, unlike the 20mm shock tunnel, the 1-3/4-inch shock tunnel has a restricted nozzle in order to increase the blowing time in the test section. At the present time the 40mm shock tunnel is operated without a nozzle. The working gas is allowed to expand freely from the end of the low-pressure chamber inside the dump chamber. Provision has been made to mount a pick-up nozzle away from the end of the low-pressure chamber to convert the radial flow into parallel flow. The 4-inch shock tunnel is to be operated in a similar manner.

In contrast to the size of the 4-inch facility, the 20mm shock tunnel has an overall length of 17 feet, 6 feet of which are required for the nozzle, test section, and dump chamber. Although the blowing time of this tunnel is about 180 microseconds, of which only 60 microseconds can be considered as being steady, a number of measurements have been carried out in the test section. The measurements include those of static pressure, pitot pressure, and heat transfer, as well as the photographing of the flow over models by means of high-speed camera techniques.

The 20mm shock tunnel is shown in Figure 2. In the background appears a Beckmann-Whitley high-speed framing camera used for recording the flow in the test section. The simple loading and control panel for the 20mm shock tunnel is shown in Figure 3. At the left appears a free-piston compressor and oil pump for compressing hydrogen to pressures in excess of 8000 psi.

In Figures 4 and 5 are shown the 40mm shock tunnel and control room for that facility. The bank of oscilloscopes shown in the center of Figure 5 is used for recording pressure distributions over models placed in the test section of the 40mm tunnel.

The 1-3/4-inch shock tunnel appears in Figure 6.

II. Operating Conditions for the Shock Tunnels

Today attention is being focussed on the re-entry problem where missiles re-enter the earth's atmosphere at very high velocities. In addition to making heat transfer and pressure measurements on aerodynamic

shapes under re-entry conditions, observation of boundary layer build-up and wake associated with the high-speed missile flight is highly desirable. In order to observe boundary layer and wake in the laboratory using scaled-down models, the density of the air flowing in the test section of a shock tunnel must be at least 0.01 amagat, where 1.0 amagat unit is the density of air at 0°C and 1 atmosphere pressure.

Simulation, for example, of Mach 13 flight in air at a temperature of 0°C and 0.01 amagat density is not easily achieved in a shock tunnel. In order to provide these conditions, the working gas, initially at a pressure of 6.5 atmospheres, must be compressed to a pressure of 11,000 psi by a shock wave traveling at Mach 9.5.

The production of a strong shock wave in such dense air requires a driver gas raised to a very high pressure and temperature. Such pressures and temperatures can be obtained simultaneously using combustible gas mixtures in the high-pressure chamber. Hydroger and oxygen mixtures with or without helium added, appear to be the most popular in use. Measurements made on the 40mm shock tunnel indicate that approximately 50,000 psi combustion pressure in an oxygen-hydrogen-helium mixture produces a Mach 9 shock wave in initially 4 atmospheres of air. In this case the air behind the shock wave is compressed of 6500 psi. It appears, therefore that a combustion pressure in excess of 100,000 psi is required in the high-pressure chamber of the 40mm shock tunnel in order to drive the necessary Mach 9.5 shock wave in 6.5 atmospheres of air and thus simulate the flight conditions of Mach 13 at 0.01 amagat density in the test section. Increasing the combustion pressures above 100,000 psi in this case is not a feasible solution since one must contend with the ultimate strength of the high-pressure chamber itself. The high-pressure chamber of th. 40mm tunnel is able to withstand pressures in excess of 100 000 psi. It would be quite unwise, however to operate at this pressure level which leaves little or no margin of safety.

Because of the practical limitations of physical size, cost, and safety, it is quite unlikely that we shall be able to simulate the desired flight conditions using the conventional single-stage shock-driving technique. For this reason, our group at the Naval Ordnance Laboratory has turned its attention to investigating more efficient drivers and shock-driving methods. One such method[2] for producing strong shock waves more efficiently involves the use of the two-stage driver. The high-pressure chamber in this case consists of two sections and is essentially a shock tube. This shock tube, however, differs from the conventional shock tube in that the gases in both chambers are combustible mixtures. After the gas in the low-pressure chamber has been ignited and reaches its combustion pressure and temperature, the mixture in the high-pressure chamber is ignited resulting in further

---

[2] A. E. Seigel and Z. I. Slawsky, NavOrd Report 4345, 30 July 1956.

compression and heating of the gas in the low-pressure chamber by the shock wave which is formed. By properly designing the fold-back diaphragm separating the driver section from the working gas section of the main shock tunnel, the diaphragm can be made to open only after the incident shock wave in the driver section has been reflected. The reflected shock wave further heats and compresses the driver gas, making it much more efficient as a driver or producer of shock waves in the working gas. Sound speeds in the driver gas as high as 10,000 feet per second should be easily obtainable with the two-stage driver. A unit is being constructed at the Laboratory at the present time, and we hope to be able to report on its success in the near future.

III. New Ignition Systems for Combustion Drivers

One of the possible dangers involved in the use of oxygen-hydrogen mixtures as combustion drivers is that the gas may detonate rather than burn when it is ignited. When a detonation occurs, the pressure behind the detonation front may reach many times the normal combustion pressure of the mixture. Because of the possibility of detonation, for safety reasons an upper limit must be placed on the loading pressure for a particular high-pressure chamber. If detonation could be prevented from occurring, then it would be possible to operate at much higher loading pressures.

It is generally known that detonation in mixtures of oxygen and hydrogen with or without helium can be largely prevented by igniting the mixture at many points simultaneously. The method generally used by shock tunnel groups to ignite driver gas without detonation employs separate spark plugs at each ignition point along the high-pressure chamber. This requires a separate capacitor to store electrical energy for each spark plug and separate thyratrons for permitting the capacitors to dump their charges simultaneously. The worst feature of this arrangement is that a detonation can occur when one or more of the spark plugs or thyratron circuits becomes inoperative. Another problem results from the large electrical discharge which takes place during the ignition pulse. For long chambers requiring a large number of spark plugs and capacitors, the electrical discharge can set up an electrical field resulting in interference with measurements of pressure, velocity, and heat transfer. For these reasons our group has devoted some time to finding an ignition system which does not have these two inherent faults.

Two ignition systems based on the injection of hot gas into the high-pressure chamber have been developed at the Naval Ordnance Laboratory and have been used successfully for igniting combustion mixtures in high-pressure chambers.

One of the methods of injection for igniting the gas at a number of points simultaneously makes use of a small ignition chamber external to the high-pressure chamber, with equal-length tubes leading from it to various points along the high-pressure chamber. Figure 7 is a picture of the "spider" arrangement. A single spark plug is used to ignite the gas mixture in the ignition chamber. The injection tubes are mounted symmetrically around the spark plug. These tubes, having an inside diameter of 1/16 inch and an outside diameter of 1/4 inch, are of steel, able to withstand pressures in excess of 100,000 psi.

When the combustible mixture in the small chamber is ignited, the burning gas in the chamber causes the gases in the various injection tubes to be ignited simultaneously. Since these tubes are of equal length and the burning rates in the tubes are the same, burning gas is expelled from the ends of the tubes at the same time. With this arrangement it is possible to ignite the gas mixture in the high-pressure chamber at any number of points simultaneously using a single spark plug.

An alternate to this external injection system of ignition is a more simple internal injection. Figure 8 is a photograph of the injection rod used to ignite the gas in the high-pressure chamber of the 20mm shock tunnel. This arrangement consists of a single steel rod fastened to one end of the breech plug. The rod, which seals the end of the high-pressure chamber, has an inside diameter of 3/16 inch and an outside diameter of 9/16 inch with 1/16-inch diameter holes drilled through the wall of the tube every three inches. The breech plug is bored out at one end to create a small ignition chamber for the gas in the injection tube. The gas in the ignition chamber is ignited by means of a single spark plug located in the end of the breech plug. When the gas in the injection tube is ignited by the flame front produced in the ignition chamber, the reaction proceeds down the injection tube. Hot gas from the injection tube is expelled through the 1/16-inch holes in the walls of the injection tube as the reaction proceeds down the tube, causing ignition of the gas in the main volume of the high-pressure chamber. This method of ignition has been used successfully in oxygen-hydrogen mixtures for almost 100 firings, and it appears that in none of these cases did detonation occur.

IV. Pressure and Temperature Measurements on Models

The 40mm shock tunnel is at present used as an aerodynamic model testing facility. A second similar facility is soon to be in operation for the same purpose. Emphasis is being placed here on pressure distributions and heat transfer measurements over models under missile re-entry conditions. At present these tests are being carried out using free jet flow rather than a contoured nozzle flow. While use of this system necessarily means testing in a radial flow, the system has the advantage of simplicity; it reduces the time for establishment of flow in a nozzle.

Figure 9 is a schlieren photograph of a set of small spheres mounted about the axis 7-1/2 inches from the shock tube exit with 3/4-inch spacing. Figure 10 shows a similar set of spheres located off axis. These schlieren photographs illustrate the radial nature of the flow in the jet.

Figure 11 is a schlieren photograph of the free jet flow over a 3/4-inch diameter sphere showing wake configuration and luminosity, somewhat optically suppressed in this case. The wake is clearly visible despite the crudeness of the schlieren system used. The flow velocity here is about 12,000 ft/sec (Mach 5) with 60 atmospheres of stagnation pressure and 3 amagats of free stream density.

A typical pressure distribution measurement taken over a hemisphere cylinder is shown in Figure 12. This measurements was made on a model 22 inches from the jet in a flow of Mach number 8.5. Here the flow is so slightly radial as not to influence the pressure distribution; this can be seen from the variance of the data from the data corrected for radial flow. The transducers used in these measurements were both of the piezoelectric and strain gage type. The strain gages bonded to magnesium beams were developed at NOL by Mr. V. C. Dawson and Mr. R. H. Waser.

Because miltichannel techniques are believed to be very advantageous in testing facilities of this type, the development of miniature ceramic piezoelectric pressure transducers and of mounting techniques for the ceramic elements is being emphasized. A 22-channel system of 3-inch oscilloscopes is expected to be in operation soon for these recording purposes.

V. Stagnation Temperature

Stagnation temperature measurements have been attempted using a sound velocity probe. This probe is essentially an open ended cylindrical acoustical cavity shown diagrammatically in Figure 13. At the closed end of the cavity there is placed a pressure transducer of barium titanate ceramic used to electronically record the cavity oscillations. The oscillation wave length is constant and depends only on the cavity dimensions; there the sound velocity of the gas in the cavity is directly determined by measuring the oscillation frequency. By directing the probe into the flow of a shock tunnel or shock tube, the cavity becomes a self-excited stagnation temperature probe for a gas of known equation of state. Such a condition is illustrated by the oscilloscope record shown in Figure 14. In this figure a probe of 0.2-inch cavity length was excited by the low velocity flow behind a weak shock wave. Blanking of the trace occurs at ten microsecond intervals. Small bleed holes (not shown in the figure) are used to allow the gas heated by the reflected shock to escape.

In the case of a shock wave or the flow in the shock tunnel, the probe becomes self-excited because the increase in ambient pressure in the cavity occurs in a time interval which is short compared to the natural period of oscillation of the cavity. When excitation by pressure pulses do not occur, oscillations may be produced by an electronic means. It is interesting to note that the pressure in the cavity may also be obtained from the gage reading. The device seems very promising, and quantitative evaluation is now being conducted.

VI. Force Measurements

Force measurements have been problematic in shock tunnels since their inception. The difficulty lies in the extremely short flow periods, usually of the order of 10^{-3} seconds available for measurements. A high-speed photographic technique has been developed at NOL which makes such measurements possible. This method utilizes a high-speed framing camera, the Beckmann-Whitley Model 189 and very light models.

The models are suspended in the test section by fine wires. A series of exposures is then made of the stationary model with the framing camera. Next, a second series of exposures is made on the same film strip during the flow period of the shock tunnel. The resulting film strip consists of a series of double exposures, one exposure before the flow and the other during the flow showing the displacement of the body relative to its initial position. Each frame therefore indicates the change in position of the model due to aerodynamic forces, while the framing rate of the camera gives the period of time between frames. This set of data is found to be sufficient to determine the drag forces on light spheres and models of missiles during the very short flow time of the shock tunnel.

A typical double exposure is shown in Figure 15 of a ping pong ball 2.51 gm of 3.78 cr diameter. This photograph was taken 32 microseconds after the onset of flow. The suspension wire, clearly visible on the stationary model, broke and blew away after the first few microseconds of flow.

Figure 16 is a plot of the trajectory of one other such sphere. The solid curve is a parabola fitted through the three points indicated by vertical bars. The acceleration due to this drag force here is 18,000 g's.

VII. Shock Wave Attenuation by Microwave Technique

A large number of shock wave attenuation studies have been made at NOL. Two experimental techniques have in the main been used in these studies. The first of these, a standard technique, makes use of ionization probes located in the shock tube wall. The second technique is a microwave method.[3] Here a microwave signal is reflected head-on from the ionized shock front. The phase of this reflected signal is continually compared with that of the microwave oscillator by conventional waveguide circuitry, so that the passage of the shock wave through a distance equal to one half of a wavelength gives rise to an oscillatory signal from a microwave detector. Now each period of the detected signal represents the transit of the shock wave over a distance of exactly one half wavelength. By suitably displaying this signal on an oscilloscope raster in conjunction with timing markers, the shock velocity history can be obtained over a large number of experimental data points, each at every half wavelength distance.

Some typical data are shown in Figure 17. The uppermost points represented by triangles are the data for a shock produced in one atmosphere of air by a hydrogen-oxygen combustion which ruptured a scribed steel diaphragm. The circles are the data for a free-piston driven shock, a 2.5 gram magnesium piston. The first seven points are the piston velocity points since there is surely no ionization at these velocities. As the piston accelerates it produces a stronger shock wave which becomes ionized. This strong shock then begins to reflect the microwaves, thus accounting for the break in data points.

Both sets of shock wave attenuation data were made in a one half inch diameter tube with the same hydrogen-oxygen driving pressure into one atmosphere of air.

---

[3] E. H. Winkler, "Latest Results in the NOL Shock Tube Wind Tunnel" Conference on Supersonic Flow, University of Maryland (March 1954)

NOMINAL DIMENSIONS OF N.O.L. SHOCK TUNNEL FACILITIES

Name of Facility	20 mm H.S.T.	40 mm H.S.T.	1 3/4 in. H.S.T.	4 in. H.S.T.
Low Pressure Chamber				
1. I.D.	20 mm	40 mm	1.734 in.	4.0 in.
2. Length (cal.)	161	200	200	182.8
High Pressure Chamber				
1. I.D.	2 in.	2.75 in.	4 in.	10 in.
2. Length	19.25 in.	41 in.	60 in.	160.8 in.
3. Ratio of length of L.P.C. to H.P.C.	6.60	7.68	5.75	4.54
Type Nozzle	30° cone	Free exp.	30° cone w. restriction	Free exp.
Test Section and Dump Chamber				
1. I.D.	10.25 in.	40 in.	28 in.	93.63 in.
2. Length	4.33 ft.	30 ft.	13 ft.	53 ft.

Figure 1 Table Giving NOL Shock Tunnel Dimensions

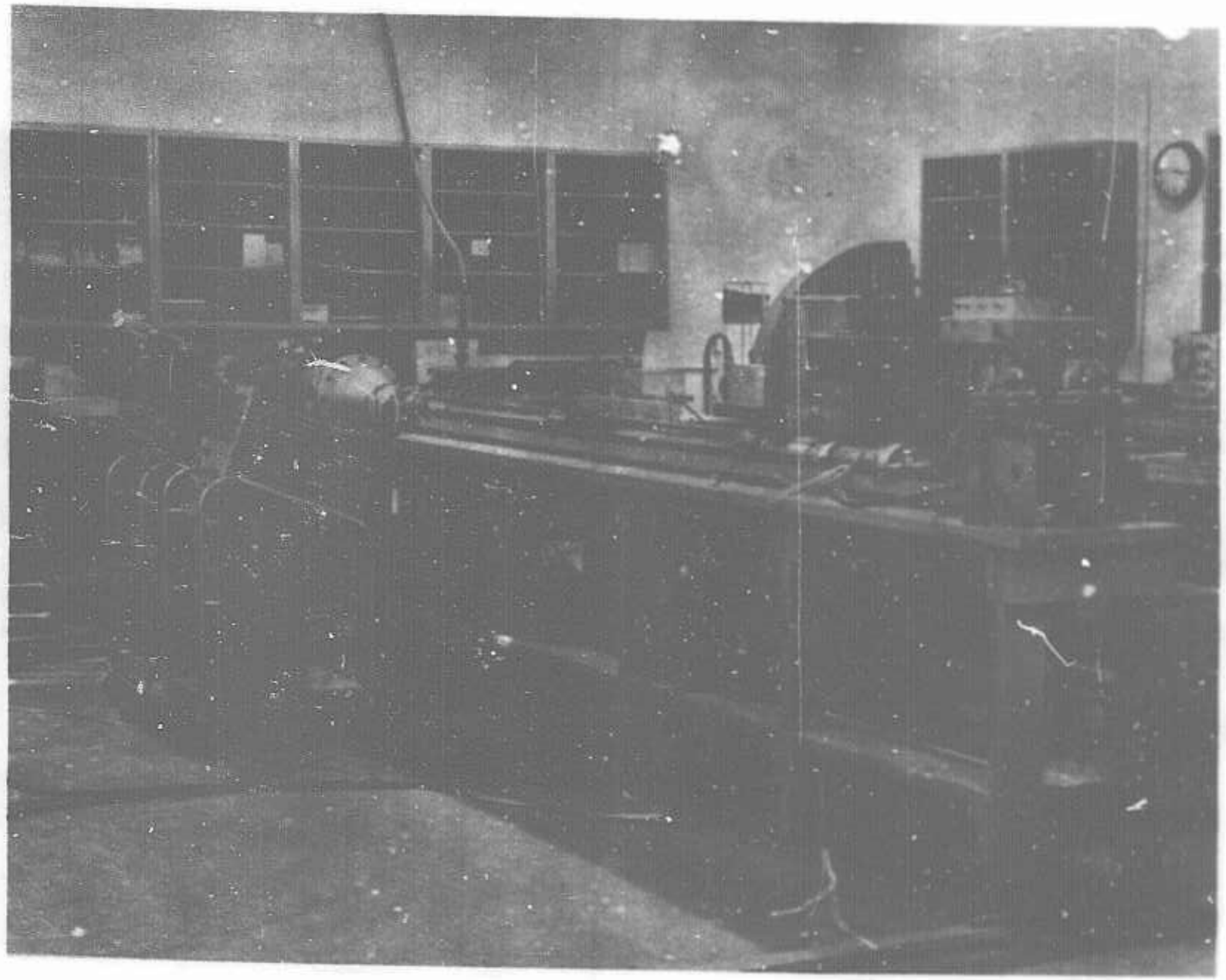

Figure 2 20mm Shock Tunnel

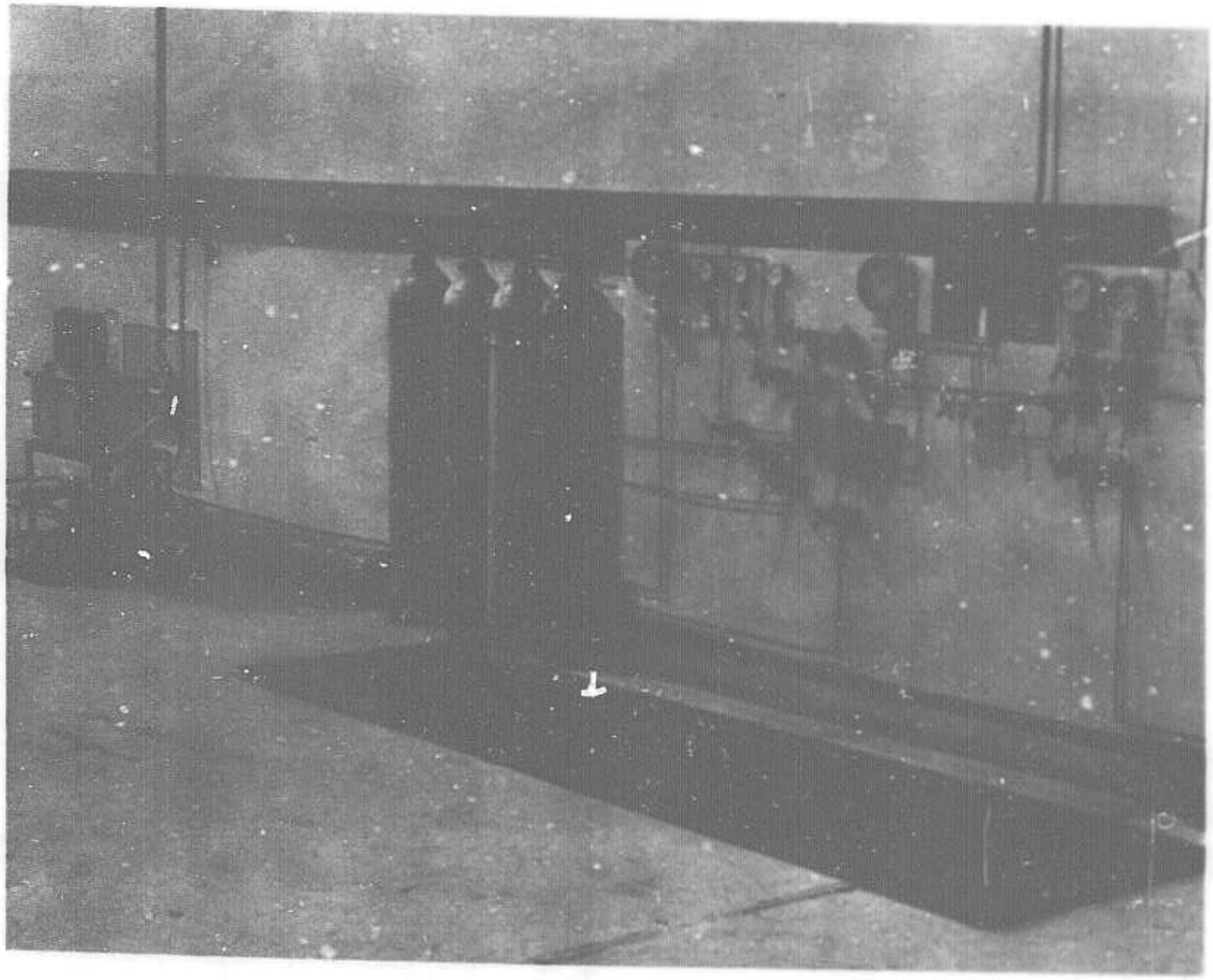

Figure 3 Loading and Control Panel for 20mm Shock Tunnel

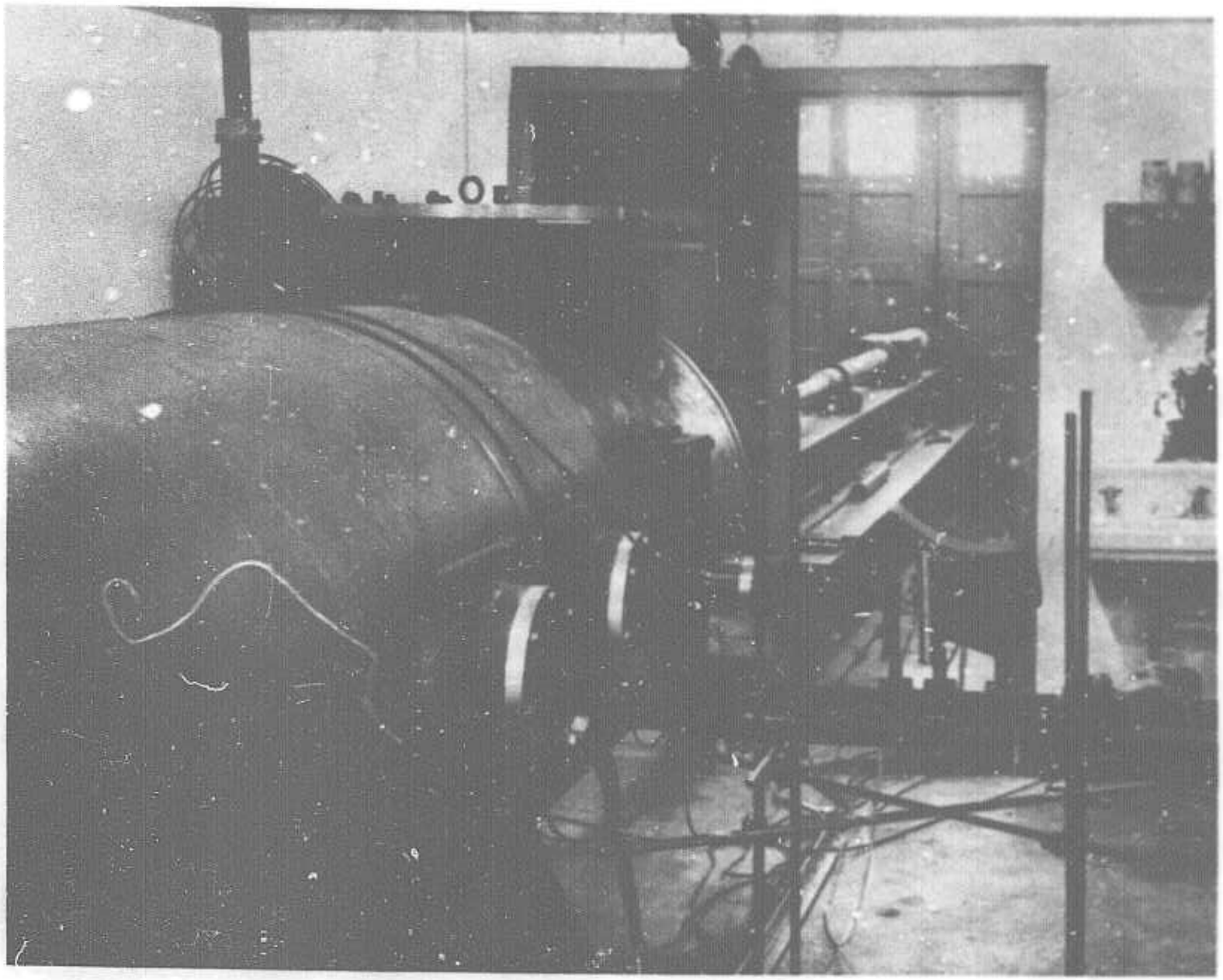

Figure 4 40mm Shock Tunnel

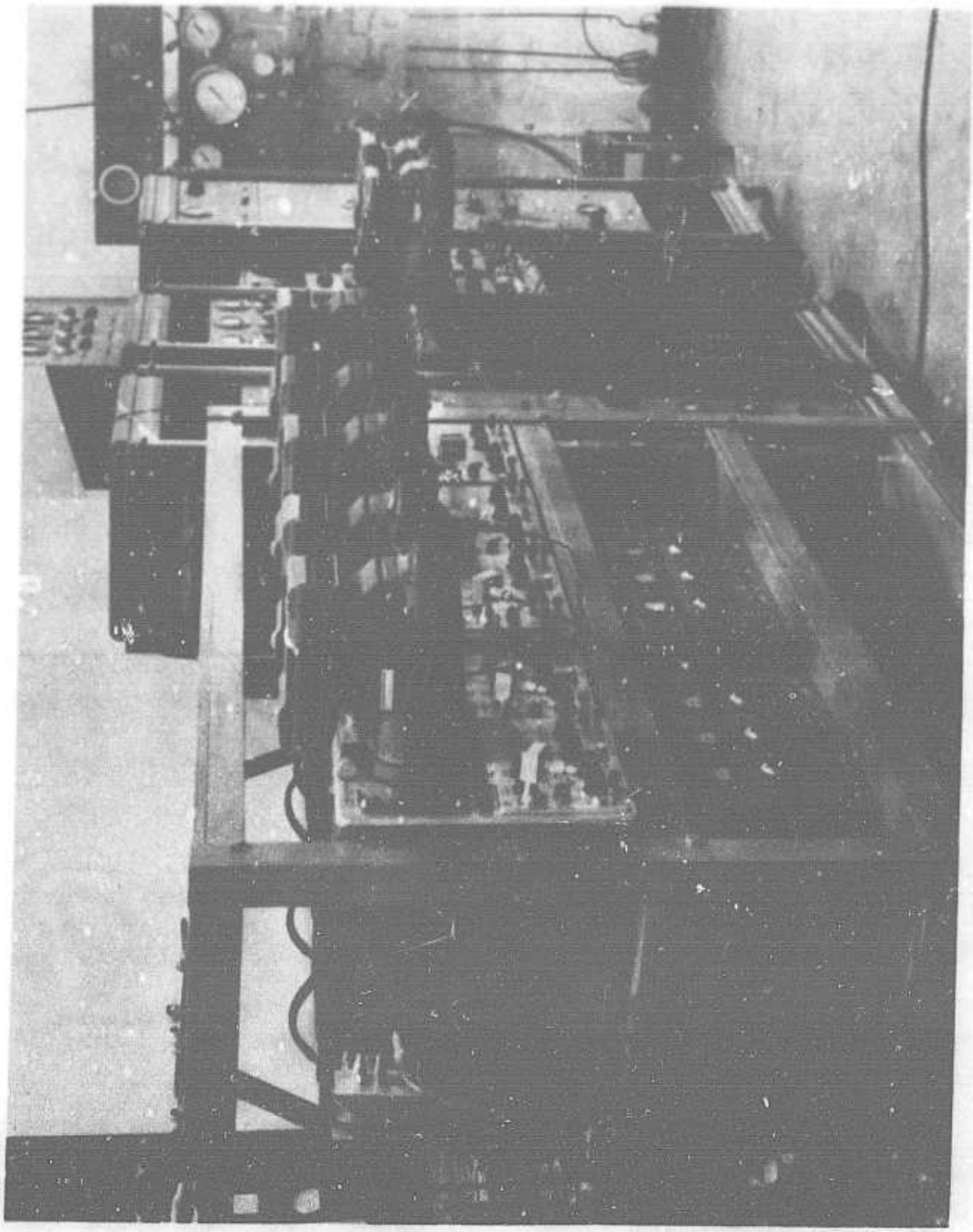

Figure 5 40mm Control Room Showing Loading Panel and Rack of Oscilloscopes for Recording Pressure on Models

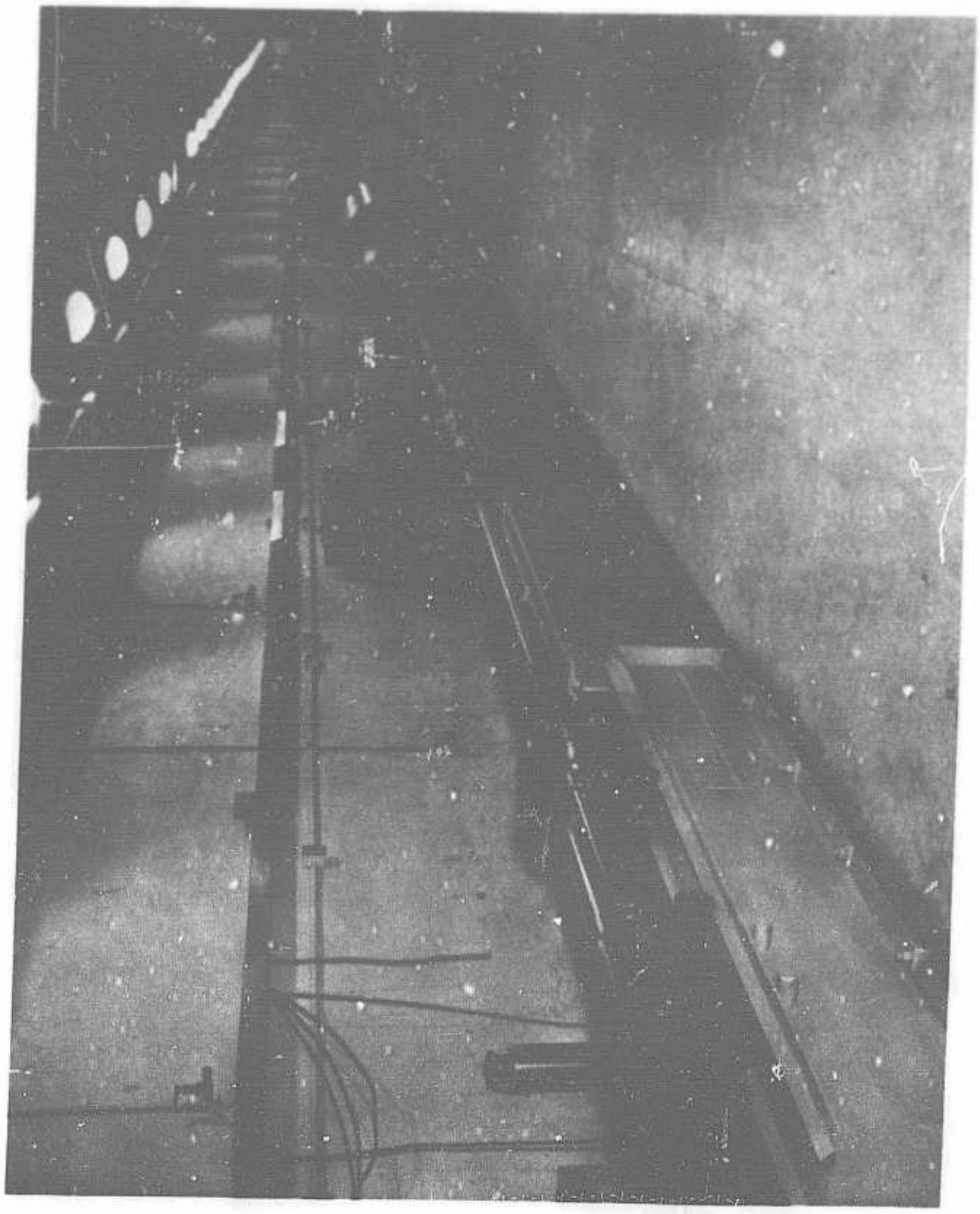

Figure 6 1-3/4 Inch Shock Tunnel

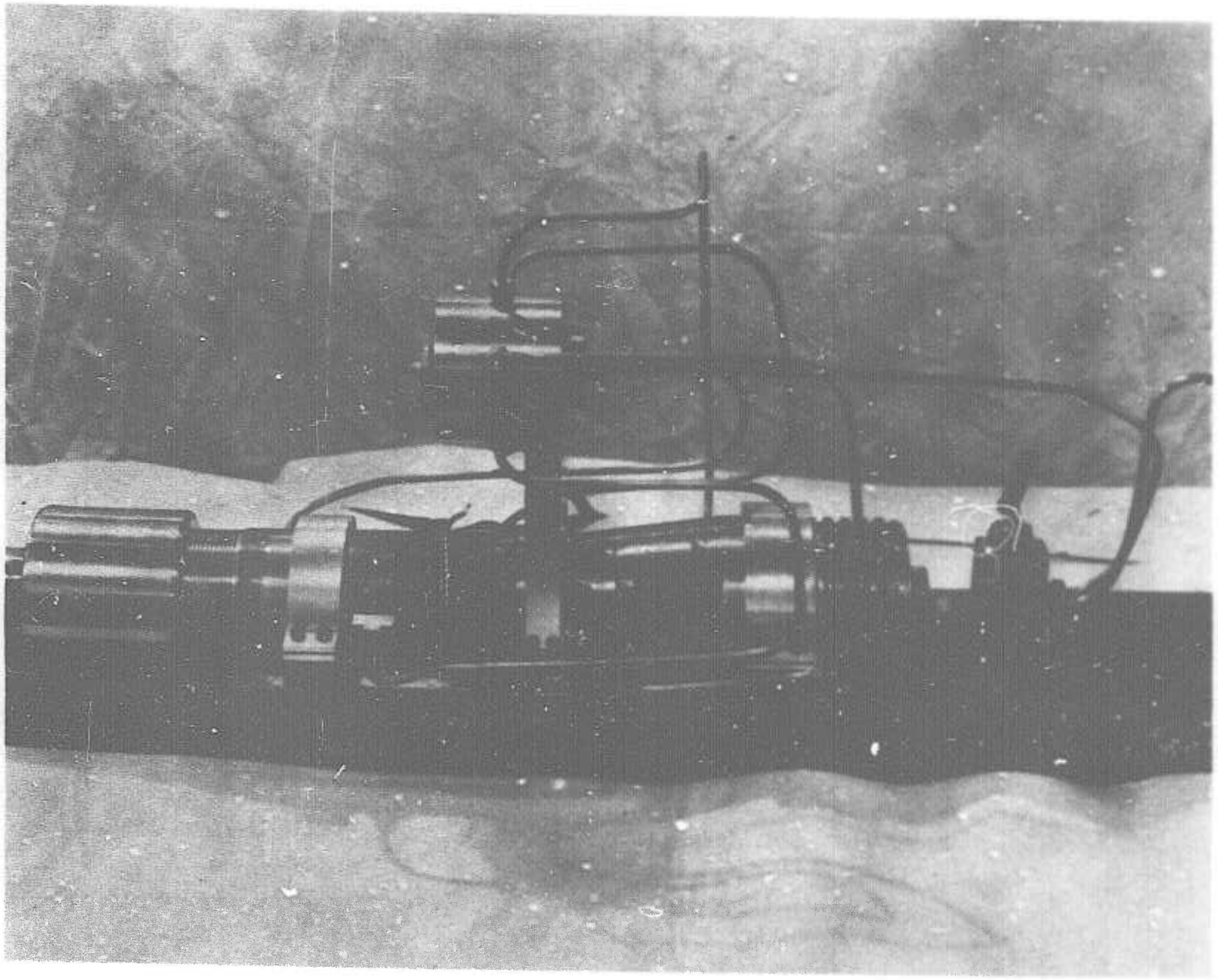

Figure 7 External Jet Ignition System

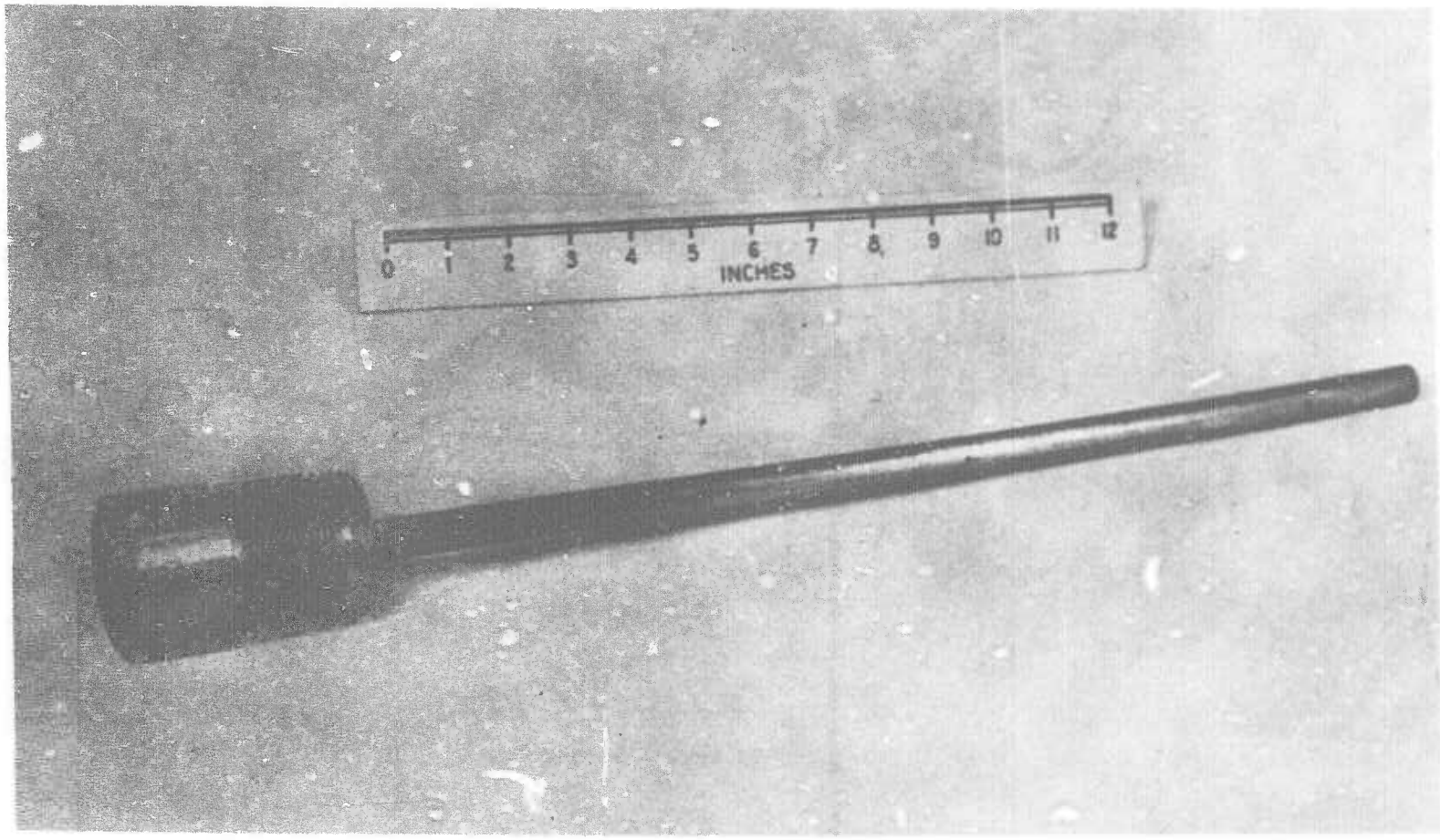

Figure 8 Internal Jet Ignition System

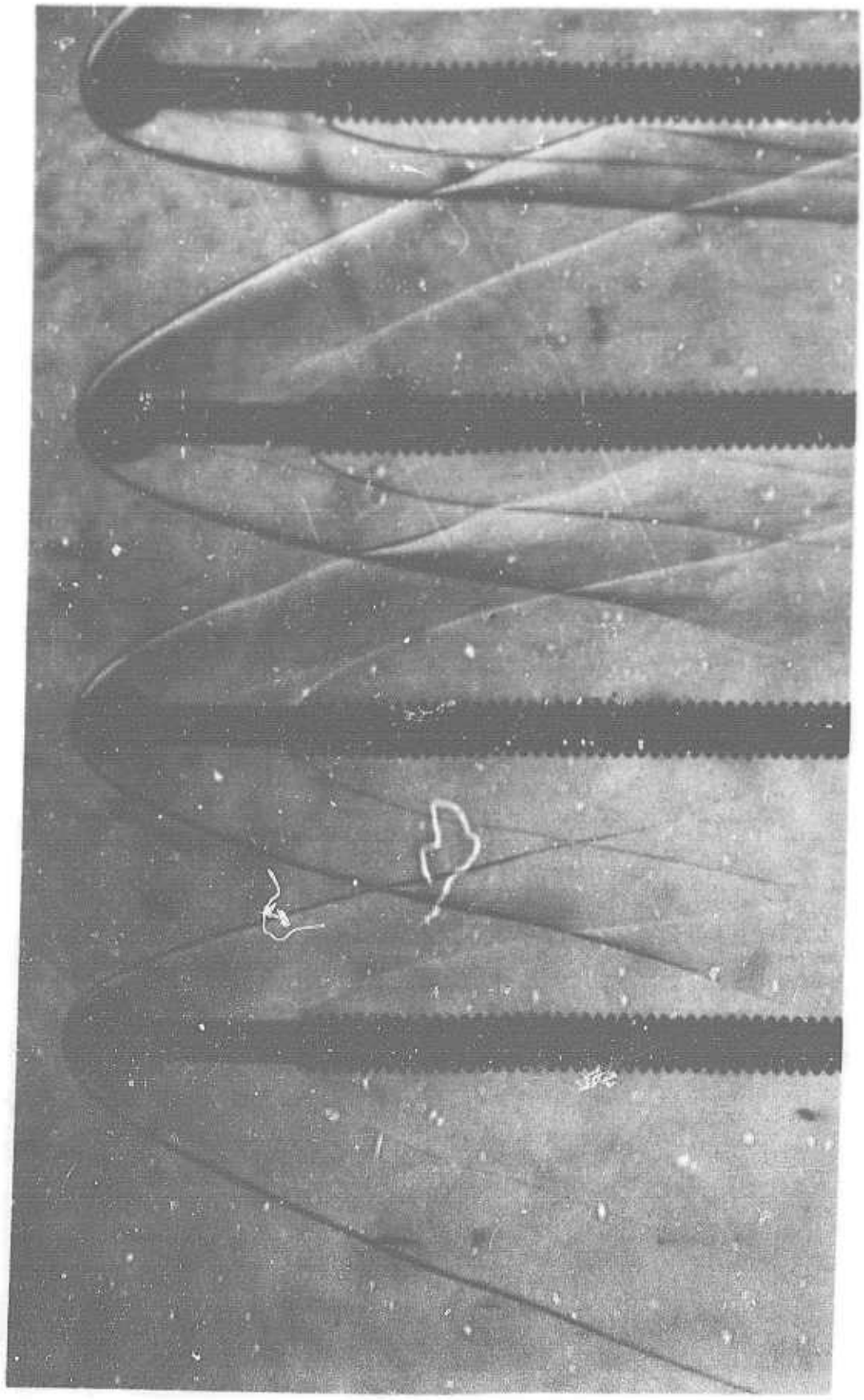

Figure 9

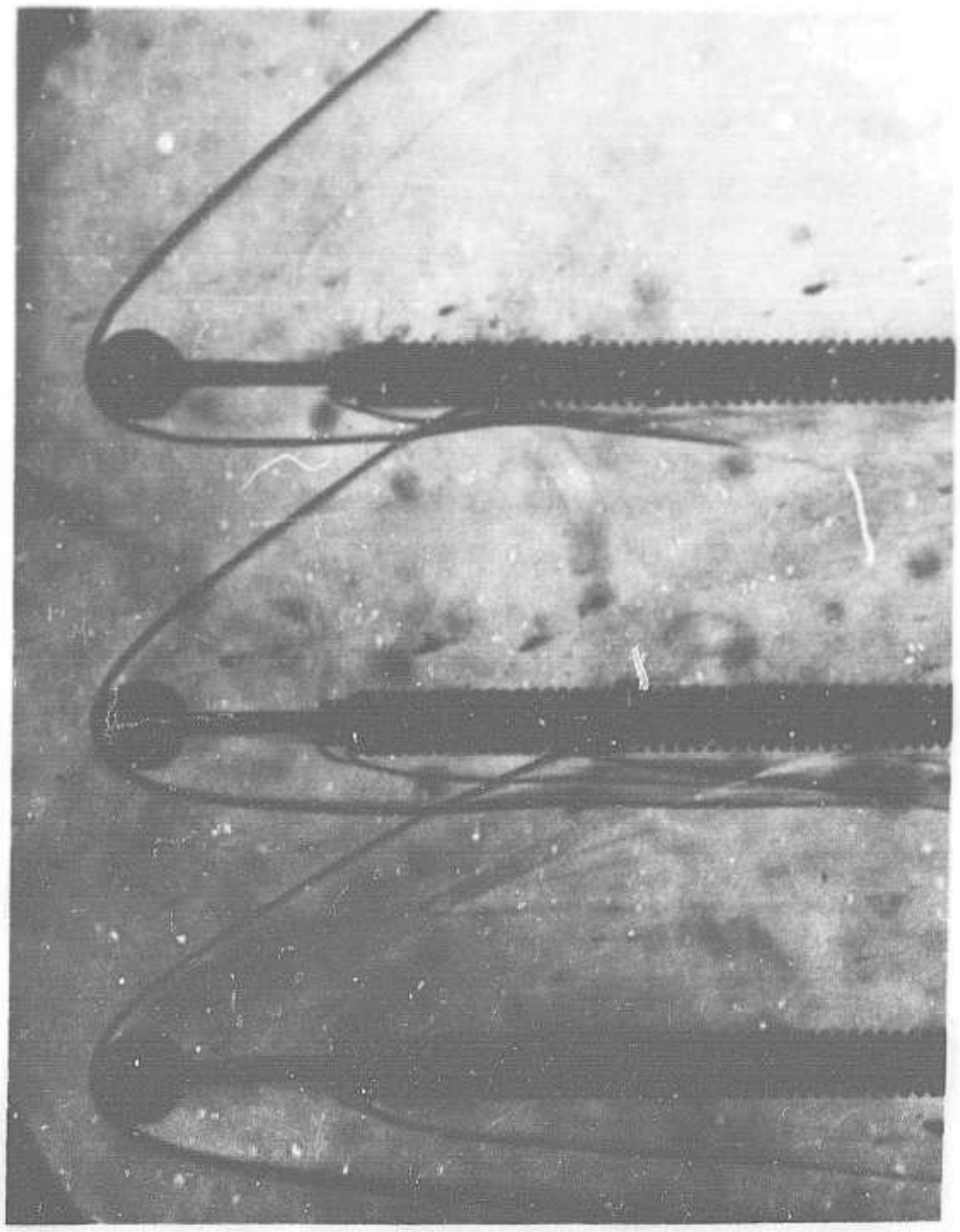

Figure 10

Figure 11

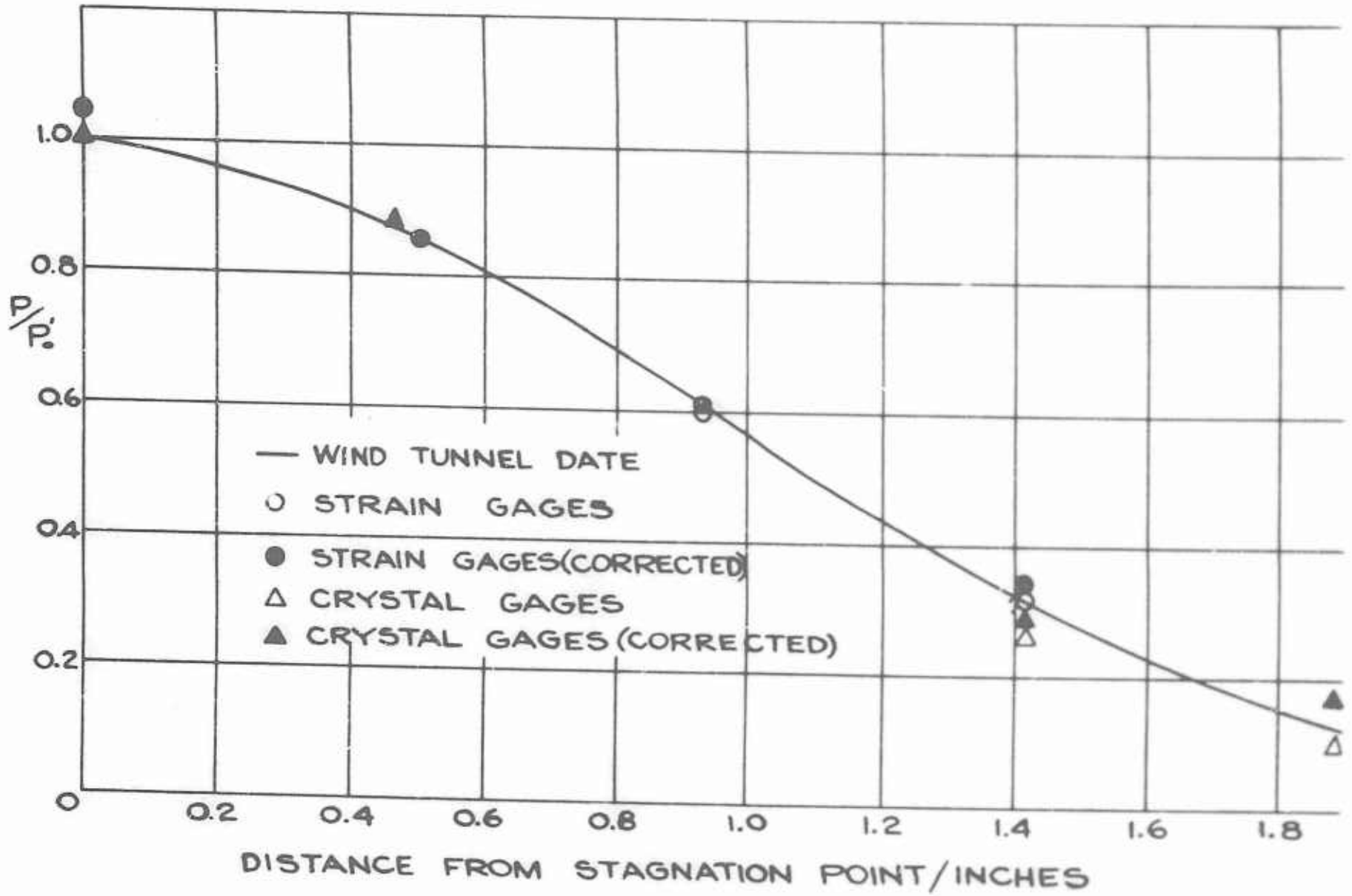
1.0
0.8
P/P'o
0.6
0.4
0.2
0
0.2
0.4
0.6
0.8
1.0
1.2
1.4
1.6
1.8
— WIND TUNNEL DATE
O STRAIN GAGES
● STRAIN GAGES(CORRECTED)
△ CRYSTAL GAGES
▲ CRYSTAL GAGES (CORRECTED)
DISTANCE FROM STAGNATION POINT/INCHES

Figure 12

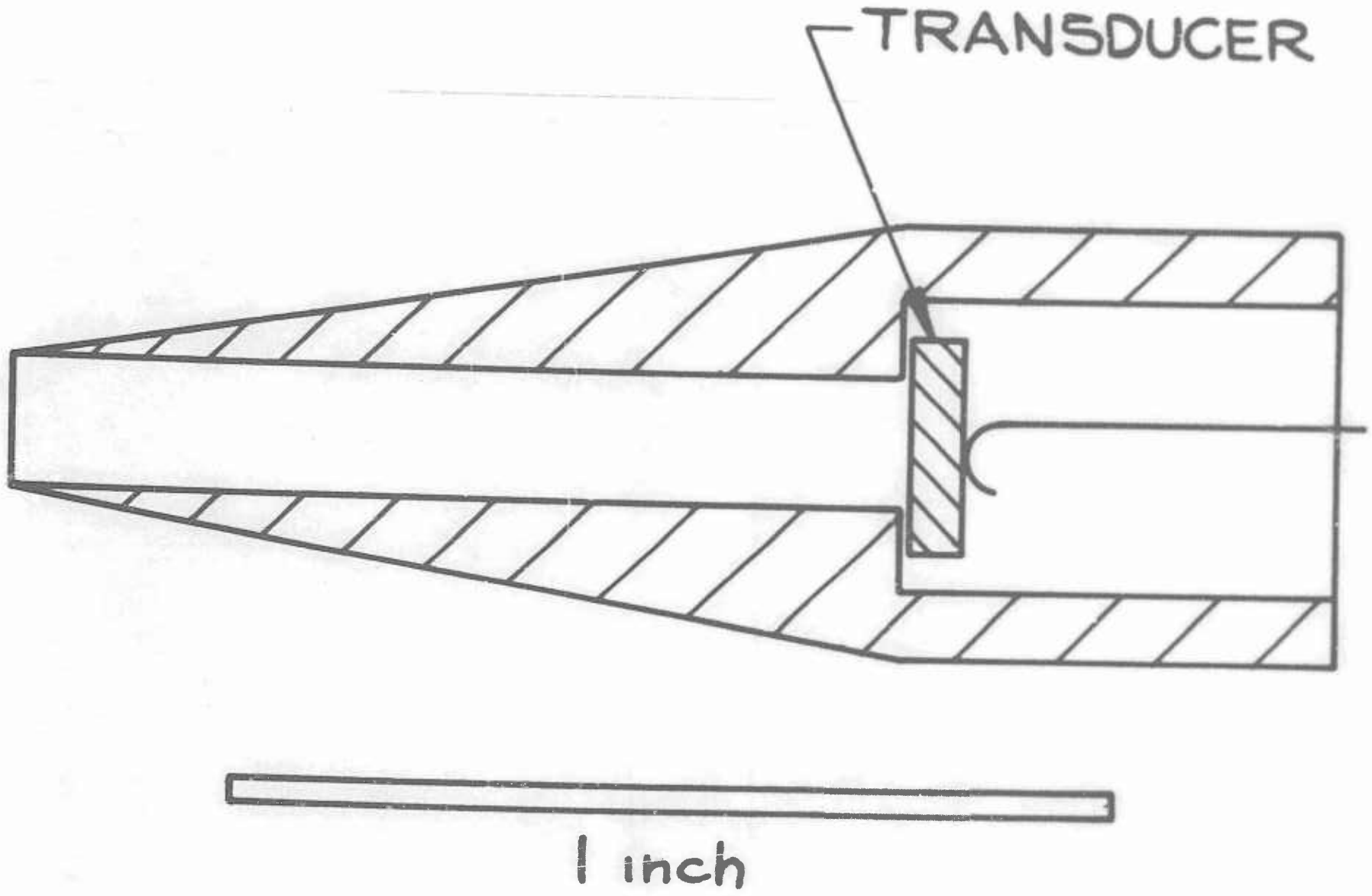

Figure 13

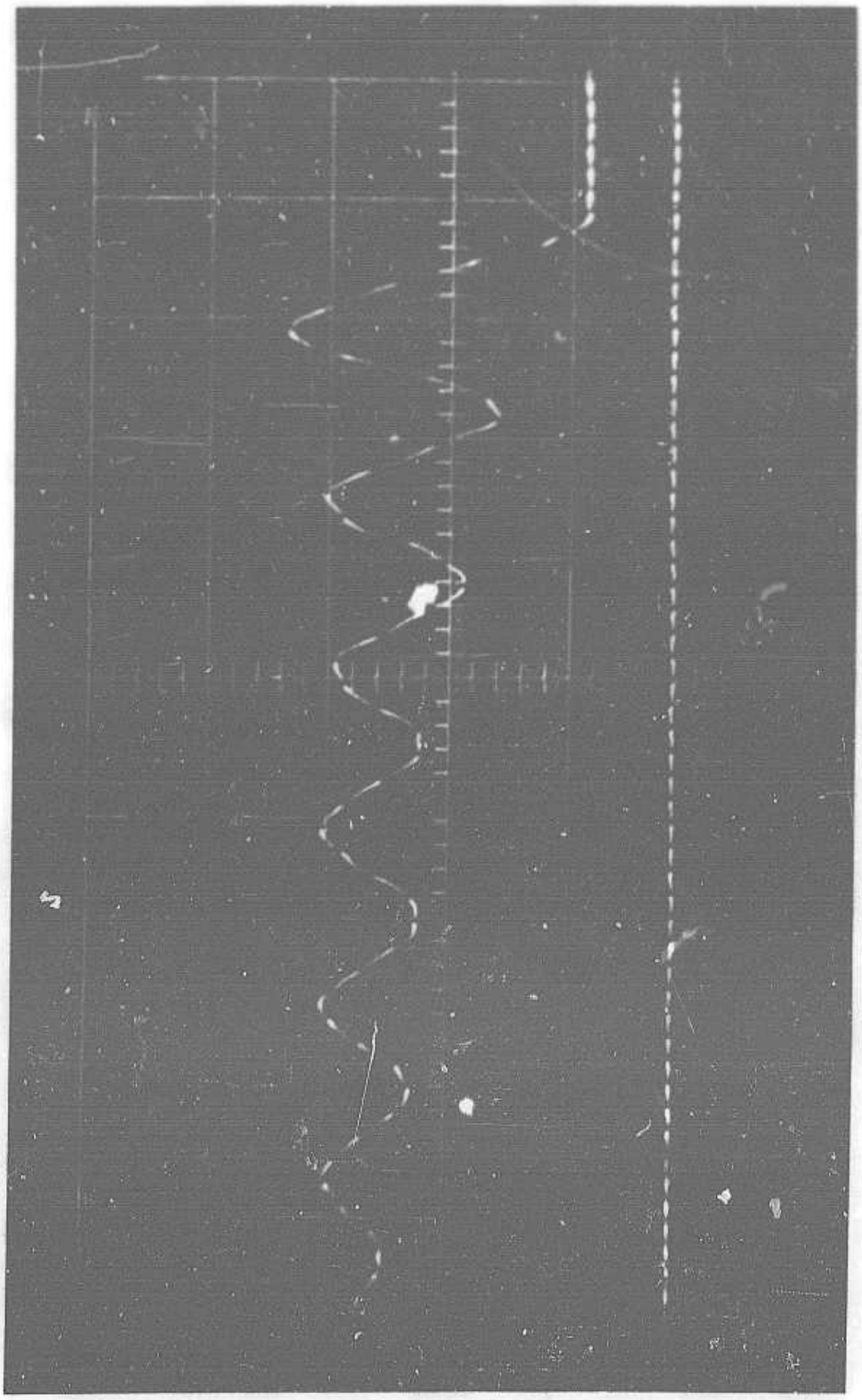

Figure 14

Figure 15

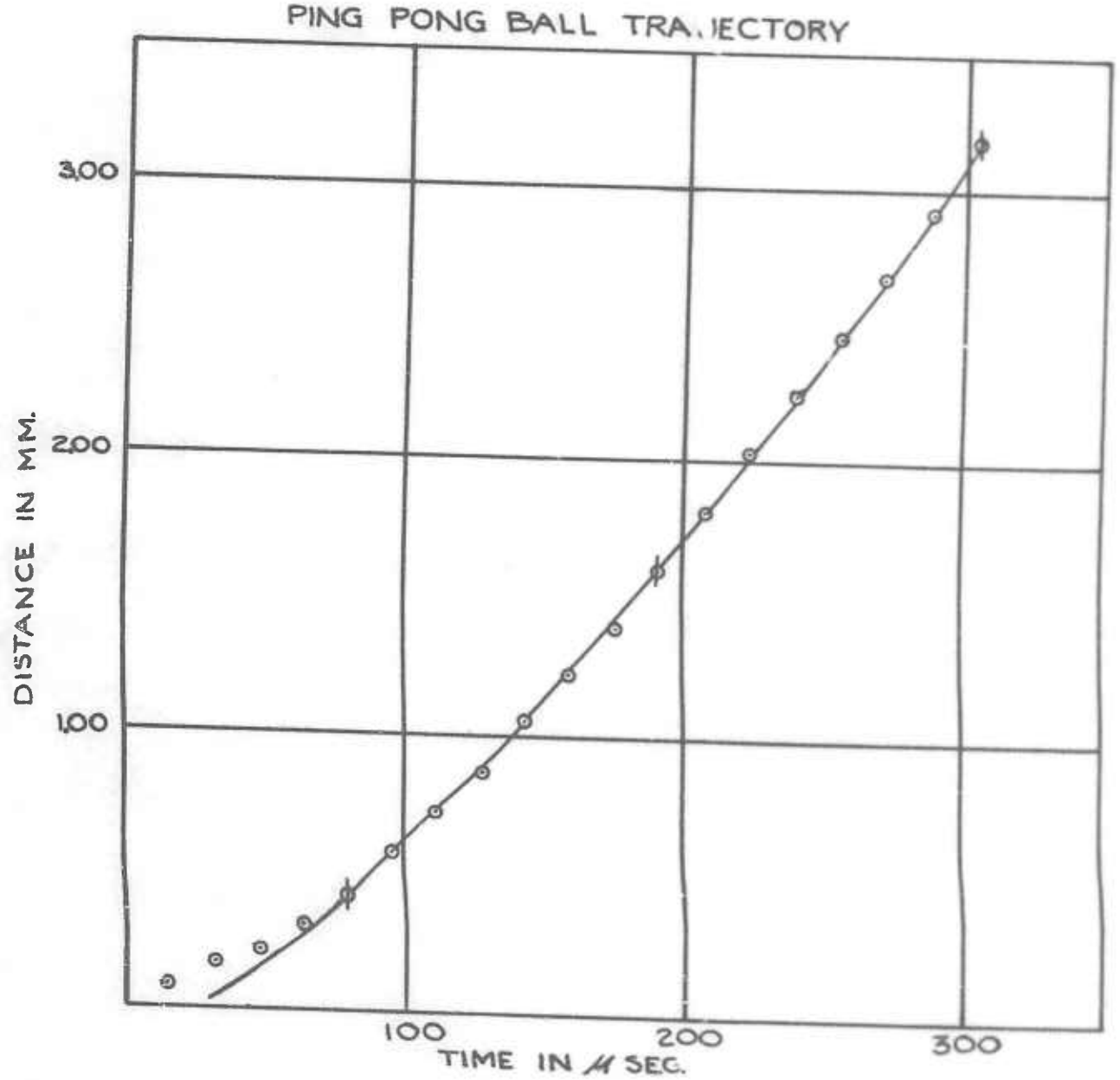
PING PONG BALL TRAJECTORY
DISTANCE IN MM.
300
200
100
100
200
300
TIME IN μ SEC.

Figure 16

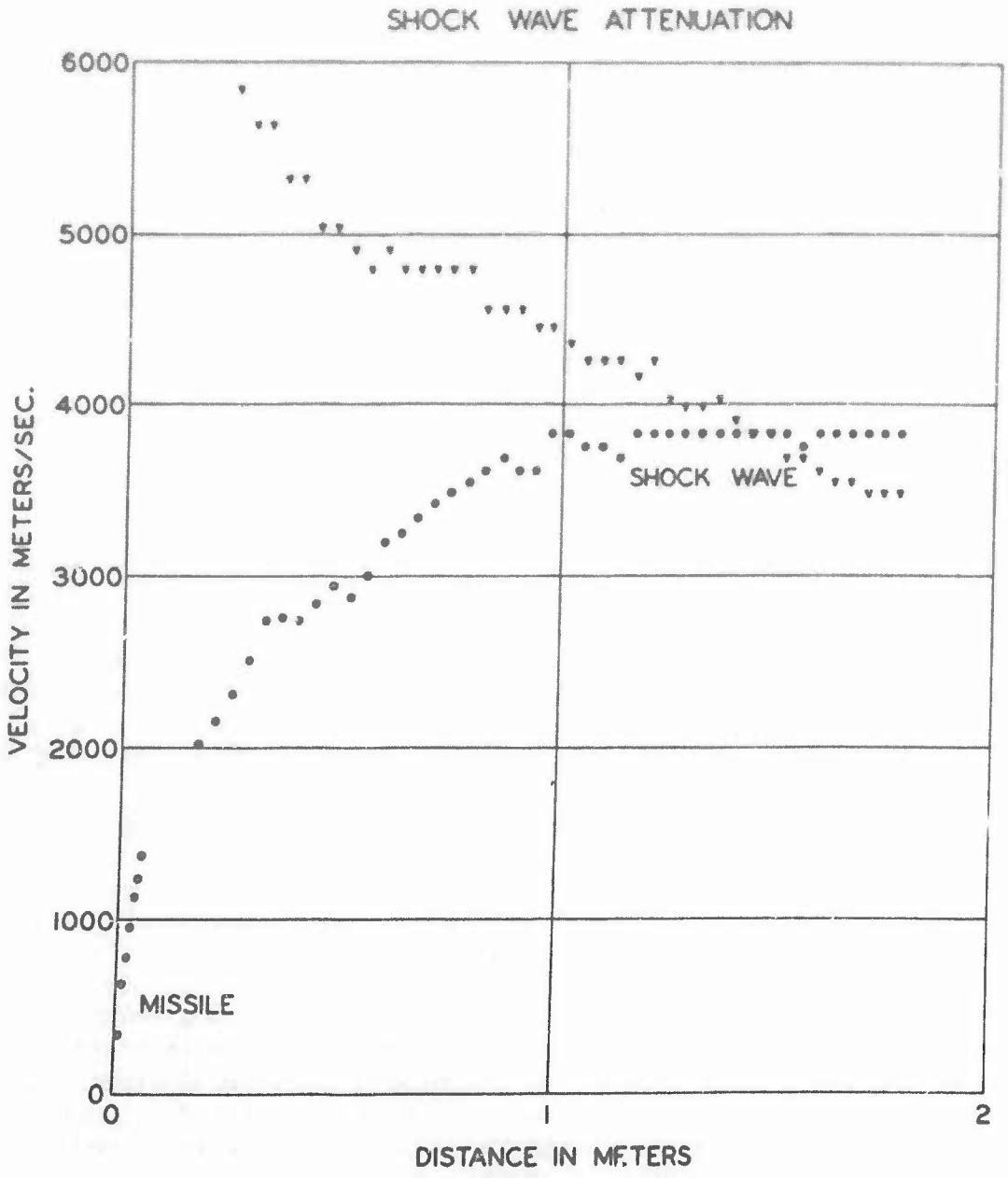
SHOCK WAVE ATTENUATION
6000
5000
4000
3000
2000
1000
0
VELOCITY IN METERS/SEC.
SHOCK WAVE
MISSILE
0
1
2
DISTANCE IN METERS

Figure 17

SHOCK TUBE STUDIES OF BLAST PRESSURES BEHIND FRANGIBLE WALL PANELS

Thomas A. Zaker

Armour Research Foundation

INTRODUCTION

In the course of an experimental program to determine blast pressures in the interior of buildings having frangible exterior wall panels, some interesting phenomena were observed. The investigation is an application of shock tube laboratory research to phenomena controlled by the interaction of blast pressure loading and model response. The experimental work reported herein was sponsored by the Air Force Special Weapons Center and performed at the Air Force Shock Tube Laboratory, Gary, Indiana.

When a blast wave (i.e., a shock wave followed by either uniform or decaying flow) is incident normally on a frangible surface of a hollow block, the disturbance entering into the interior after failure of the panel is a finite amplitude compression wave whose maximum overpressure is generally less than the incident shock overpressure. Both the overpressure decrease and the time of pressure rise are strongly influenced by the panel characteristics.

SHOCK TUBE EXPERIMENTS

This program attempted to relate pressure decrease and buildup time to the physical properties of the frangible panel for a suitably idealized system. The shock tube model used in the study was a rectangular block having exterior dimensions of 4 in. and 6 in. normal to the flow, and a length of 12 in. Figure 1 shows a longitudinal section of the model. The side and rear walls and the roof are of 1/2-in. aluminum plate. The wall facing the flow was of frangible plastic material, either Bakelite or Plexiglas, ranging in thickness from 1/32 in. to 1/8 in. The aluminum clamps indicated in the figure permitted rapid interchange of panels on successive tests.

Shocks were generated by means of a high explosive, Primacord, in the two-foot diameter tube at Gary. The freestream side-on overpressure ranged from 5 to 60 psi. Positive phase durations were well in excess of 20 msec. Transient pressure measurements were made using piezoelectric barium titanate crystal gages. As shown in Fig. 1, four gages located on the centerline of the model measured interior side-on overpressure. A gage located upstream from the model monitored the freestream side-on overpressure, and another gage placed immediately in front of the panel recorded the arrival of the shock. A continuous pattern of electrical conducting paint was placed on the surface of each frangible panel. Leads were attached to the ends of the pattern, and an alternating current power input to the circuit produced a sinusoidal oscilloscope signal until the time at which the circuit was broken by failure of the panel. In this way, an indication of the time of failure of the panel was established. The test series included a total of 82

shots against four thicknesses of each of the two materials. A post-shot photograph of the test setup is exhibited in Fig. 2.

A typical interior pressure record is shown in Fig. 3. In this instance, a panel of Plexiglas 1/32 in. in thickness was subjected to a blast wave having a peak side-on overpressure of 46.2 psi. A maximum overpressure of 33.2 psi was transmitted, and the rise time was 0.42 msec. The time of failure of the panel was 0.11 msec. The reflection of the compression wave from the rear wall of the model can easily be identified. This particular record is taken from the gage located 3 in. from the panel. No consistent major variations in the phenomena of interest could be detected as the wave progressed down the line of interior gages, except that the gage nearest to the panel showed that a markedly erratic flow field existed in its vicinity. This is to be expected since pressure fronts which propagate through newly-formed openings in a failing panel probably do not merge to a clean front until a distance of the order of the panel dimensions has been traversed. In a few tests which exhibited very long rise times, the reflection from the rear face arrived at the gages farthest downstream before the initial pressure maximum was reached, and pressure buildup at a rate initially slow but increasing with time was evidenced.

A good deal of "scatter" is found even in the experimental data gathered for a single panel material and thickness. In Fig. 4 the initial interior pressure maxima are plotted against incident side-on overpressure for the series of 12 tests on 1/32-in. thick panels of Bakelite. The scatter can be attributed in part to the sensitivity of the phenomena of interest to small inhomogeneities in the panel material and to chance variations in edge conditions. Failure of a panel is generally initiated in regions of stress concentration due to flaws in the material, and such imperfections can substantially reduce resistance to loads even statically applied.

In general it is found that, where panel failure just occurs, the interior side-on overpressure builds up to a maximum of more than half of the shock overpressure. As the strength of the incident wave is increased, the transmitted maximum overpressure appears to increase to a limiting value of about 85 per cent of the shock overpressure. The associated rise time ranges from two to five times the panel failure time, irrespective of the strength of the incident blast wave. Panel failure is found to occur so early in the loading period that the decay of incident overpressure with time is not important.

PANEL RESPONSE CONSIDERATIONS AND ANALYSIS OF RESULTS

In order to develop a meaningful method of presenting the results, we turn now to a consideration of the response of a panel to dynamically applied transverse pressure. Consider a thin rectangular panel of lateral dimensions a, b and thickness h in the x-y plane. If the panel material is isotropic and linearly elastic, and if transverse displacements $w(x, y, t)$ are sufficiently small, the motion is governed by the linear differential equation

$$\left(c^2 r^2 \nabla^4 + \frac{\partial^2}{\partial t^2}\right) w = \frac{p(x, y, t)}{\rho h} \qquad (1)$$

In Eq. (1), ρ is the density of the panel material, c is the velocity of low-frequency longitudinal stress waves in the plate, and r is the radius of gyration of the plate cross-section. The operator ∇^4 is defined as

$$\nabla^4 = \left(\frac{\partial^2}{\partial x^2} + \frac{\partial^2}{\partial y^2}\right)^2 .$$

The resistance of the plate to the transverse pressure is generated solely by bending stresses in the plate.

In principle, one could solve Eq. (1) subject to appropriate boundary conditions, and express the solution in terms of the infinite number of normal modes of free vibration of the plate, each of which possesses a distinct frequency. Certain of these modes are excited to a greater degree than others, depending on the spacewise distribution of the pressure. We are interested primarily in loading which is spacewise nearly uniform, such as that experienced by a panel struck by a normally incident blast wave. Satisfactory approximate solutions to the problem can be obtained by arbitrarily assuming a deflection surface satisfying the necessary edge conditions and containing a single deflection parameter such as the center deflection itself. One obtains a single-degree-of-freedom system whose equation of motion has the form

$$M \frac{d^2 w_o}{dt^2} + k_1 w_o = p(t), \qquad (2)$$

where M is an equivalent mass per unit area, and k_1 is the slope of the static load-center deflection curve. The center deflection, w_o, conveniently serves as the single generalized coordinate.

When the panel undergoes transverse displacements greater than about 20 per cent of its thickness, membrane stresses begin to contribute appreciably to the total resistance. The dynamic response problem then becomes extremely complicated, because the associated equations of motion become nonlinear even if the panel material remains elastic and linear. However, satisfactory approximate solutions are again obtained by arbitrarily assuming a one-parameter deflection surface and arriving at an equation of motion in the form

$$M \frac{d^2 w_o}{dt^2} + q(w_o) = p(t), \qquad (3)$$

in which the resistance function $q(w_o)$ is approximated by

$$q(w_o) = k_1 w_o + k_3 w_o^3, \tag{4}$$

where k_1 and k_3 are constants. The first term of the right-hand side represents the contribution of the bending stresses and the second that of the membrane stresses to the resistance.

The large-deflection theory of isotropic, elastic plates suggests that Eq. (4) can be put in the nondimensional form

$$\frac{qa^4}{Eh^4} = A_1\left(\frac{w_o}{h}\right) + A_3\left(\frac{w_o}{h}\right)^3, \tag{5}$$

where a is the short span of the panel, E is Young's modulus, and A_1 and A_3 are dimensionless constants depending on the panel aspect ratio and on conditions of fixity at the panel edges.

The panels utilized in the shock tube tests had clear spans of 3 in. and 5 in., and the clamps at the panel edges prevented rotation at the boundaries. The specimens clearly exhibited nonlinear resistances of the type discussed here, and their failure under static loading is of the brittle fracture type, so that the entire resistance function up to failure is in the form given by Eq. (4).

The compression chamber of an 8-in. square cross-section shock tube owned by Armour Research Foundation was modified for use in static testing of 23 samples of the plastic panels. The panels were loaded by compressed air, and center deflections were measured directly by a dial gage. Close simulation of the shock tube test geometry in regard to bearing and fixity conditions at the panel edges was achieved. A typical load-deflection curve obtained in the static tests is shown in Fig. 5. This test was performed on a 1/16-in. thick panel of Bakelite, and sudden, almost explosive, failure occurred at a pressure of 45 psi. Young's modulus for each of the two materials was calculated from the initial slopes of the load-deflection curves, and it was found that all of the static test data was satisfactorily approximated by the relationship

$$\frac{qa^4}{Eh^4} = 50\left(\frac{w_o}{h}\right) + 10\left(\frac{w_o}{h}\right)^3. \tag{6}$$

Neglecting strain rate effects, the area under the static load-center deflection curve for a panel to its failure deflection, w_{fo}, measures the energy absorbed during deformation, regardless of the shape of the load-deflection curve. If we equate this energy to that imparted to the system by a uniformly distributed pressure impulse I per unit area, we obtain the "failure impulse"

$$I = \sqrt{2M\, q_{av}\, w_{fo}}, \tag{7}$$

where q_{av} is the average ordinate of the load-deflection curve to failure.

The loading on the upstream face of a rectangular block due to an explosive-generated blast wave consists of two distinct phases, a diffraction loading phase and a drag loading phase. The initial reflection of the incident wave clears in a time given approximately by $t_d = 3\,\bar{H}/U$, where $\bar{H}$ is a minimum clearing distance associated with the front face of the block, and U is the undisturbed shock velocity. The loading on the panel is shown schematically in Fig. 6. After clearing of the diffracted shock pressures, the panel experiences the much lower pressures characterizing the pseudo-steady drag loading phase.

We can define a criterion of panel strength having the units of pressure as the peak of a triangular pulse having a duration equal to the clearing time, t_d, and an area equal to the failure impulse, I. This "failure pressure" p_f, is then given in terms of loading and response parameters by

$$p_f = \frac{2}{t_d}\sqrt{2\, M\, q_{av}\, w_{fo}}. \tag{8}$$

Evidently p_f will be very nearly equal to the reflected peak pressure which will insure failure due to the diffraction loading alone, provided the response of the panel is slow in comparison to the clearing time, t_d. The ratio of the actual reflected peak pressure, p_r, to this failure pressure is a measure of the strength of the incident blast relative to the strength of the panel.

We can similarly define a measure of the speed of panel response as the duration of a rectangular pressure pulse having the ordinate q_{av}, and an area equal to the failure impulse, I. This characteristic time, T', is then given by

$$T' = \sqrt{\frac{2M\, w_{fo}}{q_{av}}}\ . \tag{9}$$

After experimentation with several schemes of data presentation, it appeared that a useful presentation for weapons effects purposes consisted of plots of pressure transmission ratio, or ratio of interior maximum over-pressure, p_i, to incident side-on overpressure, p_σ; ratio of rise time, t_r, to the characteristic time, T'; and ratio of failure time t_b, to the characteristic time, T'. These ratios are shown as functions of the ratio of reflected pressure, p_r, to the failure pressure, p_f, in Figs. 7, 8 and 9. All of the data was found to lie within the region bounded by the dashed lines on each chart. The form of presentation itself implies that certain simple physical laws govern the phenomena of interest, but there is no guarantee

that the quantities which have been used to nondimensionalize the data are indeed true normalizing factors. The intent has been to generalize wherever possible in order to provide information for estimates of weapons effects phenomena, and this representation confirms certain intuitively anticipated trends.

From Fig. 7, it can be seen that below a reflected pressure-failure pressure ratio of about two, the panels remain intact. In a sense this implies the existence of a universal failure criterion for panels, to be viewed in the light of the preceding discussion and the intended weapons effects application. Immediately after the ratio of two is exceeded, more than half of the incident overpressure is transmitted to the interior. Thereafter, the transmission ratio continues to increase rapidly and approaches what appears to be a limiting value of 0.85.

Figure 8 shows that, where failure is just attained, the dimensionless rise time descends from infinite values to the neighborhood of 2.5, and subsequently decreases still further to an apparent limiting value of about 1.25. The dimensionless failure time (Fig. 9) similarly descends from infinite values to the neighborhood of 0.8 when failure is just attained, and decreases to a value of about 0.3 for stronger shocks. The rise time appears to range from two to five times the failure time, irrespective of the reflected pressure-failure pressure ratio.

GENERAL COMMENTS AND APPLICATIONS

The experimental results and analysis described in this paper represent an exploratory effort in an area not previously investigated, and so certain idealizations regarding geometry and physical properties were necessary in the shock tube model selected for study. A single panel aspect ratio, 0.6, was investigated, but this ratio is typical of an actual building bay. There were no openings in the frangible panels, and a variation in stiffness was studied to the extent that two different plastics were tested. The selection of the particular materials was dictated by the demand for homogeneity of material and ready availability of a variety of thicknesses. No variations in edge conditions or ductility were considered.

Although the materials chosen for study have the characteristics of a large class of exterior wall coverings, no real attempt was made to scale specific structural components. Rather, the objective has been to study basic phenomena and theory. The form of presentation of the data permits application of the results to panels having other types of resistance functions, in that quantities like average resistance can be calculated equally easily for elastic-plastic or elastic-decreasing plastic (unstable) resistance functions. The possibility of more general application of the present results was in fact suggested by the qualitative agreement with the result of an earlier full-scale test on a masonry panel, and full-scale tests subsequently conducted lend support to the conclusion that the shock tube model data adequately predict the gross characteristics of blast pressures behind failing wall panels.

REFERENCES

1. Timoshenko, S. Theory of Plates and Shells, McGraw-Hill Book Company, New York, 1940

2. Hearmon, R. F. S. "The Frequency of Vibration of Rectangular Isotropic Plates", Journal of Applied Mechanics, Vol. 19, September, 1952

3. Manufacturing Chemists Association Technical Data on Plastics, Washington, D. C., October, 1952

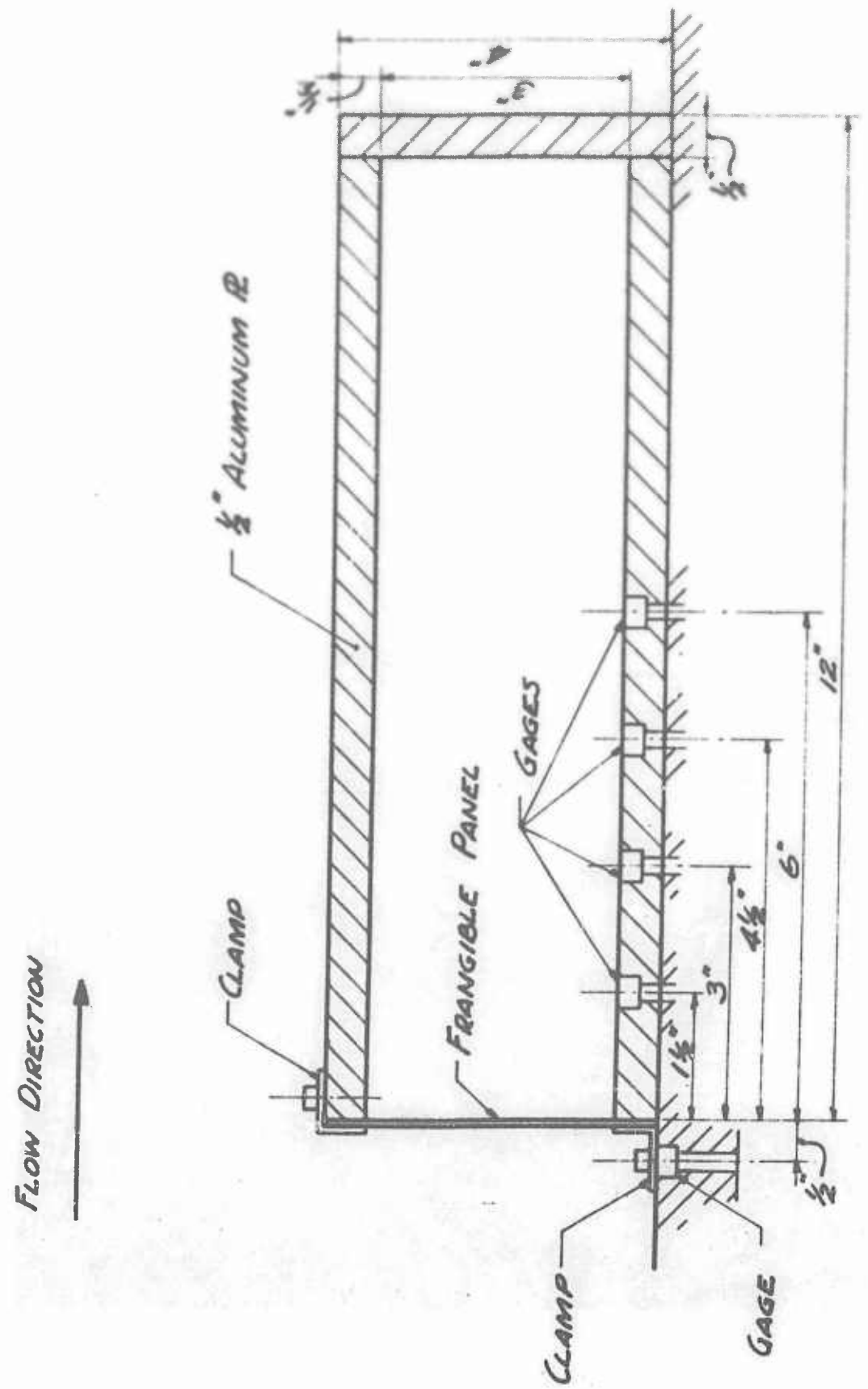

Figure 1 Shock Tube Model

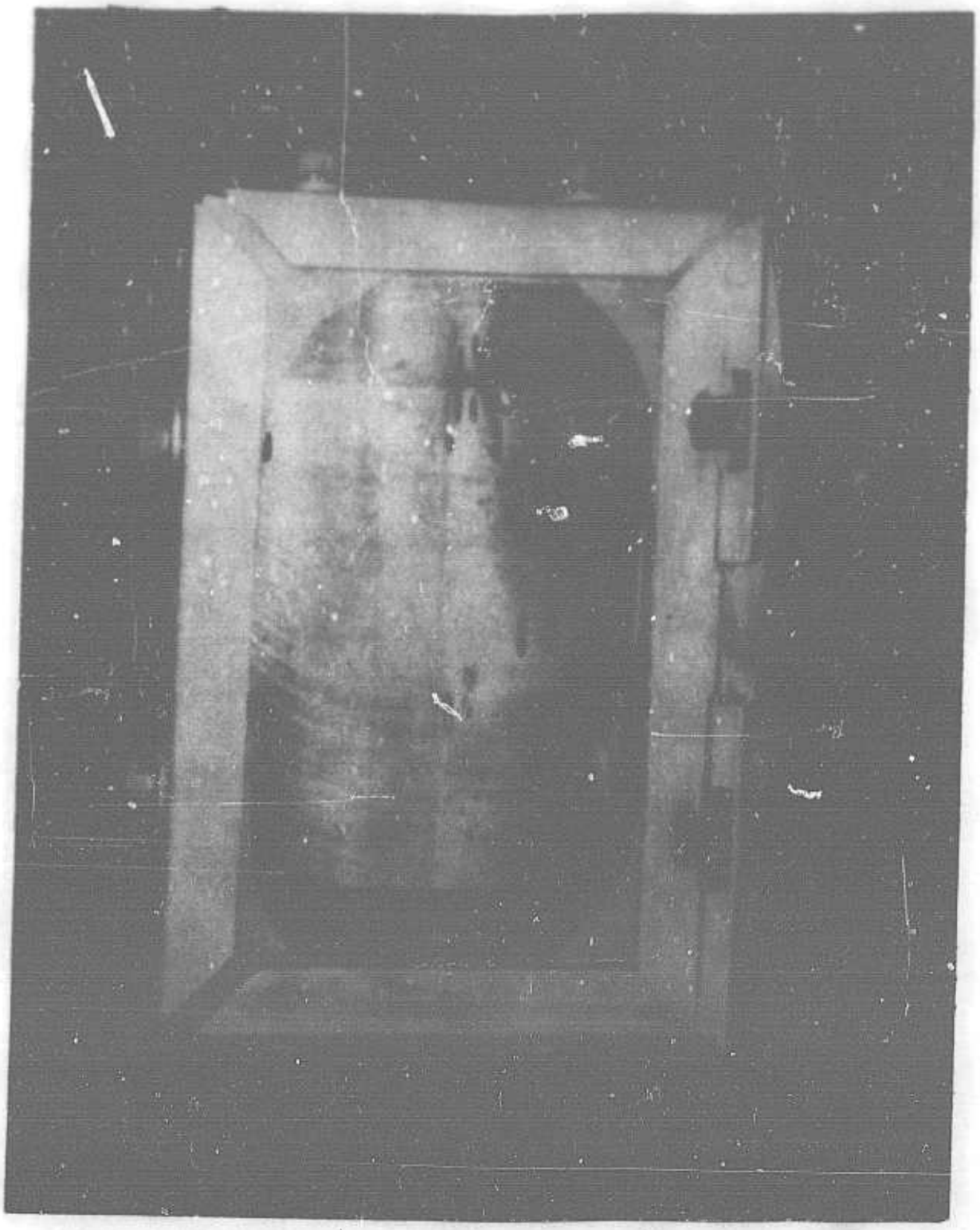

Figure 2 Post-Test Front View of Shock Tube Model

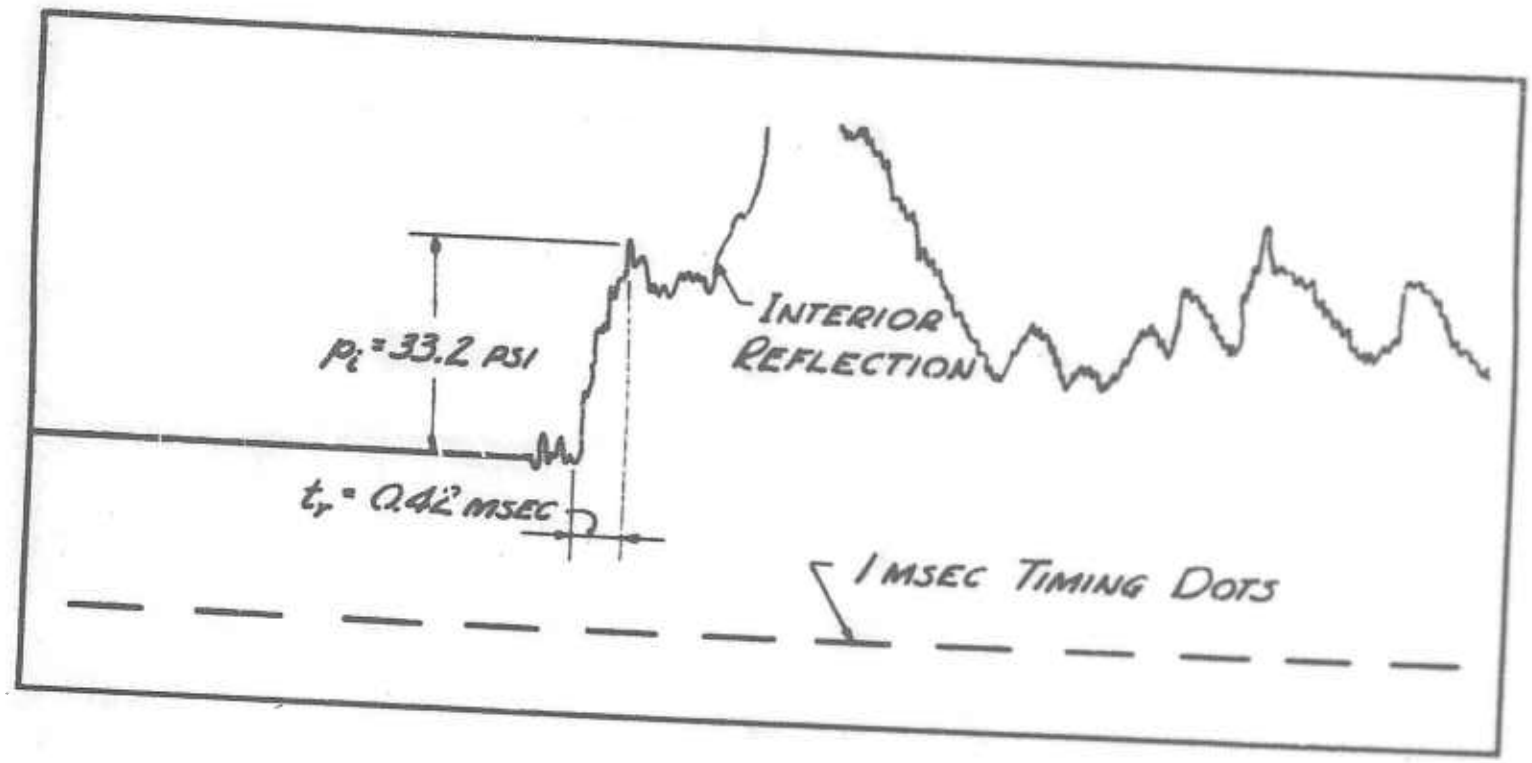

Figure 3 Typical Interior Pressure Record

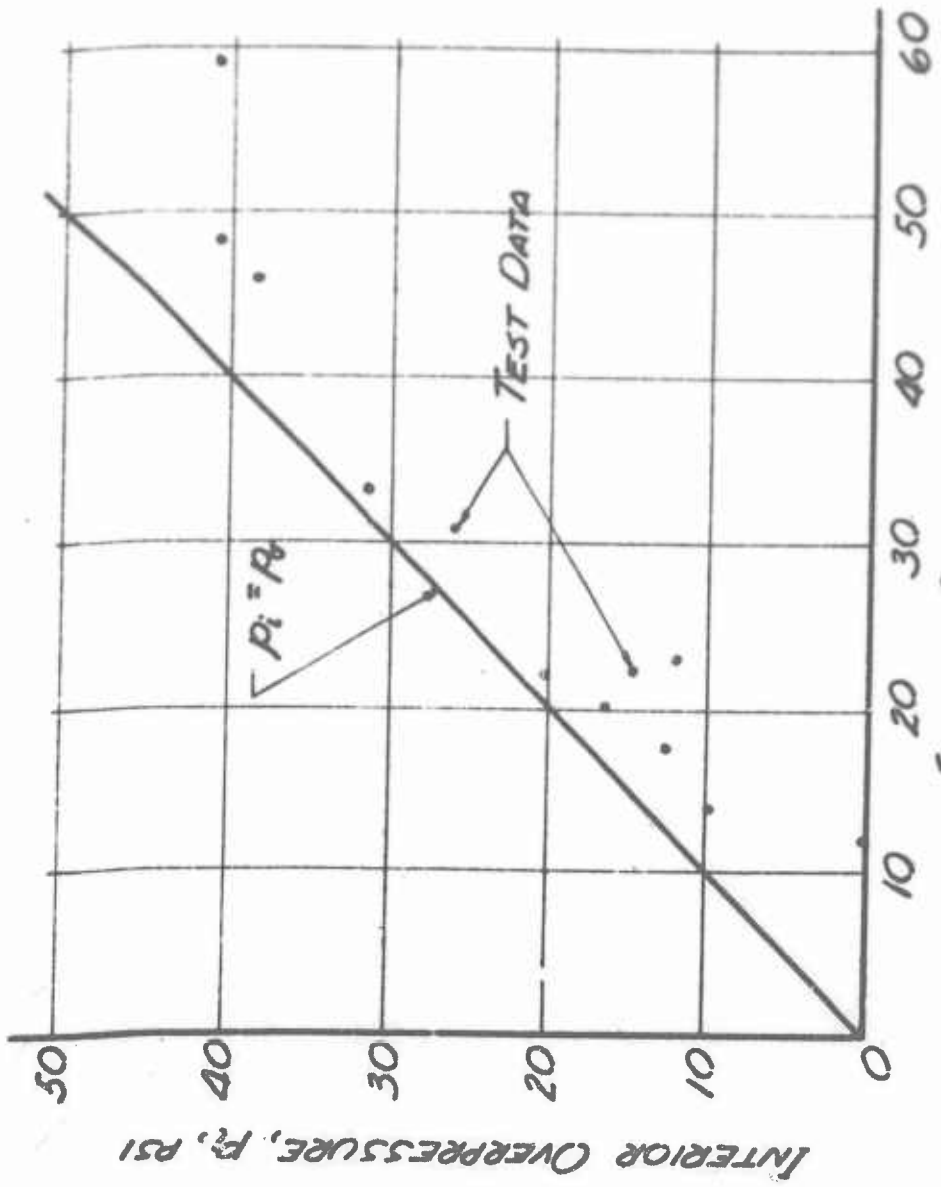

Figure 4 Interior Pressures, 1/32" Bakelite

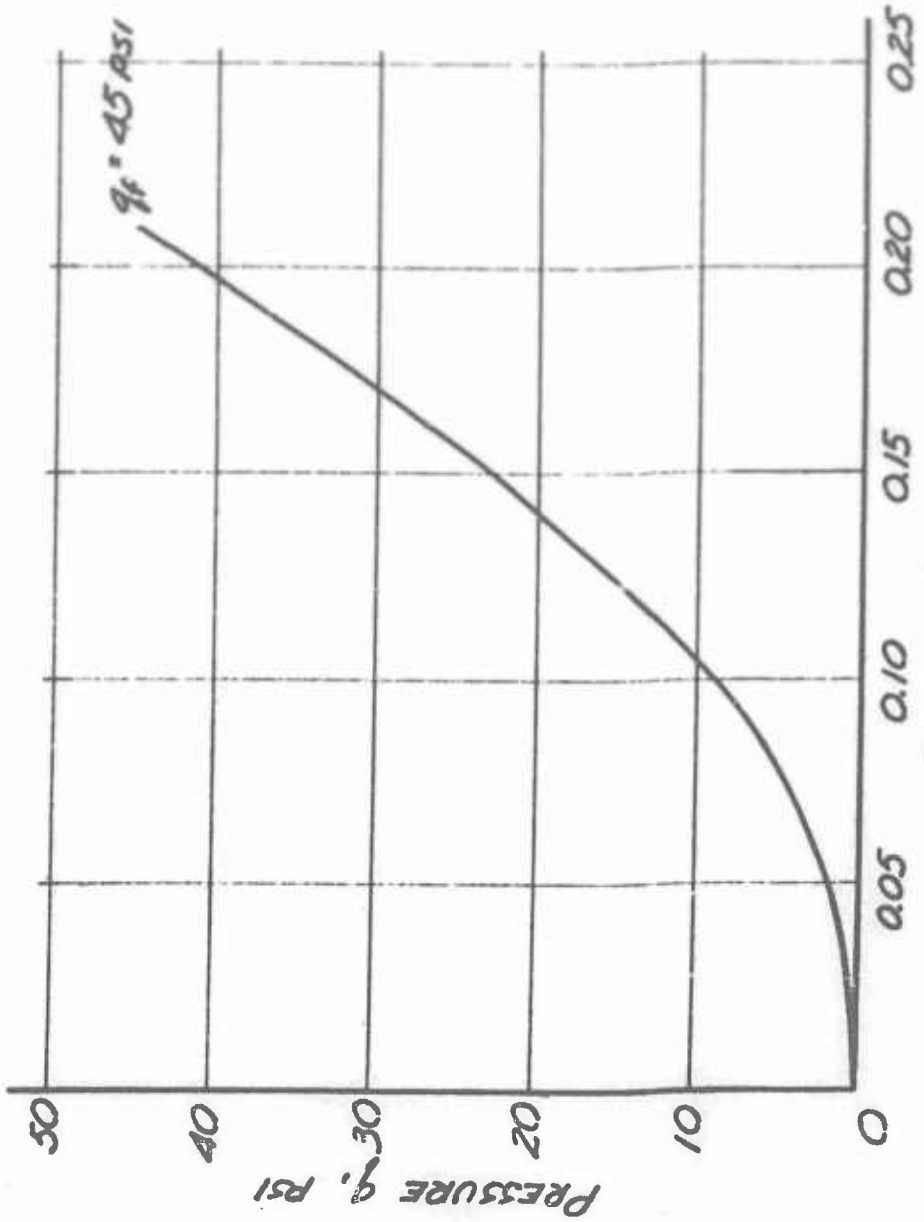

Figure 5 Load-Deflection Curve, 1/16" Bakelite

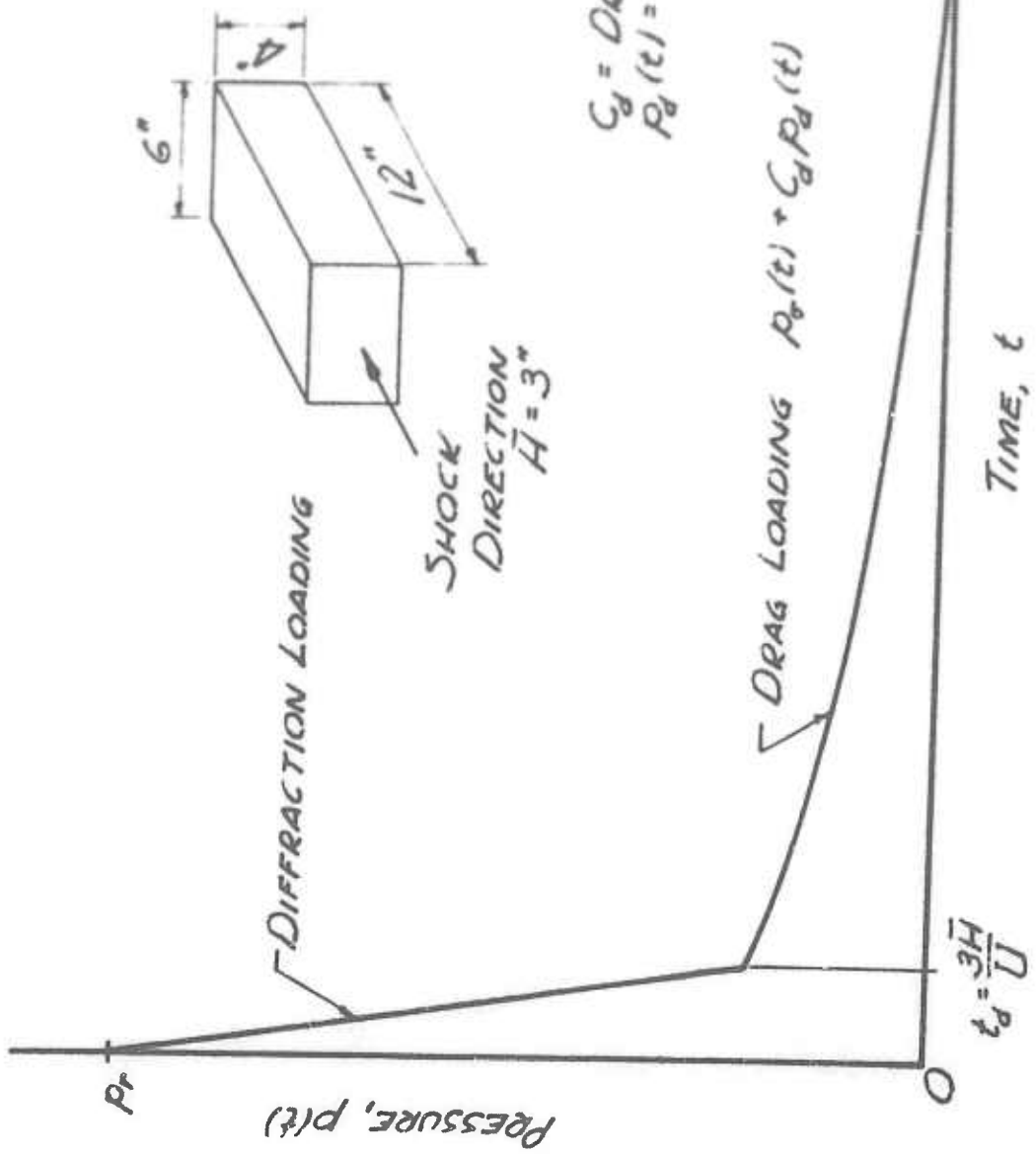

Figure 6 Blast Loading on Front Face of Block

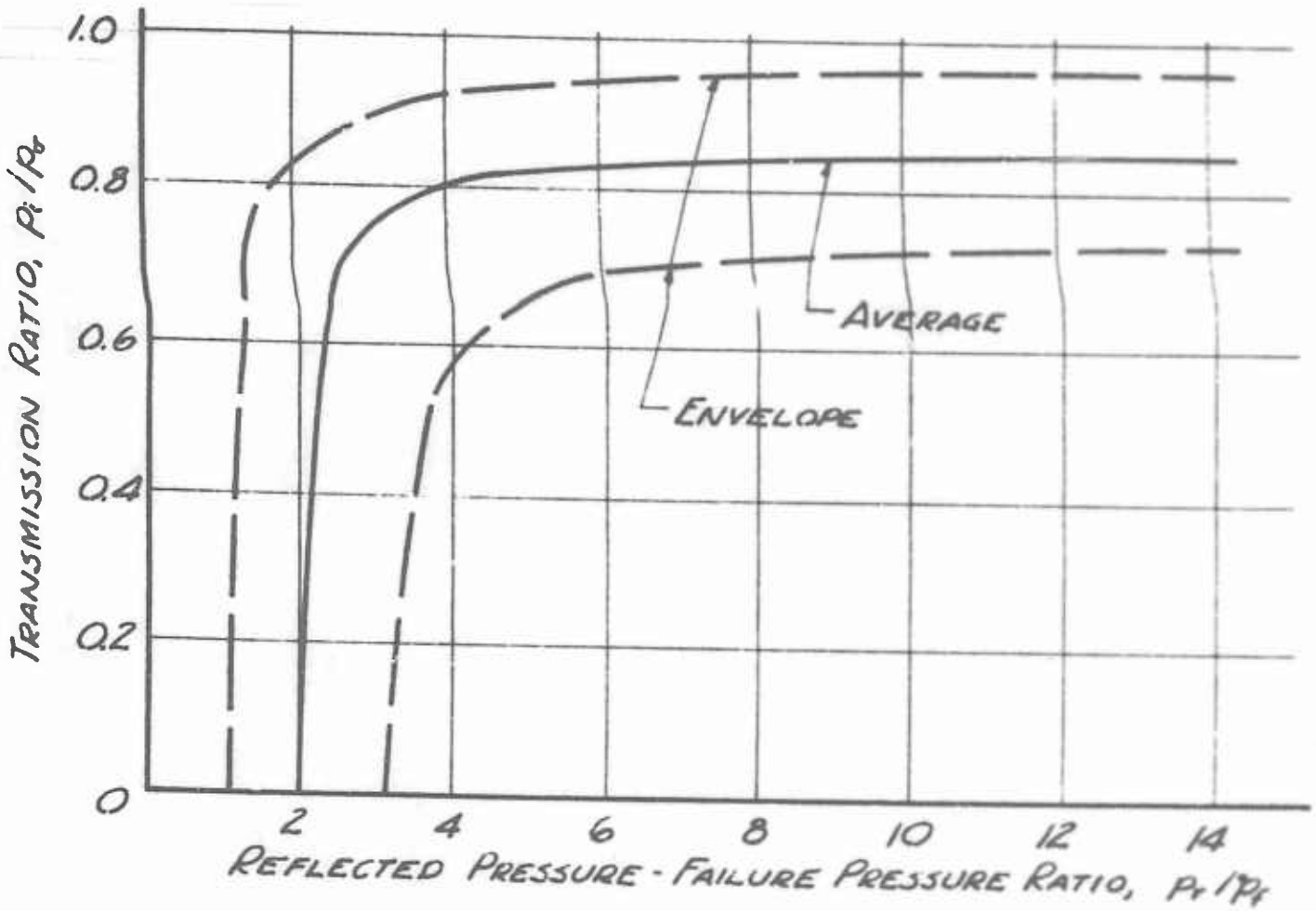

Figure 7 Test Results: Interior Pressures

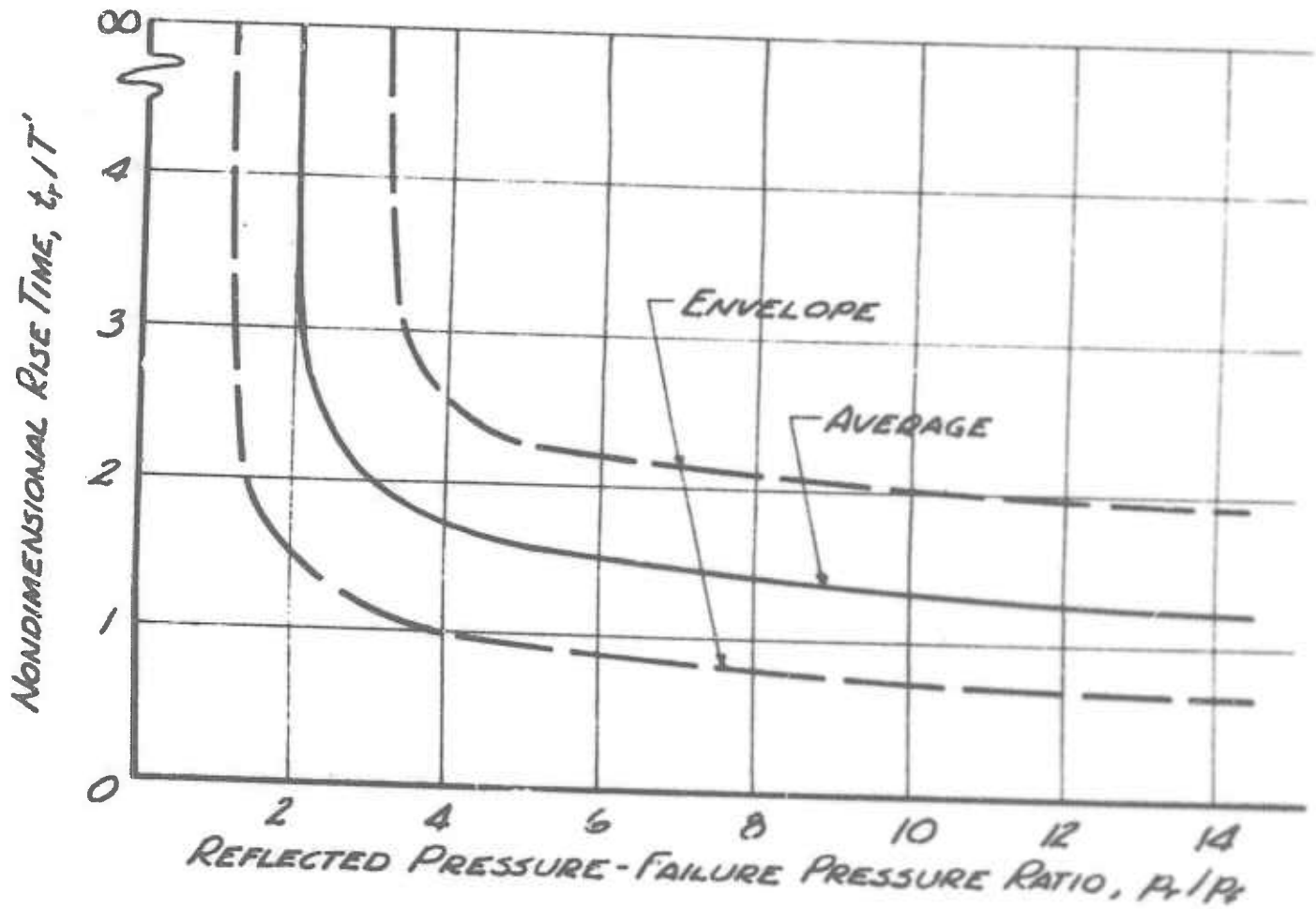

Figure 8 Test Results: Rise Times

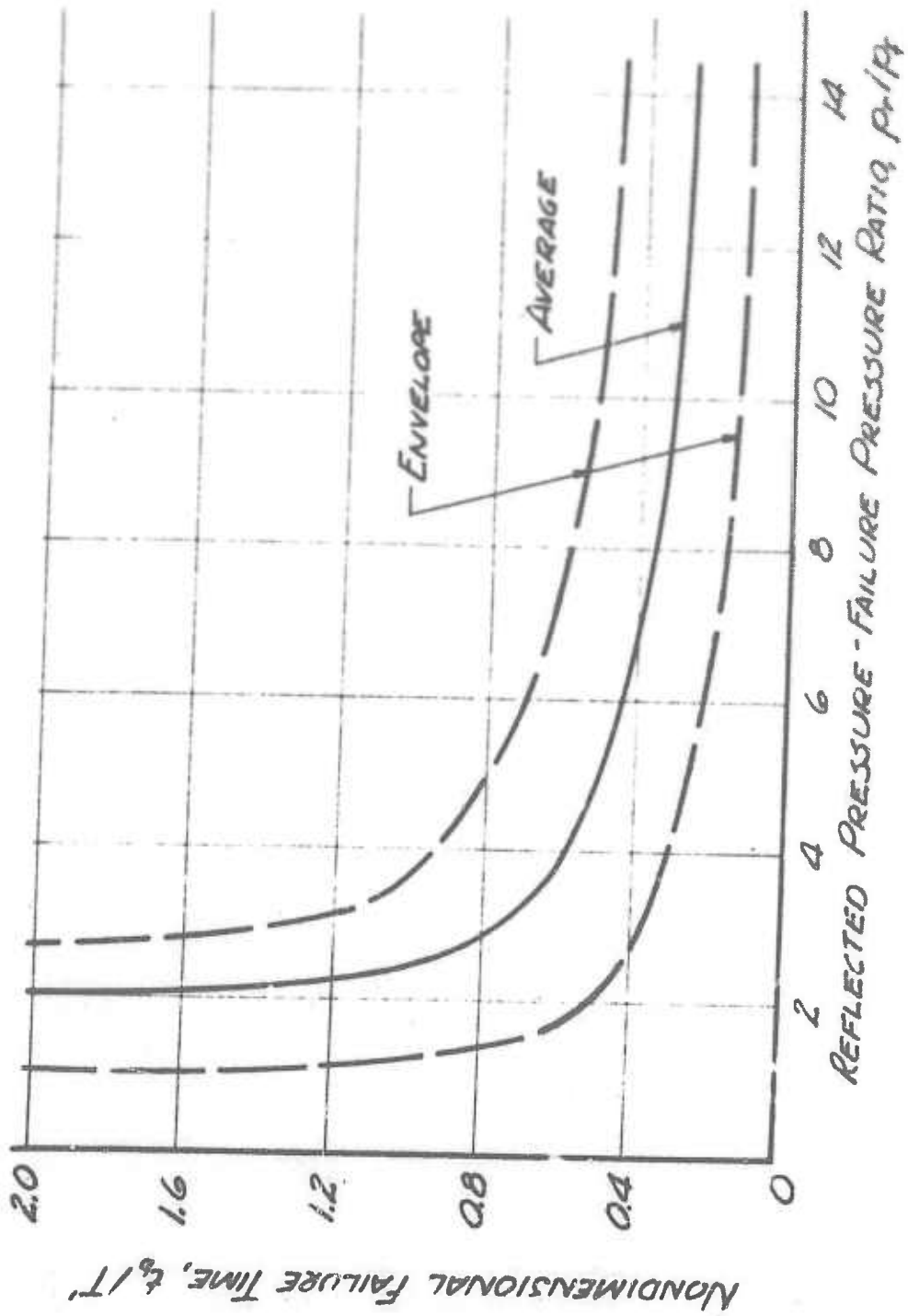

Figure 9 Test Results: Failure Times

UNCLASSIFIED

AD 211239

Armed Services Technical Information Agency

ARLINGTON HALL STATION
ARLINGTON 12 VIRGINIA

FOR
MICRO-CARD
CONTROL ONLY

2 OF 6

NOTICE: WHEN GOVERNMENT OR OTHER DRAWINGS, SPECIFICATIONS OR OTHER DATA ARE USED FOR ANY PURPOSE OTHER THAN IN CONNECTION WITH A DEFINITELY RELATED GOVERNMENT PROCUREMENT OPERATION, THE U. S. GOVERNMENT THEREBY INCURS NO RESPONSIBILITY, NOR ANY OBLIGATION WHATSOEVER; AND THE FACT THAT THE GOVERNMENT MAY HAVE FORMULATED, FURNISHED, OR IN ANY WAY SUPPLIED THE SAID DRAWINGS, SPECIFICATIONS, OR OTHER DATA IS NOT TO BE REGARDED BY IMPLICATION OR OTHERWISE AS IN ANY MANNER LICENSING THE HOLDER OR ANY OTHER PERSON OR CORPORATION, OR CONVEYING ANY RIGHTS OR PERMISSION TO MANUFACTURE, USE OR SELL ANY PATENTED INVENTION THAT MAY IN ANY WAY BE RELATED THERETO.

UNCLASSIFIED

A COMPARISON OF SHOCK TUBE AND FIELD TEST DATA ON THE PRESSURE BUILDUP BEHIND FRANGIBLE WALLS

E. Sevin
Armour Research Foundation

INTRODUCTION

This paper presents a comparison of laboratory and full scale field test data relating to the buildup of air pressure behind a structural panel which has failed under blast loading. Since there are no established techniques in this area for small scale modeling of structural behavior, this comparison requires a means of predicting structural action up to failure for the types of panel construction involved. The laboratory tests were conducted in the Air Force 6-foot diameter shock tube and utilized plastic sheets for the panels. These tests are reported in Reference 1, which also presents a theory of structural behavior for the plastic panels. The field tests involved panels of conventional curtain wall construction exposed to an atomic blast, and were conducted as part of a recent full scale structures effects test. The pertinent aspects of these tests are presented herein.

A detailed analysis is carried out for a panel of cinder block construction. The required analysis of the response of the panel to blast loading is based on a general theory of the strength of masonry-type walls presented in References 2 and 3. It is found that the shock tube tests correctly predict the initial rate of pressure buildup and the general form of the interior pressure wave observed in the field tests. However, it was not possible to compare maximum pressure or rise times due to essential differences in geometry between the laboratory and field test structures.

BACKGROUND

Before entering into the necessary details of the analysis, it will be helpful to consider certain aspects of the area of intended application of results. There is currently much interest regarding design techniques for various types of protective construction. A good deal of our knowledge in this area stems from the military's past and continuing interest in the blast loading and response of structures, both from a defensive and offensive point of view. For offensive applications one might be interested in, say, gross damage to the structural frame of a building. If the building were covered with solid curtain walls of conventional materials and construction, it is certain that the covering would be destroyed at substantially lesser loads than would seriously impair the structural frame. The interest in the behavior of the wall cover then would not be concerned with its contribution to the over-all strength of the building, but rather with its influence on the blast loads incident upon the frame once the cover had been destroyed. In such cases it is commonly assumed that the frangible wall cover would have no effect on the incoming blast, and the load on the framework could be computed as if the building had no wall cover. Serious questions concerning the adequacy of this approach were raised as a result of the UPSHOT-KNOTHOLE series of

[1] Senior Research Engineer, Structural Analysis Section, Dept. of Mechanical Eng. Research, Armour Research Foundation of Ill. Institute of Tech.

weapon effects tests conducted in the spring of 1953. As part of an Air Force sponsored test on wall and roof panels, a single pressure gage was placed behind an unreinforced brick masonry wall which formed the front of a closed call. The wall was struck by a clean shock wave and, as expected, the panel was completely destroyed in a fraction of a second. The pressure gage recorded a compression wave having a relatively long rise time and a peak which was slightly less than the incident side-on pressure. While this one test was by no means conclusive, and not even representative of conventional building geometry (the rear wall was less than the wall span length behind the front wall), it did reflect upon the adequacy of existing load prediction methods for buildings with frangible wall cover.

Largely as a result of this test the series of shock tube tests utilizing plastic panels reported in Reference 1 was undertaken. In view of the uncertainty concerning the influence of the mechanism of panel failure on the character of the interior pressure wave, the shock tube tests were intended to explore the influence of incident shock strength and panel break time on the interior wave for one type of panel behavior. The test data obtained was in general qualitative agreement with the one pressure record from the field tests, even though there were substantial differences between the mechanism of failure for the plastic panel and the brick wall. This suggested that the shock tube data might be more generally applicable than originally anticipated and, accordingly, an effort was made to present the test data in a generalized form incorporating the resistance properties of the panel.

An opportunity arose for another full scale field test in connection with the recent PLUMBBOB series. There existed a number of structures from previous tests which could be converted to panel test structures by simply adding the desired front wall panel. These structures could accommodate panels up to 10 by 16 feet with 16 feet between the front and rear walls. Accordingly a test involving one corrugated asbestos (transite) panel and one unreinforced cinder block panel was undertaken by the Air Force.

While this test was largely motivated by the desire to obtain a comparison with the available shock tube results, it is to be emphasized that the field test structures were not specifically designed for this purpose. Rather existing structures, originally designed for entirely different purposes, were utilized as advantageously as possible.

SHOCK TUBE TESTS

Reference 1 contains a detailed description of the shock tube tests in which pressures were determined behind frangible plastic sheets, and also proposes a generalized form of data presentation based upon an elastic, large deflection (membrane) theory of panel failure. The tests are summarized in this section to the extent required for the subsequent application.

The test structure was a rectangular box with an opening in the front to accommodate the plastic panels. Both Bakelite and Plexiglas sheets were tested, the thickness of the sheets varying between 1/32 and 1/8 inches.

The short-to-long-span ratio of all panels was 0.6. The range of overpressure considered was from 5 to 60 psi. The data obtained included incident pressure wave form, interior pressure wave forms at various interior points of the structure, and panel failure time. Typical incident and interior pressure waveforms are shown in Fig. 1. The interior initial maximum overpressure, rise time to this initial maximum, and panel failure time were presented as functions of the incident blast and structural parameters.

There is an important limitation on the test data as finally presented; namely, the maximum interior pressures occurred before pressure reflections from the back wall of the test structure reached the gage. Hence, the results are dependent on the panel characteristics only, and not on the interior geometry of the test cell.

Under static tests the plastic panels exhibited a load-displacement relationship up to failure which could be approximated very closely by considering only elastic behavior of the panel. Taking this as the mechanism of panel response under dynamic load, the shock tube data was normalized in terms of a characteristic pressure, p_f, and characteristic time, T', which are given by

$$p_f = \frac{2}{t_d} \sqrt{2\, p_{av}\, M\, x_f} \qquad (1)$$

$$T' = \sqrt{\frac{2M\, x_f}{p_{av}}} \qquad (2)$$

where

t_d = diffraction phase clearing time for panel (Figure 1a)

M = equivalent mass per unit area of panel

x_f = center displacement of panel at failure (displacement corresponding to zero panel resistance)

p_{av} = average resistance of panel (average ordinate of load-deflection curve to failure)

FIELD TESTS

The detailed description of the field test in which pressures were determined behind failing transite and unreinforced cinder block panels mentioned earlier is currently to be found in the classified literature. Fortunately, sufficient information can be reported for present purposes.

Both the transite and cinder block panels tested were of conventional construction, and had a short-to-long-span ratio of 0.625. This is directly comparable to the 0.6 ratio for the model panels. The test panels were located at the same distance from the source of the blast and the incident

pressure wave form was representative of the shock tube conditions (Fig. 1a). One BRL-type self recording pressure gage was installed at the center of the floor of each test cell. The interior wave forms recorded behind the two types of panels are shown in Fig. 2.

As shown in Fig. 2a, the transite panel did not effectively influence the incoming pressure wave. The gage record clearly shows the incoming shock front and the reflected shock from the rear wall. For some reason the gage failed at this time, possibly due to being struck by debris. As is evident from Fig. 2b, the failing cinder block panel markedly influenced the character of the incoming wave. Comparison of Figs. 1b and 2b show a marked similiarity between the interior wave forms obtained from tests in the shock tube and in the field. A posttest photograph of the structure which contained the cinder block panel is shown in Fig. 3. This figure gives an indication of the complete structural failure of the panel. Note from Fig. 3 that the rear wall of the cell sustained some deformation. However, this did not affect the test results, at least to the extent considered here.

COMPARISON OF SHOCK TUBE AND FIELD TEST DATA

A comparison between shock tube and field data requires that the normalization parameters given by Eqs. (1) and (2) be evaluated for the field test panels. This in turn requires some detailed theory of panel response up to failure in order to evaluate the quantities x_f and p_f. Such a theory is presented in References 2 and 3 for both types of panels. Inasmuch as the transite panel represents a situation well beyond the range of the model tests, a comparison is carried out only for the cinder block wall. However, it may be noted that extrapolation of the shock tube data corresponding to the parameters for the transite panel supports the field test results to the extent that no distortion of the incident pressure wave is indicated.

According to the theory presented in Reference 2, the resistance of a masonry panel to transverse loads is generated by arch-like thrust forces developed at midspan and at the supports, provided that the panel is constrained between essentially rigid supports. This so-called arching action theory of masonry wall behavior represents a rather radical departure from conventional bending failure theories, and in effect predicts a substantially greater strength for such panels than would normally be determined from a bending analysis. The theory is generally supported by static test data and by tests involving dynamic loads derived from both high explosive and nuclear blasts. (References 2, 3 and 4).

The static load-deflection relationship for the cinder block panel, computed according to the arching theory, is shown in Fig. 4. This type of resistance function differs essentially from that of the plastic panels, the latter being represented by a curve that increases at a gradually increasing rate until failure. For the plastic panels, the failure displacement, x_f, must be determined empirically. However, according to the arching theory, the failure displacement can be found in terms of the panel parameters.

The computation of the resistance function shown in Fig. 4, involves assumptions as to the crushing stress and strain of the cinder block material, the panel cross-section, and an equivalent beam length. The stress-strain relationship for a masonry material is assumed to be linear up to a so-called crushing stress, s_c, (and strain e_c), after which the stress is assumed to remain constant with increasing strain. The results shown in Fig. 4 correspond to values of s_c = 500 psi and e_c = 0.001. The panel cross-section has been idealized to the extent that the web area of the blocks has been neglected. An equivalent beam length was determined from Reference 3. The equivalent mass of the panel was determined from Reference 5 on the basis of a rectangular panel of aspect ratio 0.625 supported on four edges.

The pertinent panel material properties, blast parameters and normalizing quantities are listed below:

Mass per unit area, $\rho = 5.66 \times 10^{-4}$ lb sec^2/in.^{3}

Equivalent mass, $M = 0.56\,\rho = 3.17 \times 10^{-4}$ lb sec^2/in.^{3}

Failure center deflection, x_f = 7.6 in.

Average resistance, p_{av} = 1.3 psi

Peak overpressure, p_σ = 7.5 psi

Reflected pressure, p_r = 18.4 psi

Diffraction clearing time, t_d = 24 msec

Characteristic pressure, p_f = 6.6 psi (From Eq. 1)

Characteristic time, T' = 61 msec (From Eq. 2).

Based on these values the shock tube results predict a maximum interior overpressure of p_i = 5.5 psi, and rise time to this maximum of t_r = 122 msec. Recall that these results apply to the condition of no reflection from the rear wall of the test structure. However, under the field test conditions the time of travel of a pressure signal from the gage to the rear wall and back to the gage is about 29 msec, or about one-quarter of the predicted rise time based on no rear wall reflection.

The shock tube results thus predict that reflected signals from the rear wall reach the gage before the interior pressure builds up to a maximum. This is in accordance with the field data, and the maximum pressure shown in Fig. 2b is evidently the result of an involved interaction process. It might be noted that the rise time corresponds almost exactly to three transits of a pressure signal across the length of the cell.

While it is not possible to compare directly the measured maximum pressure and rise time with the shock tube results, a less direct comparison can be made. The pressure records obtained in the shock tube showed the initial pressure buildup to be essentially linear. Thus, the ratio of the

predicted quantities p_i/t_r should be comparable to the initial slope of the pressure record shown in Fig. 2b. The shock tube results yield p_i/t_r = 4.5 psi/100 msec. This value compares most favorably with the initial slope of 4.0 psi/100 msec obtained from Fig. 2b.

DISCUSSION

We have considered application of shock tube scale model data to field predictions in a situation where the load phenomena are significantly influenced by the response of the structure. The field test results have shown that a cinder block wall, though completely destroyed by a shock wave, converts the incident shock into a compression wave in the interior of the chamber. Under the field test conditions the rise time of the compression wave corresponded to three transits of the wave across the cell. Thus the maximum pressure is influenced by internal reflections of the wave. The shock tube data, when converted to field test conditions, correctly predicts the occurrence of an interior compression wave, the initial rate of pressure buildup, and the fact that the maximum pressure will not be reached prior to the time that reflections of the wave from within the cell are felt at the gage position. Due to the last stated result it was not possible to compare maximum pressures and rise times since the shock tube data did not involve any reflection effects.

The above comparison hinges on the ability to evaluate certain parameters which depend on the structural characteristics of the test panel. This, in turn, requires a rather detailed theory of the response of the panel to blast loading. At the very least such a theory must correctly predict whether or not the panel is destroyed under a given blast load. The arching theory of masonry wall behavior was utilized for this purpose. The fact that the predicted rate of pressure buildup is within 13 percent of the measured value is certainly of interest, but not particularly conclusive due to uncertainty regarding the adequacy of arching theory and/or the numerical values of material properties assumed for the cinder block panel. To this must also be added the uncertainty in the shock tube prediction itself due to the relatively wide scatter of the data. Nonetheless, it is the writers opinion that, all things considered, this comparison is sufficiently encouraging to recommend extended use of the shock tube as a means of providing estimates of field conditions in this general area of interest. Additional shock tube tests in which the test cell geometry is more representative of field conditions are desirable in order to more conclusively establish this result. In the event that additional shock tube tests are contemplated, it would be of interest to consider panel materials which more closely model the response behavior of conventional wall covering materials than do the plastic materials so far tested.

REFERENCES

1. Zaker, T.A., Effect on Wall Panel Failure of Shock Parameters; Final Test Report No. 8, ARF No. D087, July 1956; Air Force Contract No. AF33(616)-2644; Armour Research Foundation.

2. McDowell, E.L., McKee, K.E., and Sevin, E., Arching Action Theory of Masonry Walls; Journal of the Structural Division, ASCE, Vol. 82, No. ST 2, March 1956.

3. Armour Research Foundation, Dynamic Characteristics of Structural Clay Masonry Walls, Phase Report No. IV, ARF No. K576, October 1956.

4. Armour Research Foundation, "High Explosive Test Program", Phase Report III, ARF No. K576, July 1956.

5. Armour Research Foundation, Investigation of Sympathetic Detonation and Evaluation of Structures for Ammunition Manufacture, Final Report, Part II, November, 1955.

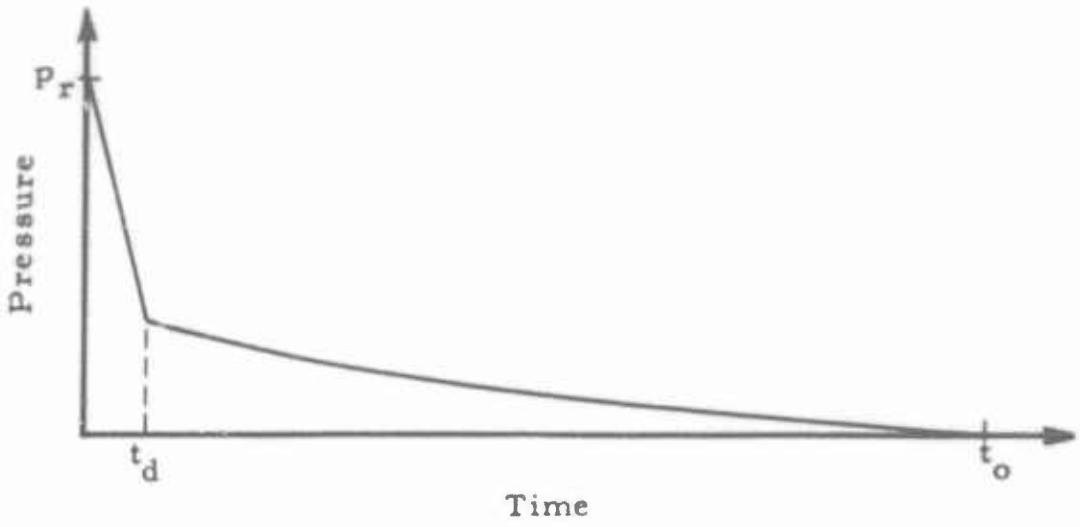

(a) Typical Pressure Wave Form Incident on Panel (Shock Tube and Field Tests)

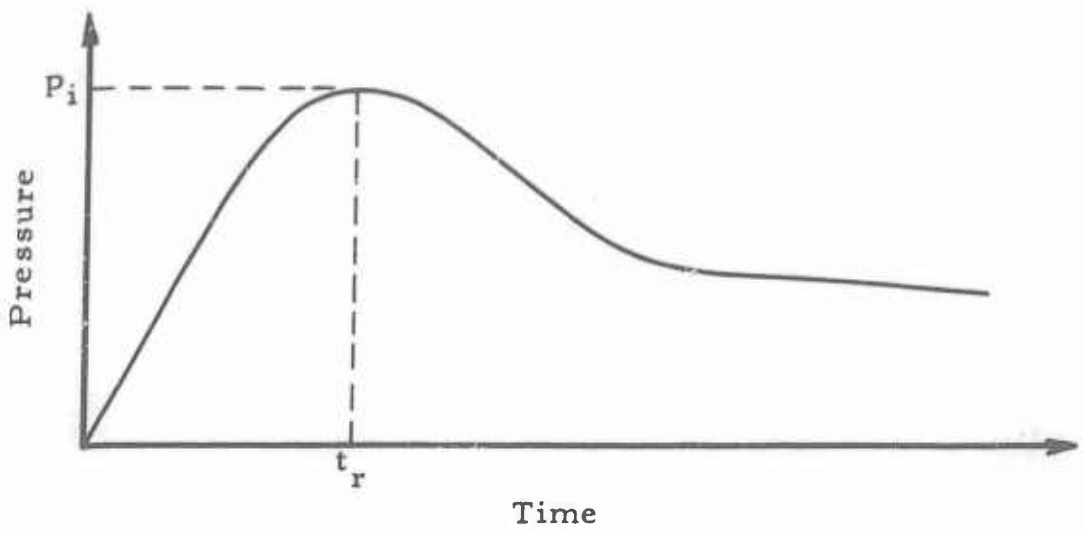

(b) Typical Pressure Wave Form in the Interior of Test Cell (Shock Tube)

Figure 1 Typical Incident and Interior Pressure Wave Form From Shock Tube Tests

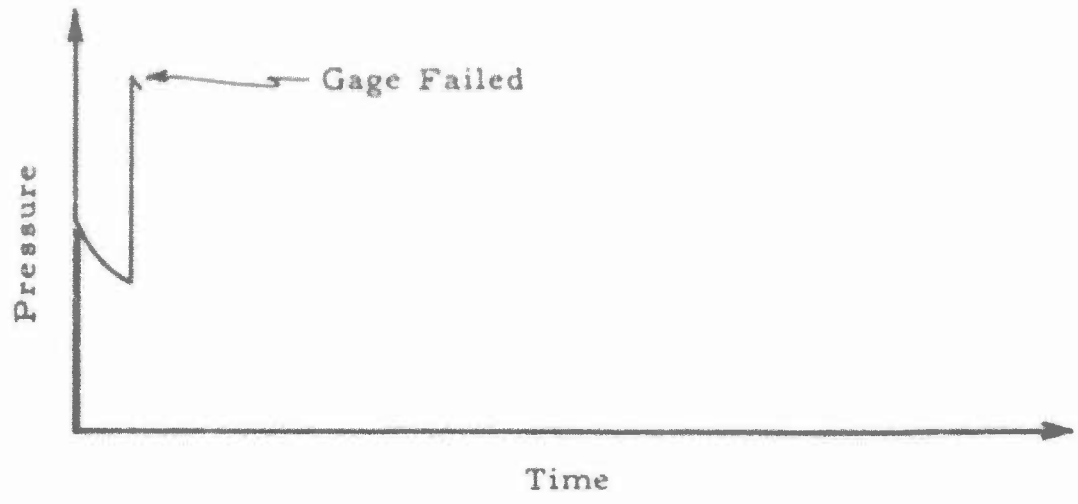

(a) Pressure Wave Form Behind Transite Panel

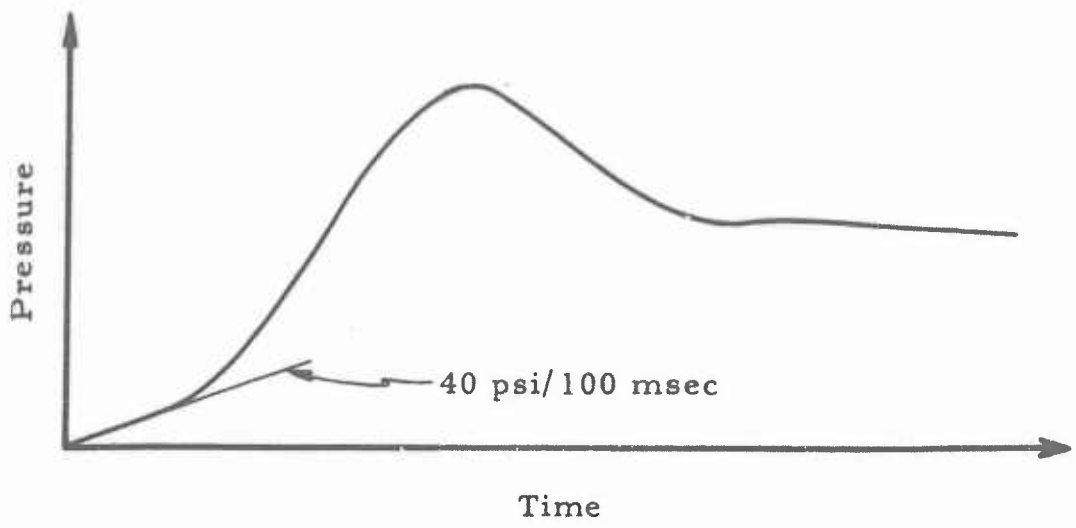

(b) Pressure Wave Form Behind Cinder Block Panel

Figure 2 Interior Pressure Wave Forms from Field Test

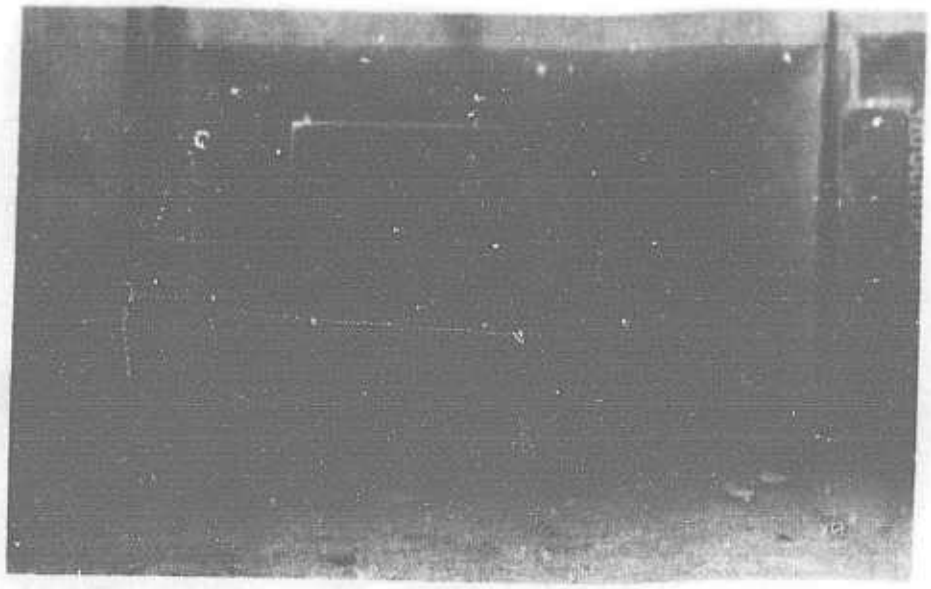

Figure 3 Cinder Block Panel and Supporting Structure, Posttest

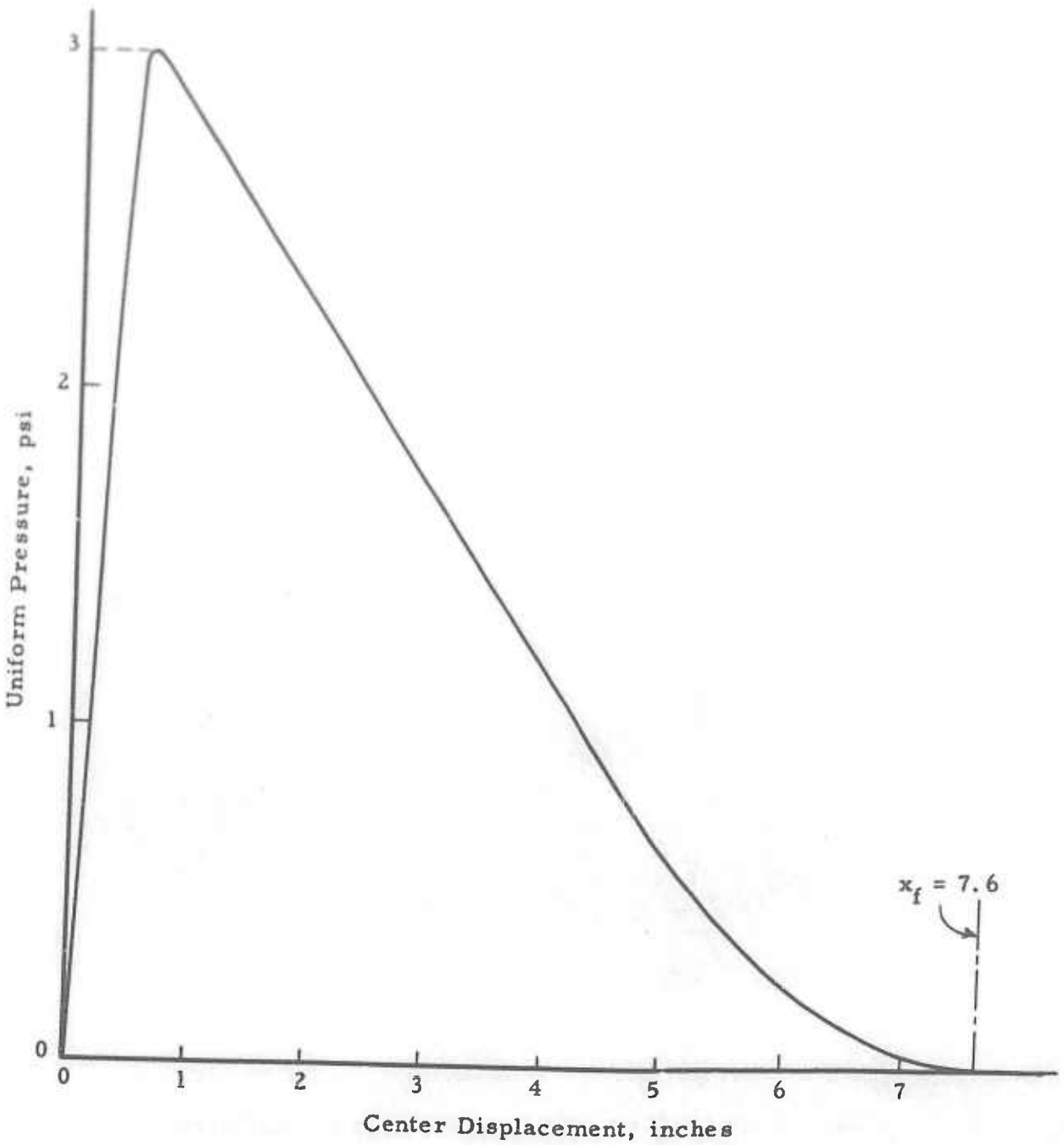

Figure 4 Predicted Resistance Function for Cinder Block Panel

ACKNOWLEDGMENTS

The authors wish to express their appreciation to the Sandia Corporation for their assistance and knowledgeability in instrumenting the shock tube, and to the Department of Medical Illustration of the Lovelace Foundation for preparing the illustrative material.

SOME RESULTS OF A SHOCK TUBE FOR BIOMEDICAL INVESTIGATION*

Donald R. Richmond and Rinaldo V. Taborelli

I. INTRODUCTION

This shock tube was designed to investigate the biological effects of long duration overpressure phenomena as recorded inside protective shelters subjected to nuclear blast. It had to be capable of modifying the different parameters of the blast wave such as maximum overpressure, time to maximum pressure and duration and, in addition, produce single, and multiple reflections as recorded in shelters of different geometric configurations. Also, it had to be of sufficient size to test the larger species of experimental animals.

Although the aerodynamic characteristics have not been studied in detail, its general performance as determined empirically shows this to be a versatile apparatus capable of producing a wide range of pressure-time phenomena.

II. DESCRIPTION

Compression Chamber

The over-all size of the system can be appreciated from Figure 1. The cylindrical compression chamber measures 19 ft x 40-1/2 in. I. D. with a volume of approximately 134 cu ft.

A transition section allows the attachment of either a 12-in. -diameter flange with diaphragm or a 24-in. -diameter flange with diaphragm.

Like the conventional shock tube it employs a rupturable diaphragm separating the high pressure side (or reservoir) from the expansion chamber.

Expansion Chamber

Downstream of the diaphragm a variety of flanged components can be assembled in many different arrangements to provide expansion chambers of many configurations. The test chamber (shown in Figure 1) can be placed in the main axis of the system, or, in combination with a Tee section, at right angles. In addition, metering orifices and/or additional tubes may be added between any of the flanges numbered in the figure. The test tank contains a removable wind protective baffle, and its center flange allows the use of either half of the chamber--accomplished by simply bolting a steel plate to the center flange.

By using long lengths of tubes as the expansion chamber the system becomes a 12 in. or 24 in. shock tube, see Figure 2.

*This work was sponsored by the Division of Biology and Medicine of the Atomic Energy Commission.

Air Source

Air is supplied to the compression chamber by a Schramm Compressor, Model 60 to pressures of 70 psi and to higher pressures by two I-R compressors of 600 psi and 250 psi capacity.

Diaphragm and Rupturing Mechanism

The diaphragm material consists of Du Pont Mylar polyester film of either 0.010, 0.0075, 0.0050 or 0.0025 in. thickness. The Mylar sheets have holes predrilled to match those through the flanges. For its installation it is simply bolted between the distal flange of the reservoir and the first flange on the low pressure side. The various componets of the expansion chamber are on wheels to facilitate changing of diaphragms. Experience has established the specific number of layers which will hold a given pressure in the reservoir. Pressures of 250 psi have been successfully held by this diaphragm material. Diaphragm rupture is initiated by a .22 caliber pistol bullet. The gun is mounted externally in a block that can be mounted on the various components. It fires through a small hole in the tube wall. The pistol firing switch is located in a shielded control room. Other control devices include a U. S. Gage to show the pressure in the reservoir, stop switches for the compressors and a remote control for an exhaust valve on the reservoir. The pressure-time recording equipment is also located in the control room.

Pressure and Time Measurements

Wiancko pressure gages are used to obtain the record of the slower pressure-time phenomena in the test chamber and are supplemented by a Piezoelectric Gage* to define shorter time intervals.

Wiancko pressure gage signals with 3-kc carrier amplification (Consolidated Engineering Corporation System D) used with CEC Type 7-223 galvanometers are recorded on a Consolidated Type 5-114 Recording Oscillograph.

The output of the Piezo Gage**(Model BC-65) is displayed on a Tektronix Model 512 Oscilloscope, modified for self-trigger from signal input and single sweep operation. The sweep on the oscilloscope is photographed for a record with a Polarioid Land type of camera.

The Wiancko gages are calibrated statically--the Piezoelectric by explosive decompression and more recently by pairing it with the Wiancko gage on the shock tube.

---

*Atlantic Research Corporation Barium Titanate Gage, range 0-500 psi.

**Gages supplied by Sandia Corporation, Albuquerque, New Mexico.

III. APPLICATION

Pressure Pulses

The test chamber when used as the expansion source provided a pressure pulse type phenomena. The rise time, maximum pressure and the duration of the pulse were varied by different combinations of reservoir pressures, metering orifices and volumes of test chamber. To date the volume of the compression chamber has not been altered.

Several arrangements, along with the pressure-time records, are illustrated in Figure 3, 4, 5 and 6. These records are typical of those from a series of experiments in which the effect of high pressures applied at various rates on dogs was being studied. In all cases the durations were prolonged in order to eliminate biological complications due to decompression. From Figures 3 and 4 it can be seen that with a 12 in. throat, the entire test chamber fills in approximately 85 msec and half the chamber in 63 msec. With half the tank and a 24 in. throat, a rise time of 30 msec was recorded, see Figure 5. To obtain rise times longer than 30 msec with 24 in. flanges and diaphragms a metering orifice plate was inserted at the entrance of the test section. With such an arrangement a rise time of 155 msec was recorded, see Figure 6.

Pressure pulses are quite reproducible and for a given arrangement the pressure curve shape does not vary importantly over a wide range of diaphragm pressures, see Figure 7.

In connection with the above pressure-time patterns, 16 dogs sustained relatively minor pathology. At maximum overpressures ranging between 74 and 170 psi with time to maximum pressure approximately 30, 60, 85 and 155 msec, animals exhibited ruptured eardrums, hemorrhagic sinuses and trivial pulmonary hemorrhages probably caused by the lungs' lower borders being pinched between the rib cage and the diaphragm. This study will be extended and additional cases will be added to each of the four groups in which the maximum pressure will be above 200 psi. It is also planned to assess pressure pulses in which the pressure peaks in times less than 30 msec. By employing smaller test chambers, rise times of 17 and 13 msec have been produced. Figure 8 shows the arrangement in which the pressure peaked in 13 msec.

Shock Waves

Actually little has been done as far as employing the components as an open shock tube. Some physical materials were tested and calibrated prior to the Nevada tests in 1957 by personnel from Sandia Corporation. Shock waves of 9 psi and 180 msec duration to 26 psi of 530 msec duration were recorded in 12 in. shock tubes. As far as animal tests are concerned, the winds associated with the shock wave present a special problem, and in addition make it difficult to successfully mount specimens in the open tube.

Reflected Shocks

Many of our biological tests have been carried out with the 24 in. shock tube closed. High pressures, with steep fronts, are provided by the reflection of the shock front from the end plate. The pressure-time records obtained measured with Wiancko gages face-on in the end plate, and side-on at 1 and 11 ft from the plate are illustrated in Figure 9. The relationship between mortality and peak reflected pressure indicated that the mortality dropped markedly for a given pressure shot when the animal cage was moved 1 ft from against the end plate. In other words, the pressure curve recorded from Gage 1 in Figure 9 with a peak reflected shock of 41 psi killed approximately 70 per cent of the guinea pigs located against the end plate. On an identical shot, those located 1 ft from the end (in a cage below Gage 2) survived.

Apparently a time step of less than 1.5 msec between the incident shock and its reflection is of tremendous importance biologically and the problem is under further investigation.

To obtain a reflection at the closed end of the tube without repeated reflections, the cross section--opened laterally--was included in the system. Figures 2 and 10 show this arrangement together with pressure-time recordings taken at the indicated points along the tube. This arrangement shows promise that, on a larger scale, it will allow the exposure of larger animal species (dogs) side-on at various distances from the end plate to assess various time steps.

IV. CONCLUSIONS

The primary aim in the designing of this shock tube was to develop a laboratory facility capable of reproducing a given pressure wave from records in nuclear field testing in order to study its effects on experimental animals in more detail. Experience with the present system has shown it has satisfied its primary requirement. In addition, this device permits a broad basic study of the biological significance of overpressure.

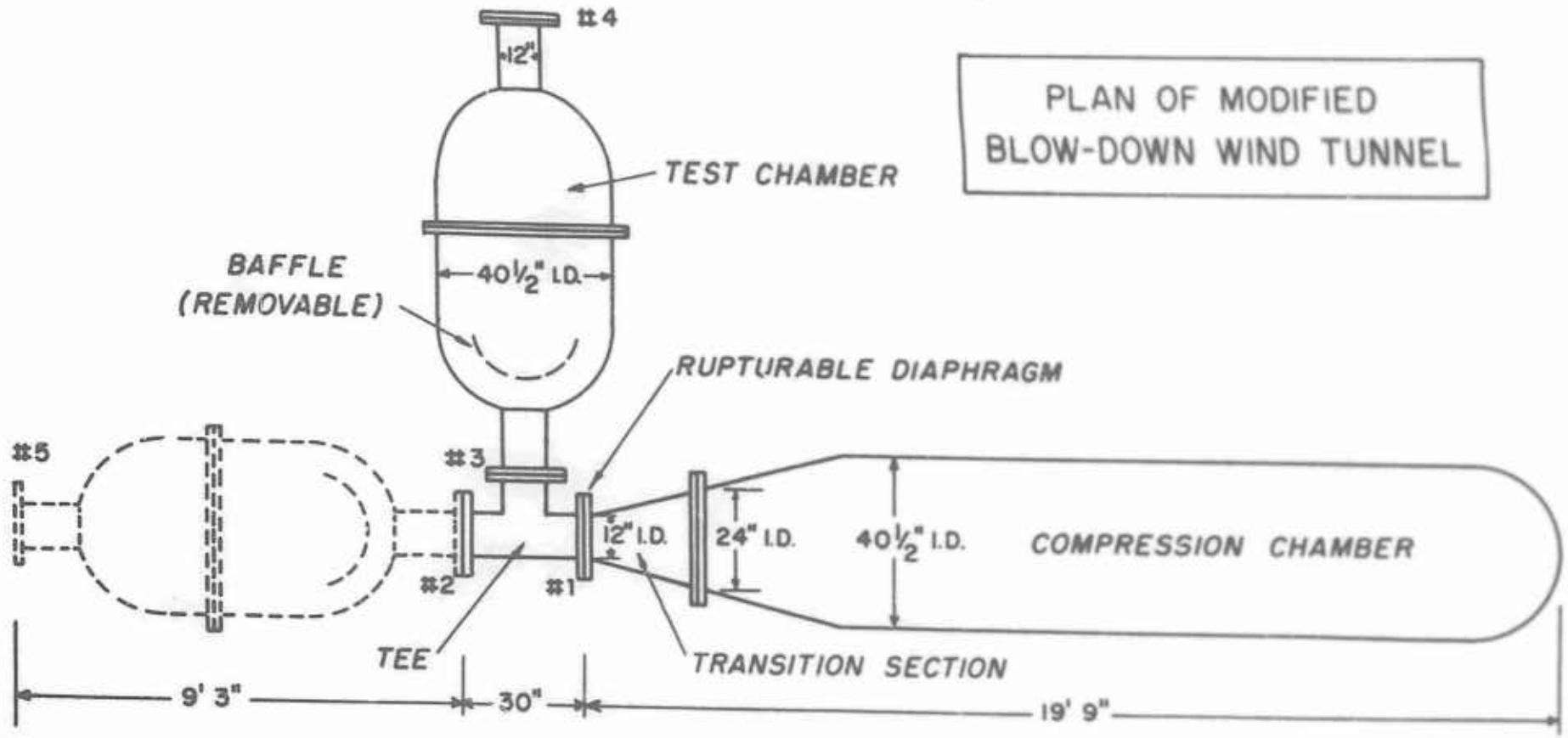

Figure 1 Plan of Shock Tube

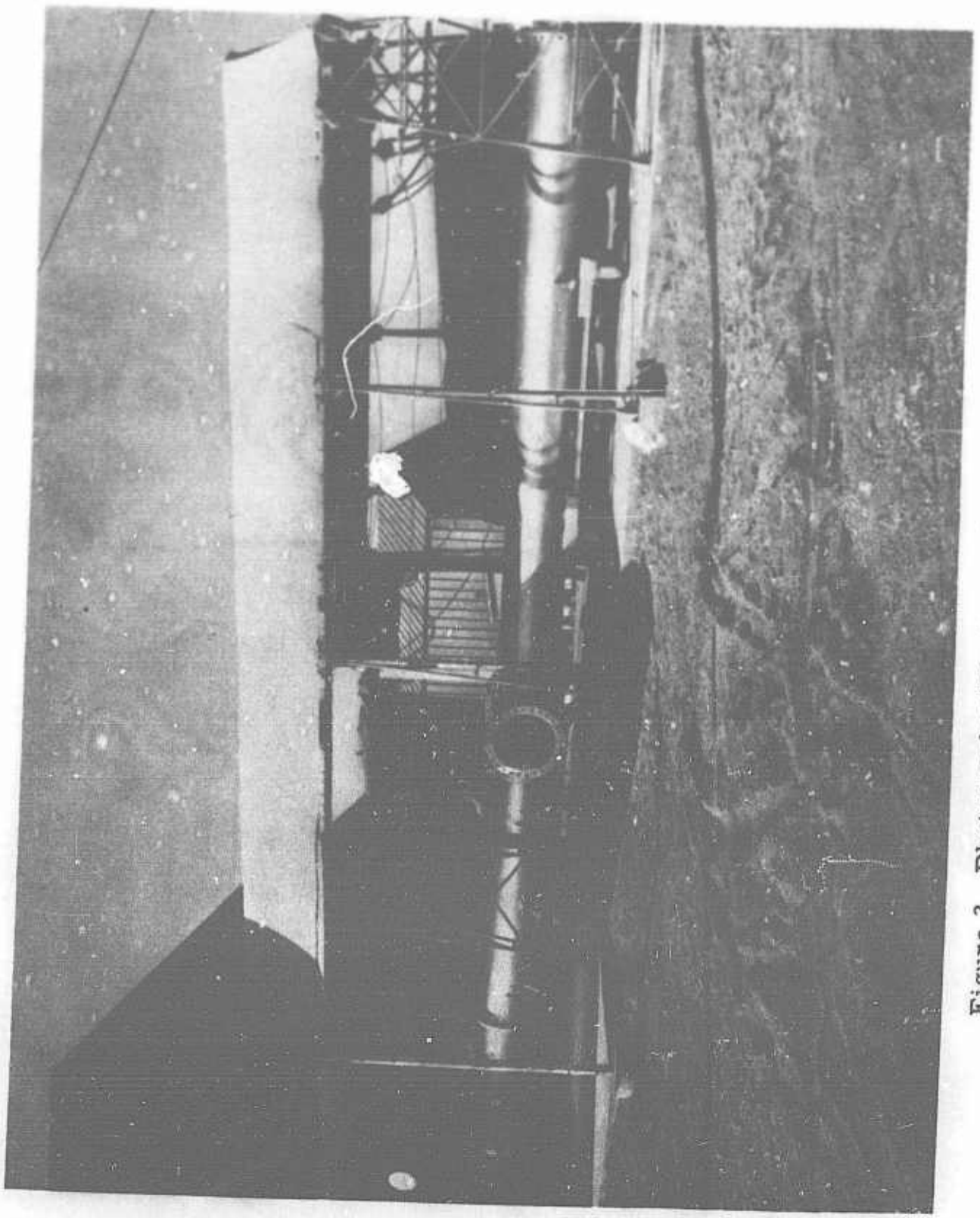

Figure 2 Photograph of Device used as a 24 in. Closed Shock Tube with Open Lateral Exhaust Ports

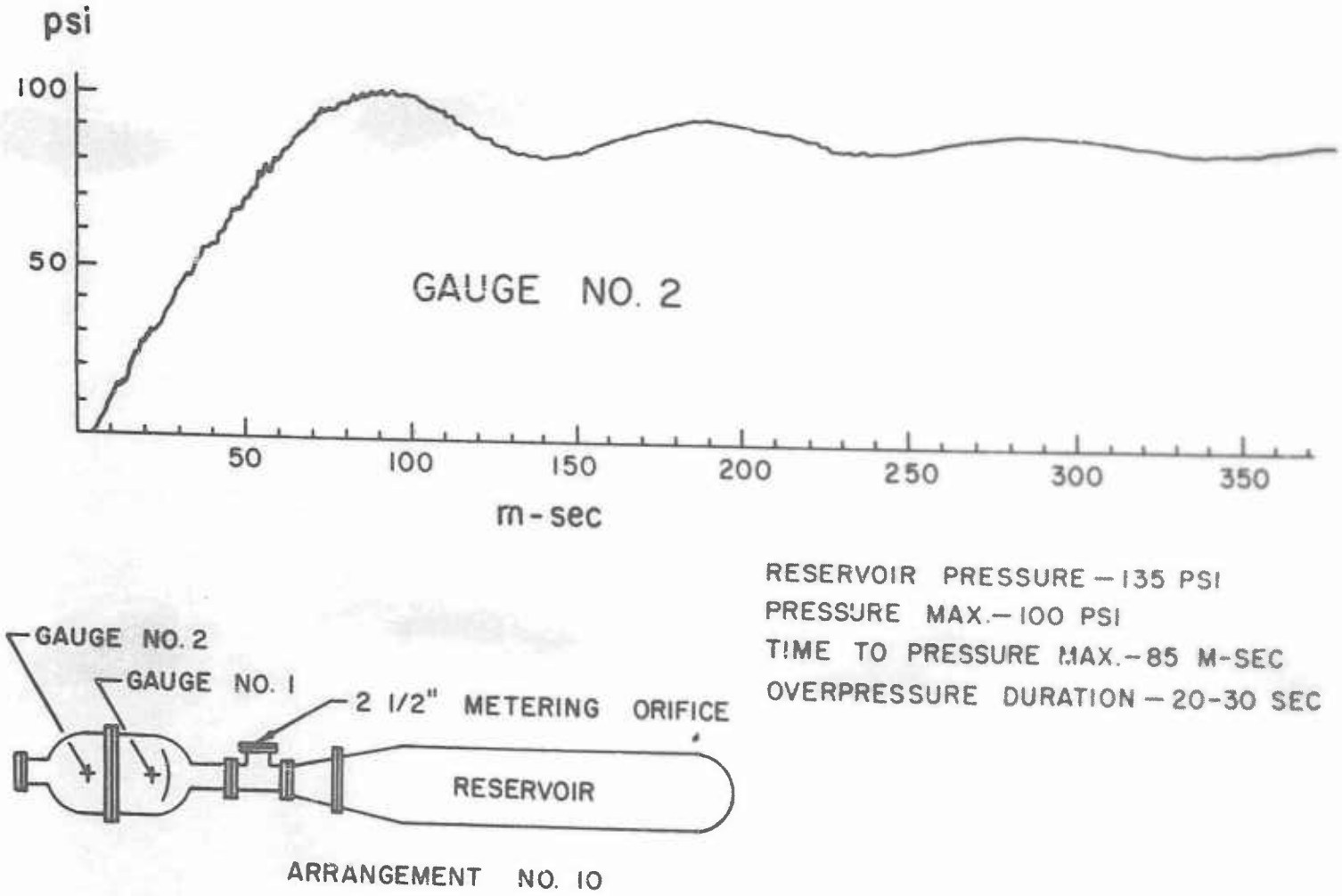

Figure 3 Arrangement Employed to Obtain a Rise Time of 85 msec

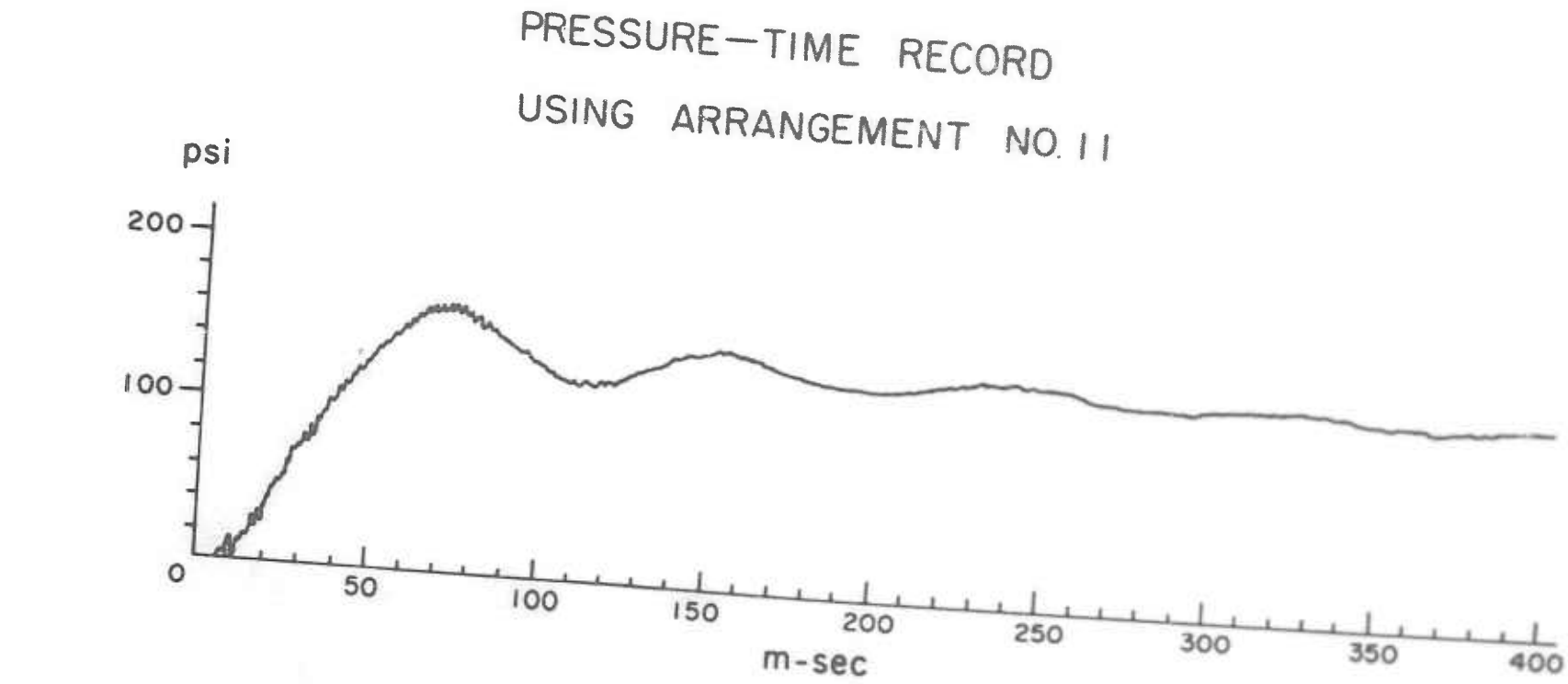

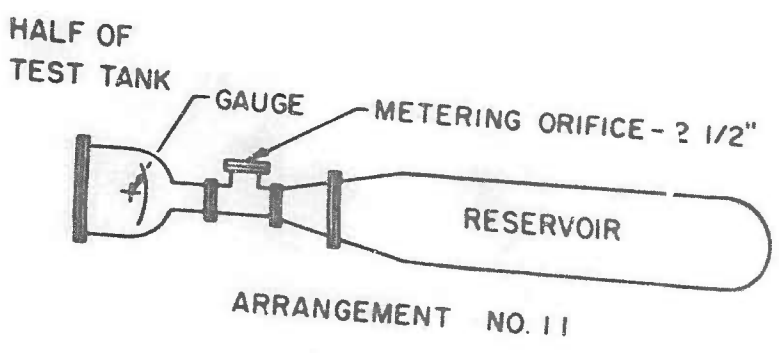

RESERVOIR PRESSURE — 178 PSI
PRESSURE MAX. — 163 PSI
TIME TO PRESSURE MAX — 63 M-SEC
OVERPRESSURE DURATION — 10 SEC (APPROX.)

Figure 4 Arrangement Employed to Obtain a Rise Time of 63 msec

PRESSURE–TIME RECORD

USING ARRANGEMENT NO 12

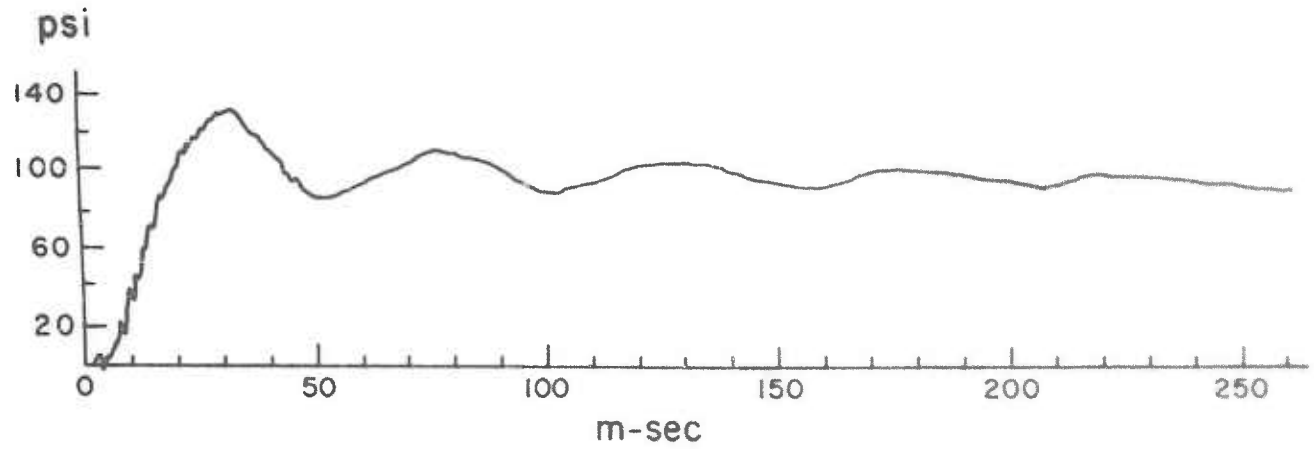

RESERVOIR PRESSURE – 135 PSI
PRESSURE MAX. – 130 PSI
TIME TO PRESSURE MAX. – 30 M-SEC
OVERPRESSURE DURATION – 20 SEC (APPROX.)

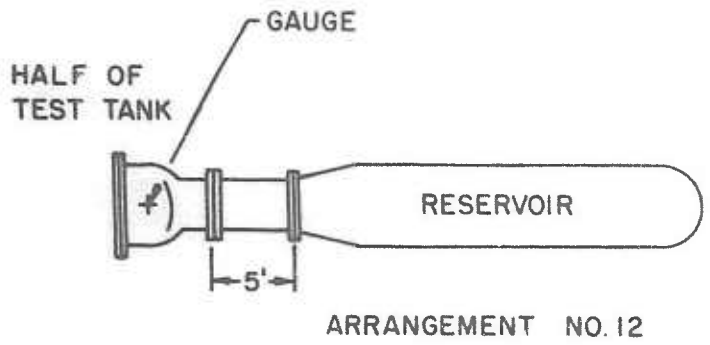

ARRANGEMENT NO. 12

Figure 5 Arrangement Employed to Obtain a Rise Time of 30 msec

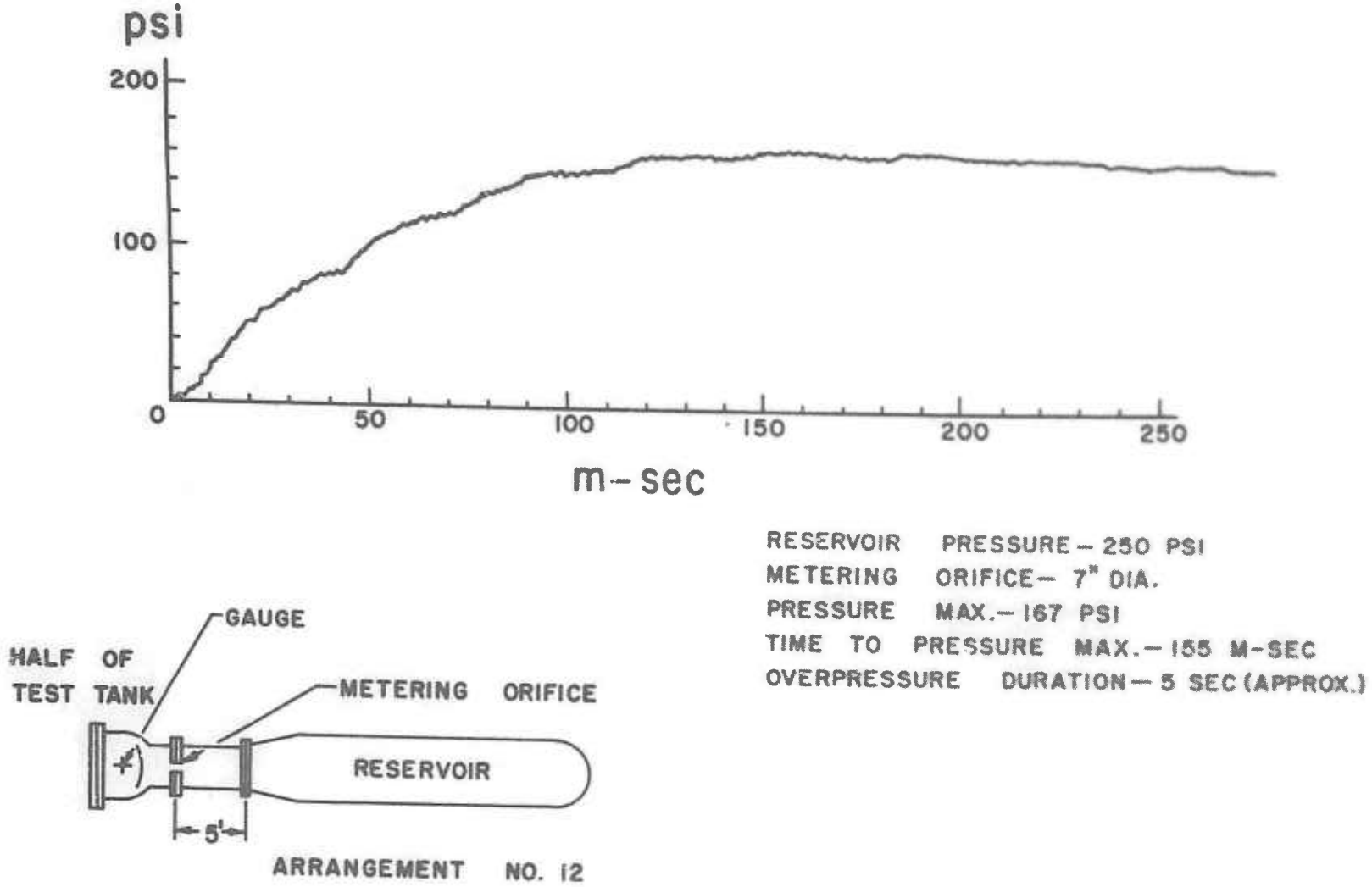

Figure 6 Arrangement Employed to Obtain a Rise Time of 155 msec

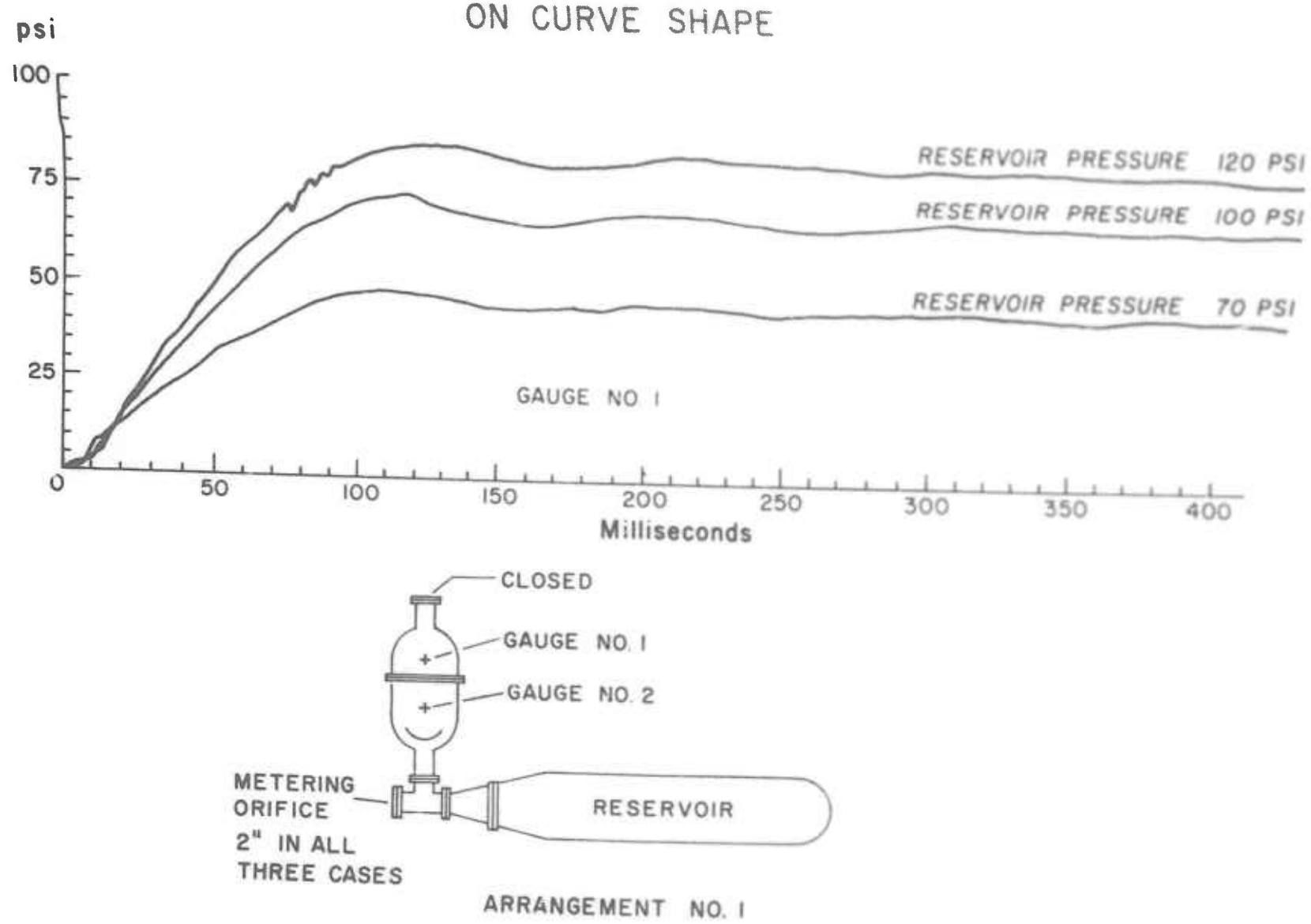

Figure 7 Pressure Pulses Recorded in a Given Arrangement at Different Diaphragm Pressures

PRESSURE—TIME RECORD

USING ARRANGEMENT NO. 16

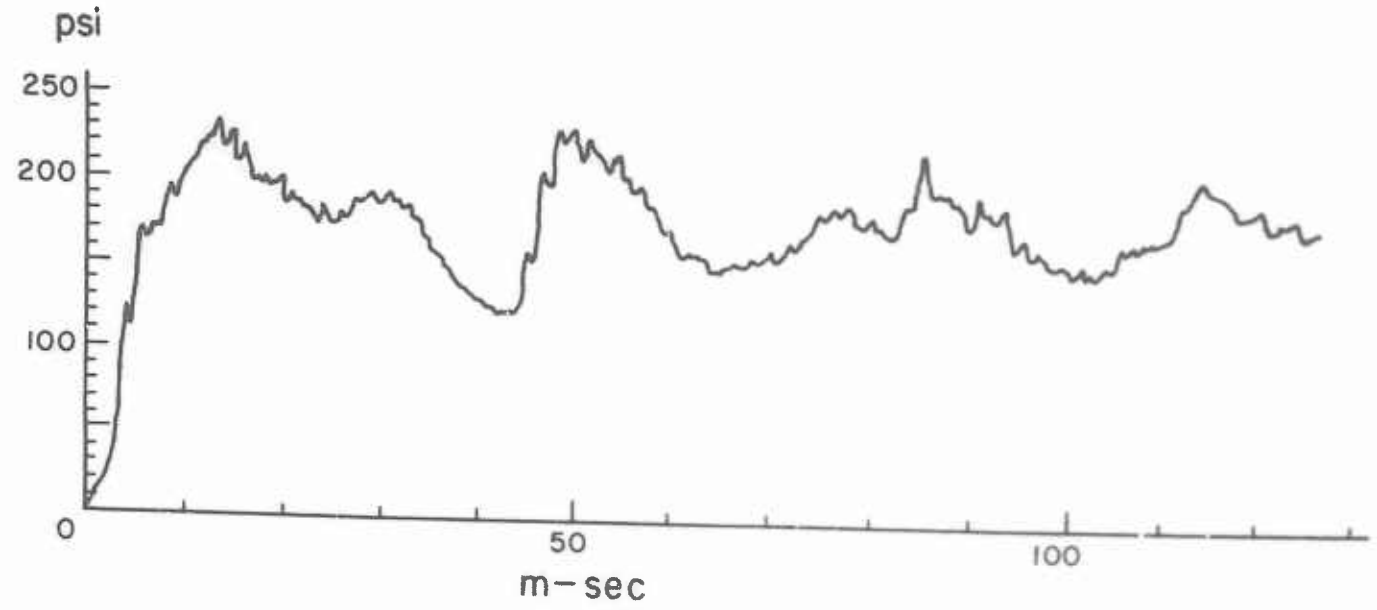

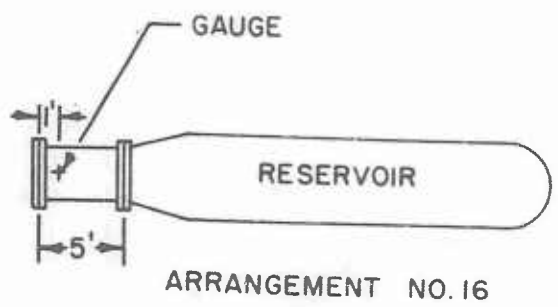

ARRANGEMENT NO. 16

RESERVOIR PRESSURE — 200 PSI
PRESSURE MAX. — 230 PSI
TIME TO PRESSURE MAX. — 13 M-SEC
OVERPRESSURE DURATION — 2 MIN (APPROX.)

Figure 8 Rise Time of 13 msec Obtained with Small Test Chamber

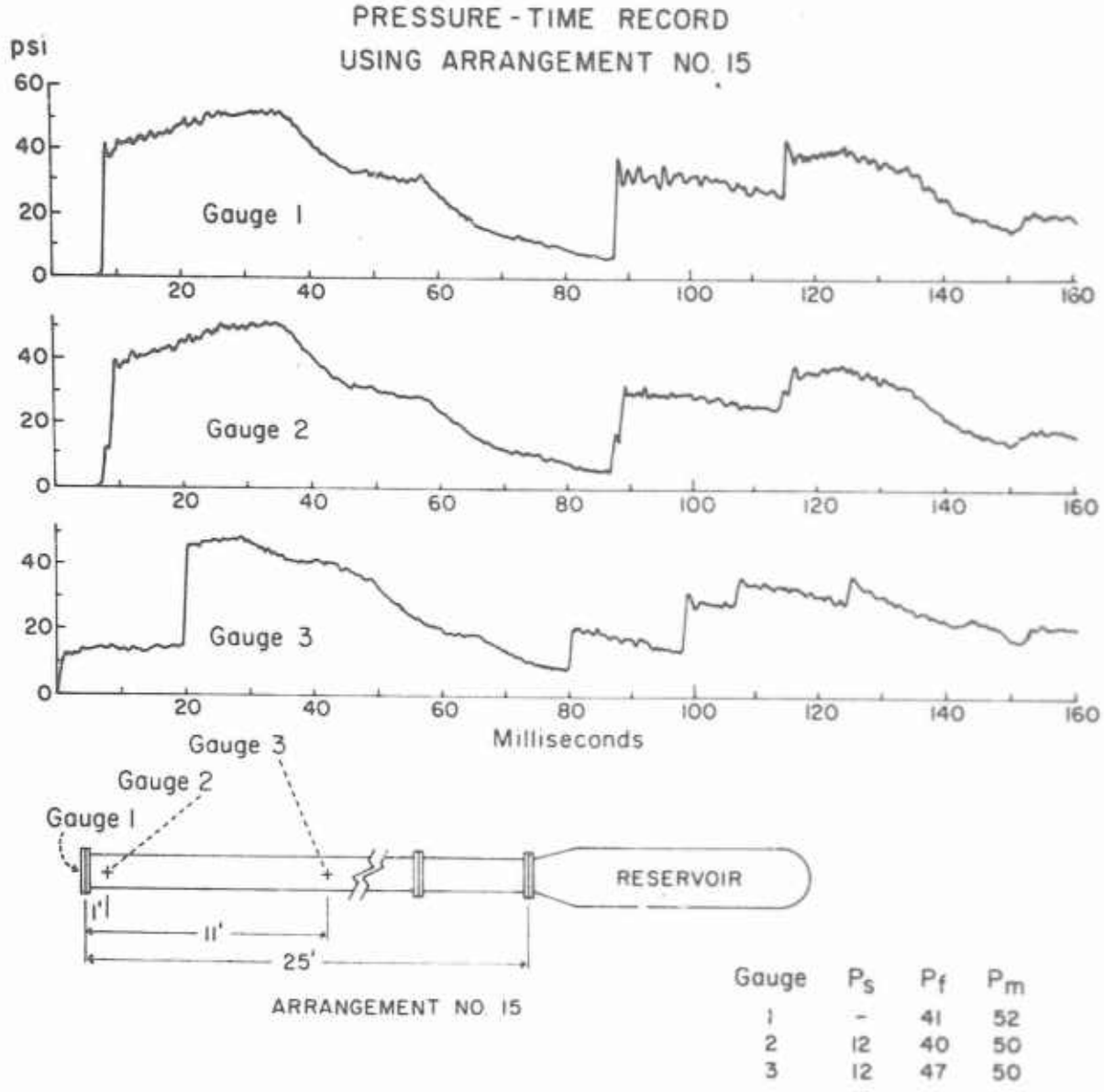

Gauge	P_s	P_f	P_m
1	-	41	52
2	12	40	50
3	12	47	50

Figure 9 Records of Pressure-Time Along Closed Tube

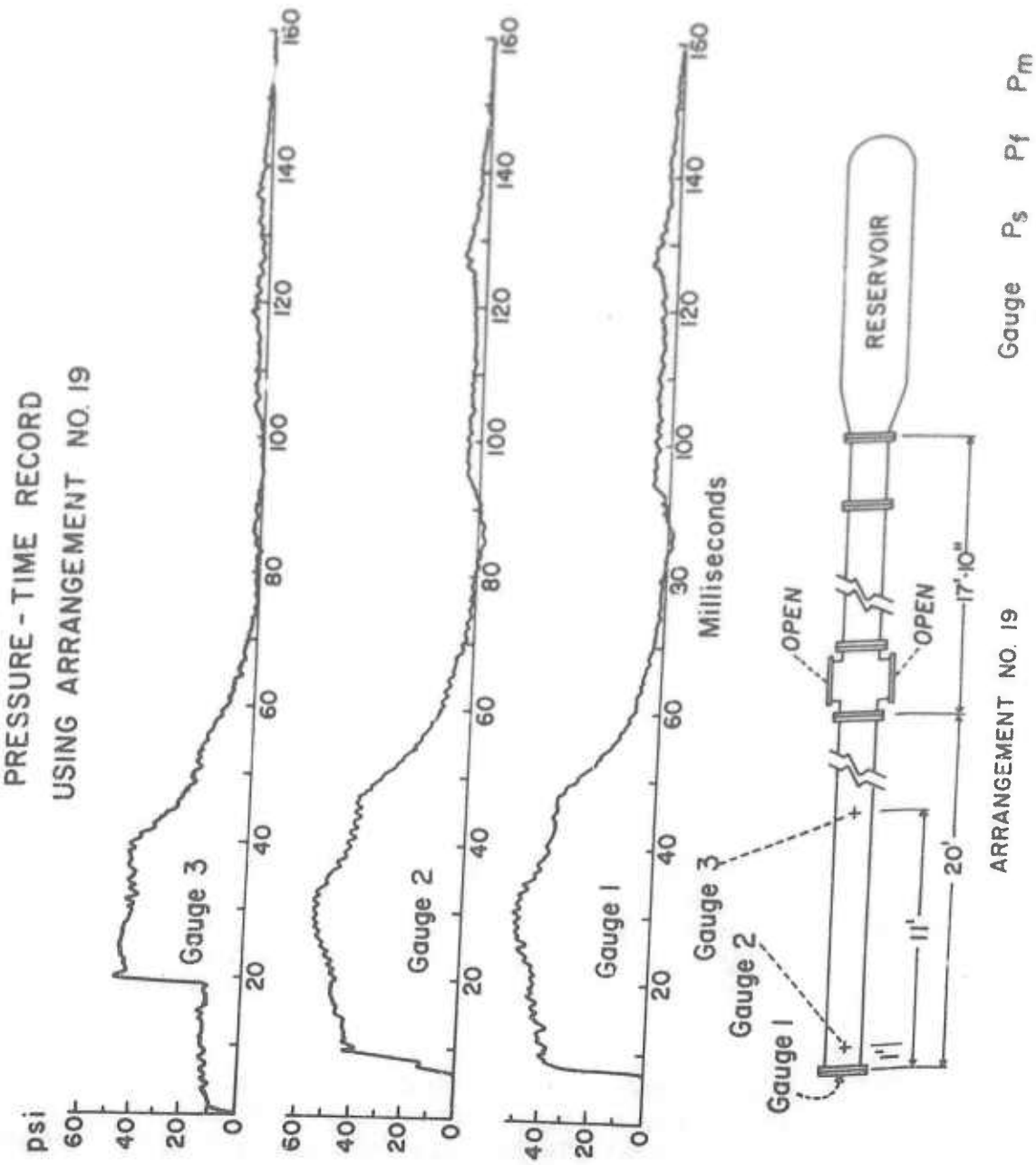

Figure 10 Records of Pressure-Time Along Tube with Lateral Ports Open

EXPERIMENTATION WITH THE GENERAL ELECTRIC SIX-INCH SHOCK TUNNEL

E. M. Kaegi, W. R. Warren and A. J. Vitale
Missile & Ordnance Systems Department
General Electric Co.
Philadelphia, Pa.

INTRODUCTION

For atmospheric flight above Mach number of approximately 7, realistic considerations of the heated flow about a vehicle must include the "real gas" effects associated with vibration, dissociation, and ionization. For example, a satellite body will be exposed to gases with equilibrium temperatures of the order of 7,500°K during re-entry into the atmosphere; at these temperatures in air, nearly all of the oxygen molecules and some of the nitrogen molecules are dissociated. Because the flow environment is so appreciably different from that of low temperature applications, both experimental and theoretical techniques used for the study of the aerodynamics of such situations should include the effects of these high temperature phenomena.

The shock tube has been found to be a satisfactory tool for the study of high energy quasi-steady flows about bodies for short time periods. However, the simple shock tube is limited in one important respect for the simulation of steady high Mach number flight conditions: in the desirable testing region it is possible to reach test Mach numbers only of the order of three. For several types of studies, useful experimentation may be done under this restriction. Accurate simulation of hypersonic flow over all regions of a body, however, should include the simulation of flight Mach number or, at least, the variation of Mach number over an appreciable range.

The shock tunnel combines the features of a shock tube - high thermodynamic properties of the gas - with the variable test section Mach number property of a wind tunnel. Essentially, a shock tunnel is a blow-down wind tunnel which uses a shock tube to provide a working gas of high stagnation enthalpy and pressure. With such a facility, wide ranges of test section Mach number, Reynolds number, and stagnation enthalpy may be covered and the effects of these variables on the flow properties may then be studied.

The object of this paper is to present theoretical and experimental performance data and some of the results of the work done during the first year of operation of the General Electric six-inch shock tunnel. Presented are the theoretical regions of testing available for the three tunnel configurations. The problem of establishing the flow through the nozzle is discussed. Comparisons are shown between experimental and theoretical stagnation heat transfer rates and pressures for a range of conditions using the reflected nozzle. Heat transfer rates and pressure distributions on a hemisphere-cylinder body are also shown.

Schlieren photographs of the flow over various cone sphere configurations are presented and a comparison is made between theoretical and measured shock detachment distances for two basic shapes.

Description

Figure 1 illustrates the General Electric six-inch shock tunnel facility. As a safety precaution, the combustion driver is housed in a building set apart from the laboratory. The driver is 22 feet long and has an 8 inch inside diameter. Although other mixture ratios have been used, the standard combustion charge consists of 70% helium, 20% hydrogen, and 10% oxygen (mole fractions). Twenty spark plugs located symmetrically along the tube are employed to ignite the charge. Nitrogen is used in purging the system. Operation of the facility is remotely controlled from the control room. The driven tube has a six-inch inside diameter and at present is 113 feet long. It consists of a series of interchangeable sections. The conical nozzle has a 30° included angle, and the test section is 30 inches in diameter. A more detailed discussion of the facility is given by Warren (1).

Figure 2 shows the nozzle and test section. The tubular sections house the two-axis schlieren system. The horizontal axis is used for single, short duration photographs, and a Fastax camera monitors the entire flow on the vertical axis.

Theoretical Performance

With the General Electric Shock Tunnel, there are three types of high stagnation enthalpy flows available. Figure 3 explains these tunnel configurations schematically. The first is the straight shock tube. The flow behind the incident shock wave (region 2) provides high Reynolds number simulation; however, flow Mach numbers are restricted to 2 or 3. It is also necessary to restrict the model size. The addition of the non-reflected nozzle allows expansion of the flow behind the incident wave through an area ratio of 25. This results in flow Mach numbers between 4 and 6 and in flows of moderate Reynolds numbers. With a 30-inch diameter test section, model size is somewhat flexible. The reflected nozzle configuration generates a reflected wave that propagates back up the driven tube after the arrival of the incident wave. The resulting high enthalpy stagnation gas accelerates through a small diameter throat into the nozzle and test section. With the present 3/4-inch diameter throat, the flow Mach numbers range between 6.0 and 12.6. Smaller throat inserts now available will extend the flow Mach number to 22. The relatively low free stream Reynolds numbers allow only for laminar boundary layer studies.

Some of the performance calculations for the three test sections will now be discussed. The free stream Reynolds numbers, flow Mach numbers, model stagnation pressure and temperature, and the simulated free flight conditions are considered. The calculations were made using the properties of air in thermodynamic equilibrium presented by Hilsenrath and Beckett (2).

Figure 4 presents the free stream Reynolds numbers as a function of initial driven tube pressure and shock Mach number. The limits to the right are due to driver tube design pressure limits (10,000 psi). It can be seen that Reynolds numbers as high as 10^7 per inch are possible in the straight tube. There is sufficient overlap in the ranges of the three test sections so as to allow studies at constant Reynolds numbers over a wide range of flow Mach numbers.

Figure 5 gives the flow Mach numbers for the three configurations at an initial driven tube pressure of 10 mm of Hg. With the present 3/4-inch diameter throat, which provides an area ratio A_m/A_t of 1600, the reflected nozzle produces a M_m value of 12.6 for $\gamma = 1.4$ flows. However, at the higher shock Mach numbers the real gas effects reduce this to approximately 6.6.

The model stagnation pressure ratio for an initial driven tube pressure of 10 mm is depicted in Fig. 6, as are the values for a constant γ of 1.40. There are 1 to 2 orders of magnitude difference between pressure levels for the 3 different testing conditions.

The stagnation temperature ratios for initial driven tube conditions of 10 mm Hg pressure and 530°R are presented in Fig. 7. While the stagnation enthalpy for the reflected nozzle configuration is greater than for the straight-through nozzle, the real gas effects cause lower stagnation temperatures in the former than in the latter.

The range of simulation for a vehicle in free flight in the atmosphere, based on stagnation point conditions for a blunt body, is shown in Fig. 8. The upper limits are dictated only by satisfactory operation of the shock tunnel facility. These limits occur at initial driven tube pressures of about 1 mm of Hg.

Tunnel Operation

An important consideration in shock tunnel work is the establishment of test flows through the nozzles and test sections. Work at CAL (3) has shown that evacuation of the nozzle to pressures much lower than initial driven tube values will allow the starting waves to pass through the test section and cause the establishment of the desired test flow. First attempts to do this involved separating the nozzle from the driven tube with a thin myler diaphragm. Unfortunately, the diaphragm shattered and contaminated the test flow with small particles; these damaged the model and caused model instrumentation to be practically useless. To overcome this problem in the reflected nozzle, the following technique is employed: a stopper is inserted in the 3/4-inch diameter throat (Fig. 9); approximately one second before firing, this stopper is mechanically pulled back into the dump tank; the initial driven tube pressure drops about 10% before firing time t_1; the starting waves pass through the test section, and the test flow is established as shown (at time t_2). The establishment of the flow in the test section for a run at shock Mach number 6.5 is depicted in Fig. 10. A Fastax camera is used and the gas provides its own illumination. The model stagnation pressure history is shown to the right. Quasi-steady state testing time is obtained for a period

of about 1.5 milliseconds for this run; expansion waves begin to reduce the reflected region pressure after the test period.

Since the stopper method is impractical for the straight-through nozzle, a different scheme was considered. Calculations have shown that with helium in the nozzle and test section at the pressure of the air in the driven tube, the starting waves will pass through quickly enough to allow the establishment of the test flow. This method has been proven to be successful.

One of the important experimental results in a shock tunnel run is the incident shock wave velocity. Three measurement systems are presently in use, all of which use the standard SLM piezo-electric gage for sensing the shock wave passage. One incorporates a time calibrated Raster sweep on an oscilloscope and the gage responses appear as pulses. Another uses a counter that is tripped and stopped between two stations near the end of the tube. A pressure history for six stations along the tube is obtained from a Hathaway oscilloscope recorder. In a portion of one of the films (Fig. 11), a 100 micro-second timing pulse can be seen superimposed on each trace.

Figure 12 shows the average incident shock wave velocities over the last 60 feet of the driven tube. The nominal driver pressure is 300 psi. For an initial driven tube pressure of 10 mm of Hg, it can be seen that shock Mach numbers of approximately 9.5 are obtained at the end of the driven tube.

Experimental Model Testing

All of the experimental results discussed here were obtained using the reflected nozzle configuration. Three types of instrumentation were used: pressure, heat transfer, and schlieren photographing.

Model pressure measurements have been made using the standard SLM quartz crystal gage. Values as low at 0.05 psi have been successfully measured. To obtain satisfactory response with this gage, it was necessary to locate the gage in a cavity (Fig. 13). A small diameter hole extends to the model surface. Shock mounting with rubber O-rings reduces extraneous oscillations. The gages were calibrated in the side wall of the driven tube during low shock Mach number runs. The outputs were found to be linear with pressure over the range of testing conditions. The response of a gage located at the stagnation point on a model and the corresponding reflected region pressure record are presented in Fig. 14. Time increases to the left. The trace of the reflected region pressure was accentuated by the photo reproduction. A second wave can be seen at a later time in the driven tube. It is believed that this is a product of the combustion process.

In Fig. 15 experimental model stagnation region pressures are compared with calculated values over a range of shock Mach numbers. It is seen that at shock Mach numbers below 8.5, the data scatters about predicted values for the nominal design area ratio of 1600. Above 8.5 the experimental data falls substantially below predicted values. No explanation is offered for these results. However, calculations assuming completely frozen flow through the nozzle for this facility indicate such a trend in pressures.

A brief survey was conducted to determine the uniformity of flow conditions in the test section. Pressure gage measurements were made along the stagnation point line on a cylindrical rake. Figure 16 shows the results of these runs. Measurements indicate that models with a maximum diameter of greater than 6-inches can be tested in a fairly uniform flow.

Some of the experimental pressure distributions obtained for basic shapes will now be discussed. Shown are comparisons between experimental data and modified Newtonian predictions for a hemisphere cylinder body. The data obtained at a flow Mach number of 6.7 and a stagnation temperature of 5000°K are presented in Fig. 17. The points scatter about the Newtonian curve up to S/R values of 1.2. Beyond that the data falls above the curve. Figure 18 is the distribution at Mach number 9.0 and a stagnation temperature of 3100°K. The data tends to be higher in the subsonic region about the stagnation point.

For the determination of surface heat transfer rates, thin platinum film resistance gages are used. The films, approximately 0.1 micron thick, are sputtered on pyrex and vycor plugs. A very thin coating of silicon monoxide, about 0.03 to 0.05 microns thick, is evaporated over the gage to provide protection from the ionized test gas and also to add to the durability. Figure 19 shows a 3-inch diameter epoxy hemisphere with the contoured plug gages mounted.

The response of a stagnation heat transfer gage is shown in the upper left corner of Fig. 20. The reflected region pressure is also shown. Time is increasing to the left. Vidal's solution (4) for one-dimensional heat transfer into a semi-infinite solid has been programmed for the 704 computer. The heat transfer history that corresponds to the data is shown at the bottom of Fig. 20. Quasi-steady state flow is experienced between 2 and 5 milliseconds on the time scale shown. Note that the gage was still responding after 10 milliseconds.

A comparison between stagnation point heat transfer rate measurement and some of the existing theories over a wide range of stagnation enthalpies is shown in Fig. 21. The predictions of Cohen and Reshotko (5), and Lees (6) were evaluated using the Li-Geiger approximation (8) for the stagnation point velocity gradient. The data was corrected to the given stagnation pressure and nose radius by assuming $\dot{q}_s \frac{p_s}{r_n}$. The points fall substantially higher than both theories in the low enthalpy high flow Mach number range. However, at the low Mach numbers, the experimental values tend to approach the predicted ones.

Figure 22 shows the results of a brief study of the heat transfer distribution about a hemisphere. The data tends to fall below the Lee's theory except near the tangency point.

Some of the schlieren photographs obtained on various cone-sphere configurations are shown in Fig. 23. The average flow Mach number was about 12.

Figure 24 shows a comparison of measured shock detachment distances and theoretical predictions for a flat-faced cylinder and for a hemisphere. The data tend to fall above the predicted results.

Conclusions

It is concluded that the shock tunnel facility is a useful laboratory tool for the study of high temperature aerodynamic problems. Through the use of different test configurations, flows with wide ranges of flow Mach number, stagnation enthalpy, and Reynolds numbers may be produced. The quasi-steady test flows are of short duration - a few milliseconds - but instrumentation methods are available for the measurement of many important aerodynamic properties of model flow. Present techniques are such that significant scatter is present in the test data; however, continuous improvement has been made in instrumentation methods and it is expected that future development will reduce this problem.

SYMBOLS

M	Mach number
R_e	Reynolds number
A	Area
T	temperature
u	velocity
a	speed of sound
p	pressure
$\dot{q}$	heat transfer rate
r	radius
S	surface distance of hemisphere
θ	s/r, radians, also cone angle, degrees
	bow shock detachment distance
ρ	density
h	enthalpy
RT_o	33.86 BTU/lb
ms	millisecond
$\dot{t}$	centerline of test section

REFERENCES

1. Warren, W.R.; The Design and Performance of the General Electric Shock Tunnel Facility; Proceedings of the 1st Shock Tube Symposium sponsored by the Air Force Special Weapons Center, Kirtland AFB; February 1957.

2. Hilsenrath, J. and Beckett, C.W.; Tables of Thermodynamic Properties of Argon-free Air to 15,000°K; Thermodynamics Section, National Bureau of Standards; AEDC-TN-56-12; September 1956.

3. Glick, H.S., Hertzberg, A. and Smith, W.E.; Flow Phenomena in Starting a Hypersonic Shock Tunnel; AEDC-TN-55-16; March 1955.

4. Vidal, R.J.; Model Instrumentation Techniques for Heat Transfer and Force Measurements in a Hypersonic Shock Tunnel; WADC TN-56-315; February 1956.

5. Cohen, C.B., and Reshotko, E.; The Compressible Laminar Boundary Layer with Heat Transfer and Arbitrary Pressure Gradient; NACA TN 3326; 1955.

6. Lees, L.; Laminar Heat Transfer Over Blunt-nosed Bodies at Hypersonic Flight Speeds; A.S., Vol. 26, No. 4; April 1956.

7. Shaw, J.E., Pergament, H. S., and DiCristina, V.; Convective and Radiative Heat Transfer Equations; Heat Transfer Technical Memo No. 23, M&OSD, G.E. Co.; 1956.

8. Li, T., and Geiger, R.E.; Stagnation Point of a Blunt Body in Hypersonic Flow; J.A.S., Vol. 24, No. 1; January 1957.

9. Probstein, R.F.; Inviscid Flow in the Stagnation Point Region of Very Blunt-nosed Bodies at Hypersonic Flight Speeds; WADC TN 56-395; September 1956.

10. Maslen, S.H. and Moeckel, W.E.; Inviscid Flow Past Blunt Bodies; J.A.S., Vol. 24, No. 9; September, 1957.

11. Hayes, W.D.; Some Aspects of Hypersonic Flow; Ramo-Wooldridge Corp. Memo.; January 1955.

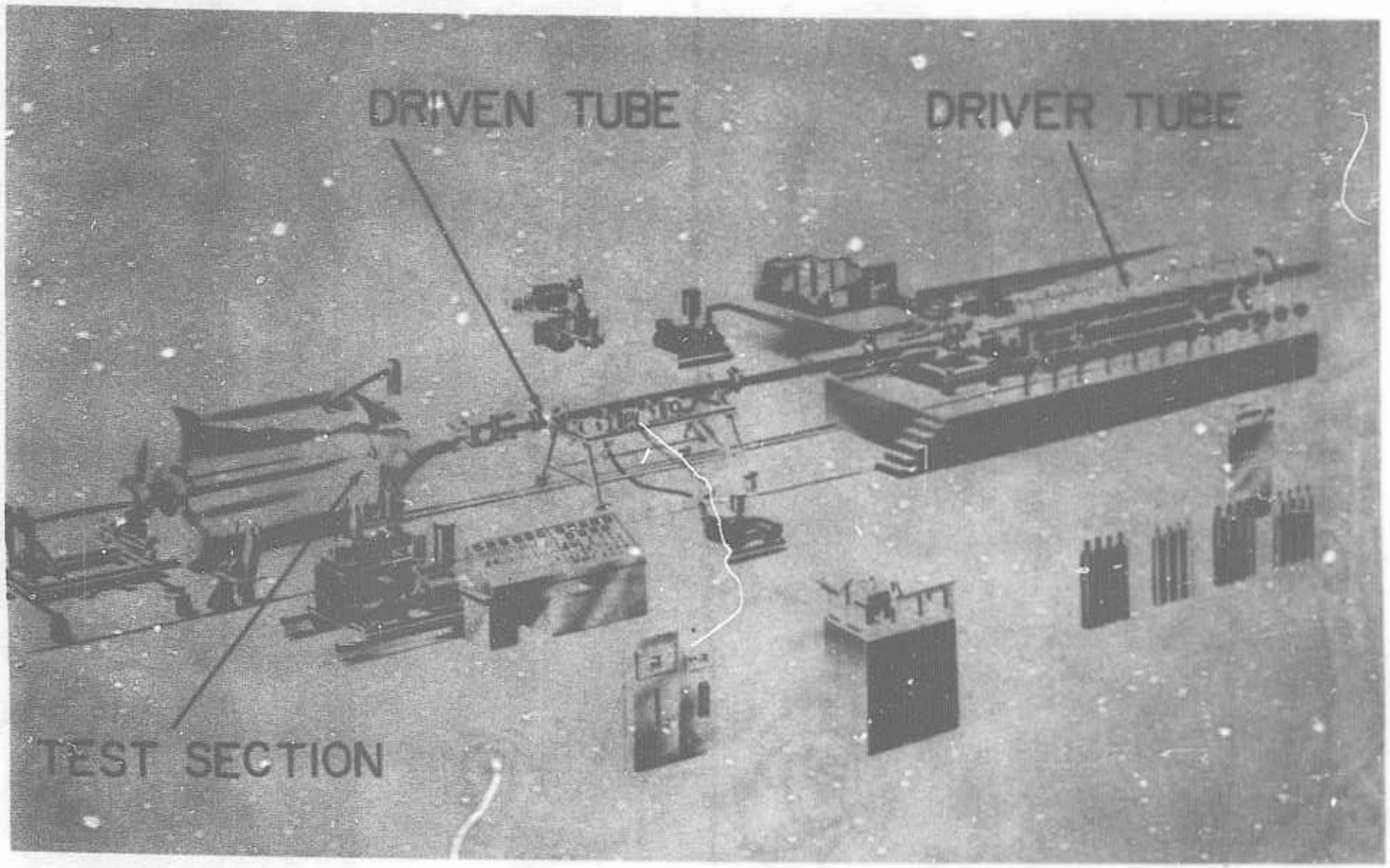

Figure 1 Six Inch Shock Tunnel

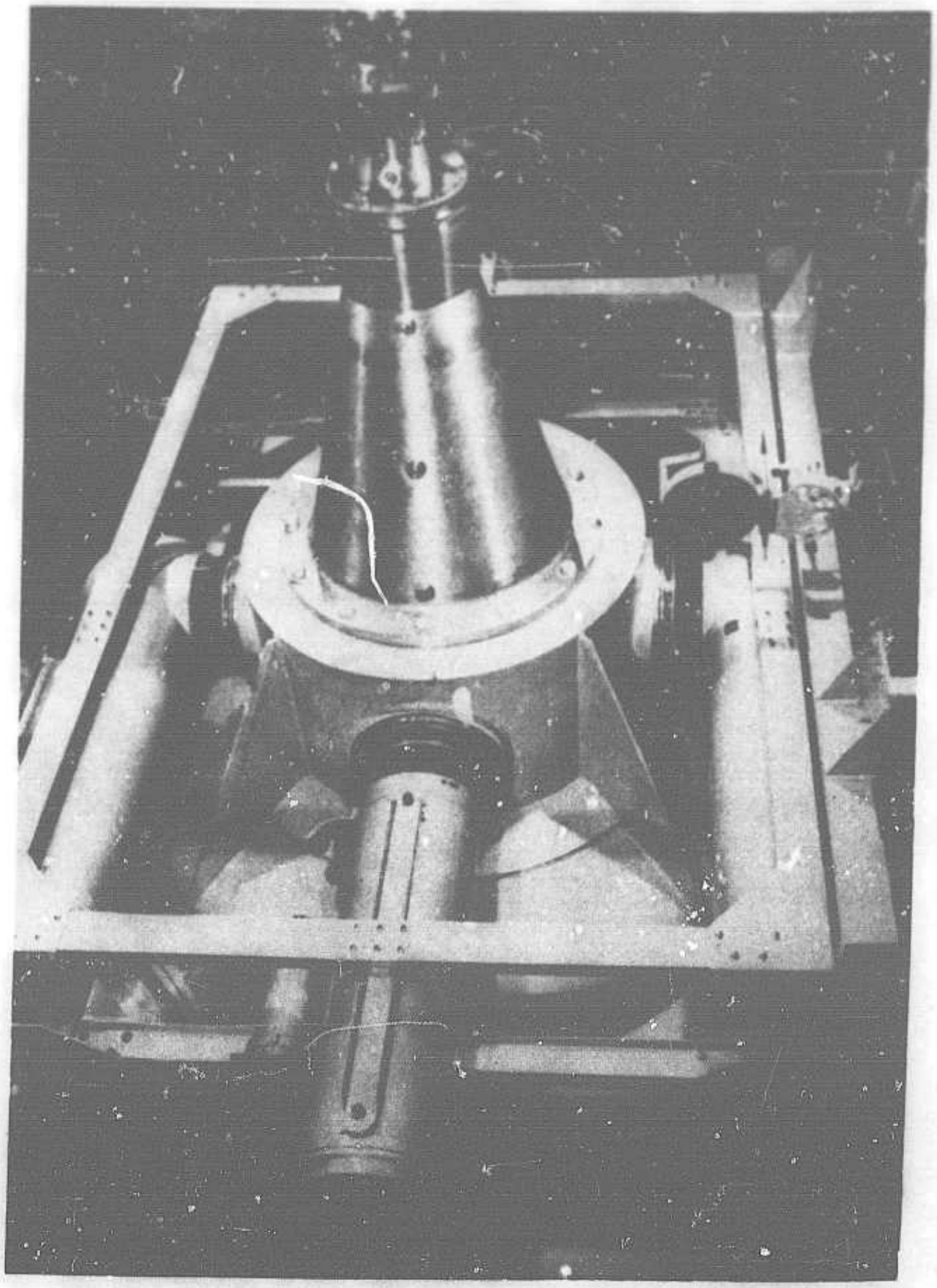

Figure 2 View of Nozzle And Test Section

REGIONS AVAILABLE FOR AERODYNAMIC EXPERIMENTATION

Model Located in Straight Driven Tube

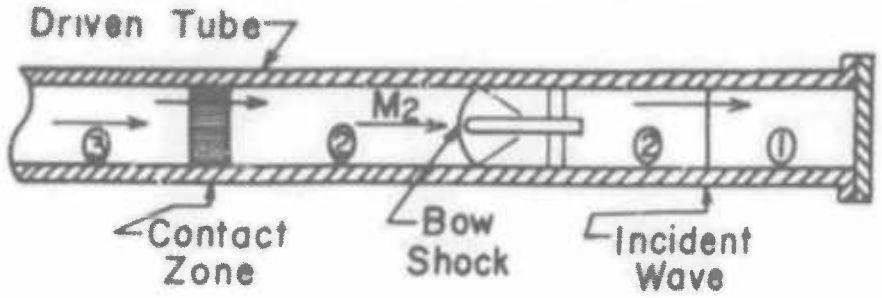

Small Model
Low M_2 (2-3)
High Re
Simulation

Model Located in Straight-Through Nozzle

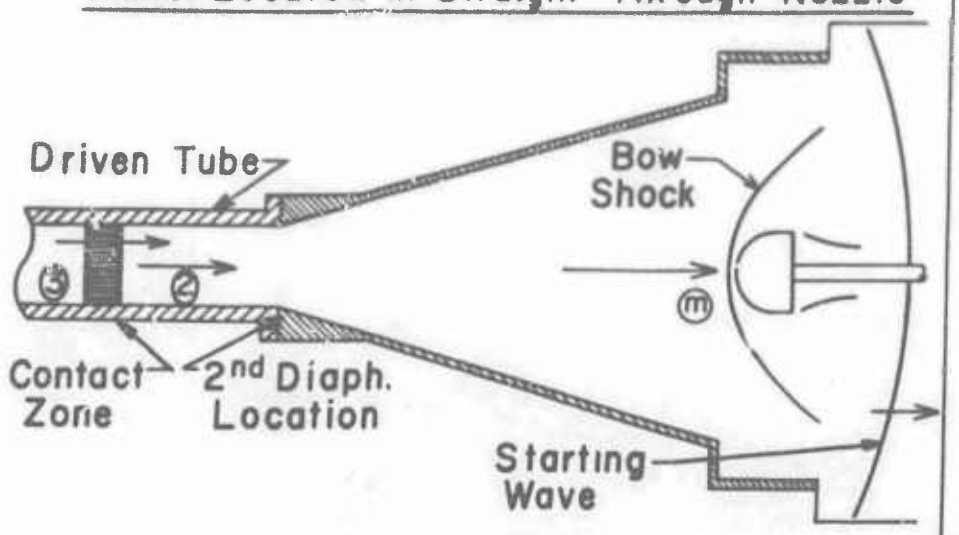

Large Model
Moderate M_m
(4-6)
Moderate Re
Simulation

Model Located in Reflected Nozzle

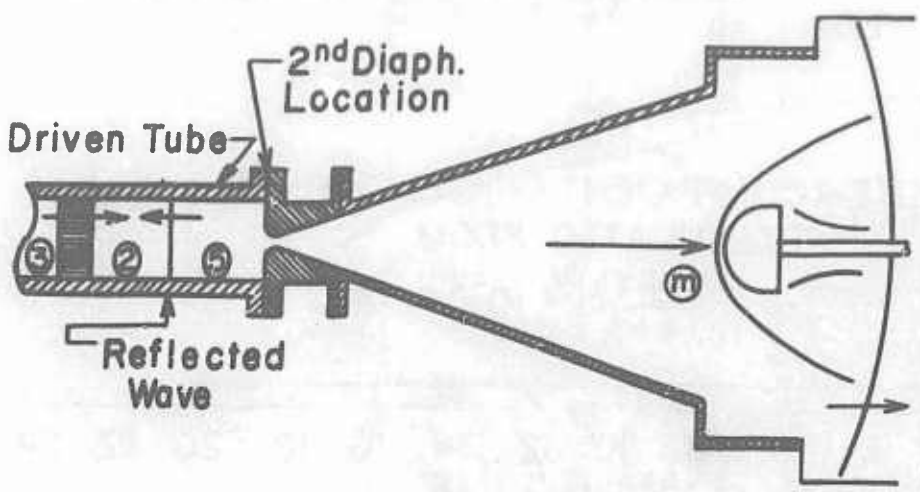

Large Model
High Mm
(6-16)
Low Re
Simulation

Figure 3

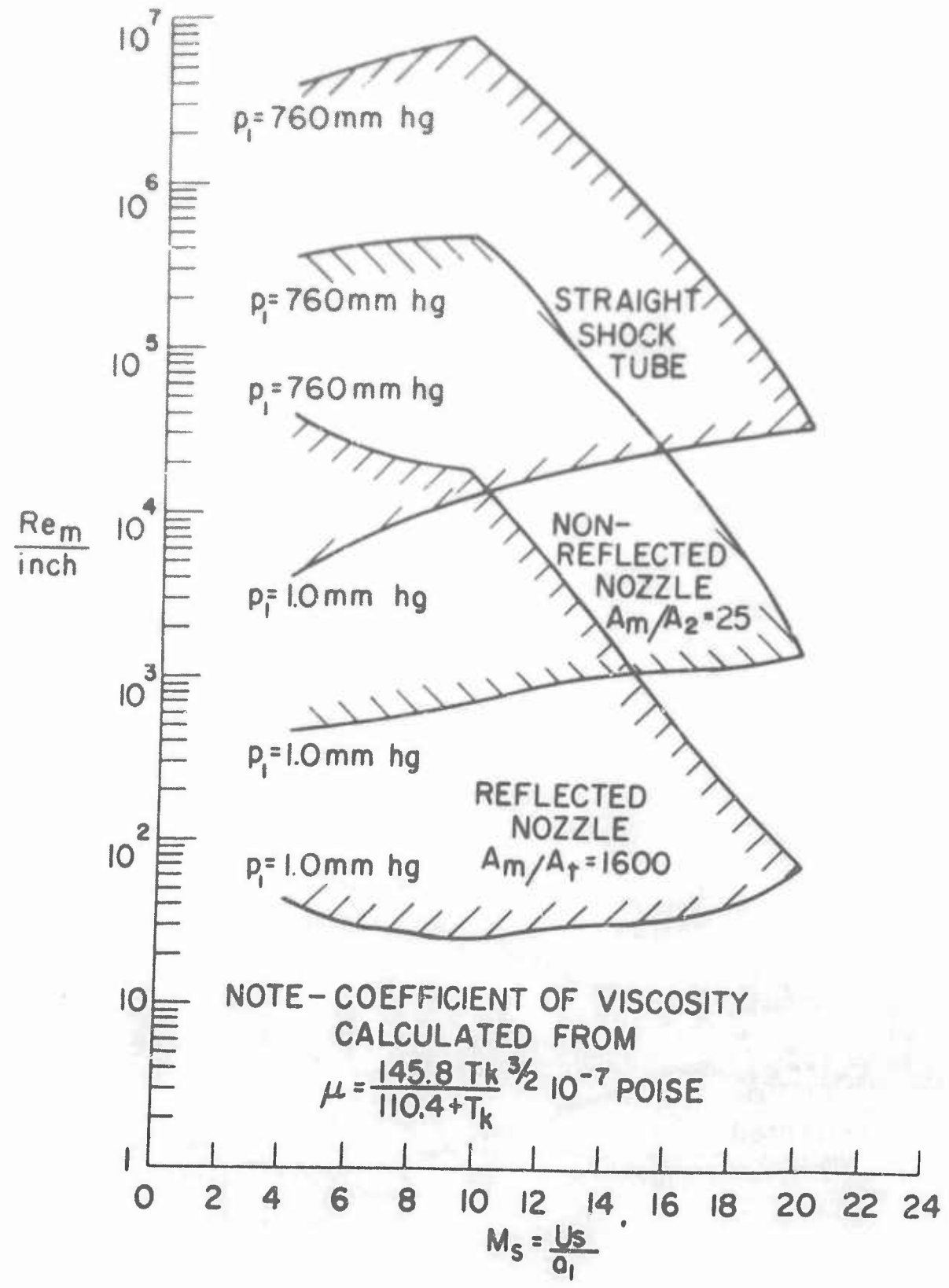
TEST SECTION REYNOLDS NUMBER
10^7
10^6
10^5
10^4
10^3
10^2
10
1
$\frac{Re_m}{inch}$
p_1= 760mm hg
p_1= 760mm hg
p_1= 760mm hg
p_1= 1.0mm hg
p_1= 1.0mm hg
p_1= 1.0mm hg
STRAIGHT SHOCK TUBE
NON-REFLECTED NOZZLE A_m/A_2 = .25
REFLECTED NOZZLE A_m/A_t = 1600
NOTE – COEFFICIENT OF VISCOSITY CALCULATED FROM
$\mu = \frac{145.8\ Tk^{3/2}}{110.4+T_k}\ 10^{-7}$ POISE
0 2 4 6 8 10 12 14 16 18 20 22 24
$M_S = \frac{Us}{a_1}$

Figure 4

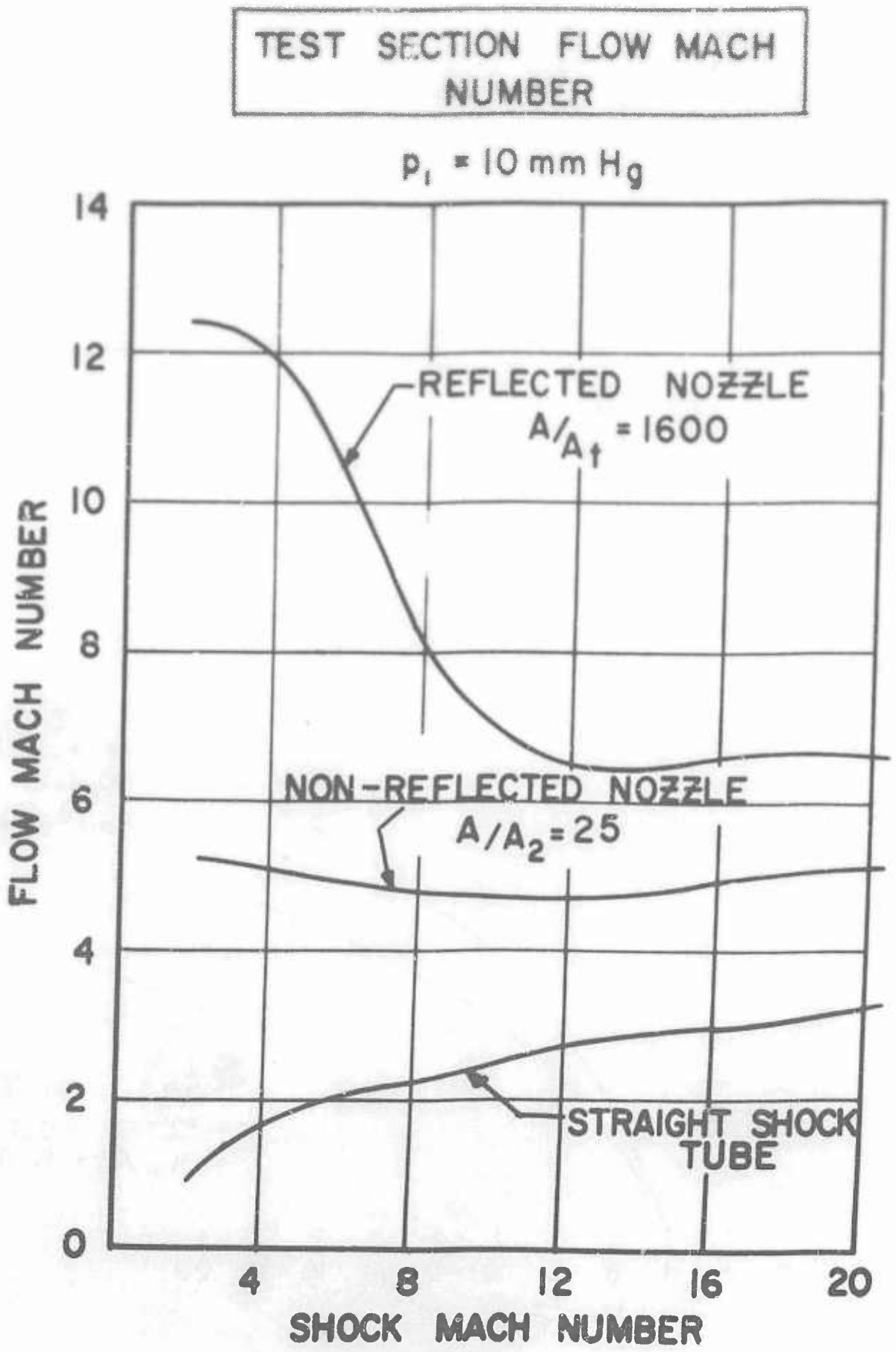
TEST SECTION FLOW MACH NUMBER
p_1 = 10 mm Hg
FLOW MACH NUMBER
SHOCK MACH NUMBER
REFLECTED NOZZLE
A/A_t = 1600
NON-REFLECTED NOZZLE
A/A_2 = 25
STRAIGHT SHOCK TUBE
0
2
4
6
8
10
12
14
4
8
12
16
20

Figure 5

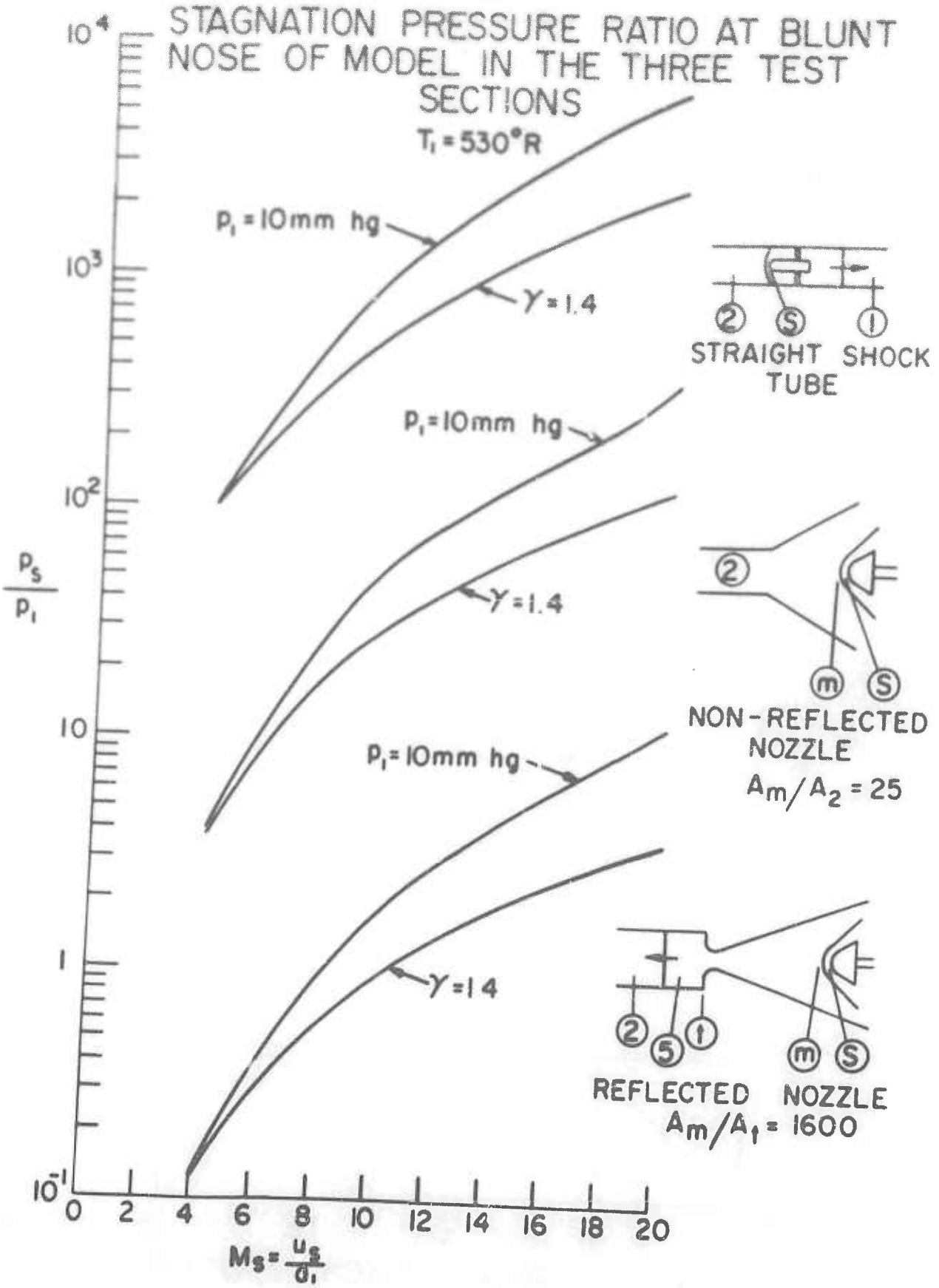
STAGNATION PRESSURE RATIO AT BLUNT NOSE OF MODEL IN THE THREE TEST SECTIONS
$T_1 = 530°R$
$p_1 = 10mm\ hg$
$\gamma = 1.4$
$p_1 = 10mm\ hg$
$\gamma = 1.4$
$p_1 = 10mm\ hg$
$\gamma = 1.4$
$\frac{p_s}{p_1}$
10^4
10^3
10^2
10
1
10^{-1}
0 2 4 6 8 10 12 14 16 18 20
$M_s = \frac{u_s}{a_1}$
STRAIGHT SHOCK TUBE
NON-REFLECTED NOZZLE
$A_m/A_2 = 25$
REFLECTED NOZZLE
$A_m/A_1 = 1600$

Figure 6

STAGNATION TEMPERATURE RATIO AT BLUNT NOSE OF MODEL IN THE THREE TEST SECTIONS.

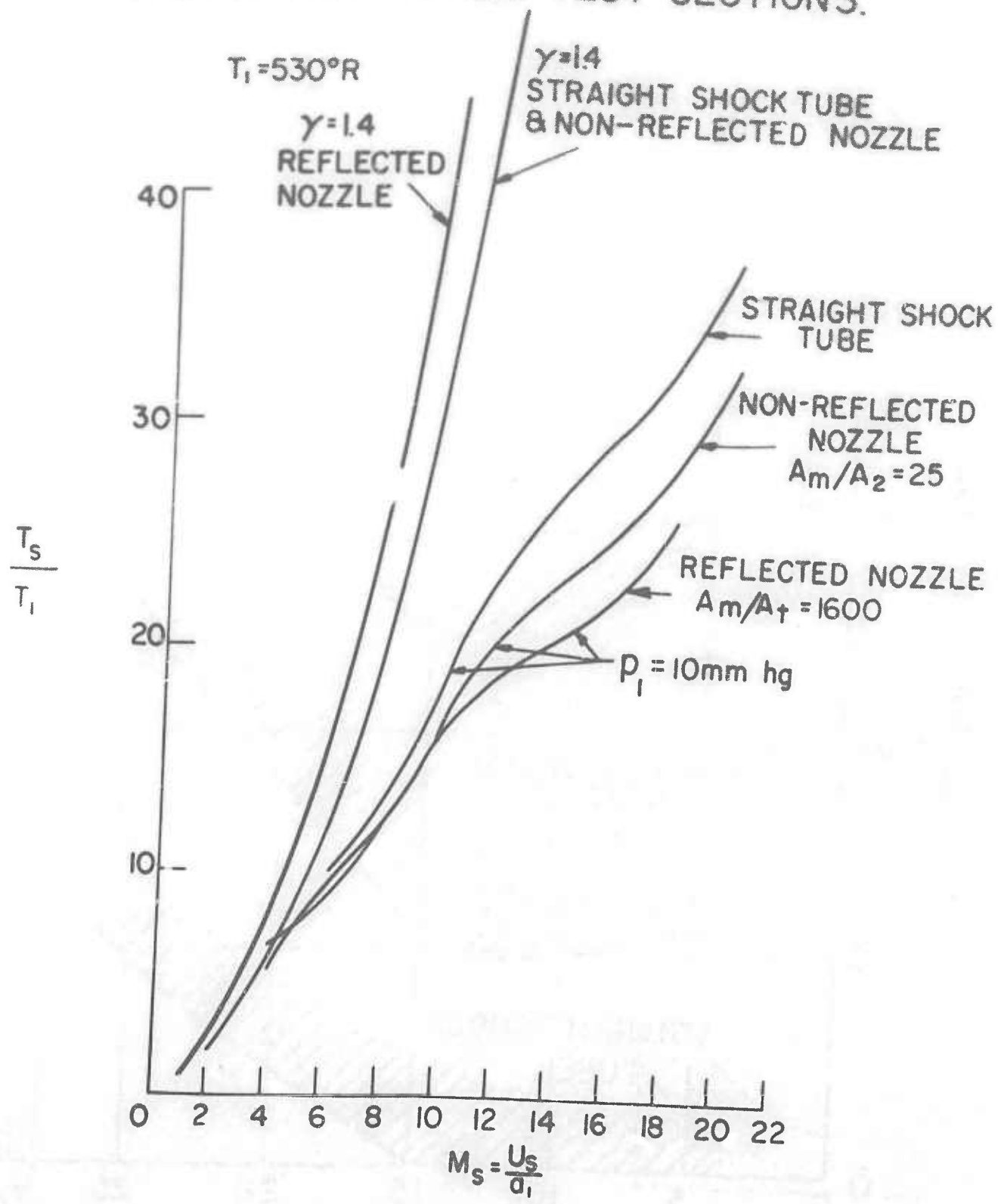

Figure 7

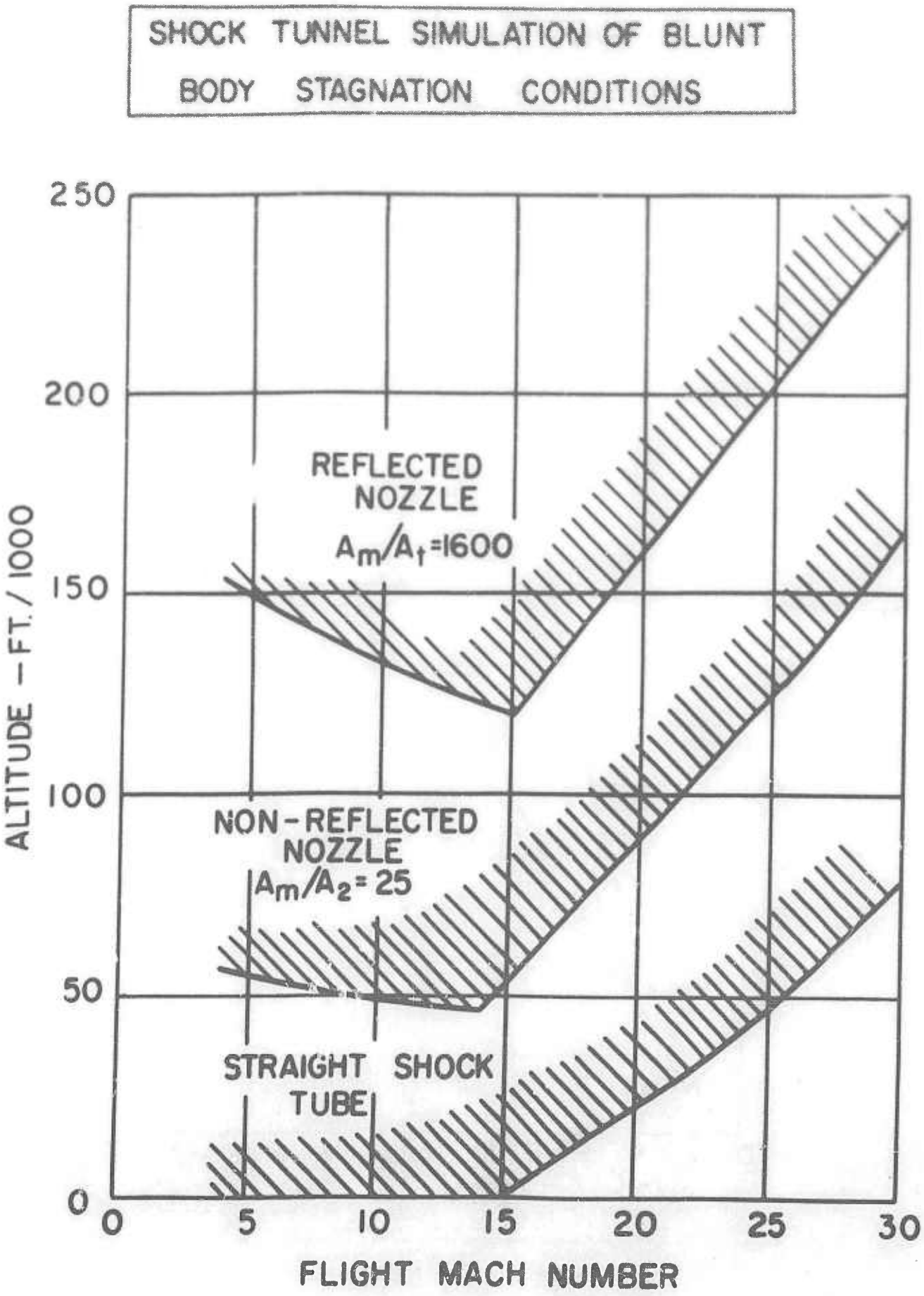
SHOCK TUNNEL SIMULATION OF BLUNT BODY STAGNATION CONDITIONS
250
200
150
100
50
0
ALTITUDE – FT. / 1000
REFLECTED NOZZLE
A_m/A_t = 1600
NON-REFLECTED NOZZLE
A_m/A_2 = 25
STRAIGHT SHOCK TUBE
0
5
10
15
20
25
30
FLIGHT MACH NUMBER

Figure 8

REFLECTED NOZZLE SHOCK TUNNEL

SCHEMATIC OF PULLED STOPPER FLOW STARTING METHOD

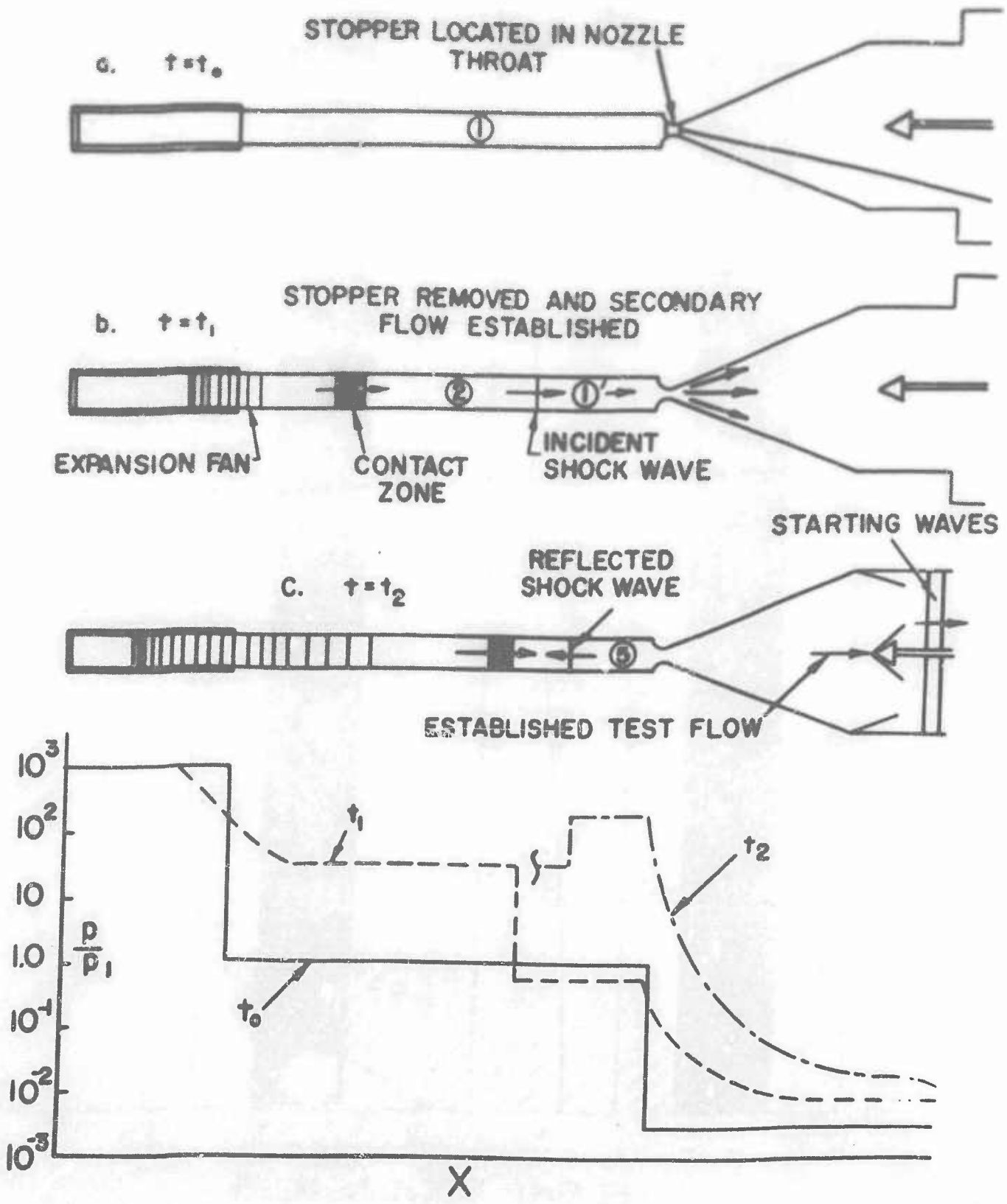

Figure 9

SEQENCE OF EVENTS
IN TUNNEL TEST SECTION

REFLECTED NOZZLE

Ms=5.50 p_1=183 MM Hg Mm=10.8

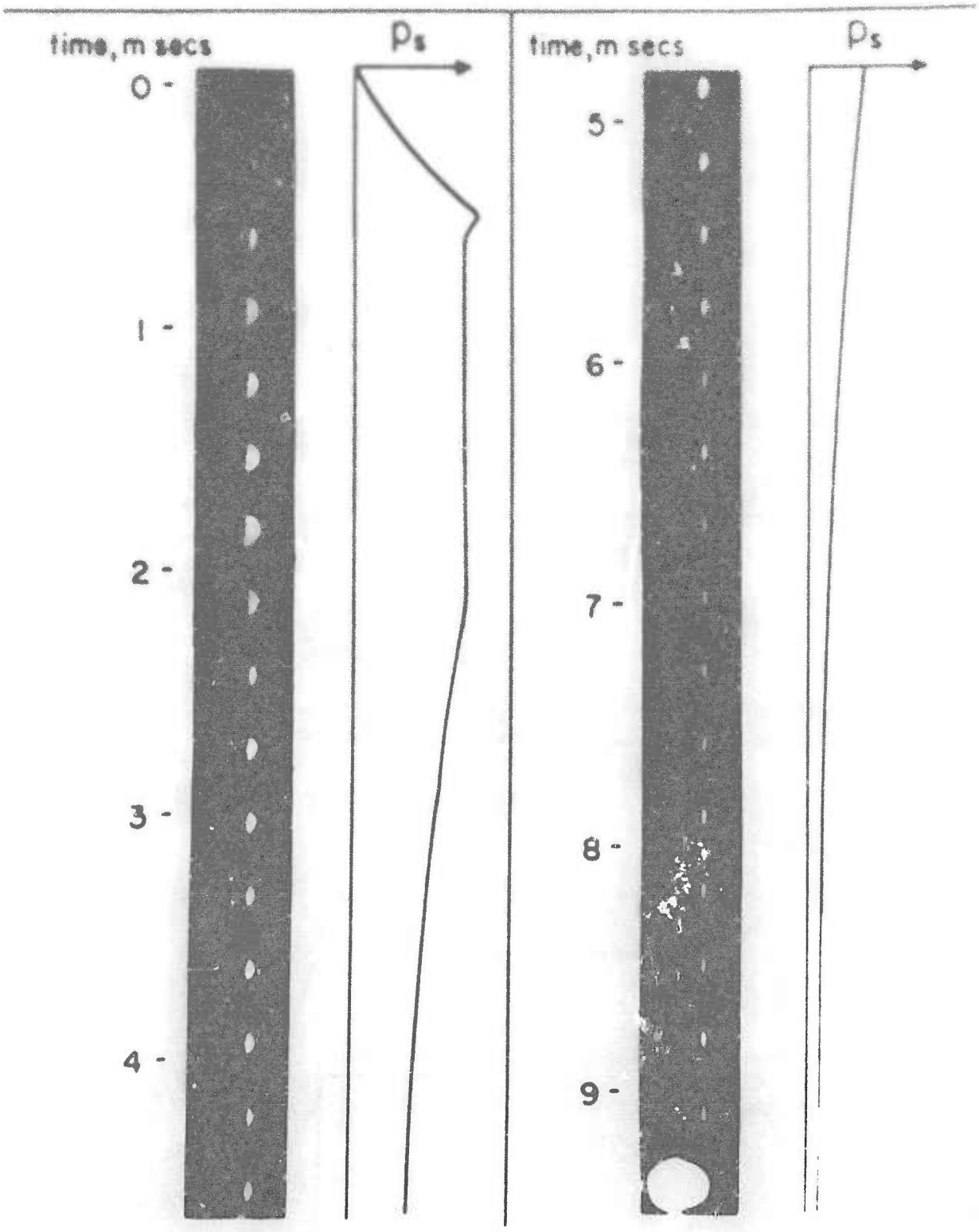

Figure 10

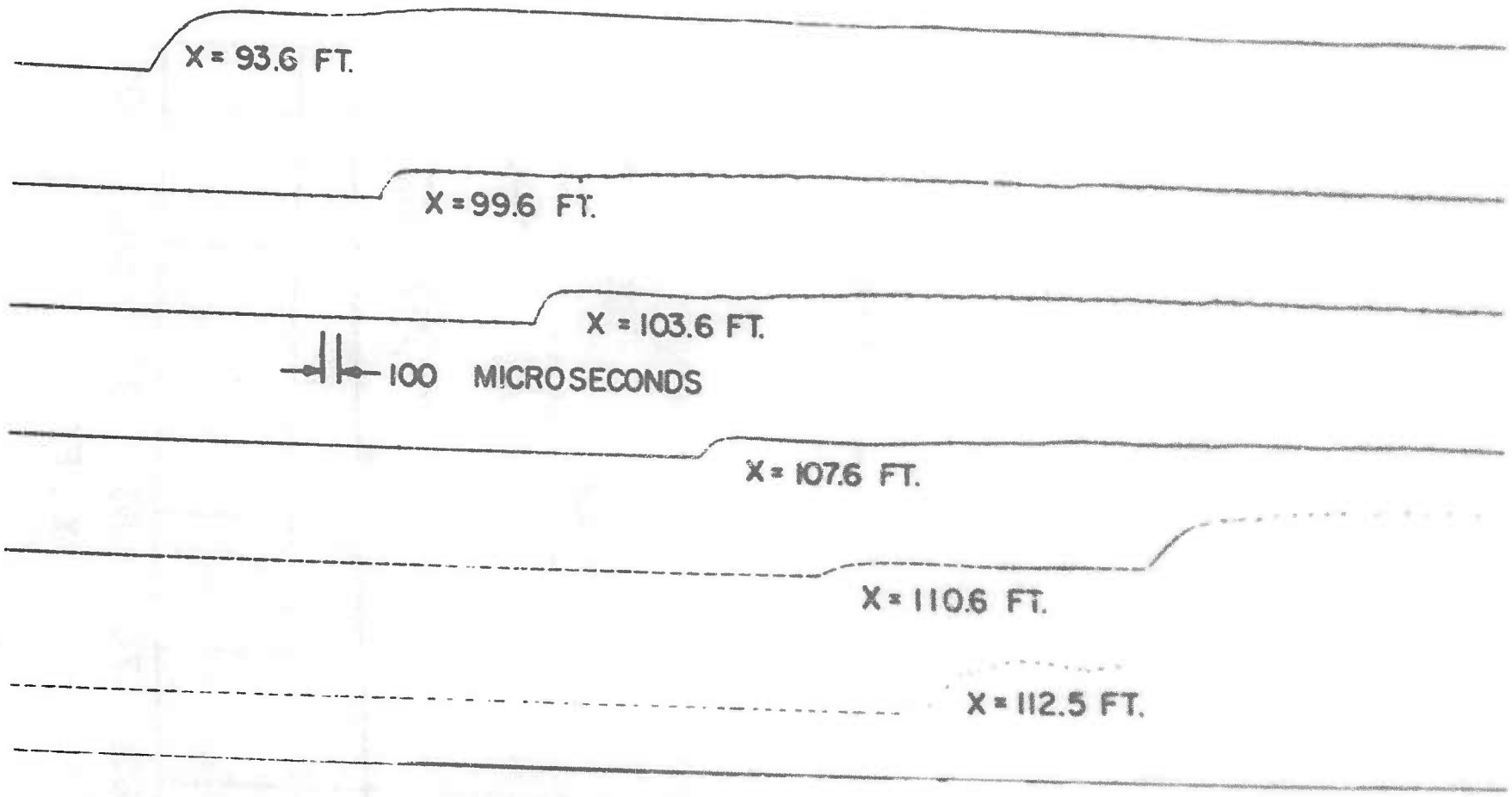

SHOCK TUBE PRESSURE HISTORIES

STANDARD KISTLER QUARTZ CRYSTAL GAUGE
INITIAL DRIVER PRESSURE = 270 PSI
P_1 = 680 mm ng. M_s = 3.5

Figure 11

AVERAGE INCIDENT SHOCK WAVE ATTENUATION

NOMINAL DRIVER PRESSURE - 300 psi
DRIVER GAS - 70% He, 20% H_2, 10% O_2
DRIVEN GAS - AIR

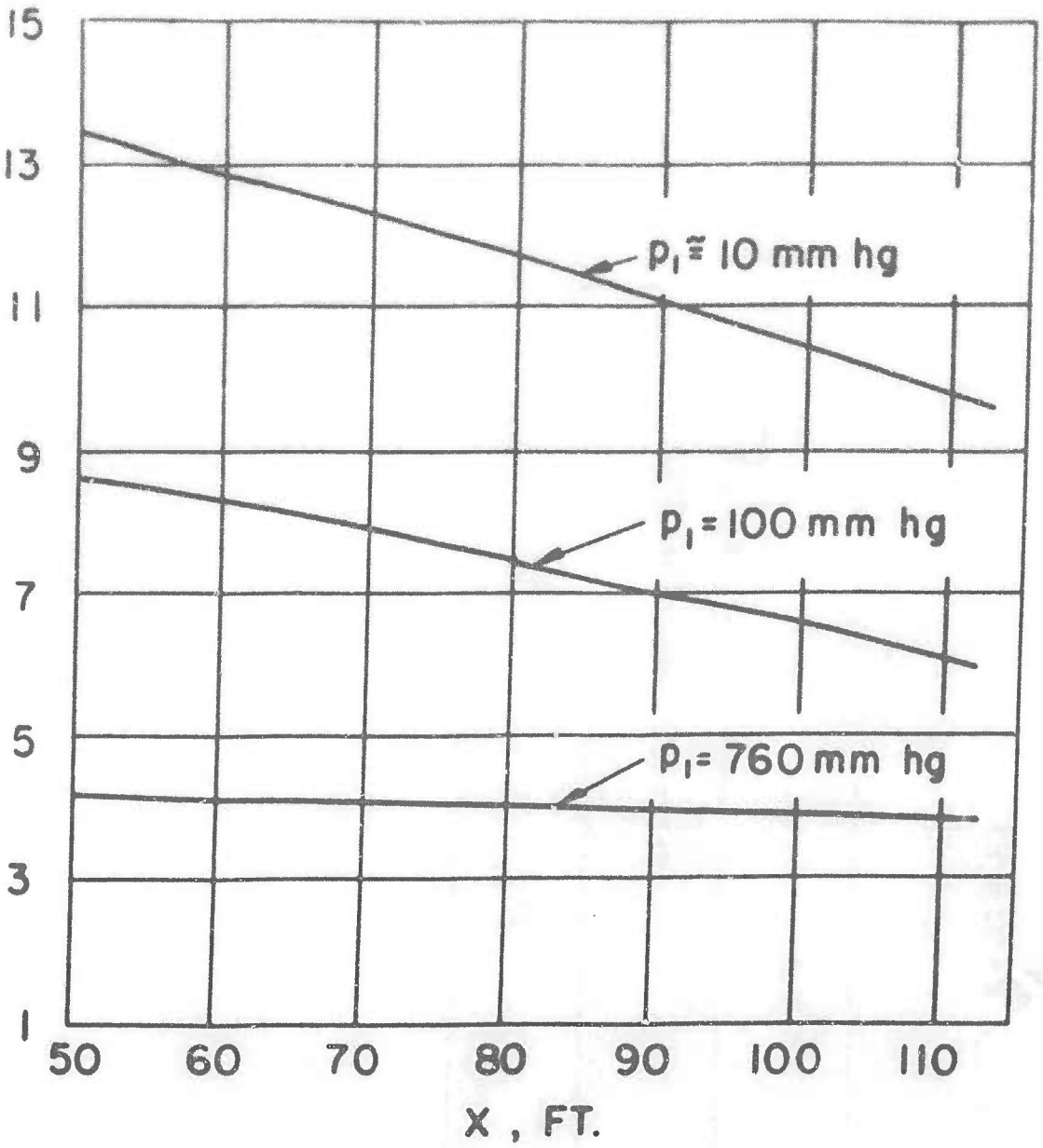

Figure 12

RECESSED-SHOCK MOUNTED PRESSURE GAUGE

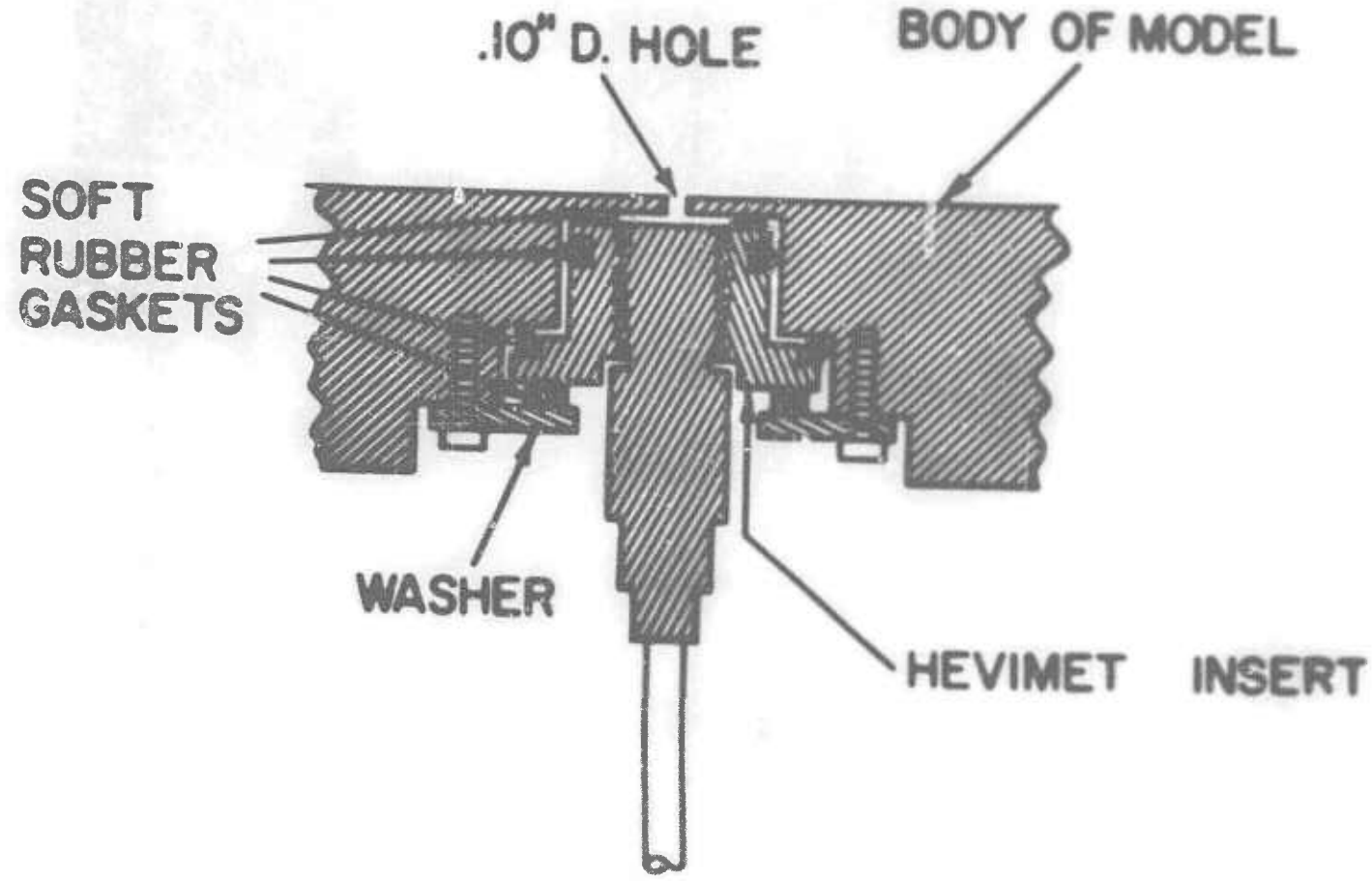

Figure 13

REPRESENTATIVE MODEL PRESSURE DATA

$M_s = 8.0$ $P_1 = 31$ mm hg $T_s = 3770°K$

SHOCK TUBE REFLECTED REGION PRESSURE RECORD

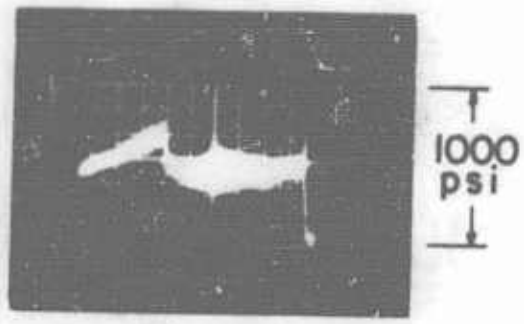

MODEL STAGNATION REGION PRESSURE RECORD

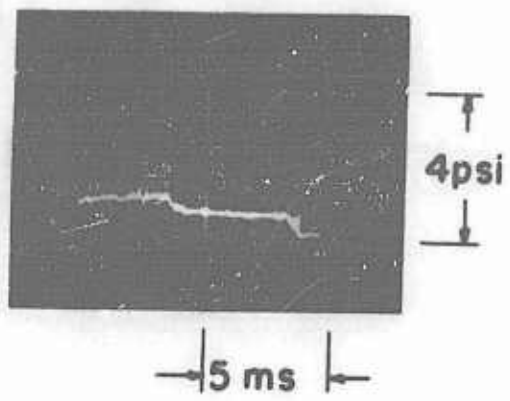

Figure 14

COMPARISON OF EXPERIMENTAL AND THEORETICAL STAGNATION REGION PRESSURES.
REFLECTED NOZZLE
DESIGN $A_m/A_t = 1600$

EXP. DATA CORRECTED TO p_i=100 mm h_g LEVEL

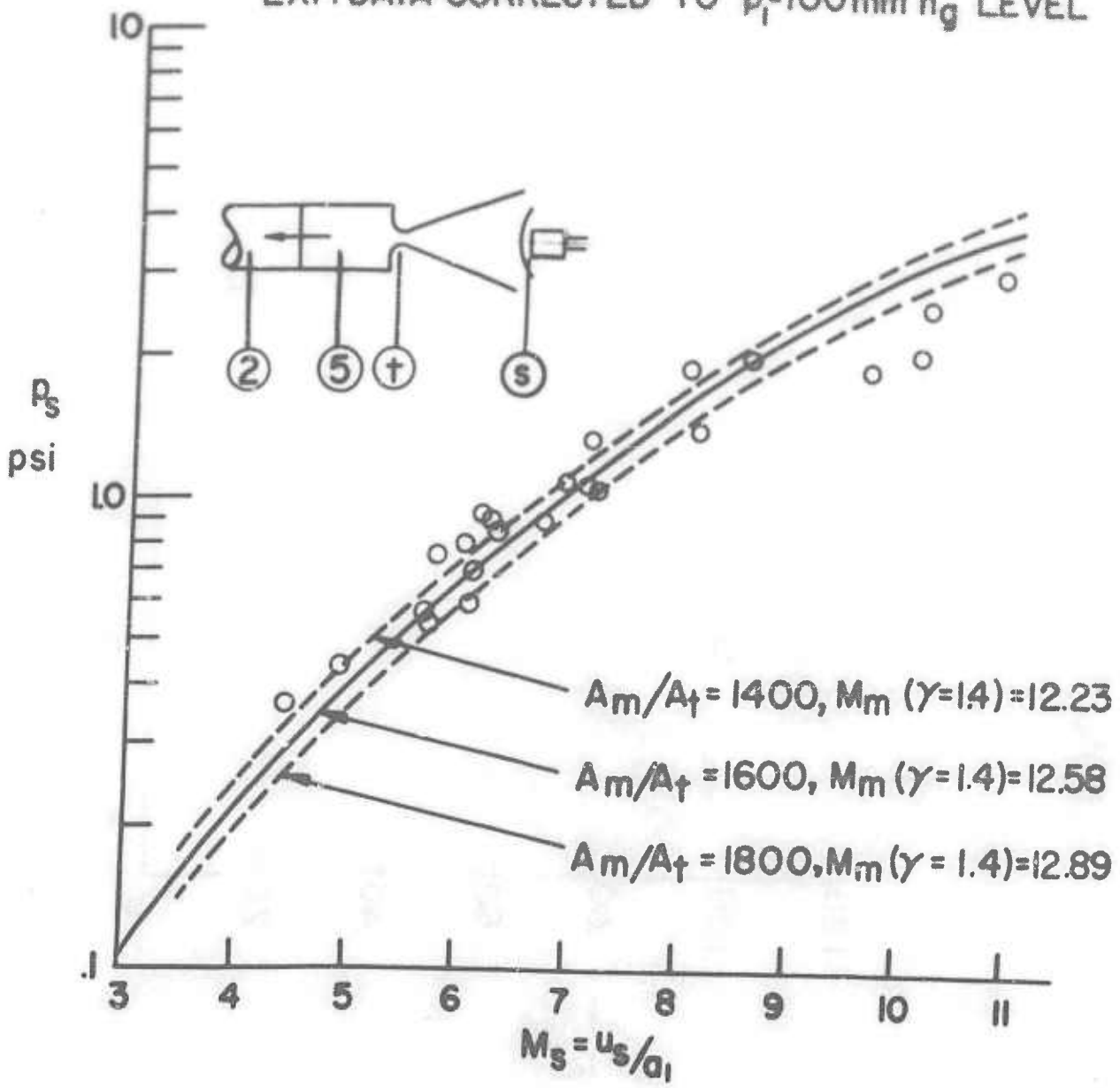

Figure 15

STAGNATION PRESSURE ACROSS TEST SECTION
REFLECTED NOZZLE

$M_s = 6.7$ $p_1 = 90$ mm hg

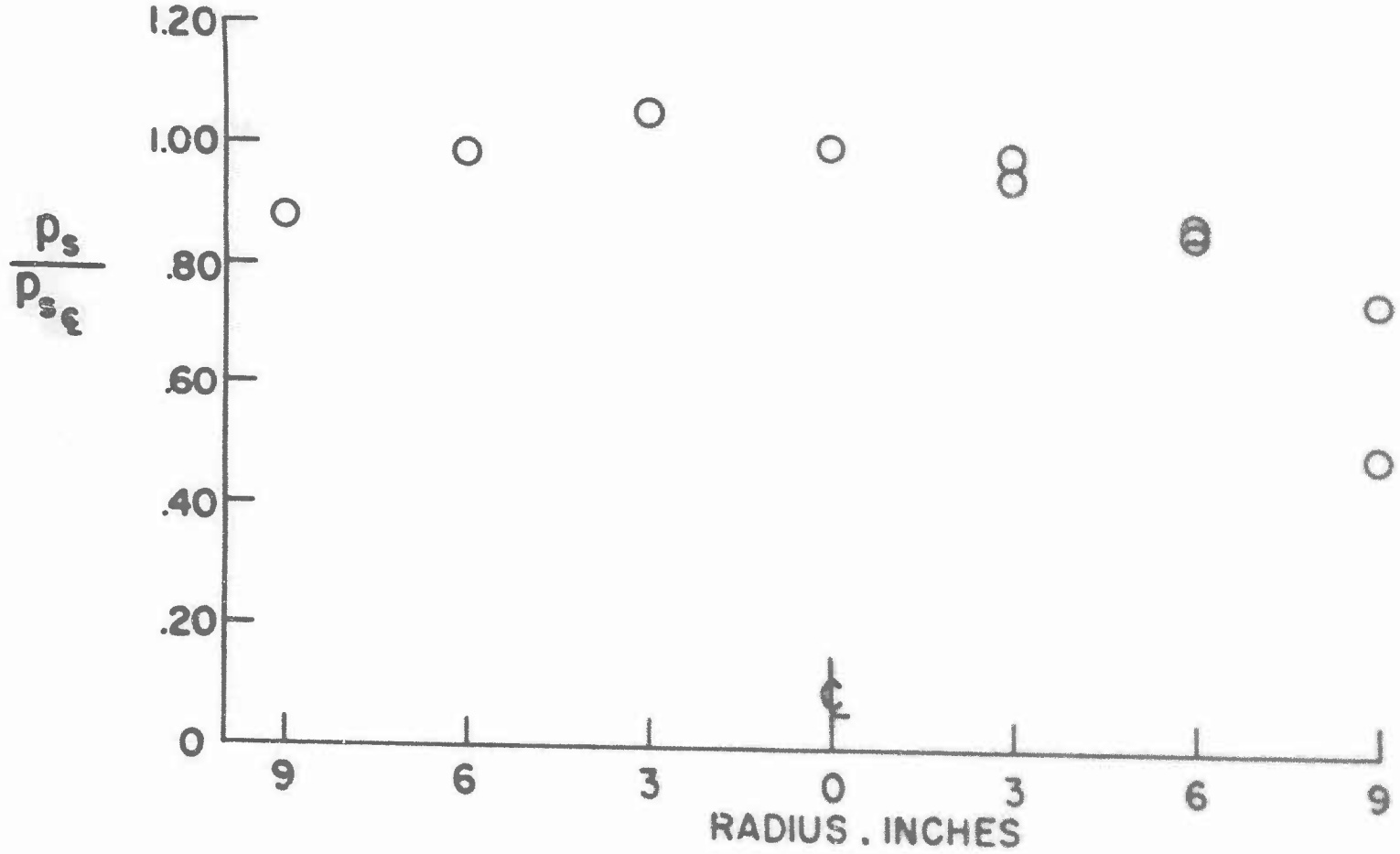

Figure 16

PRESSURE DISTRIBUTION ON HEMISPHERE - CYLINDER

$M_m \approx 6.7$

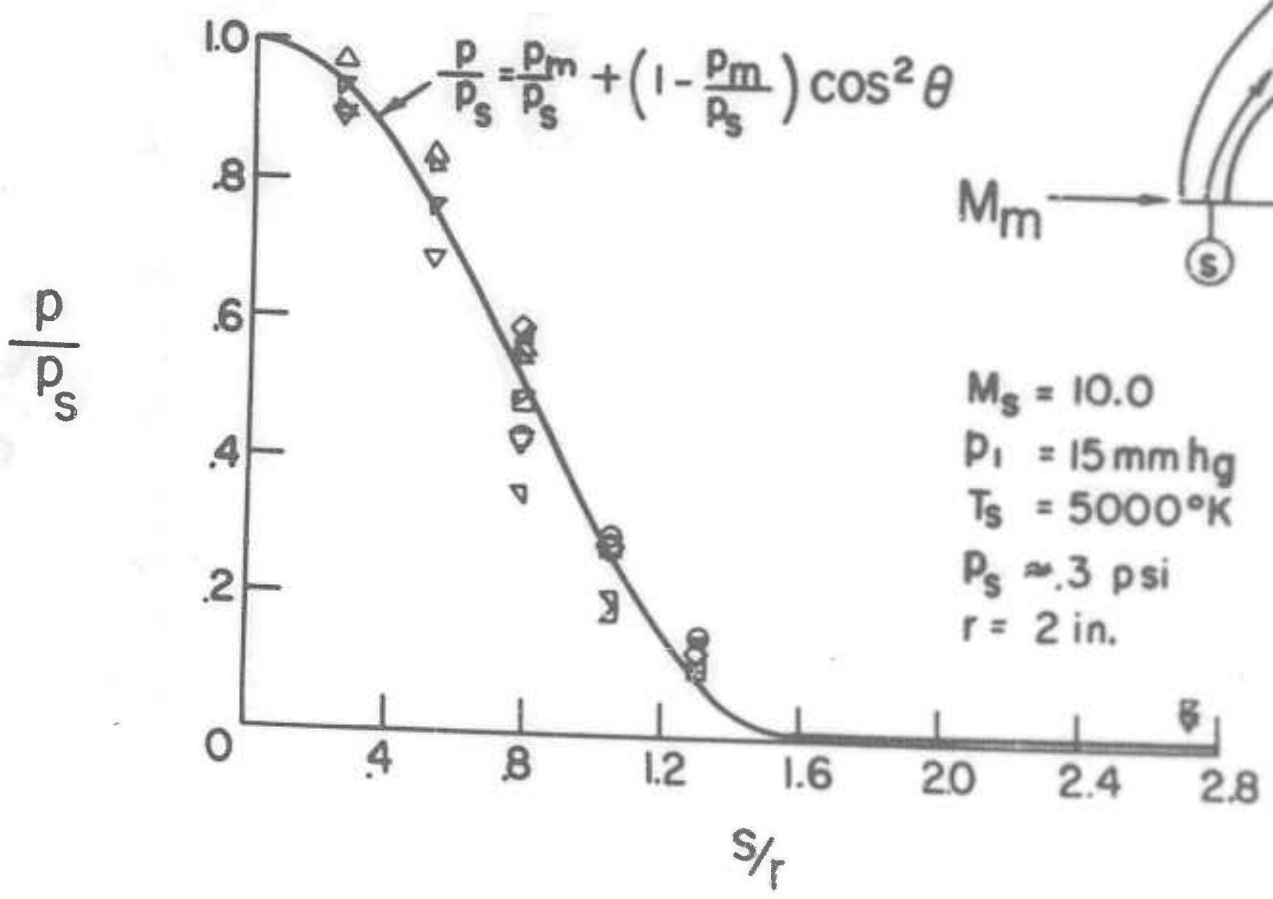

FIGURE 17

Figure 17

PRESSURE DISTRIBUTION ON HEMISPHERE CYLINDER
$M_m = 9.0$

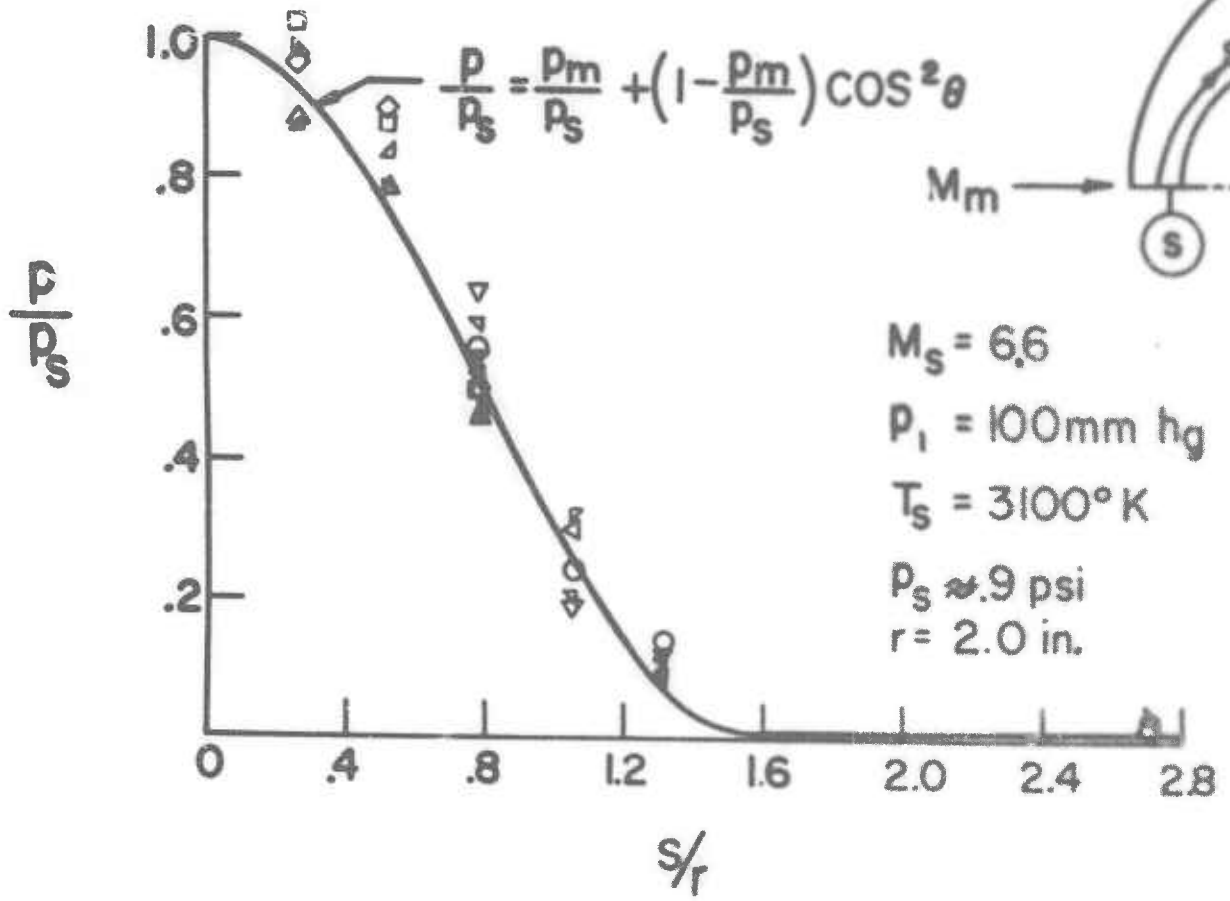

Figure 18

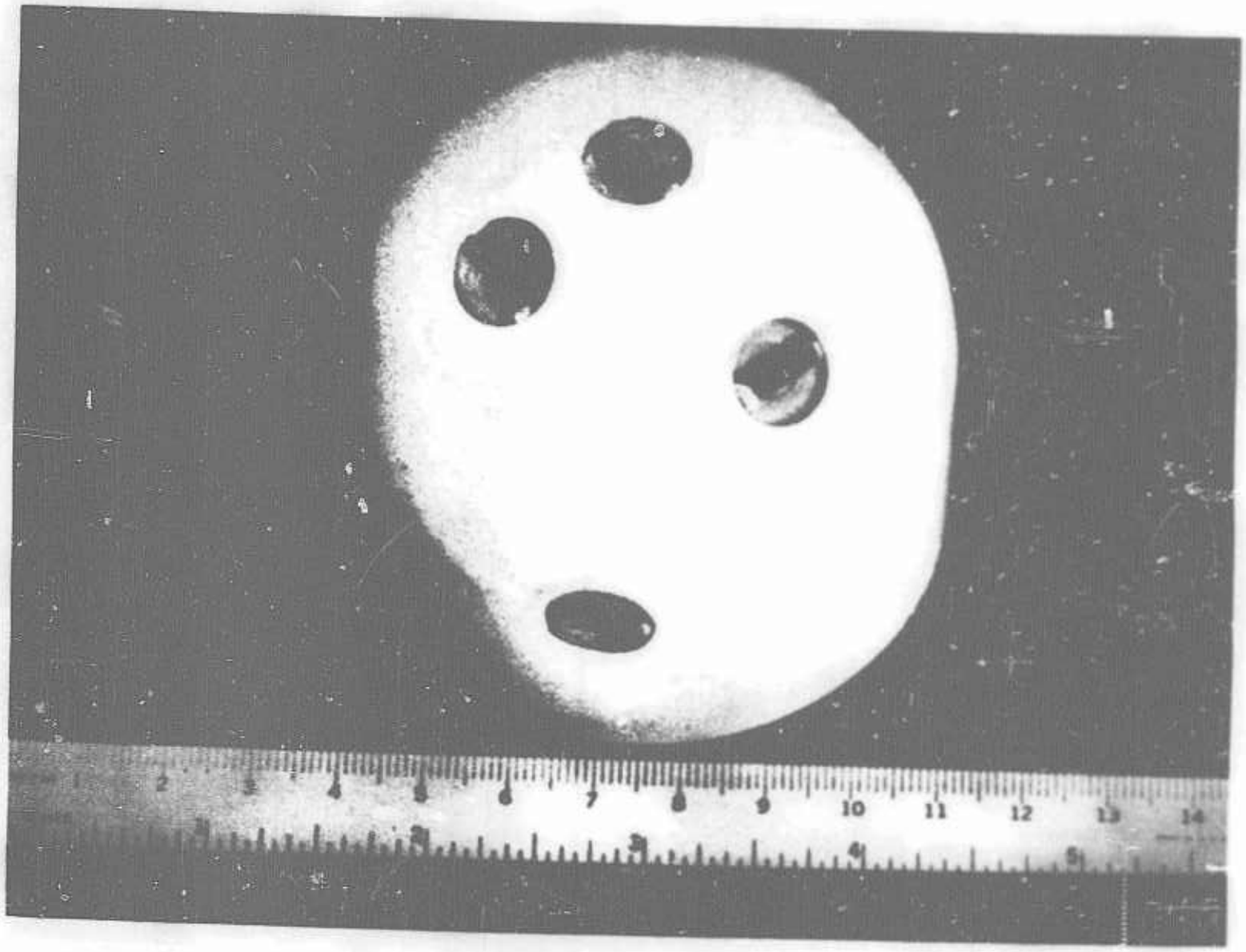

INSTRUMENTED HEAT TRANSFER MODEL

Figure 19

REPRESENTATIVE MODEL HEAT TRANSFER DATA

$M_s = 10.8$ $p_1 = 4.6$ mm hg $p_s = 27$ psi $T_s = 5000°r$

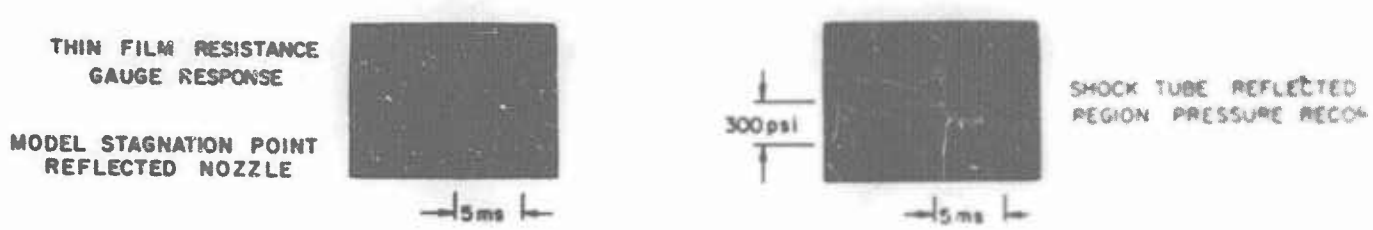

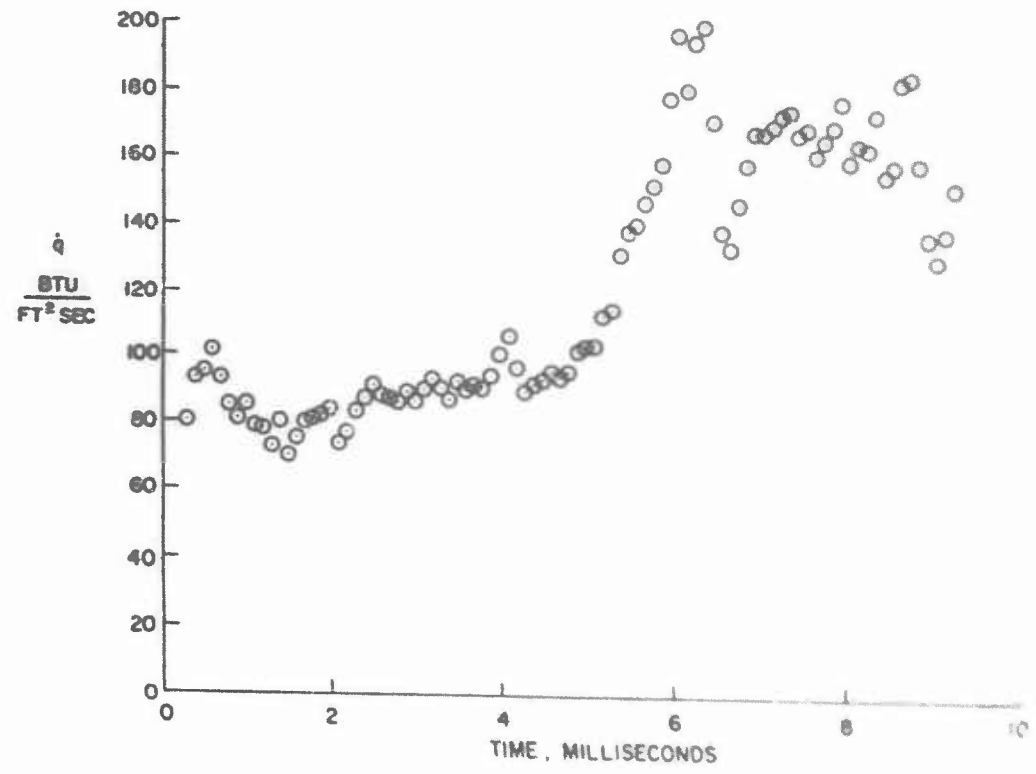

Figure 20

COMPARISON OF EXPERIMENTAL & THEORETICAL STAGNATION POINT HEAT TRANSFER RATES.
REFLECTED NOZZLE

p_s = 5 psi r_{nose} = 1.0 inch

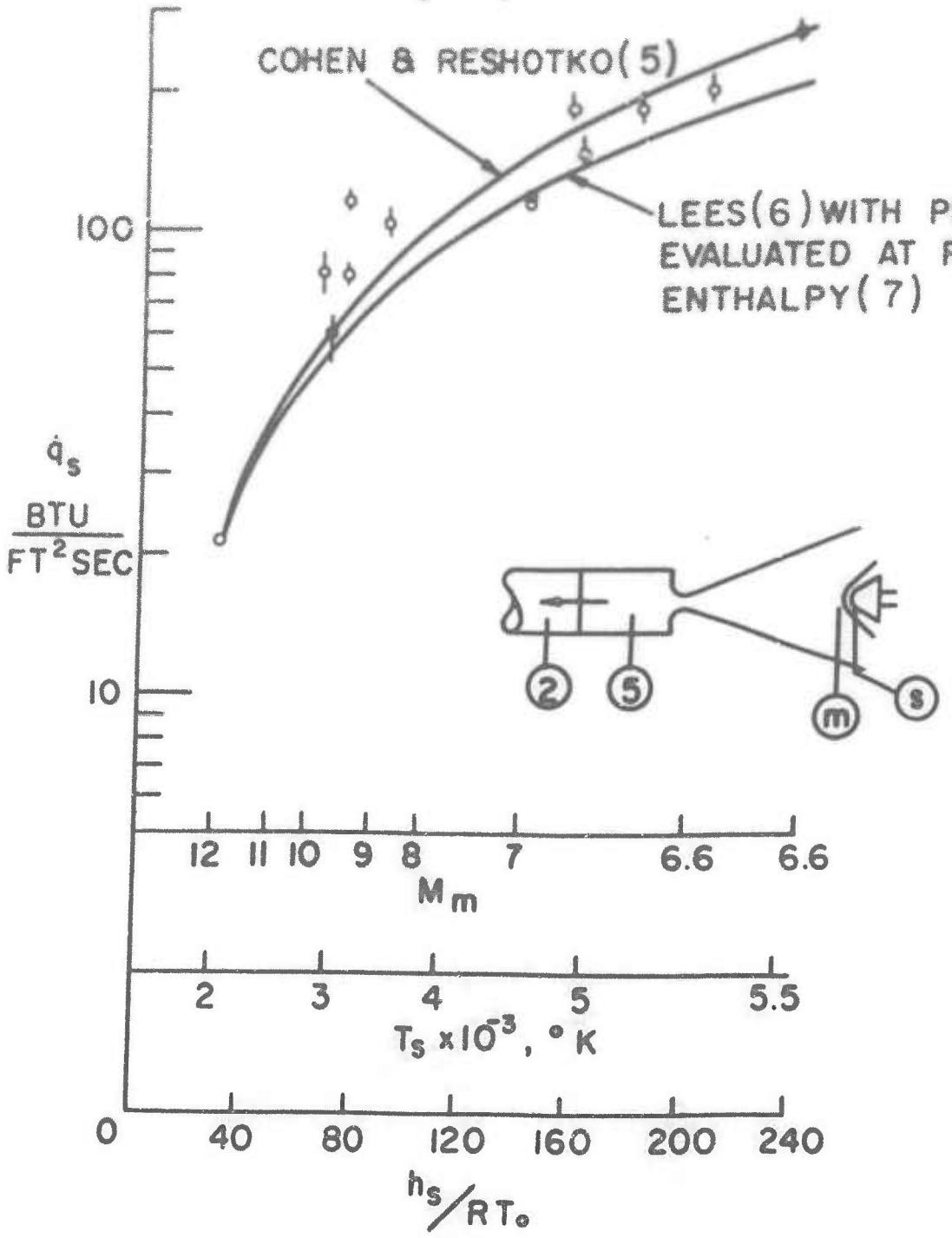

Figure 21

COMPARISON OF EXPERIMENTAL AND THEORETICAL HEAT TRANSFER RATE DISTRIBUTION ON A HEMISPHERE.(REFLECTED NOZZLE.)

$M_m \approx 6.7$

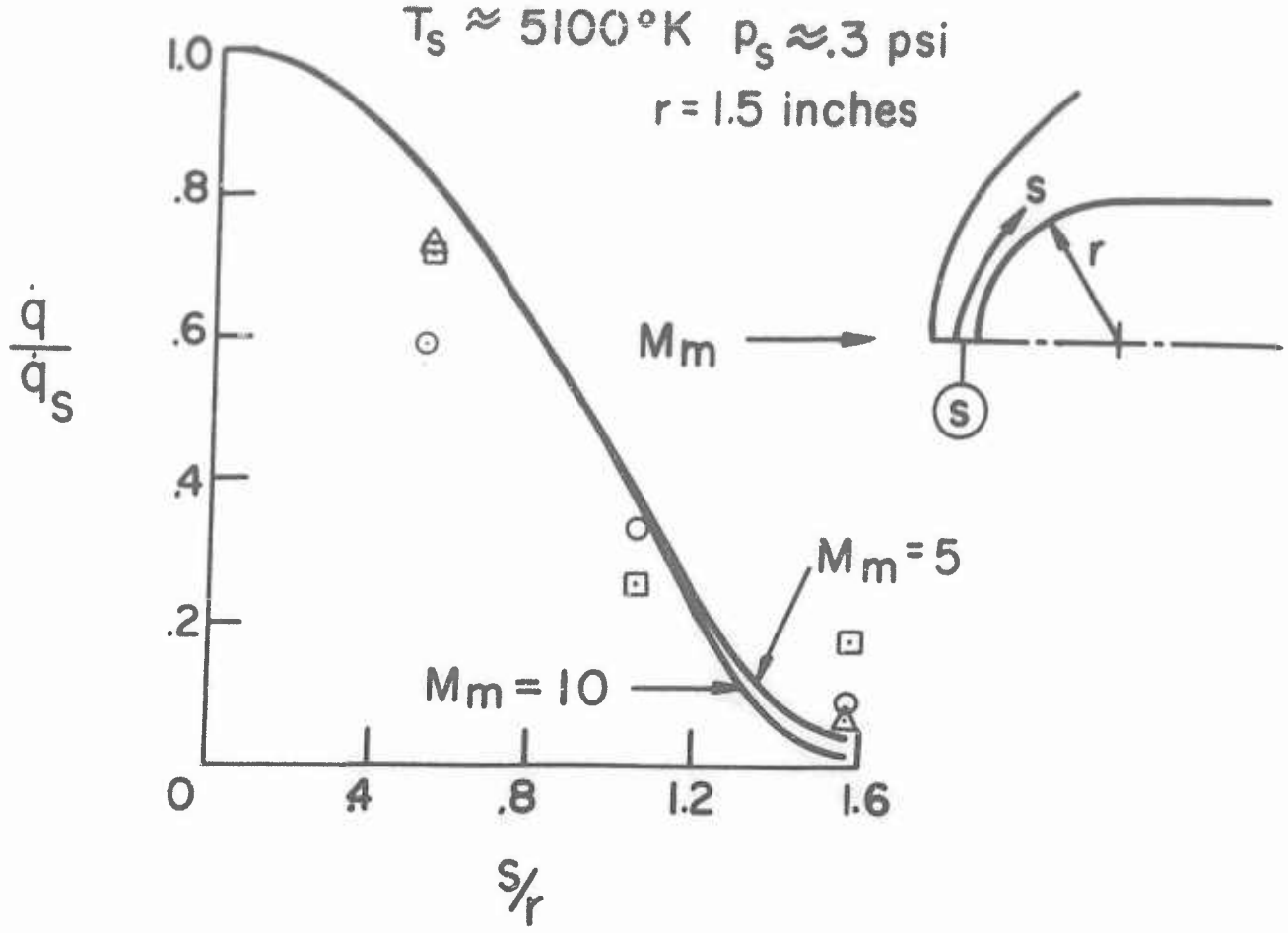

Figure 22

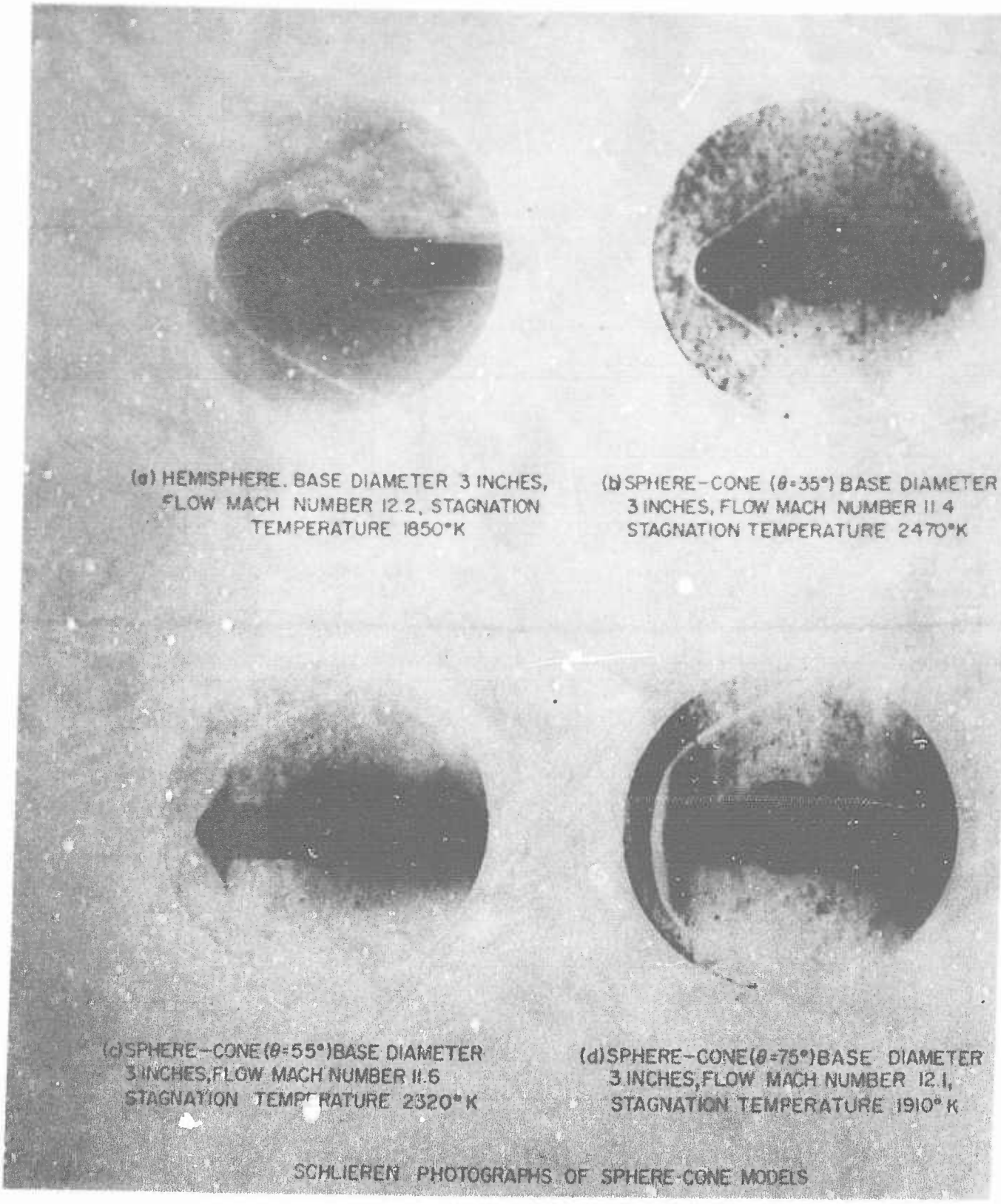
(a) HEMISPHERE. BASE DIAMETER 3 INCHES, FLOW MACH NUMBER 12.2, STAGNATION TEMPERATURE 1850°K
(b) SPHERE-CONE (θ=35°) BASE DIAMETER 3 INCHES, FLOW MACH NUMBER 11.4 STAGNATION TEMPERATURE 2470°K
(c) SPHERE-CONE (θ=55°) BASE DIAMETER 3 INCHES, FLOW MACH NUMBER 11.6 STAGNATION TEMPERATURE 2320°K
(d) SPHERE-CONE (θ=75°) BASE DIAMETER 3 INCHES, FLOW MACH NUMBER 12.1, STAGNATION TEMPERATURE 1910°K
SCHLIEREN PHOTOGRAPHS OF SPHERE-CONE MODELS

Figure 23

SHOCK DETACHMENT DISTANCE AT STAGNATION POINT

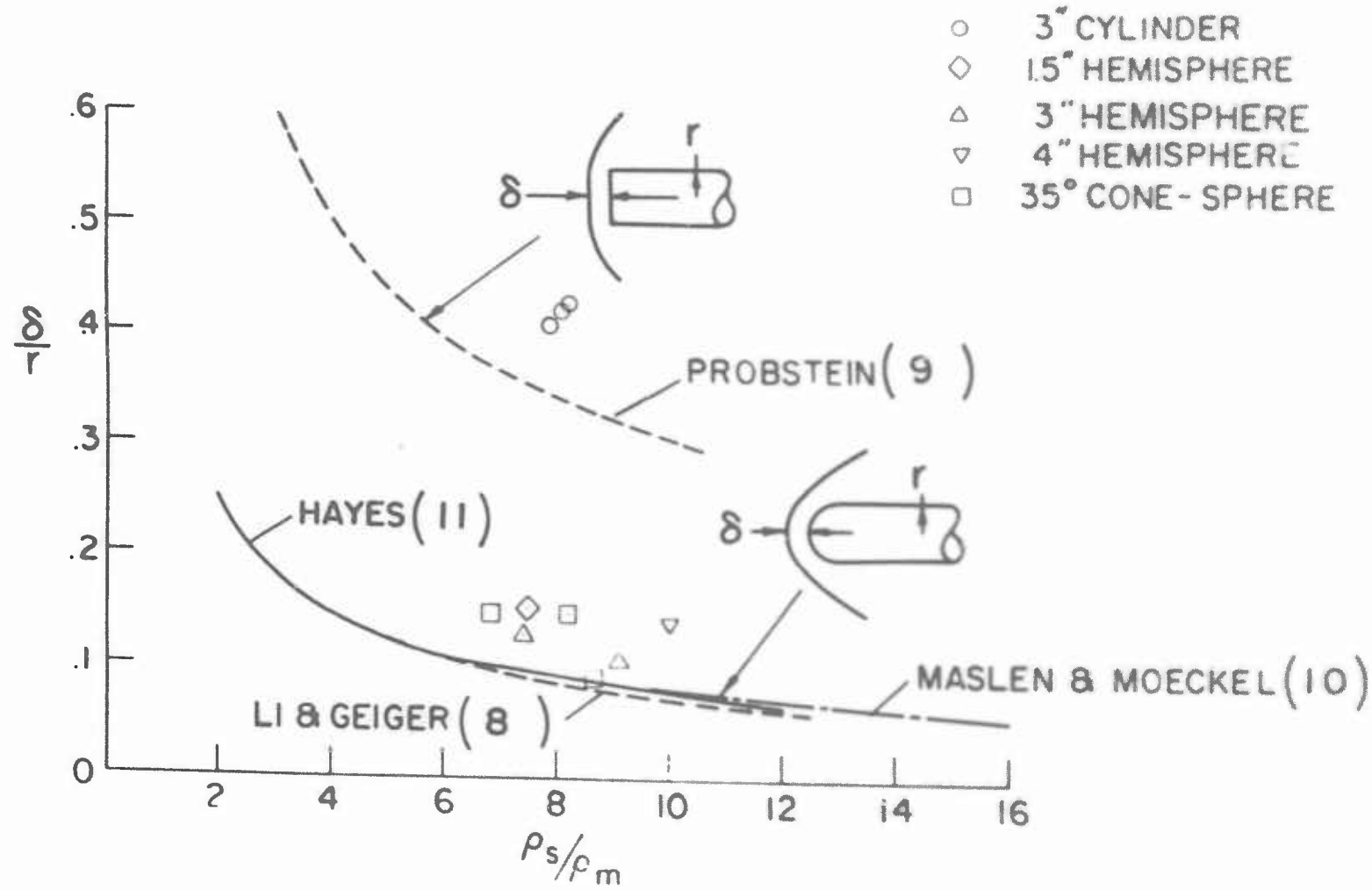

Figure 24

PRESSURE-TIME HISTORY IN A CHAMBER SUBJECTED TO SHOCK WAVE FILLING THROUGH AN ORIFICE

R. Clark, Ballistics Research Laboratories

I. INTRODUCTION

In the Spring of 1953, a communal type air raid shelter was exposed to the blast wave resulting from a nuclear explosion. Prior to this test a scaled model of the shelter was tested in the 24" shock tube at BRL. The objective of the shock tube test was two fold (1) to establish pressure ranges so that gages of the proper range were installed in the prototype, (2) to make recommendations on methods of reducing the blast wave that enters the seating chamber.

Subsequent to these tests a second agency requested BRL to obtain pressure-time histories in regions within complex entranceways. These tests were followed by test on more specific design shelters and on ventilation devices. It was found that the complex designs tested were of little help in prediciting the blast pattern in another design. It was felt that a need existed for work on shapes that would provide information in a general form, so that prediction could be made for a particular form. To this end some general experiments were conducted in the 24" shock tube.

This paper deals with three sets of shock tube tests on the shock wave filling of chamgers. This topic however has two distinct thorough related aspects: The shock front or peak pressure discontinuity which enters the chamber, and the pressure increase in the chamber resulting from the flow following the shock front. These aspects are related in the sense that if the fill rate is high, the shock front is usually of high pressure.

II. EXPERIMENT

Shock tube test were conducted on chambers with the orifice openings facing 0°, 30°, 45°, 60°, and 90° to the shock wave flow: and with tunnels of various forms leading into the chamber. Shock overpressures between 5 and 30 psi were applied to the system and the pressure phenomenon within the chamber was recorded with a piezo-electric recording system.

The first series of test were run with the orifice opening flush with the wall of the shock tube. These data showed the rigorous quasi-steady flow theory to be impractical for general use. When the theory is applied in the following manner the application of equation (1) differs from the empirical data by a factor of 2.

UNCLASSIFIED

AD 210239

Armed Services Technical Information Agency

ARLINGTON HALL STATION
ARLINGTON 12 VIRGINIA

FOR
MICRO-CARD
CONTROL ONLY

3 OF 6

NOTICE: WHEN GOVERNMENT OR OTHER DRAWINGS, SPECIFICATIONS OR OTHER DATA ARE USED FOR ANY PURPOSE OTHER THAN IN CONNECTION WITH A DEFINITELY RELATED GOVERNMENT PROCUREMENT OPERATION, THE U. S. GOVERNMENT THEREBY INCURS NO RESPONSIBILITY, NOR ANY OBLIGATION WHATSOEVER; AND THE FACT THAT THE GOVERNMENT MAY HAVE FORMULATED, FURNISHED, OR IN ANY WAY SUPPLIED THE SAID DRAWINGS, SPECIFICATIONS, OR OTHER DATA IS NOT TO BE REGARDED BY IMPLICATION OR OTHERWISE AS IN ANY MANNER LICENSING THE HOLDER OR ANY OTHER PERSON OR CORPORATION, OR CONVEYING ANY RIGHTS OR PERMISSION TO MANUFACTURE, USE OR SELL ANY PATENTED INVENTION THAT MAY IN ANY WAY BE RELATED THERETO.

UNCLASSIFIED

Continuity $V\, d\rho_3 = A\, \rho_2\, u_2\, dt$

energy $u_2^2 = 5\,(a_1^2 - a_2^2)$

adiabatic $\left(\frac{\rho_1}{\rho_2}\right)^{7/5} = \frac{P_1}{P_2}$

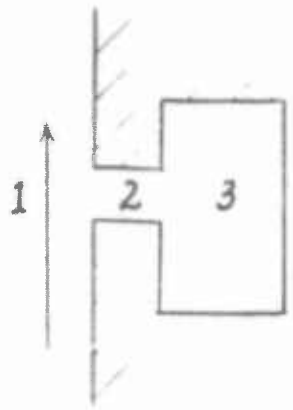

and that $M_2 < 1$, so that, $P_2 = P_3$, which may be reduced to -

$$\frac{dP_3}{dt} = \frac{A}{V}\ \frac{7\,a_o\,P_3}{V5}\ \left[\left(\frac{P_1}{P_o}\right)^{2/7} - \left(\frac{P_3}{P_o}\right)^{2/7}\right]^{1/2} \qquad (1)$$

where V = volume of chamber

A = area of orifice

$P_o = P_3$ at $t = 0$

P, ρ, u, a, and t = pressure, density, flow velocity, sound velocity and time respectively.

A simplified method for determining the pressure-time history in the chamber was determined from the empirical data and is described here. This method has been applied to $\frac{V}{A}$ ratios greater than the experimental data and to pressures in excess of the shock tube data.

III. Application of Empirical Data

Assume that the rate of pressure rise in the chamber is equal to an arbitrary function of the pressure difference through the orifice and to the area of the orifice and inversely to the volume of the chamber in feet.

Thus $$\frac{\Delta P_3}{\Delta t} = \frac{KA}{V}$$

where $K = f(P_1 - P_3)$

Figure 1 is a graph of K versus $(P_1 - P_3)$ taken from experimental data. So to find the fill time curve of a chamber, the expected (P_1, t) curve is

drawn and at $t = 0$, $P_1 - P_3$ is measured and K is read from the graph. Using this K, the volume and area, the rate of pressure-rise is determined. This is drawn as a straight line with slope $\frac{\Delta P_3}{\Delta t}$, and the first portion of this line is taken as the first segment of the fill time curve. This process is repeated, each time, assuming a point on the previous segment to measure the new $(P_1 - P_3)$.

If in going through this process, excessively large segments are chosen, the discontinuity between segments will be obviously too great and it will be apparent that shorter segments should be chosen. In 5 to 8 segment calculations, the resulting curve approaches the external pressure and its slope approaches zero.

Figure 2 shows the method applied to two chambers in the shock tube. Figure 3 and 4 show the method applied to chambers subjected to nuclear blast waves in the field, both typical and atypical, and with a great increase in the volume to area ratio over that which was shock tube tested. These data show good agreement with the predicted results even though the applied pressures are greater than the shock tube test data.

IV. Effect of Orifice Orientation

The next phase of this filling test was designed to investigate the effect of orifice orientation with respect to the direction of the shock wave flow. For this test a jig was constructed, Figure 5, and mounted on a circular shock tube port, convenient for adjusting the orientation of the orifice opening. The orifice duct leads to the chamber. Piezo-electric gauges were mounted on the surface next to the orifice, in the duct wall and in the chamber. The volume to area ratio for the system was 45.5 feet. Step shock waves (50 milliseconds flattop), of 10, 20 and 30 psi overpressure were applied to the system with angles of orientation at 0°, 30°, 45°, 60° and 90° (side-on).

The pressure rise in the chamber for the 10 and 20 psi shock is shown in Figure 6. This figure emphasizes the significance of orientation on both the pressure maximum reached and the rate of pressure rise in the chamber. Note the same rate of pressure rise occuring at the 10 psi face-on (0°) condition as at the 20 psi side-on (90°) condition, yet the stagnation pressure for the 10 psi shock is only 12.3 psi. A further reduction in the rate of pressure rise should be expected when the orifice opening is more than 90°

Pressure measured in the orifice duct reveals some interesting results. The initial part of these records show a shock discontinuity followed by a short non-steady rarefaction and then by quasi steady flow. If the flow is subsonic, the pressure in the duct will adjust to the pressure in the chamber. If the flow in the duct is sonic, then the pressure in the duct will be dependent of the pressure in the chamber.

The shock front overpressure in the duct is increased by a factor of 2.5 for the same applied shock by changing from side-on to face-on (90°→ 0°) orientation of the orifice opening, see Fig. 7.

The condition for Mach 1 flow in the duct is a function of P_{o1} and orientation angle.

There is a Mach 1 curve on the applied pressure versus orientation angle plane below which, subsonic flow occurs, and above which sonic flow occurs in the duct.

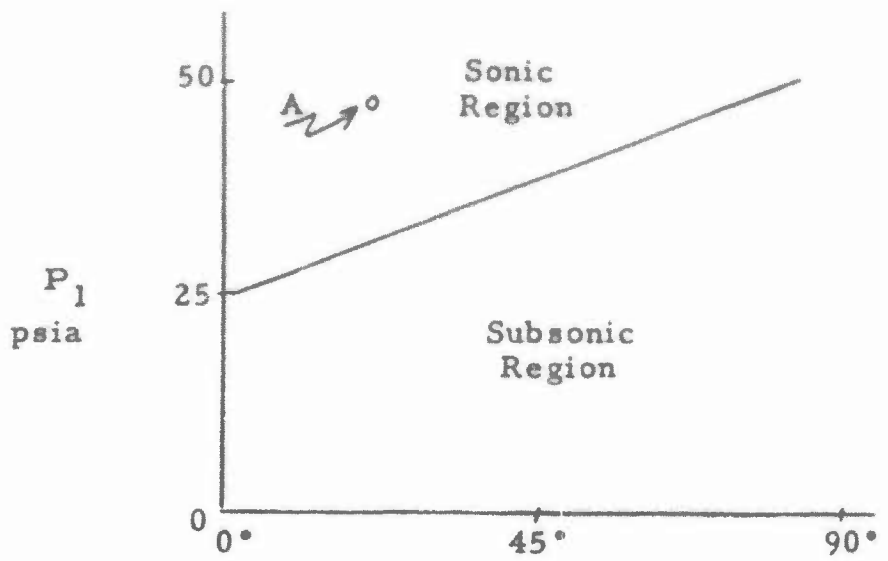

In the sonic region the pressure in the duct is equal or greater than the ambient pressure, depeniding on whether the pressure and angle fall on or above the Mach 1 curve. If, for example, the pressure and angle are at A, the pressure in the duct, P_2^*, will remain constant until the chamber fills to this critical pressure (P_3 P_2^*).

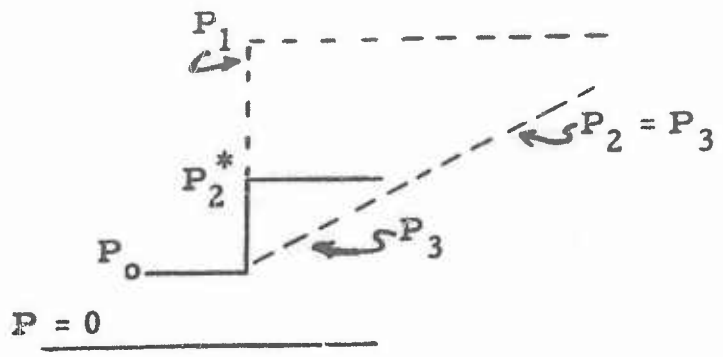

This constant or critical pressure in the duct appears to have a particular relationship to the side-on pressure of the applied shock wave for the face-on (0°) orifice opening. According to the experimental data, the ratio of the absolute applied pressure to the critical flow pressure in the duct is a constant:

thus $$\frac{P_1}{P_2^*} = 1.65$$

where $P_1 > 24.7$ approximately; $M_2 = 1$, with orifice opening face-on.

If the stagnation pressures of the face-on shock wave (P_1) is P_{o1} and critical conditions exist in the duct P_2^*, $u_2 = a_2$, the theoretical relation,

(P_{o1} = Stagnation pressure at Location 1)

$$\frac{P_{o1}}{P_2^*} = 1.893,$$ or slightly less for shock waves in the pressure range tested, should hold. According to the experiment this does hold at the minimum critical pressure $P_2^* = 14.7$ and $P_{o1} \approx 27.5$; however, for stagnation pressures greater than 27.5, this ratio $\frac{P_{o1}}{P_2^*} = 1.893$ does not hold, but the ratio $\frac{P_1}{P_2} = 1.65$ does hold. If this relation $\frac{P_1}{P_2} = 1.65$ proves to be an aerodynamic shock principle and not just a characteristic of the experimental set-up, a useful tool for a direct relation to all of the parameters in the filling process may be on hand. (P_{o2} denotes stagnation pressure in region 2.)

For an example $$\frac{d\rho_3}{dt} = \frac{A}{V} u_2 \rho_2$$

since for $P_2 > 14.7$, $u_2 = a_2$

$$\frac{d\rho_3}{dt} = \frac{A}{V} a_2 \rho_2 = \frac{A}{V} a_o \rho_o \left(\frac{P_2}{P_o}\right)^{6/7} = \frac{A}{V} a_o \rho_o \left(\frac{P_1}{1.65\, P_o}\right)^{6/7}$$

and for the stagnation pressure in the duct

$$u_2^2 + 5a_2^2 = 5a_{o2}^2$$

$$\frac{a_{o2}^2}{a_2^2} = \frac{6}{5}$$

$$\frac{P_{o2}}{P_2} = 1.893$$

since

$$\frac{P_1}{P_2} = 1.65$$

$$P_{o2} = 1.145\ P_1$$

Plans to verify this relation by using a similar system but with a larger baffle and a straight duct are in process.

V. Effect of Tunnels

The third part of this paper deals with the effect of tunnels in the filling of chambers. A tunnel of some configuration is usually used to enter an underground structure. So the purpose of this test was to determine some general effects of tunnel forms used in reducing the rate of pressure rise to the chamber.

Figure 8 shows the diagram of three tunnel forms considered to represent a good cross-section of possible effective tunnel forms. The results of these tests may be applicable to more complex forms. The details of the tests which go into the p-t sequence in each leg of the tunnels have been neglected for the more distinct concluding effects of the pressure rate of rise in the chamber.

The small circles on the diagram designate the location of piezo-electric gauges. Figure 9 shows the p-t history taken from the gauges in the chamber of each of the three tunnel forms for the 20 psi externally applied overpressure shock. This same characteristic set of curves was obtained for the weaker 10 psi shock. The "double entry tunnel" shows the fastest rise and the highest pressure reached (the double entrance has the effect of allowing a delayed reflected pressure to be applied to the chamber). In the by-pass tunnel the low rate of pressure rise occurs because the original flow divides into two streams and hence reduces the mass flow into the chamber. This reduced rate of filling (by-pass effect) terminates in about 13 milliseconds when a sudden increase in the slope occurs. This increase is due to the reflected pressure from the blind end of the by-pass, returning to the chamber. So the duration of the by-pass effect is determined

by the time for the shock to move down the by-pass arm, reflect and return to the chamber. If the by-pass arm is extended the by-pass effect is extended. However, an optimum length of this arm is reached over which the by-pass effect cannot reduce the rate of pressure rise. The optimum by-pass duration will last until the pressure difference $(P_1 - P_3)$, is small enough so that no increase in the rate of filling will occur when the by-pass effect is discontinued. The optimum by-pass length (L) for the flat top wave is associated directly with the chamber volume and the orifice area by the relation $L = \frac{V}{A}$.

Figure 10 shows the single entry form, the by-pass form and the optimum length by-pass form as a broken line. Here there appeared to be a unique way of utilizing a tunnel to reduce pressure rate of rise in a chamber. However, from an economy of volume point of view, if the optimum by-pass tunnel system having a chamber volume of V and a by-pass arm volume of V for a total volume of 2V were replaced by the single simple tunnel system with a chamber volume of 2V, the resulting rate of pressure rise would be less than the optimum by-pass system (see bottom curves marked $\frac{V}{A} = 35$ in Figure 10. Therefore, on the basis of these results one would conclude that the use of a tunnel system as a means for reducing pressure in a chamber is impractical. There may be exceptions to this conclusion, such as the double entry tunnel form opening on each side of a mountain so that the pressure is greatly reduced as the external shock passes over the mountain, or where the tunnel lengths are in the same order as the applied shock wave length.

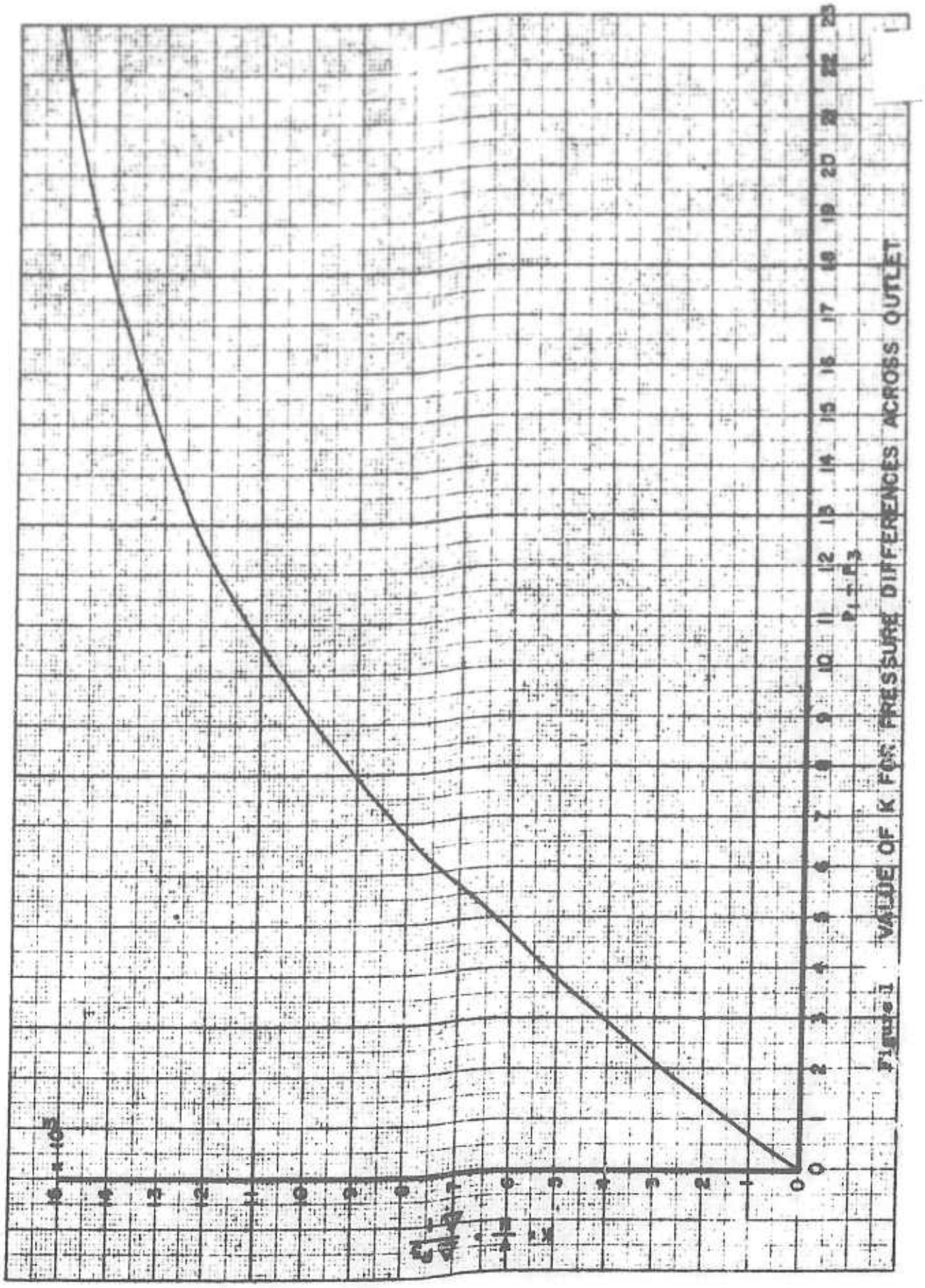
VALUE OF K FOR PRESSURE DIFFERENCES ACROSS OUTLET
P1-P3
0
1
2
3
4
5
6
7
8
9
10
11
12
13
14
15
16
17
18
19
20
21
22
23

Figure 1

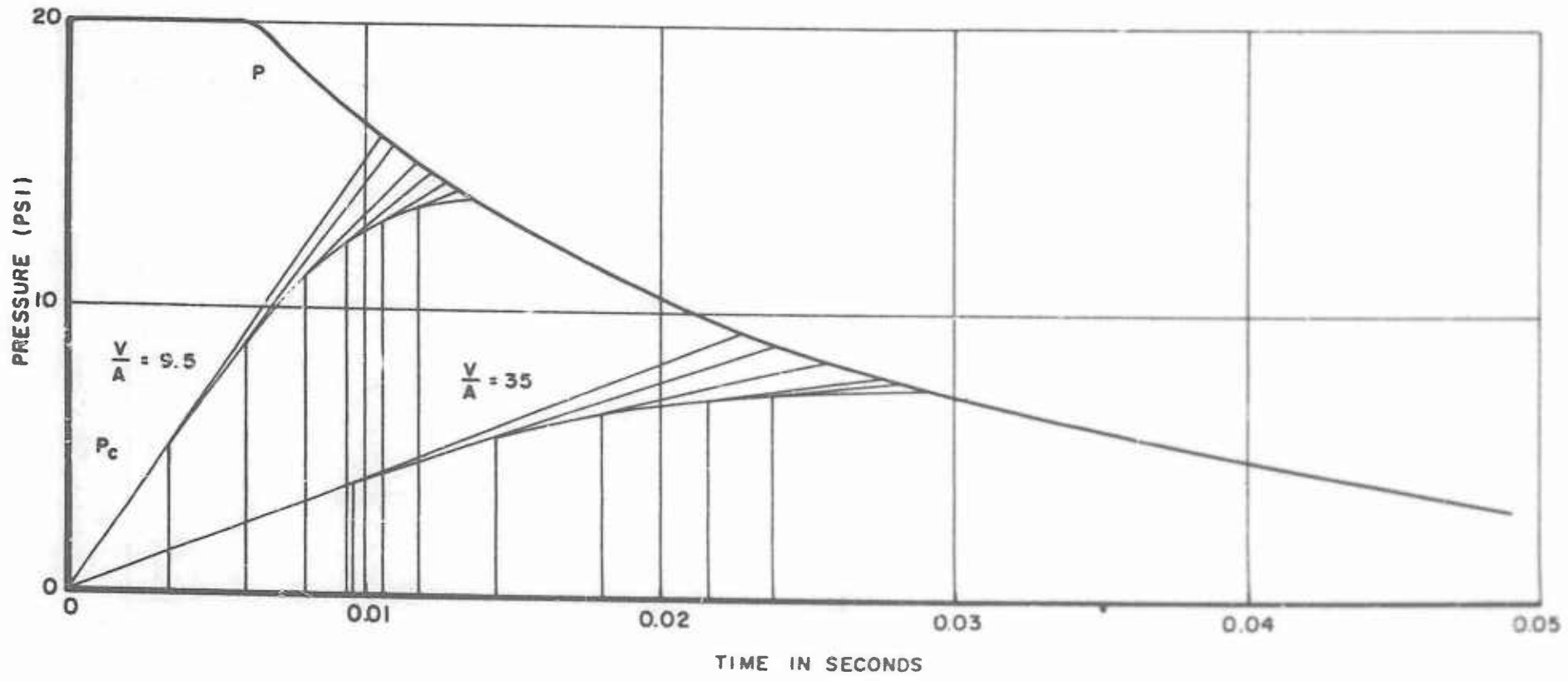

Figure 2 EXAMPLES OF FILL TIME PREDICTION METHOD APPLIED TO SHOCK TUBE WAVE SHAPE

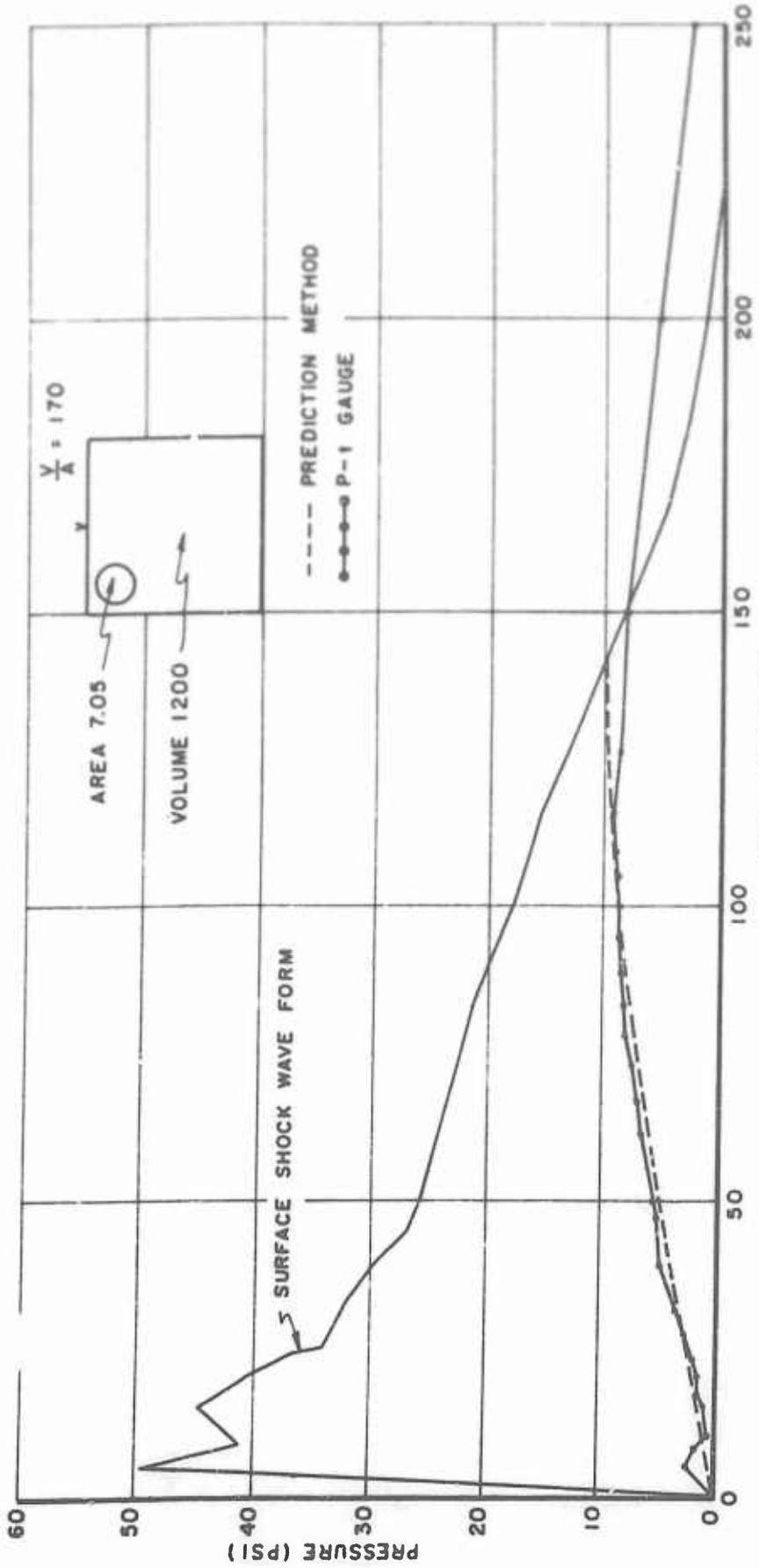

Figure 3
COMPARISON OF FIELD RECORD AND PREDICTED CURVE FOR SLOW FILL CHAMBER

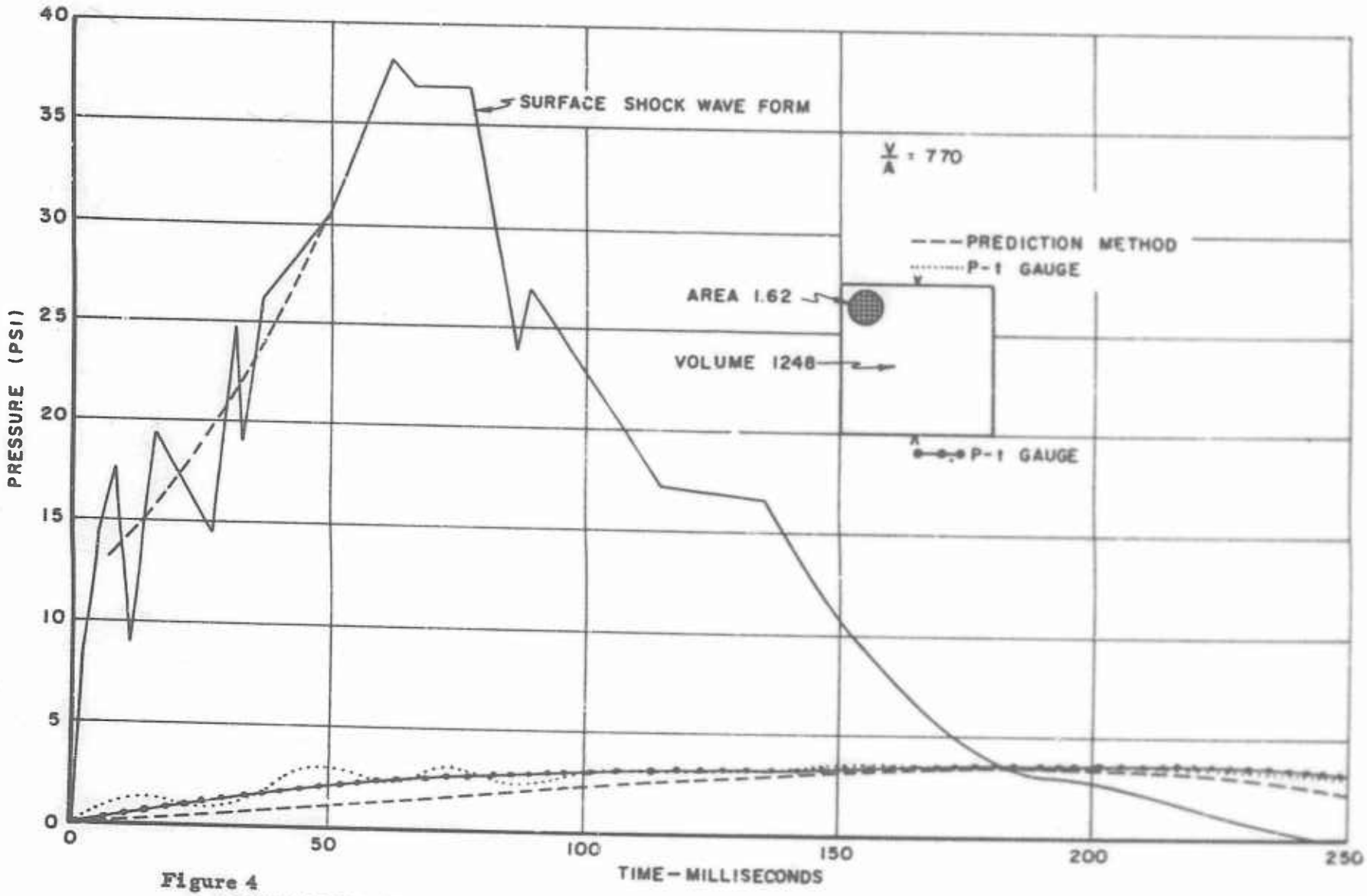

Figure 4

COMPARISON OF FIELD RECORD AND PREDICTED CURVE FOR SLOW FILL CHAMBER

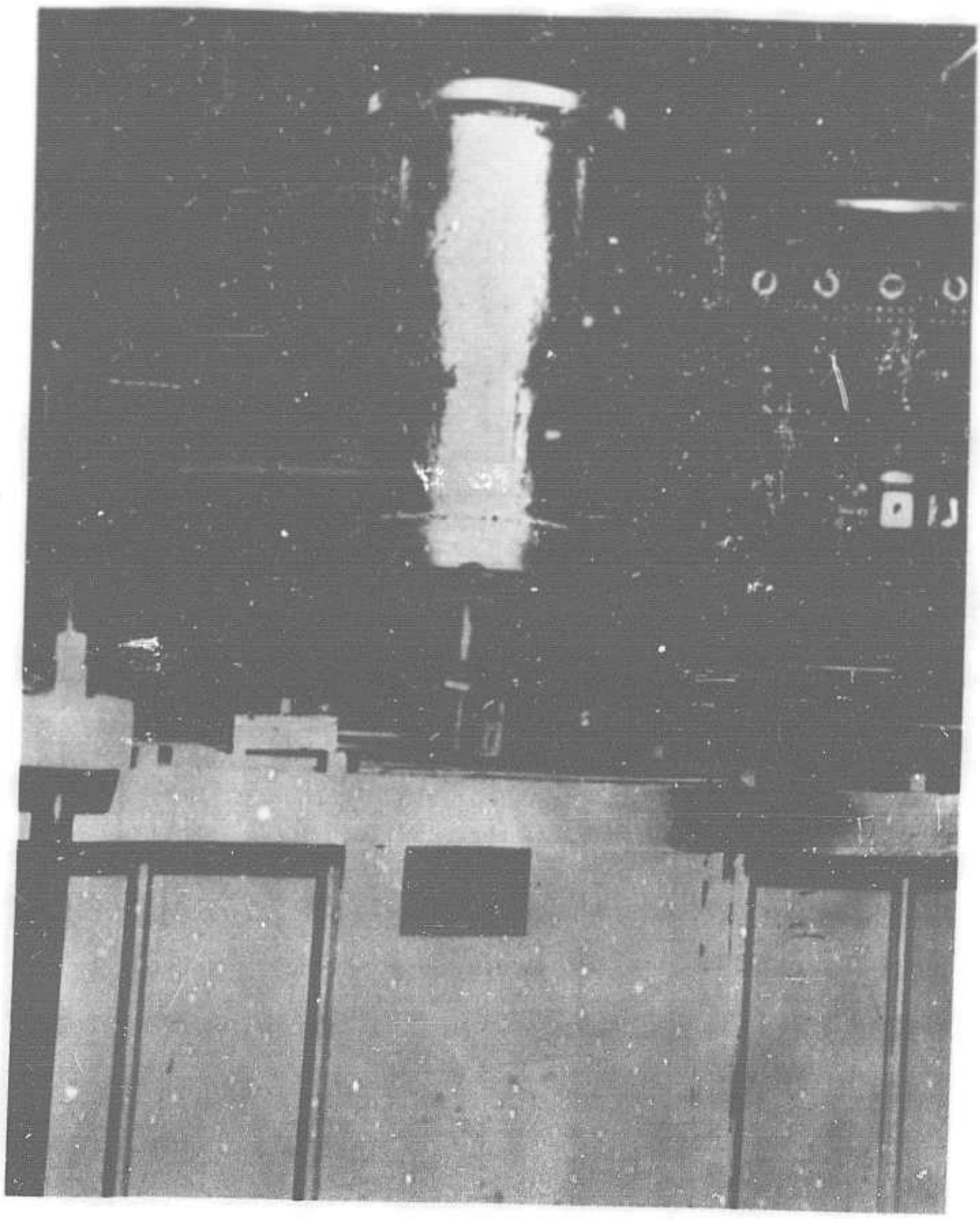

Figure 5 Chamber and Orifice Plate Attached to the Shock Tube

Figure 6 PRESSURE-TIME HISTORY IN CHAMBER WITH OPENING FACING 0°, 30°, 45°, 60° AND 90° TO SHOCK WAVE DIRECTION FOR 10 & 20 PSI SHOCK PRESSURE.

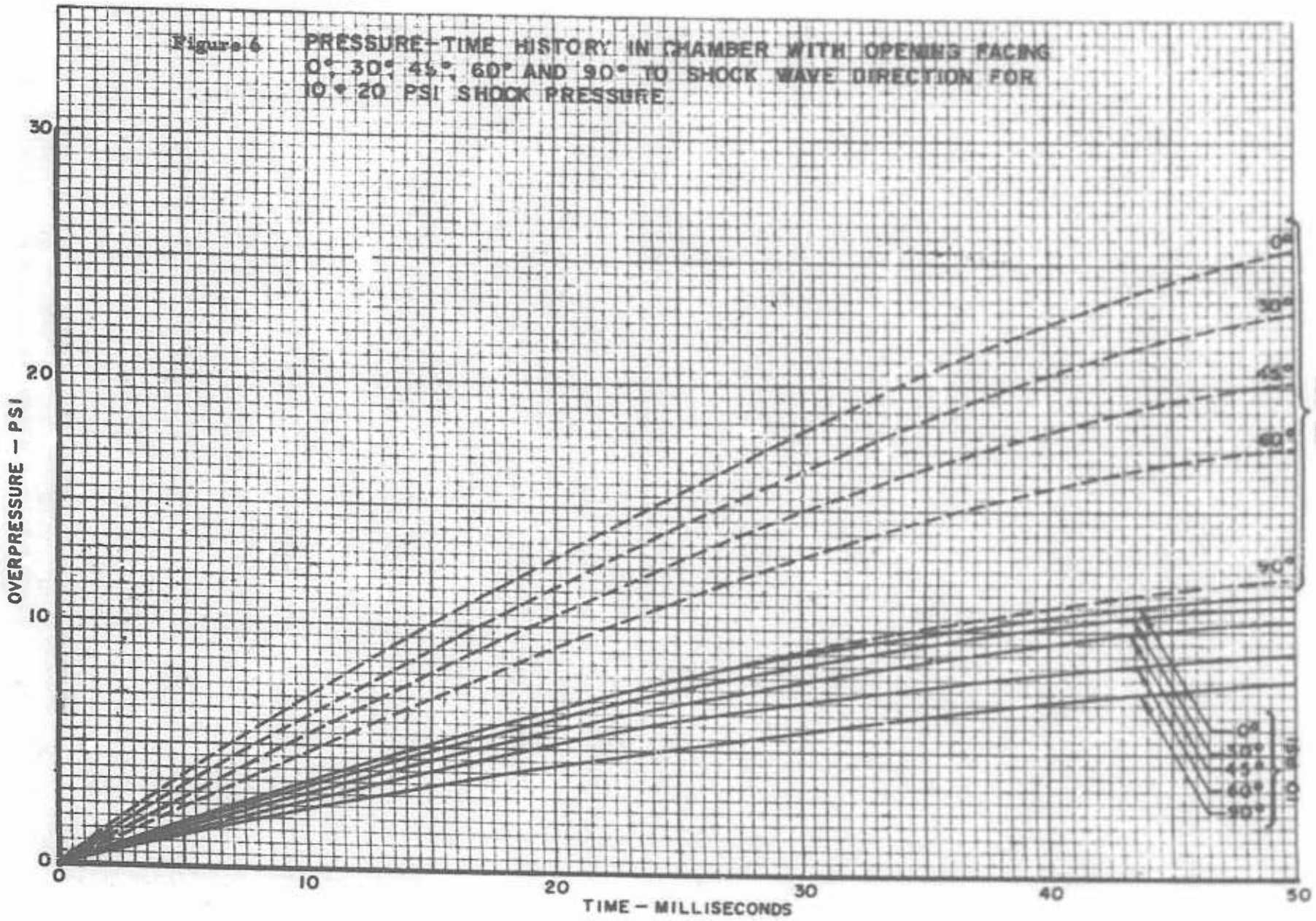

Figure 7 APPLIED SIDE ON SHOCK PRESSURE VS. PRESSURE IN TUNNEL WITH ENTRANCE FACING 0, 45° AND 90° TO DIRECTION OF SHOCK.

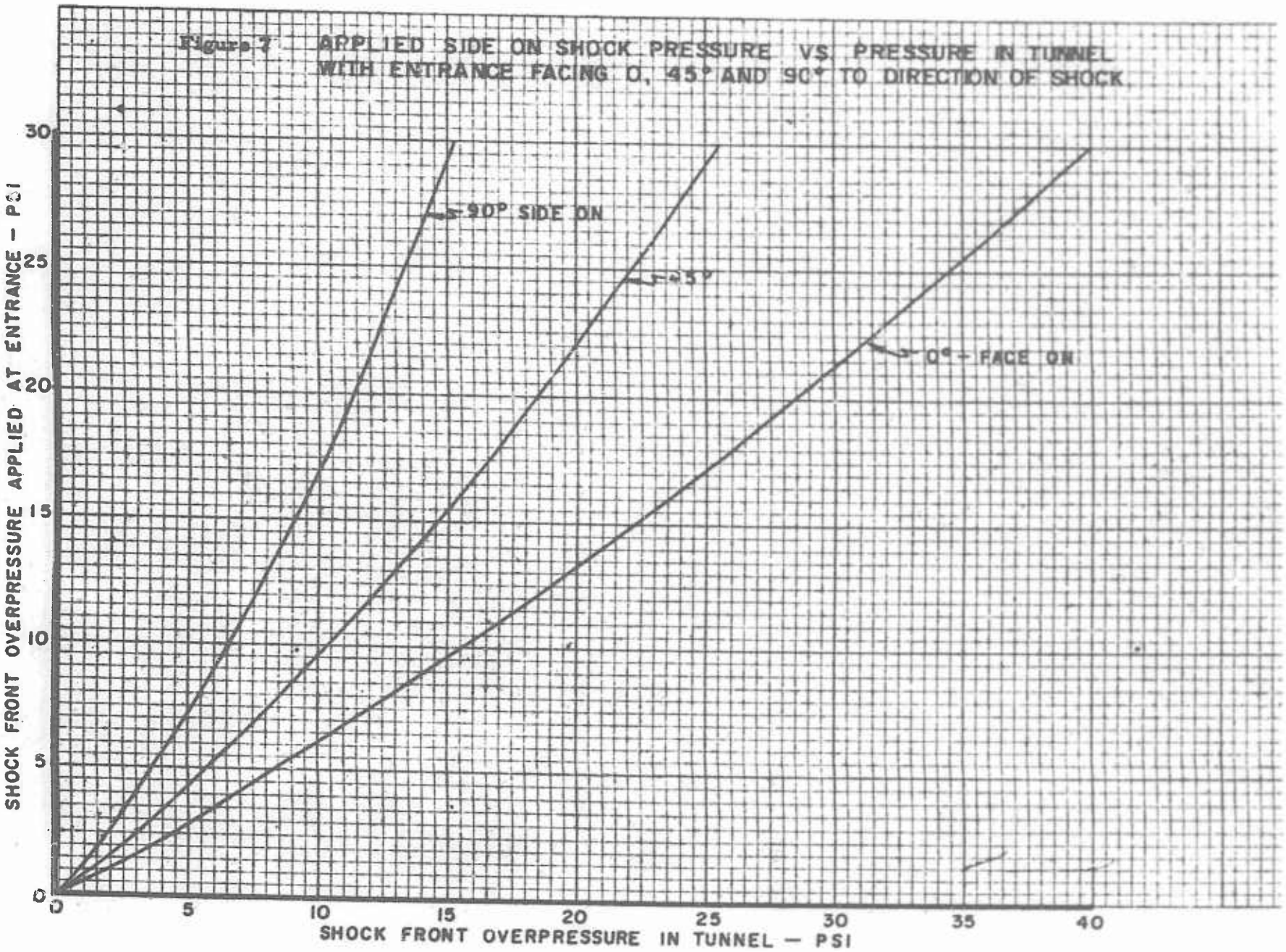

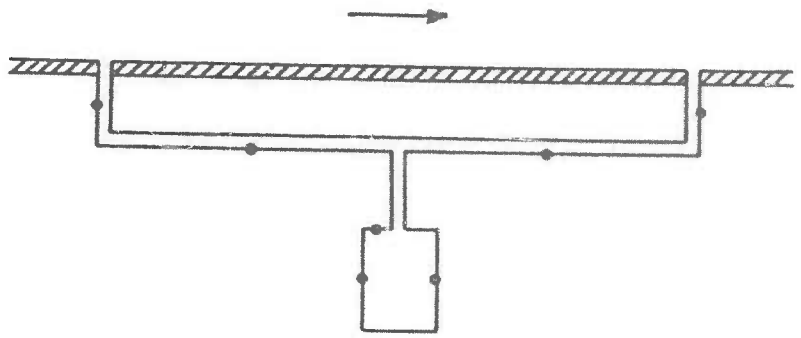

(A)

DOUBLE ENTRY TUNNEL

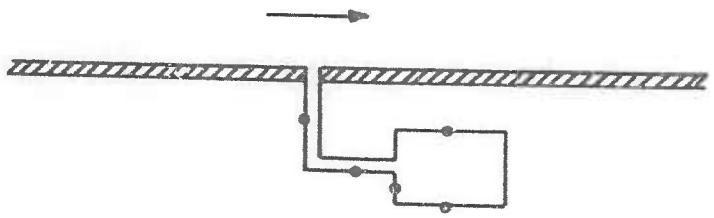

(B)

SINGLE ENTRY TUNNEL

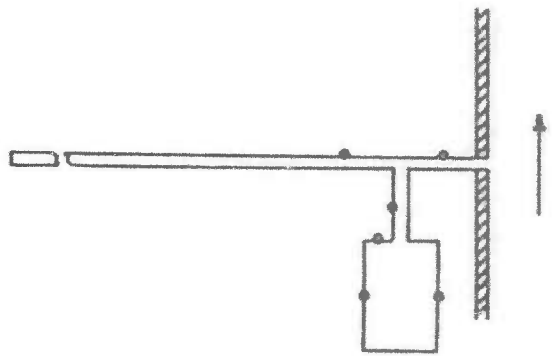

(C)

BYPASS TUNNEL

Figure 8 TUNNEL CONFIGURATIONS

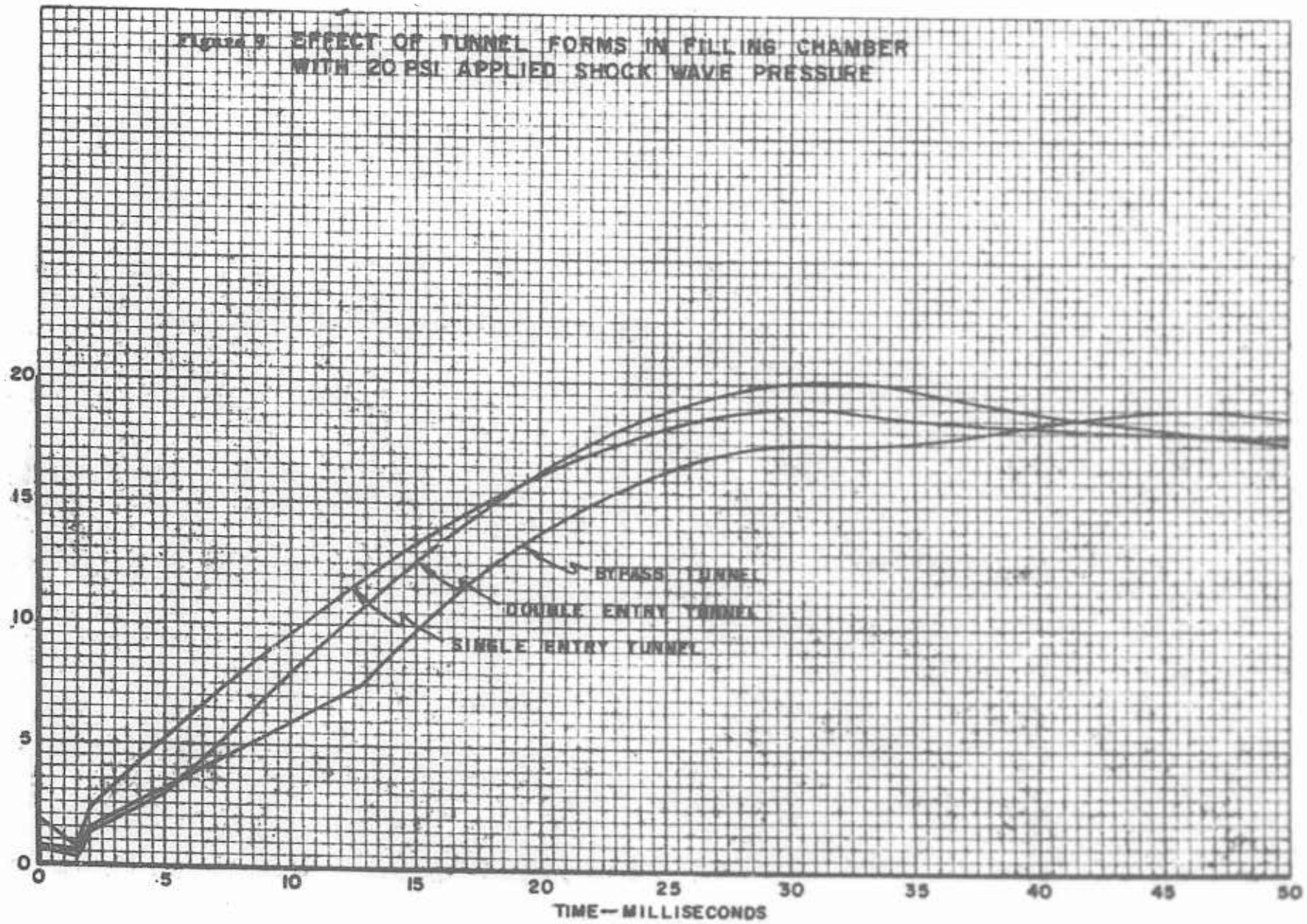
FIGURE 9. EFFECT OF TUNNEL FORMS IN FILLING CHAMBER WITH 20 PSI APPLIED SHOCK WAVE PRESSURE
20
15
10
5
0
0
5
10
15
20
25
30
35
40
45
50
BYPASS TUNNEL
DOUBLE ENTRY TUNNEL
SINGLE ENTRY TUNNEL
TIME—MILLISECONDS

Figure 18 EFFECT OF BYPASS TUNNEL FILLING COMPARED TO FILLING OF THE SINGLE ENTRY CHAMBER WHICH IS INCREASED IN VOLUME BY THE VOLUME OF THE BYPASS TUNNEL

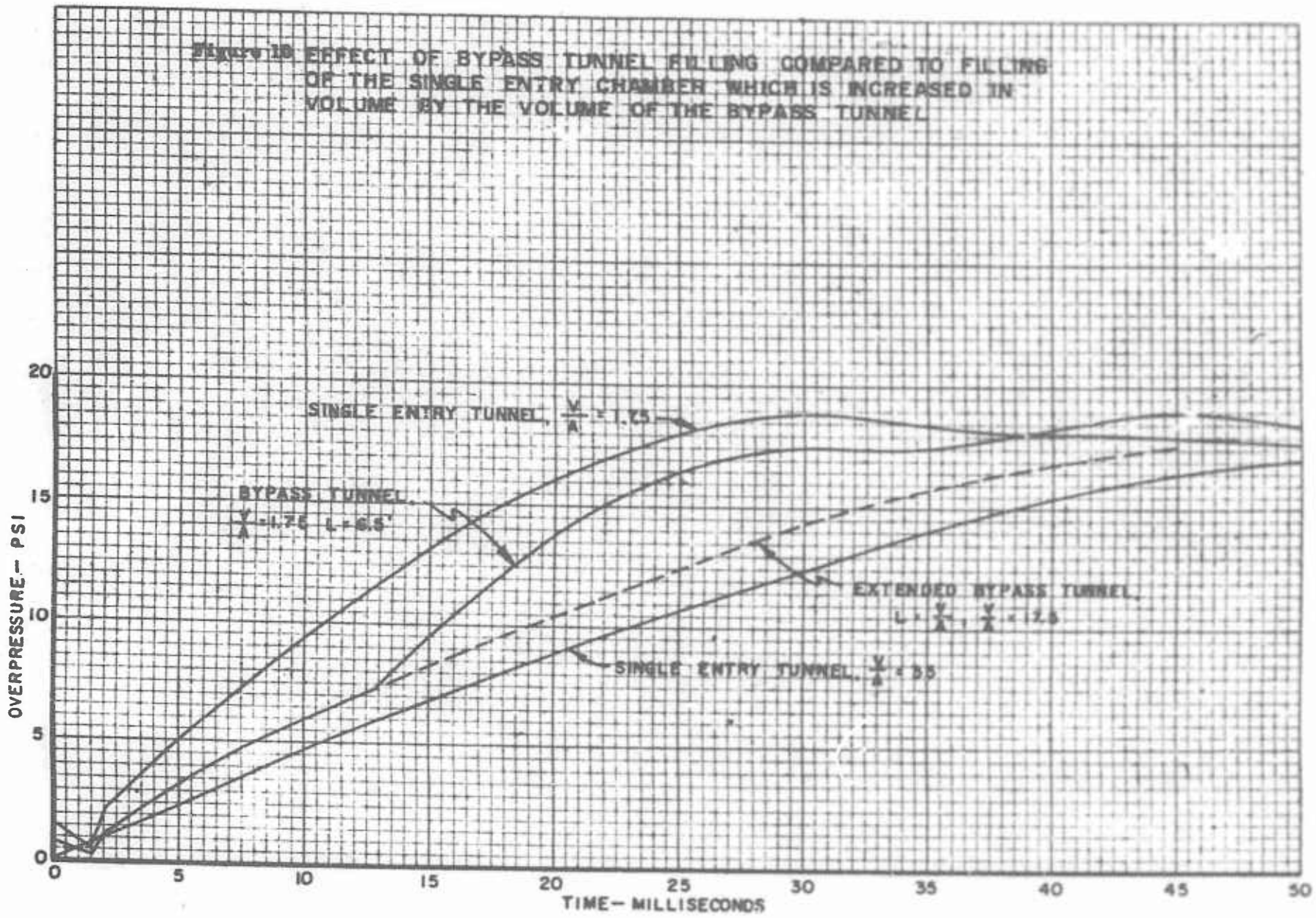

Symbols

c	specific heat
E	electrical potential
I	electric current
l	linear dimension-thickness
q	specific heat flux
R	resistance
t	time
α	temperature coefficient of resistivity
ρ	density
τ	characteristic time of experiment

Subscripts

m	material

DETERMINATION OF THE TIME HISTORY OF THE FLOW FIELD ABOUT BLUNT BODIES IN A SHOCK TUBE[1]

E. Offenhartz* and H. Weisblatt**

I. Introduction

The shock tube can be considered to be an extremely short duration supersonic wind tunnel with the advantage of enabling the stimulation of the re-entry of a blunt body into the earth's atmosphere (reference 1 and 2). The steady state testing time available in supersonic wind tunnels is in general a function of model and tunnel geometry as well as operating conditions. Specifically for blunt body tests, the duration of steady state flow within supersonic tunnels is dependent upon the tunnel boundary layer, the strength of the detached bow wave and the resulting area ratio. In addition for the shock tube case, the aerodynamics is further complicated due to attenuation (references 3 and 4).

When undertaking aerodynamic investigations within a shocktube, it is of interest to examine the influence of these parameters on the duration of steady state testing time. Therefore, in order to understand the flow field about blunt bodies during shock tube tests an experimental investigation was undertaken over a range of operating conditions within a 1.5 inch diameter shock tube.

II. Experiments and Models

The experiments to determine the time history of the flow field about blunt bodies were conducted within a 1.5 inch diameter shock tube over an approximate shock Mach number range of 6 to 10.6 and an initial pressure range of 5 to 76 centimeters of mercury.

---

1 This work was done at the Avco Research Laboratory under the sponsorship of the Air Force (BMD, ARDCO through contract AF 04(645)-18 in support of AF 04(645)-30.

* Senior Scientist - Research and Advanced Development Division, Avco Manufacturing Corporation.

** Associate Scientist - Research and Advanced Development Division, Avco Manufacturing Corporation.

The stainless steel models consisted of a hemisphere - cylinder and an arbitrary blunt body of two different diameters chosen so as to generate a stronger detached bow wave than generated by the hemisphere-cylinder. One of the blunt bodies was of the same diameter as the hemisphere-cylinder, whereas the other blunt body was taken to be .750 of the diameter of the hemisphere-cylinder. In this way it was possible to determine the effect of bluntness and model size on the time history of the flow field. In addition pyrex models instrumented with calorimeter gages were used for the tests. These models were used to determine the sensitivity of heat transfer measurements to changes in the flow field.

III. Test Technique

Because of the short duration of the characteristic test time (defined as the time between the passage of the shock wave and the arrival of the mixing region at the model) it was not possible to obtain motion pictures of the flow during a given test. Hence at a fixed operating condition, schlieren photographs were obtained at approximately 10 microsecond intervals. The time sequence was obtained over the expected duration of the test region of uniformly heated and compressed air and required many tests at a fixed operating condition. The attenuation of the shock wave was monitored for each test and within the normal attenuation scatter (reference 5) the test results were repeatable.

In order to determine the sensitivity of calorimeter gages to the time history of the flow field, heat transfer measurements were obtained over the test range for the hemisphere-cylinder and blunt body of the same diameter.

IV. Data Reduction

The schlieren photographs enabled the measurement of shock detachment distances for fixed body locations. In addition, the entire bow wave shape was measured and replotted to the same scale to enable a qualitative study of the change in shock shape with time.

For the tests using calorimeter gages, each measuring station was monitored on a different oscilloscope with each oscilloscope set for a discrete sweep rate. Thus during a given test each time interval of interest in the flow field could be examined in detail.

V. Results and Discussion

The reduction of the schlieren and heat transfer data enabled an understanding of the time history of the flow field. In general this history was analyzed by consideration of three time intervals. The first time interval, or bow wave build up time, occurred immediately after the normal shock had passed the model. During this interval the bow wave formed, moved forward from the body and assumed a steady state shape and position. The second time interval, or steady state, during which the bow wave remained in an equilibrium position lasted until the onset of the third or

unsteady flow phase. This last interval started when the bow wave interaction with the turbulent boundary layer on the shock tube walls caused changes to the bow wave. During this interval the bow wave distorted at the walls, then changed shape and became more normal with time. The onset of unsteady flow occurred before the arrival of the mixing region at the model. These changes in the flow field will be demonstrated by considering the results obtained for a particular operating condition of a shock Mach number of approximately 7.5 and an initial pressure of 10 centimeters of mercury. The heat transfer results can be analyzed by considering the following expression for the heat transfer rate to a calorimeter type gage given in reference 5 as

$$q = \frac{1}{IR} \left(\frac{\rho c \ell}{\alpha} \right)_m \frac{dE}{dt} \qquad (1)$$

It should be noted that the heat transfer rate to the gage is constant when the voltage change with time is linear. It is then of interest to determine when the voltage change with time is linear and when this takes place in the flow field.

The changes in slope of voltage with time can be seen from the heat transfer records obtained for the hemisphere-cylinder which are shown in Figure 1. The oscilloscope records show the measured variation of voltage with time as obtained for various times of interest in the flow field. The slopes of each heat transfer record are, for clarity, redrawn above the oscilloscope trace. The dashed line shown during any one time interval indicates the slope of the oscilloscope record during the preceding time interval. The difference between the dashed line and the solid line represents the change of slope during consecutive time intervals. Thus, the heat transfer records indicate the sensitivity of the calorimeter type gage to the postulated changes in the flow field.

Although these changes in slope appear to be quite small they are directly reflected in the calculation of the heat transfer rate as shown by equation 1. To indicate the effect of these slope changes, the heat transfer rates were calculated and are presented as heat transfer ratios in Figure 2 as a function of time. The heat transfer ratio is defined as the heat transfer rate at the time indicated divided by the heat transfer rate during steady state flow. Thus, interpretation of the heat transfer rate for this particular case could differ by as much as 50 per cent if one were to consider that the flow remained steady throughout the entire time of the measurement.

To further substantiate the existence of the three phases of the flow field the shock detachment distances as determined from the schlieren photographs are shown in ratio form in Figure 3 as a function of time. The shock detachment distance ratio is defined as the shock detachment distance at the time indicated divided by the shock detachment distance during steady state.

Similar plots (i.e., shock detachment distance and heat transfer ratios) were also obtained for the other blunt bodies. Within the accuracy of the measurements, it was found that the time required to establish steady state flow was the same for each body when tested at a fixed operating condition. However, the time duration of steady state flow was different for each model.

Figure 4 shows the shape of the bow wave at typical points of interest in the flow field for each of the blunt bodies tested. As time increases, the bow wave moves upstream from the body and then assumes a steady state shape and position. As time continues to increase, the bow wave distorts near the shock tube walls and finally changes shape completely. It is interesting to notice that the bow wave formed symmetrically and continued to develop symmetrically until steady state was reached.

A schematic diagram of the bow wave interaction with the turbulent boundary layer along the shock tube walls is indicated in Figure 5. The turbulent boundary layer becomes thicker upstream of the point where the bow wave intersects the layer. The thicker boundary layer acts so as to generate compression waves forward of the impinging bow wave. Thus, the shape of the impinging bow wave and its wall reflection are modified by the boundary layer shock interaction (reference 6). The boundary layer along the shock tube walls grows with time and the interaction between the impinging wave and the boundary layer becomes more pronounced until such time when the bow wave becomes distorted and the resulting flow field becomes unsteady. The location of the sonic point on the bow wave is also worthy of consideration. When the sonic point on the bow wave is in close proximity to the shock tube walls, the flow field is more sensitive to bow wave distortions at the wall than if the sonic point occurs further away from the wall.

The results of the tests to determine the time history of the flow field are summarized in Figure 6. This figure has been prepared as an operational curve based upon the test conditions of the present investigation within a 1.5 inch diameter shock tube. The lower curve of the figure represents the total build-up time during which the bow wave formed and moved upstream from the body to the steady state shape and position. Clearly then, for the models tested the build-up time was independent of the model shape and size. For comparison purposes the test result of reference 7 is also shown. This data point from reference 7 represents the time for the bow wave to reach a steady state position in the flow about a 0.25 inch diameter two dimensional cylinder tested in a 2.875 inch by 2.875 inch shock tube. The faired portion of the curve to include this data point indicates the possibility that bow wave build-up time may also be independent of body shape and indicates the similarity of results obtained by independent investigations.

The total time duration of the flow (i.e., build-up time plus steady state time) for each of the blunt bodies tested is also shown in Figure 6. For a given body shape of different diameter the smaller body yielded the larger test time. Both the time required for the bow wave to reach an equilibrium state and the total available test time decreased as the

shock Mach number increased and the initial pressure decreased. Also shown in Figure 6 is the experimentally determined time duration ($\tau/2$) of the test region taken as the time interval between the passage of the normal shock and the arrival of the mixing region at the model (reference 5). Actually, the test time as calculated from the theory was found to be equal to τ; however, experimental values were found to be one-half of the calculated values. Thus, the characteristic time of $\tau/2$ was recommended for use (reference 5).

In reference 7, it was found that the $\tau/2$ type prediction for testing time described adquately the total time duration of the flow about the 0.25 inch diameter two-dimensional cylinder. For this case the boundary layer along the shock tube walls was laminar and the interaction of the bow wave with the boundary layer did not cause any change in the available test time. However, for the present tests the unsteadiness of the flow field about the two different diameter models tested, caused by the interaction between the detached bow wave and the shock tube wall turbulent boundary layer, imposed a more severe restriction upon the test time than does the $\tau/2$ prediction of reference 5.

VI. Conclusions

The time history of the flow field about blunt bodies has been experimentally investigated within a 1.5 inch diameter shock tube over a range of operating conditions. Heat transfer measurements were found to be sensitive to the entire time history of the flow field.

The time history was found to consist of three distinct intervals. The first time interval, or bow wave build-up time, occurred immediately after the normal shock had passed the model. During this interval the bow wave formed, moved upstream from the body and assumed a steady state shape and position. The second time interval, or steady state, during which the bow wave remained in an equilibrium position lasted until the onset of the third or unsteady flow phase. This last interval started when the bow wave interaction with the turbulent boundary layer on the shock tube walls caused changes to the bow wave. During this interval the bow wave distorted at the walls, then changed shape and became more normal with time. From a study of the time history, the resulting steady state test time was found to be less than the characteristic time, defined as the time interval between the passage of the normal shock and the arrival of the mixing region at the model.

REFERENCES

1. Rose, P. H., Probstein, R. F., Adams, M. C., Turbulent Heat Transfer Through a Highly Cooled Partially Dissociated Boundary Layer, AVCO Research Laboratory, Research Report 14. (to be published in the Journal of Aeronautical Sciences).

2. Kemp, N. H., Rose, P. H., Detra, R. W., Laminar Heat Transfer Around Blunt Bodies in Dissociated Air, AVCO Research Laboratory Report 15.

3. Trimpi, R. L., Cohen, N. B., A Theory for Predicting the Flow of Real Gases in Shock Tubes with Experimental Verification, NACA, TN 3375, 1955.

4. Rose, P. H., Nelson, W., On the Effect of Attenuation on Gas Dynamic Measurements Made in Shock Tubes, (Paper presented at Second Shock Tube Symposium, Palo Alto, California, March 5, and 6, 1958).

5 Rose, P. H., Stark, W. I., Stagnation Point Heat Transfer Measurements in Dissociated Air, Journal of the Aeronautical Sciences, vol. 25, No. 2, Feb. 1958, pp 86-97.

6. Liepmann, H. W., Roshko, A., and Dhawan S., On Reflection of Shock Waves from Boundary Layers, NACA, TN 2334, 1951.

7. Rabinowitz, Josef, Aerodynamic Studies in the Shock Tube, Hypersonic Research Project Memorandum No. 38, Guggenheim Aeronautical Laboratory, California Institute of Technology, June, 1957.

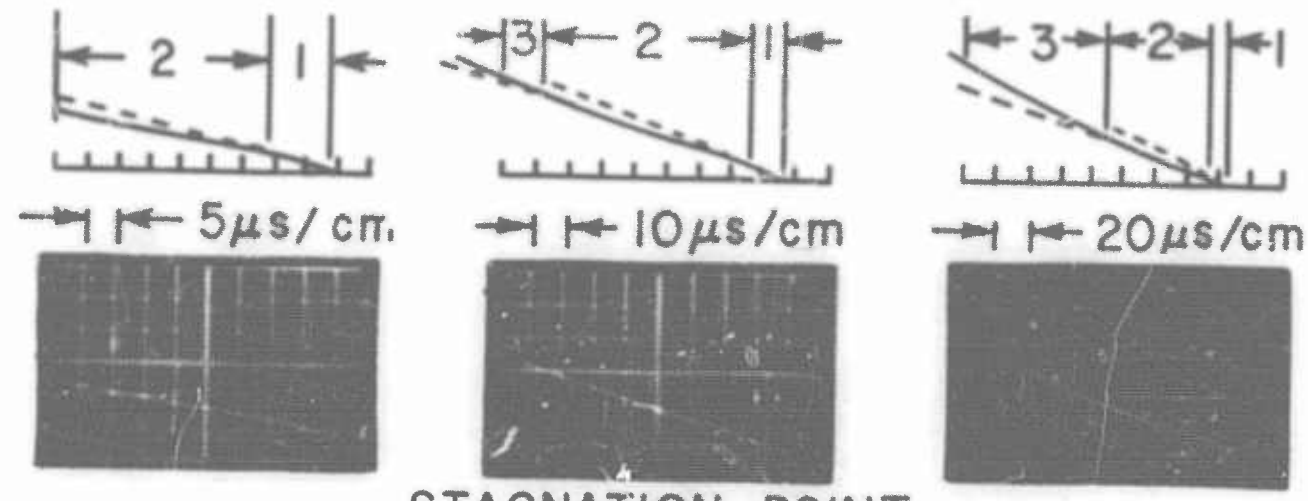

Figure 1 Typical Heat Transfer Records for Hemisphere-Cylinder.

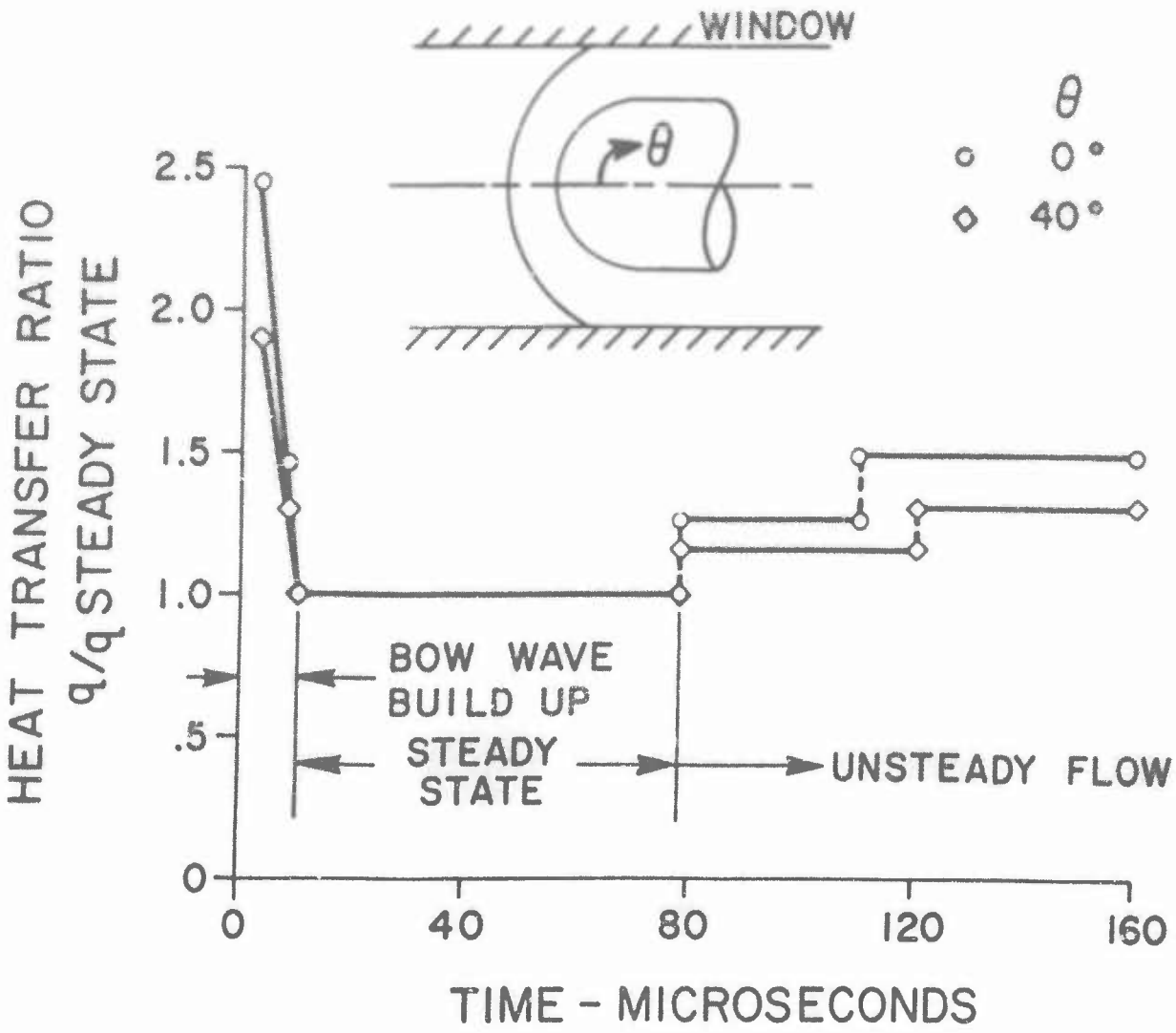

Figure 2 Heat Transfer Ratio as a Function of Time.

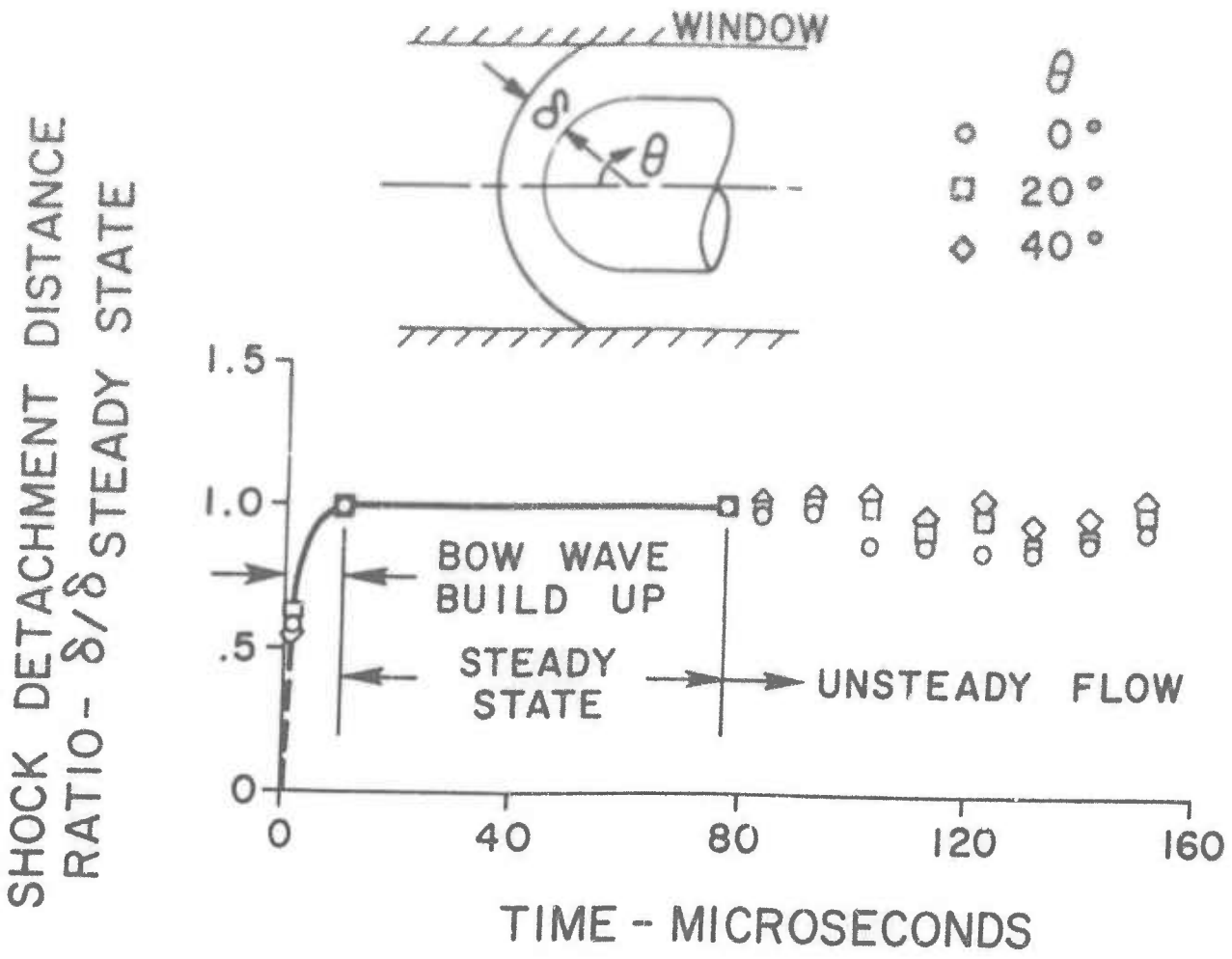

Figure 3 Shock Detachment Ratio as a Function of Time.

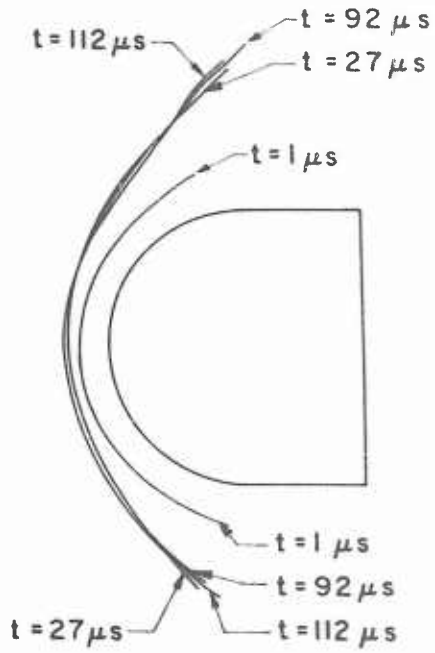

(a) HEMISPHERE-CYLINDER

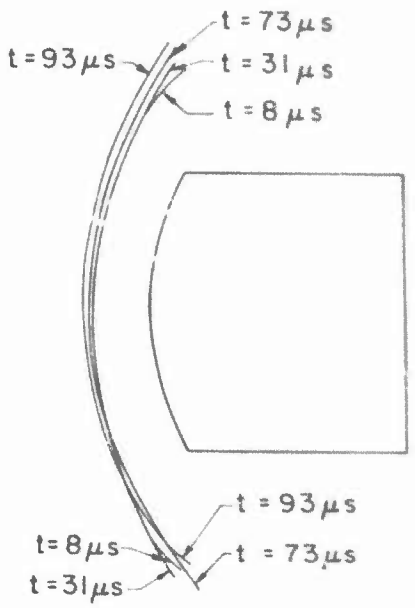

(b) BLUNT NOSE MODEL SAME DIA. HEMISPHERE - CYLINDER

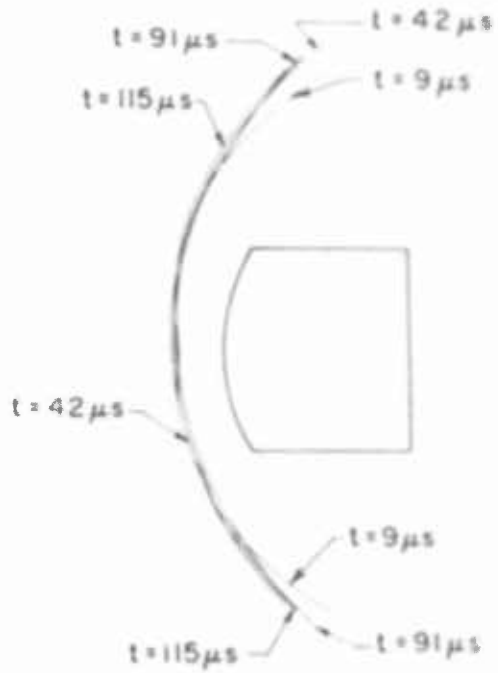

(c) BLUNT NOSE MODEL .750 DIA. HEMISPHERE-CYLINDER

Figure 4 Bow Wave Shape at Typical Times.

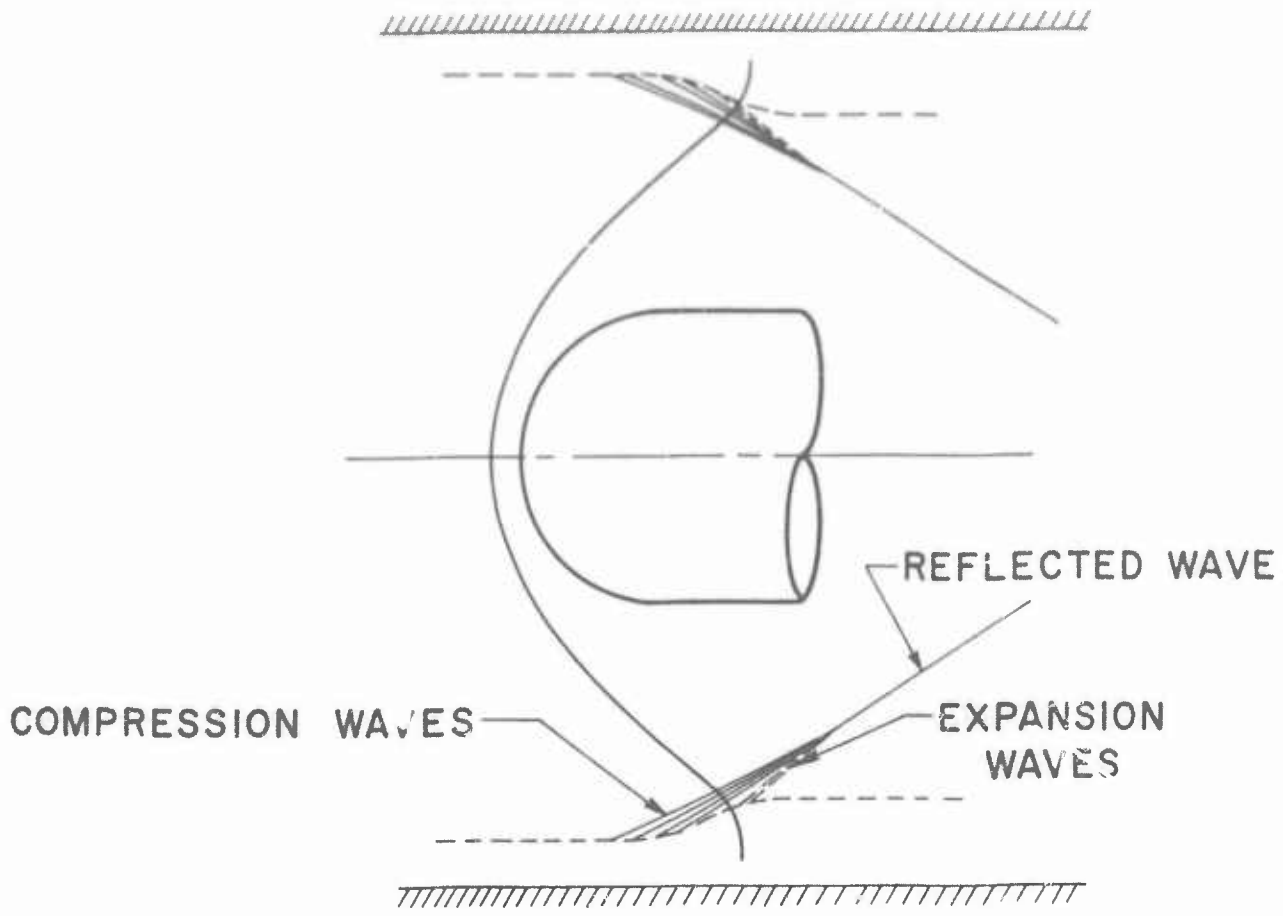

Figure 5 Schematic Diagram of Shock and Turbulent Boundary Layer Interaction.

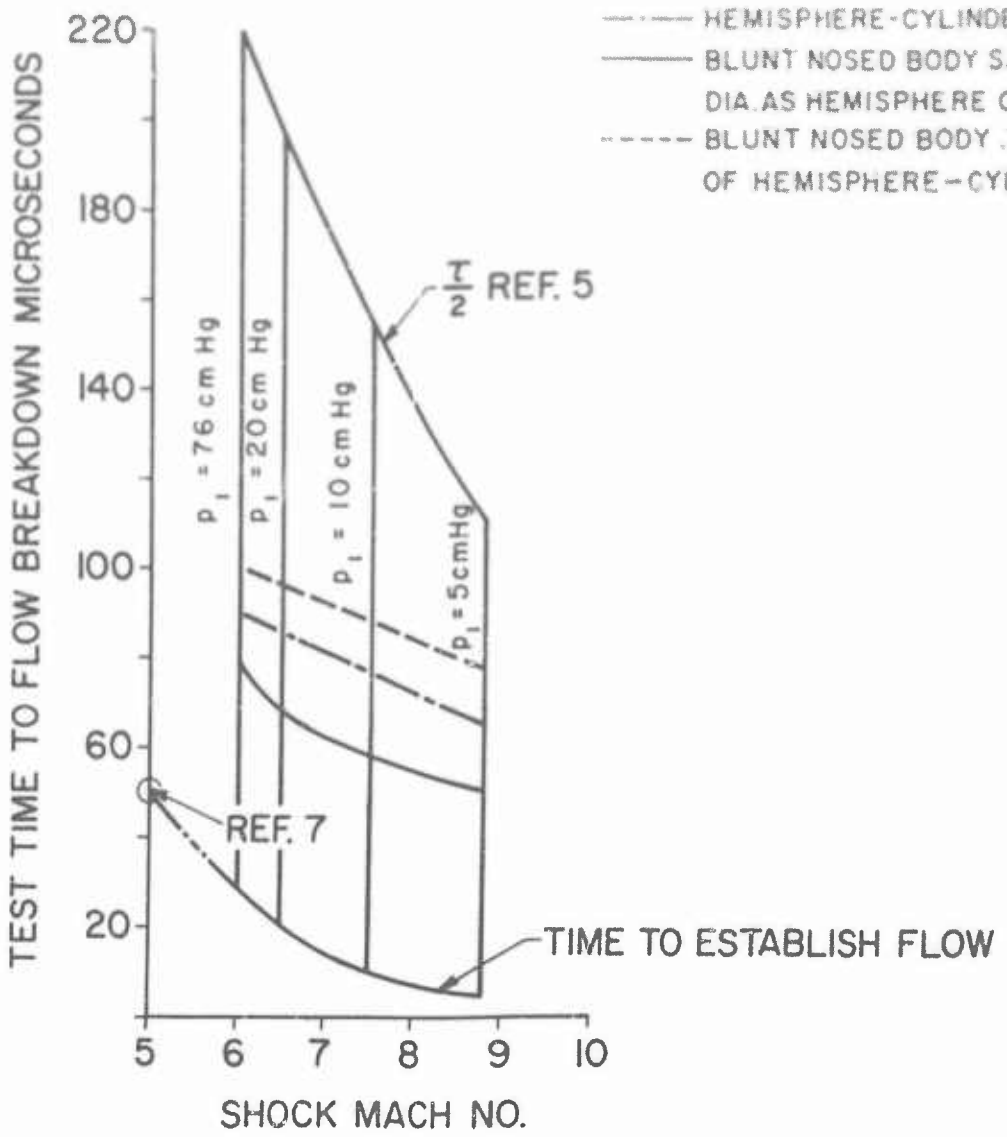

Figure 6 Total Test Time for Flow Breakdown as a Function of Shock Tube Operating Conditions.

SOME EXPERIMENTS WITH PERIODIC SHOCKS*

Jack Kotik
Technical Research Group

The early work of Hudson, Shaw, et al. (N. Y. U.) established the existence of periodic shocks in a closed tube excited by an oscillating piston. It was found that shocks occur only when the piston frequency f and tube length L satisfy (approximately) the acoustic resonance condition $L = \lambda/2$, $\lambda f = c$, where c is the velocity of sound in the undisturbed gas. Only weak shocks ($M < 1.15$) were observed, and no heating effects. The prediction of the observed data, especially shock strength as a function of the piston motion, is a difficult theoretical problem, since a periodic solution can be expected only if we consider the heat flow from the gas through the tube to the environment. A number of investigators, including Keller and Hudson, have attacked this problem with partial success.

In view of the theoretical difficulties in predicting shock excitation, an empirical approach was adopted. Two different piston assemblies ("compressors") were constructed, as well as four tubes, of two different diameters and lengths. The compressors could each be run at 3460 and 6920 rpm (nominal). Interchangeability was provided for, so that the influence of each variable could be isolated. Among the combinations are tubes of one diameter excited by compressors of another. The quantity chosen as a measure of shock strength was $\xi_M - 1$, where ξ_M is the measured pressure ratio across the single shock (per cycle) observed at the closed end of the tube. $\xi_M = \xi_I \xi_R$ where ξ_I, ξ_R are the incident and reflected shock pressure ratios. The equipment was as follows:

Compressors: C_1: Bore = 1 15/16" Stroke = 1/2"
C_2: Bore = 2 1/4" Stroke = 2"
Tubes: T_1: Inside diameter = 1 15/16"
T_2: Inside diameter = 7/8"

Tube lengths were variable. The results follow:

Change in tube length, with C_1, T_1, f = 6920 rpm;

$L = \lambda/2$, $\xi_M - 1 \sim 0.56$;
$L = \lambda$, $\xi_M - 1 \sim 0.37$.

---

*Complete paper can be obtained from Jack Kotik, Technical Research Group, 17 Union Square West, New York 3, N. Y.

Change in frequency, with C_1, T_1:

f = 3460 rpm, ξ_M - 1 ~ 0.33 ($L = \lambda/2$);

f = 6920 rpm, ξ_M - 1 ~ 0.37 ($L = \lambda$).

Change of stroke and tube diameter:

C_1, T_1, ξ_M - 1 ~ 0.33; C_2, T_1, ξ_M - 1 ~ 0.92
(small change in bore, also)
C_1, T_2, ξ_M - 1 ~ 0.56; C_2, T_2, ξ_M - 1 ~ 1.70.

These results indicate that reducing L to $\lambda/2$ is always desirable, and that the effect of various changes is in accordance with intuition. The quantitative results are of some interest but cannot safely be extrapolated, for a variety of reasons. For instance, shock attenuation limits the degree to which stronger shocks can be obtained by decreasing tube diameter. Additional experimental work will be required to develop equipment capable of heating gases to high temperatures by means of strong periodic shocks.

Periodic shocks are of interest as a method of heating gases and causing chemical reactions to occur. In this connection, it is important to have control of the peak gas temperature, its duration, and the cooling rate. By the use of certain valving arrangements, it has been possible to modify somewhat the wave shapes which are generated in the tube. Some of these modified wave shapes seem more suitable for chemical work, and this investigation is being continued.

The work described above was supported by the Air Force Cambridge Research Center, Bedford, Mass.

ON THE EFFECT OF ATTENUATION ON GAS DYNAMIC MEASUREMENTS MADE IN SHOCK TUBES

P. H. Rose and W. Nelson
Avco Research Laboratory

INTRODUCTION

The phenomenon of shock attenuation in shock tubes has been observed since the earliest use of this instrument as an experimental tool. Many investigators have commented on the shock velocity histories they have observed and a number of theoretical attacks have been made on the problem. In general it has been found that immediately adjacent to the diaphragm the shock wave accelerates. In a distance of approximately 30 tube diameters this acceleration diminishes and becomes a deceleration and the shock velocity starts to decrease in a more or less monatomic manner. It is generally considered that the initial or buildup phase involves the formation of the sharp shock front out of the pressure waves generated by the diaphragm opening. The second or attenuation phase is thought to be due to viscous and thermal losses to the shock tube walls.

An accurate description is very sensitive to the particular conditions of an experiment. Both phases of the shock velocity history are effected by the pressure level of the experiment, the enthalpy or temperature of the gases and the size or geometry of the shock tube. For instance, at very low initial pressures the second phase may be almost non-existent in some shock tubes whereas in other situations the build-up time is not measurable and the shock wave appears to decelerate right from the diaphragm on. Because shock velocity variations may significantly affect the condition of the shock heated gases, the region of interest and applicability of results collected under these conditions must be defined carefully.

In this paper we will be particularly concerned with relatively strong shock waves and high enthalpies (or temperatures) and the associated conditions which are not describable from ideal gas behavior. Unfortunately the shock tube is inherently limited by the structural capabilities of the driver chamber and in practice we must be satisfied more or less with intermediate shock velocities, such as 6-10 times the speed of sound at initial pressures of the order of one atmosphere. At lower initial pressures, say one hundredth of an atmosphere, shock velocities of the order of 15 to 20 times the speed of sound will be considered. The limiting shock velocities of a shock tube whose driver is capable of pressures of 10,000 psi after combustion* are shown in Fig. 1.

We will restrict our considerations to air as the driven or low pressure gas, and will consider only effects on the shock compressed gas region. The analysis and techniques discussed are, of course, applicable to other gases and have been applied to argon.

*Combustion of oxygen, hydrogen and helium is the driver technique employed in all the experiments described.

The theoretical treatments of the problem of shock attentuation, which have been published to date, lack the generality to make them applicable over a wide enough range to cover the conditions of interest. Among the theoretical analyses, the work of Trimpi[1] and Mirels[2-5] deserves special mention. These theoretical calculations are apparently quite representative of the observed attenuation at low shock velocities (and diaphragm pressure ratios) but are not readily extendable to predict attenuation in the region of interest in this paper.

Short of solving the shock attenuation problem analytically, and thereby defining the inviscid flow conditions in the shock compressed air region, we have attempted to use experimentally measured conditions behind attenuating shock waves to gain a more detailed knowledge about these non-ideal flows. Once the variations in the flow conditions are established, we are able to predict the effects of these deviations from the ideal on other physical measurements, such as heat transfer[6-7] flow geometry, radiation[8], or relaxation processes[9], which have been reported in the literature.

THEORY AND ANALYSIS

When the diaphragm in a shock tube is ruptured, finite relative velocities are achieved between the fluid and the shock tube walls. The processes are frequently viewed in several corrdinate systems, such as the laboratory fixed system or shock wave fixed system. In either view point, a boundary layer will be created between the inviscid flow and the shock tube wall with subsequent exchange of frictional and thermal energy. If we consider strong shock waves only then the heat capacities and the temperatures of the wall and of the shock heated gases will always be such, as to cause a heat flow from the gas to the "relatively cold" wall. The shock heated gas consequently loses energy due to both the viscous and thermal transport and the attenuation phenomena is created. Theoretical analysis necessarily involves a boundary layer calculation for the system as a function of time. Because of the various types of flow generated in a shock tube system, the several boundary layer problems can be considered separately. In the shock heated region the boundary layer history is analogous to the boundary layer growth behind a moving normal shock passing over a stationary flat plate in air initially at rest. This type of boundary layer has been considered by Mirels[2-3] for an ideal gas with $\gamma = 1.4$. Mirels also considered the contributions to the attenuation of the other boundary layer in the system, namely, the driver gas boundary layer[4]. In Mirels analysis, which extends up to shock strengths of six, it was shown that the driver gas contribution to attenuation decreases with increasing shock strength and is very small at shock strengths of Mach 6. This point can be made from a physical argument because the wave geometry is such, that it is increasingly more difficult for waves created in the driver gas to catch up with the incident shock. Also, the driver gas requirements are such that the acoustic impedance at the interface becomes more mismatched and consequently waves will not be transmitted efficiently from the driver to the driven gas. It appears reasonable therefore to restrict our considerations to the shock heated air region only. Experimental evidence to be discussed later supports this view as well.

The analytical approach of Mirels to the attenuation problem[4] is to use the solutions for the boundary layer problem[2-3] to evaluate the vertical or in-flow* velocity at the edge of the boundary layer. This information is used in the form of sink terms as boundary conditions in a one-dimensional characteristic calculation for a constant area, isentropic channel flow. Although this solution appears to be among the best analytical treatments of the subject of attenuation, there are several points which must be raised in connection with its use in the present problem. Obviously the use of ideal gas relationships is erroneous at the shock velocities of interest, i.e., above six times the speed of sound. Secondly, the boundary layer thickness cannot be neglected for all conditions, in fact, in some shock tube applications this may be one of the dominant effects in determining useful flow times[12] It may be possible that the method of Mirels can be extended to include this effect by introducing a term to represent the effective area change into the characteristic equations. This term is essentially the displacement thickness of the boundary layer. Thirdly, experimental work in turbulent boundary layers under the high degree of wall cooling indicates that the reference temperature method employed by Mirels is not representative of the situation[7].

Recognizing the shortcomings of the analysis we will nevertheless compare the calculated attenuation to the experimental data. Such a comparison is made in Fig. 2 In using the Mirels analysis, the flow conditions from real gas calculations[13] are used. This implies the belief that the functional presentation of the analysis will not be greatly altered by the real gas properties and consequently some improvement is derived from the use of the proper physical conditions.

In general, the amount of attenuation measured is somewhat in excess of the predicted magnitudes. This comparison is dependent on an assumption about the shock velocity history near the diaphragm. For a number of tube diameters downstream of the diaphragm, the shock wave is still in the formative stage, and it is actually accelerating under many conditions. The attenuating mechanism is a second order effect in these cases and consequently the analysis cannot be expected to yield meaningful results. In order to cope with this difficulty several different assumptions can be tried. One approach would be to extrapolate the monatomic portion of the shock velocity history back to the diaphragm. Another method would be to use only the monatomic attenuation curve as the effective shock tube length and locate a new origin or effective diaphragm location at some point. A third method would involve theoretically predicting the shock strength at the diaphragm from the driver gas conditions, using empirical corrections if necessary. Finally, it may be possible to add the two effects, i.e., the formation of the shock wave and the dissipation of the gas energy, in a more complex analysis.

In comparing the predicted and measured velocity histories, the boundary layer in the shock heated gases is assumed to be turbulent. This assumption has recently received some attention from several investigators[14-15].

*The mass flow is always into the boundary layer in the cases considered because for strong shocks in the shock tube the displacement thickness of the boundary layer is negative.

Another analytical approach is worth mentioning. An inverse method was attempted, i.e., starting with a shock wave of a given amount of attenuation. The flow conditions in the domain of dependence can be calculated from a characteristic calculation which can be modified to include the real gas effects. The results from this approach were in disagreement with the observed facts because the pressure calculated at a given station fell by a factor of two or more during the test time. This pressure has been observed to remain essentially constant (see Fig. 5).

Reflection about the implied significance of this calculation yields the fact that the method implies that all the attenuation is caused by the driver gases. In the hot, shock compressed gas region the waves merely interact conservatively and no loss mechanism is provided by this type of analysis. Consequently, the expansion waves*, particularly in that part of the test gas which is near the interface, must be stronger in this calculation than in a case where additional expansions are created by the losses to the walls. The comparison is made for the same attenuation, i.e., the expansion waves arrive at the shock wave with the same strength. This qualitative explanation accounts at the shock wave with the same strength. This qualitative explanation accounts for the trend of the calculations, and a more complete model would modify the result in the direction toward better agreement with the experimental evidence.

The inverse method could be improved by including the effects of channel area change. If the channel area were varied at every point in space and time in accordance with the calculated boundary layer displacement thickness, the interactions would be more properly accounted for. This is an extremely tedious calculation and has not been performed.

EXPERIMENTS

Because of the difficulties encountered with the theoretical analysis of attenuation, it was decided to attempt an experimental approach. It was hoped that this investigation would serve to specify limits of applicability of data collected under non-ideal shock tube conditions. Basically, the program consisted of making sufficient quantitative measurements so that the state of the gas was determined at each point in space and time, regardless of the shock velocity measurement. The measurements chosen for this purpose were pressure and density, from piezo-electric transducers and X-ray absorption, respectively. The two simultaneous measurements used in conjunction with the equilibrium properties of air, specify the conditions existing in the shock tube flow.

Quantitative measurements in the hot gas flow required some attention to the state of the art of these measurements. For pressure measurements, piezo-electrics have commonly been employed in shock tubes. Commercially produced instruments are available, but they have limited frequency response. Amont the most successful instruments appears to be the SLM transducer, marketed by the Kistler Instrument Corporation, which has a

*Expansion waves in the hot, shock compressed gases cause attenuation of the shock strength.

natural frequency of 40 kc. However, for many applications it has been found relatively easy to produce simple pressure transducers in the laboratory which equal or out-perform the more costly commercial gages. Frequency response of about 5 μsec and ringing oscillations reduced to $\pm$ 10% have been achieved without great difficulty. The output of such a gage is shown in Fig. 6. Other typical side-wall pressure histories behind the moving shock wave were shown in Fig. 5. These data were taken with the SLM pressure gages.

Calibration of piezo-electric transducers can be accomplished in several ways. Static calibrations appear to be sensitive to the atmospheric conditions because the leak rate of the charge of the piezo-electric elements is affected by moisture. With care, this calibration can be made quite reliable. Dynamic calibrations have been obtained by performing shock tube experiments at high pressures and low shock strengths ($M_s \approx 2.0$). Almost ideal operation can be obtained under these conditions and consequently the response of the pressure gages serves as a good calibration. The two types of calibration agreed within the accuracy to which the records can be read (about 5%).

The detailed pressure variations behind a specific attenuating incident shock wave are shown in Fig. 7 as indicated by both the SLM and ARL transducers. The data from this experiment will be considered in detail in a later section. Comparing the output from the two gages shown in Fig. 7, it appears that except for the first few oscillations the data agrees well. It should be pointed out that the SLM gage output was filtered by as much as 3 db at 100 kc to remove a bad initial oscillation. The homemade ARL gage output is shown from a two megacycle wide band amplifier.

Density measurements were made by the X-ray absorption technique. This method was chosen in preference over interferometry because of the uncertainties in the properties of high temperature gases, such as the index of refraction. The intense emitted radiation from the high temperature air region[8] also complicates interforometric technique by requiring more intense light sources than presently available. X-rays have been used for density measurements in shock tubes at Los Alamos[21] and Harvard[22]. The technique usually requires the addition of a heavy, noble gas to air to increase the absorption to levels which can be measured with reasonable accuracy at commonly encountered shock tube conditions. At the Avco Research Laboratory, Camac has been developing the X-ray technique for use in pure air. The exponential exponent in the laws governing the absorption of X-rays varies strongly with the characteristic wave length of the X-rays. Consequently, different X-ray sources can be employed to measure density at different pressure levels. A large selection of the anode material of X-ray tubes is not commercially available. To cover the range of experiments under consideration a new anode X-ray tube is under development. The combination of copper (commercially available) and aluminum anodes allows experiments to be performed over a density range of 100 at approximately the ideal degree of absorption (30%).

In this experiment the anode X-ray tube emits a narrow beam of X-rays across a two-dimensional (square) shock tube. On the opposite side of the tube, the X-ray beam is incident on a scintillation detector. The number of X-rays reaching the detector will be a function of the interposed particle density. The output of the detector can be observed by a photomultiplier. A typical oscillogram from the photomultiplier output is shown in the lower part of Fig. 7. In order to maximize the measuring accuracy the oscilloscope base line (or 100% transmission)is driven off scale by a high frequency square wave of calibrated voltage. The base line, right after the start of the oscilloscope trace, represents the absorption of X-rays by the initial air pressure. The discontinuity after 150 μ sec shows the arrival of the shock wave at the X-ray beam and the continuation of the signal after than time gives the density history of the shock heated gases. In this oscillogram the density jump represents a change in absorption of about 20%.

Most of the measurements were made in a 1-1/2" diameter shock tube, approximately 18 feet long. At the downstream end of the tube the cross section was changed from round to square by a slow, constant area transition section about a foot long. The X-ray equipment was mounted in the square section, several feet downstream of the transition. Previous schlieren studies indicated that the transition does not introduce any measurable disturbances.

The range of initial pressures of 40 cm of Hg to 1 cm of Hg was investigated. In each experiment, shock velocity history, pressure and density data were recorded. (Density data was obtained in the pressure range of 10-40 cm only because the aluminum anode X-ray tube development was not completed at this time). The shock velocity varied with pressure level as the driver conditions were maintained approximately constant (2000 psi, $O_2 - H_2$ with 75% He dilution). The shock velocities are representative of the high velocity range accessible by the chemical drivers, see Fig. 1.

RESULTS

Other investigations[23] have found the static pressure to be essentially constant at a given station in a shock tube even behind attenuating shock waves. Closer investigation indicates this to be a good approximation over a considerable range of conditions. Figure 5 showed the static pressure history behind the moving normal shocks for several pressure levels and Mach numbers. The maximum deviation from constant pressure measured in the shock compressed gas region is about 10%. (Half the theoretical testing time, τ, calculated from the Mach number at the pressure gage, is a rule of thumb for the proper testing time[6].)

As postulated by the analytical considerations of Mirels described in the previous section, the shock compressed gas should behave isentropically except in the boundary layer. In the analysis difficulties arose from the uncertainties in writing the continuity equation for this isentropic flow because both the mass and the channel area were changing. Once the static pressure has been determined at a desired station, however, one can follow the particle history by expanding isentropically from the point at which a particle traversed the incident normal shock to the measured pressure at the downstream station.

In other words, with one direct, quantitative measurement of a property of the state, i.e., the pressure, in addition to the usually measured velocity history of the incident shock wave, the state of the isentropic or inviscid part of the shock tube flow can be determined.

Because of the lack of accuracy of shock tube pressure measurements, another property of the shock compressed gas, the density, was measured. This additional measurement overspecifies the gas state and serves as a convenient check. From the two previously described measurements, the density variation could have been determined. Of course, the converse also is true, i.e., the pressure can be determined from the density measurements together with the shock velocity history in an analogous manner. In a typical experiment, if we assume that a constant pressure was measured, then a "particle isentropic" flow will require that the density be falling with time. This is, of course, exactly as was measured by the X-ray technique, as shown in Fig. 7.

The accuracy to which the above description is followed can be judged from a specific example in which the simultaneous measurements were made. The two pressure measurements and the X-ray oscillogram, described in the previous section and shown in Fig. 7, represent such a set of data. In addition the incident shock wave velocity variation, shown in Fig. 8, was measured in this experiment. For this analysis, the Mollier diagram, Fig. 9, is helpful and instructive. Line A-B represents the locus of conditions that the successive particles in the shock tube attained as they passed through the incident normal shock. As discussed previously about one half of the shock compressed gas is lost due to interface mixing. This reduces the usuable test gas to the particles which passed through shock waves of the strength lying between points A and C. At a point of interest in the shock tube, in this case, the point A, the pressure and density histories shown in Fig. 7 were measured. These oscillograms are reduced to pressure and density in Fig. 10. These pressures locate points on the Mollier Diagram if the particles and consequently their entropy levels can be identified. This can be accomplished by iteration, starting with the density at the value represented by point A. Repeating this process at small intervals of time, the points which comprise line A-D are found. The conditions represented by these points are the consecutive states of the shock heated gases as they pass point A in the shock tube, where the density and pressures were measured. Analogously the density variations measured by the X-ray instrumentation can be used to construct line A-D'. The agreement between lines A-D and A-D' indicates the degree of uncertainty in these measurements.

After conditions have been determined in this manner, they can be used to calculate the resultant effects on other physical measurements. Ideally, the pressure and density should be measured in every experiment and the analysis outlined in the previous paragraphs followed. A much simplified approximation consists of using the facts that the static pressure measurements indicate approximately constant values, and that the more detailed measurements and analysis confirm this fact to be consistent with other independent information. In the approximate calculation the pressure is assumed to be constant and the properties are calculated from the particle isentropic assumption. In this way general results can be established and effects can be evaluated without detailed measurements.

The results of this type of calculation for several diverse but typical shock tube operating conditions are shown in Figs. 11 and 12. The time scale is plotted in terms of the shock velocity at which the particle traversed the normal shock wave, making the curves independent of velocity history. The velocity history of the shock is the only measurement required to apply the curves to a given situation. The velocity history over the latter half of the shock tube only is significant due to the loss of testing time due to mixing (again assumed to be 1/2 of test time, τ). The general character of the curves is the same for all the conditions investigated. The density ratio ρ_2/ρ_1 decreases while the temperature and velocity ratios increase with time (or distance) behind the normal shock. Under the restrictions which have generally been practiced at the Avco Research Laboratory (10% attenuation allowable at high shock velocities and 20% attenuation at low shock velocities) these changes can be as large as 10%.

The effects of these changes in the flow conditions on a few physical measurements will now be considered. The laminar heat transfer at the stagnation point of a blunt body can be shown to be approximately proportional to the stagnation enthalpy, the stagnation pressure to the three-quarter power, and the stagnation density to the minus one-quarter power[6][19]. This product has been calculated with the results shown in Figs. 11 and 12. The affect of attenuation is shown to be an upward trend in the heat transfer amounting to as much as 20% under the stated conditions. For turbulent heat transfer measurements, the rates can be shown to be proportional to the stagnation enthalpy, the density and velocity of the eight-tenth power, and the viscosity to the two-tenth power[7]. The resultant variations of this product is also shown on Figs. 11 and 12. The effect of attenuation on the turbulent heat transfer measurements is apparently somewhat smaller than it was on the laminar measurements. Some typical variations of measured heat transfer are evident from the oscillograms shown in Fig. 13*. Figure 13a shows a stagnation point heat transfer record while Fig. 13b is an oscillogram from a turbulent heat transfer experiment. The upward trend of both measurements are clearly shown.

It was shown in Ref (8) that the emitted radiation from air in the region of 6000°K and approximately normal sea level density varies approximately as the tenth power of the temperature and the first power of the density. Consequently one would expect a variation of the emitted radiation both along the length of a shock tube, and with time at a given station along the shock tube. Such variations in radiation have been observed with photomultipliers. Figure 14 is an oscillogram showing the output from a number of slits along the aft portion of the length of a shock tube, all fed into a single photomultiplier. The radiation at each station can be seen to increase with time whereas at successive stations along the length of the tube the initial radiation decreases with distance. No attempt has been made to obtain exact quantitative results from this data. The variations of the flow conditions shown in Fig. 11 predict a 75 to 100 percent increase in the radioactive intensity over the testing time, $\tau/2$. The data indicates this effect quite clearly.

*The oscillograms are from calorimeter heat transfer gages and consequently the instantaneous heat transfer rate is directly proportional to the local slope.

In many physical gas dynamic measurements the results are extremely dependent on the temperature history that a fluid particle experiences. The ideal shock tube assumptions can lead to misleading results, particularly when the data is extrapolated to other conditions. One example of a measurement which displays this sensitivity is the determination of the mechanics of the approach to thermodynamic equilibrium behind a normal shock wave. This commonly referred to relaxation process may involve one or several processes, such as the equilibration of vibrational energy or the adjustment of the dissociation and recombination rates to produce a steady state. Some of these processes have exponential temperature dependences and consequently the small temperature changes caused by attenuation may represent much larger effects in the measurement, say the relaxation time of the dissociation or recombination of the oxygen molecules or atoms in the air. In the experiments reported by Camac[9], the relaxation data was correlated by following the particle as it expanded isentropically from station to station along the length of the shock tube. The variation of the measurement at a particular shock tube station, in some cases, appeared to be quite different from the anticipated exponential process. After proper consideration of the temperature variation due to attenuation the data and theory were brought into agreement. A sample oscillogram of the relaxation of the dissociation process of the oxygen molecule in an oxygen-argon mixture is shown in Fig. 15. The initial level portion of the relaxation process was identified as the intermediate steps of relaxations from higher temperatures.

Many other shock tube measurements can be considered and the effect of the non-ideal behavior of the shock compressed gases can be evaluated. As an example of the effects of incident shock wave attenuation on the inviscid flow about bodies in the shock tube, the shock detachment distance at the stagnation point was considered. No completely satisfactory explanations for this distance are available, but the trends are well agreed upon by all the theories. Van Dyke has published numerical results[24] calculated for an ideal gas, i.e., $\gamma = 1.4$. One approach is to interpret these results in terms of the density ratio across the bow shock. Data taken in air under real gas conditions can then be compared to the calculated result at the same density ratio*. Hayes[25] has also considered the detachment distance and developed an expansion in terms of the density ratio. The variation of the density ratio across the normal shock due to attenuation can be calculated from the analysis of the previous sections. The variations of the detachment distance measured, as well as calculated from the above theories, are shown in Fig. 16. The data was taken by analyzing schlieren photographs taken at 50-70 μ sec. intervals, usually four pictures per shock tube experiment. Even though less than half the testing time was observed, a quantitative agreement of the trend of the data with the trend of the theories is rather good. This observation is another verification of the method of analysis proposed in this paper.

In some shock tube experiments, when the incident normal shock is reflected from the closed end of the tube, the reflected shock wave has been observed to accelerate as it travels upstream. This trend can be predicted

*Van Dyke's method is a numerical calculation claimed to be usable at other values of γ and better results should be obtainable this way.

from the condition shown in Figs. 11 and 12. The increase in temperature and velocity behind the initial incident shock are equivalent to stronger shock waves, and consequently stronger reflected shocks. The observed reflected shock velocities increase considerably more than predicted by the present method. Other mechanisms involved in this phenomena are discussed by Mark[25].

CONCLUSIONS

The problem of shock wave attenuation has been considered, particularly from the point of view of its effects on physical gas dynamic measurements which have been performed in shock tubes. An experimental approach, consisting of simultaneous measurement of pressure and density, was followed and general trends of the flow conditions were established.

The resultant effects on a number of measurements were evaluated. It was shown that heat transfer measurements have a tendency to increase with time, radiative emissivity also increases and the shock detachment distance decreases. A number of other measured anomalies such as are encountered with reflected shocks and relaxation measurements can also be explained from the proposed considerations.

REFERENCES

1. Trimpi, R.L. and Cohen, N.B., "A Theory for Predicting the Flow of Real Gases in Shock Tubes with Experimental Verification," NACA TN 3375, March 1955.

2. Mirels, Harold, "Laminar Boundary Layer Behind Shock Advancing into Stationary Fluid," NACA TN 3401, March 1955.

3. Mirels, Harold, "Boundary Layer Behind Shock or Thin Expansion Wave Moving into Stationary Fluid," NACA TN 3712, May 1956.

4. Mirels, Harold, "Attenuation in a Shock Tube due to Unsteady Boundary Layer Action," NACA TN 3278, August 1956.

5. Mirels, Harold and Braun, W. H., "Nonuniformities in Shock Tube Flow due to Unsteady Boundary Layer Action," NACA TN 4201, April 1957.

6. Rose, P. H. and Start, W. I., "Stagnation Point Heat Transfer Measurements in Dissociated Air," Jour. of Aero. Sciences, Vol. 26, No. 2, Feb. 1958.

7. Rose, P. H., Adams, M. C. and Probstein, R. F., "Turbulent Heat Transfer through a Highly Cooled Partially Dissociated Boundary Layer," Avco Research Laboratory Research Report No. 14, Jan. 1958 (submitted to Jour. of Aeronautical Sciences).

8. Keck, J.C., Kivel, B. and Wentink, T., "Emissivity of High Temperature Air," Avco Research Laboratory Research Report No. 8, April 1957.

9. Camac, M.C., Camm, J., Feldman, S., Keck, J., and Petty, C., "Chemical Relaxation in Air, Oxygen and Nitrogen," Inst. of Aeronautical Sciences Preprint No. 802, presented at 26th Annual Meeting, Jan. 1958.

10. Logan, J.G. and Treanor, C. E., "Polytropic Exponents for Air at High Temperatures," Jour. of Aero Sciences, Vol. 24, pp. 467-468, June 1957.

11. Feldman, S., "Hypersonic Gas Dynamic Charts for Equilibrium Air," Avco Research Laboratory, Jan. 1957.

12. Offenhartz, E. and Weisblatt, H., "Determination of the Time History of the Flow Field about a Blunt Body in a Shock Tube," paper presented at the 2nd Shock Tube Symposium, Palo Alto, Calif., March 1958.

13. Teare, D., "Shock Tube Calculations for High Temperature Gas Mixtures," Avco Research Laboratory Research Report 18 (to be published).

14. Emrich, R. J. and Chabai, A.J., "Transition from Laminar to Turbulent Flow in the Shock Tube Boundary Layer," paper presented at American Physical Society Division of Fluid Dynamics Meeting, Nov. 1957.

15. Martin, W.A., "An Experimental Study of the Boundary Layer behind a Moving Plane Shock Wave," UTIA Report No. 47, May 1957.

16. Bershader, D. and Allport, J., "On the Laminar Boundary Layer Induced by a Traveling Shock Wave," Princeton Univ., TR 11-22, May 1956.

17. Rott, N. and Hartunian, R., "On the Heat Transfer to the Walls of a Shock Tube," Graduate School of Aeronautical Engineering, Cornell Univ., Nov. 1955.

18. Bromberg, Robert, "Use of the Shock Tube Wall Boundary Layer in Heat Transfer Studies," Jet Propulsion, Vol. 26, No. 9, Sept. 1956.

19. Fay, J.A. and Riddell, F.R., "Theory of Stagnation Point Heat Transfer in Dissociated Air," Avco Research Laboratory Research Report No. 1, Jan. 1958 (submitted to Jour. of Aeronautical Sciences).

20. Rubesin, M.W. and Johnson, H. A., "A Critical Review of Skin Friction and Heat Transfer Solutions of the Laminar Boundary Layer of a Flat Plate, ASME Transactions, Vol. 71, No. 4, May 1949.

21. Knight, H.T. and Duff, R. E., "Flash X-ray Determination of Density Ratio in Gaseous Detonations," Los Alamos Scientific Lab., paper presented at the American Physical Society Division of Fluid Dynamics Meeting, Nov. 1957.

22. Kistiakowsky, G.B. and Kydd, P.H., "Gaseous Detonations: IX. A Study of the Reaction Zone by Gas Density Measurements," Jour of Chemical Physics, Vol. 25, No. 5, pp 824-835, Nov. 1956.

23. Jones, Jim J., "Experimental Investigation of Attenuation of Strong Shock Waves in a Shock Tube with Hydrogen and Helium as Driver Gases," NACA TN 4072, July 1957.

24. Van Dyke, Milton D., "The Supersonic Blunt Body Problem -- Review and Extension," Inst. of Aeronautical Sciences Preprint No. 801, presented at the 26th Annual Meeting, Jan. 1958.

25. Hayes, Wallace D. and Probstein, R.F., "Hypersonic Flow Theory," Academic Press, N.Y., 1958 (to be published).

26. Mark, Herman, "The Interaction of a Reflected Shock Wave with the Boundary Layer in a Shock Tube," Cornell University, AFOSR TN 57-345, June 1957.

27. Hartunian, R., Russo, A. and Marrone, P., "Boundary Layer Transition and Heat Transfer in Shock Tubes," (to be presented at 1958 Heat Transfer and Fluid Mechanics Institute, June, 1958.)

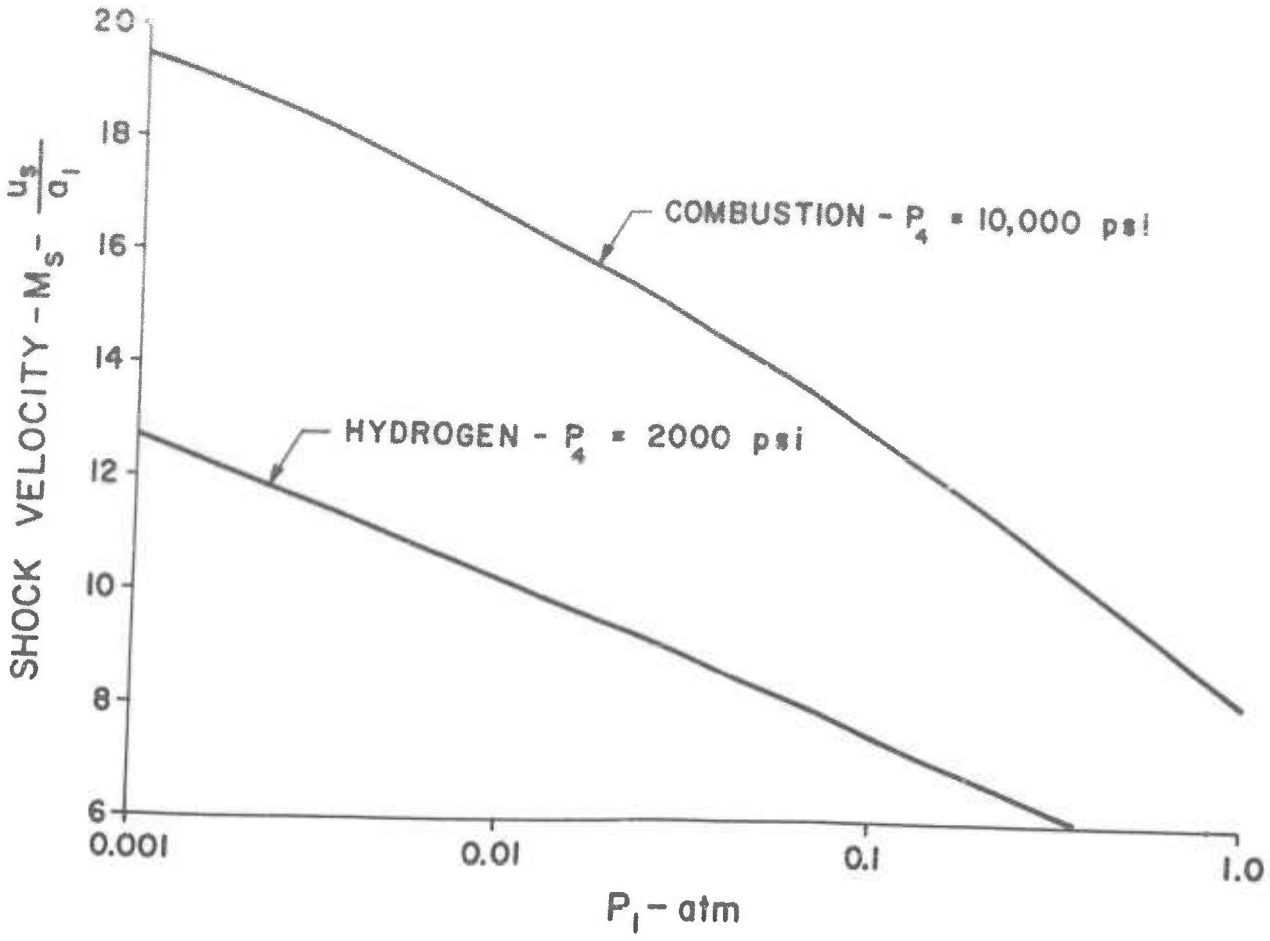

Fig. 1. Theoretical maximum shock velocity attainable within the driver's structural limitations.

SHOCK VELOCITY HISTORY

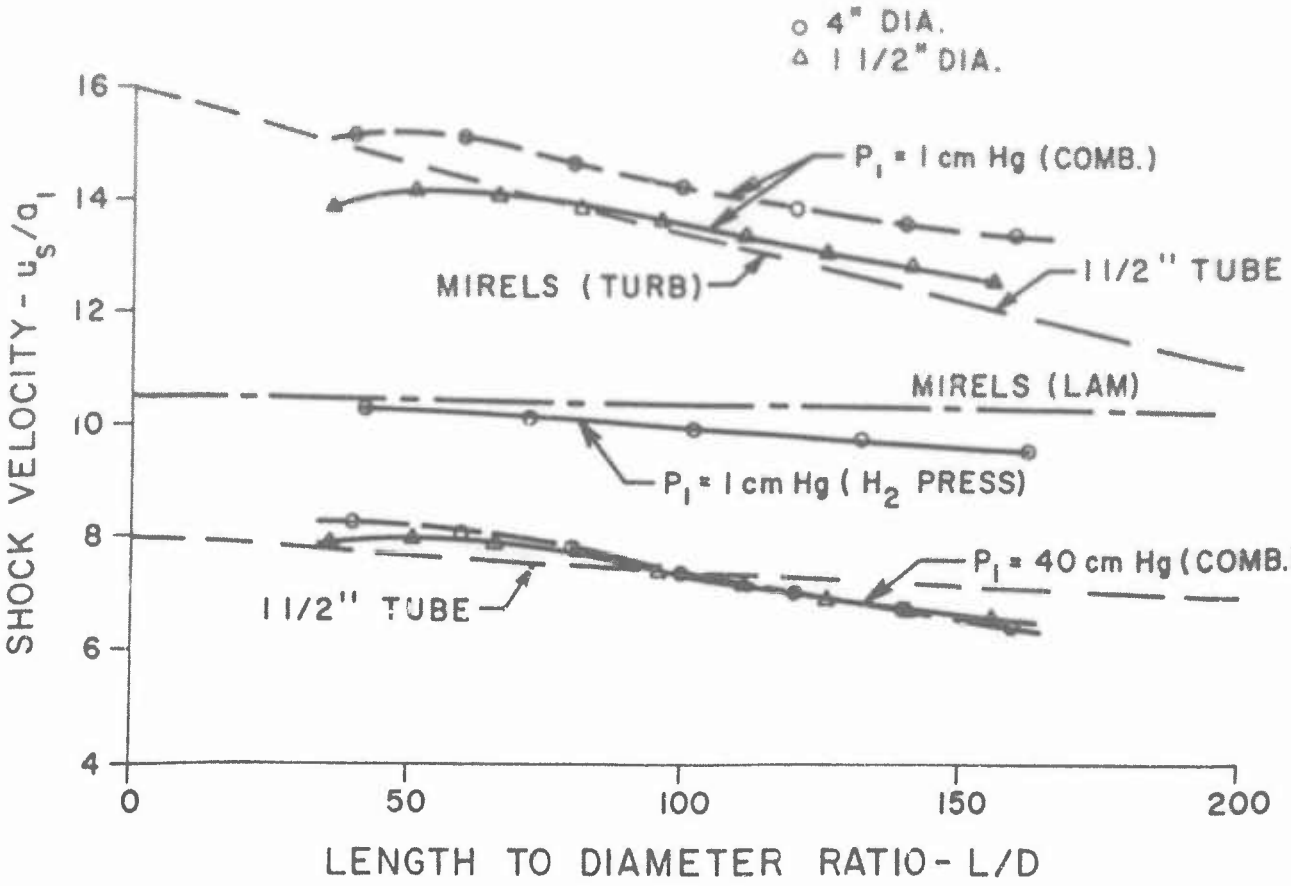

Figure 2 Effect of attenuation on shock detachment distance for a hemisphere-cylinder.

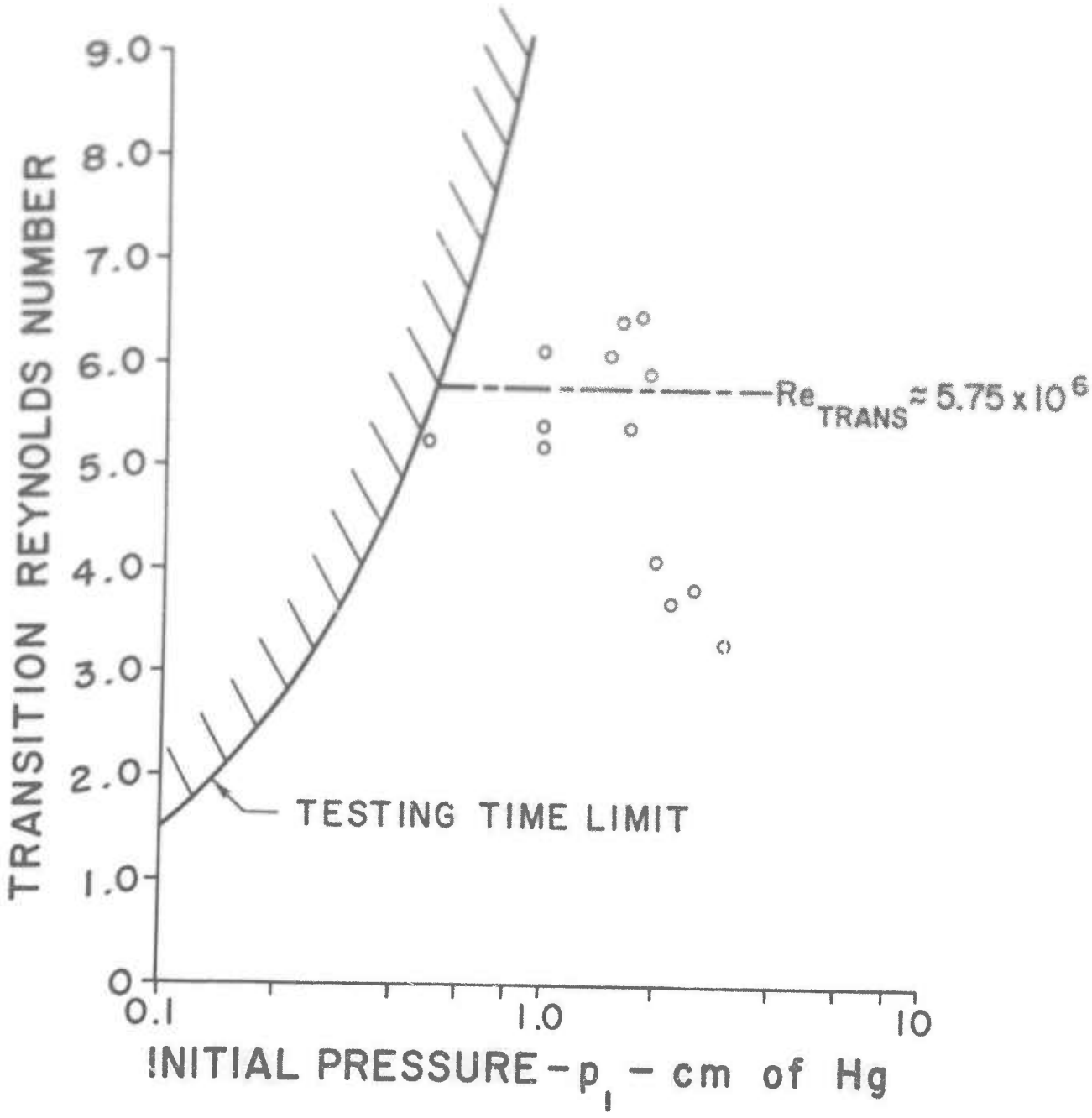

Fig. 3. Transition Reynolds number measured on the side wall of a shock tube by thin film heat transfer gages.

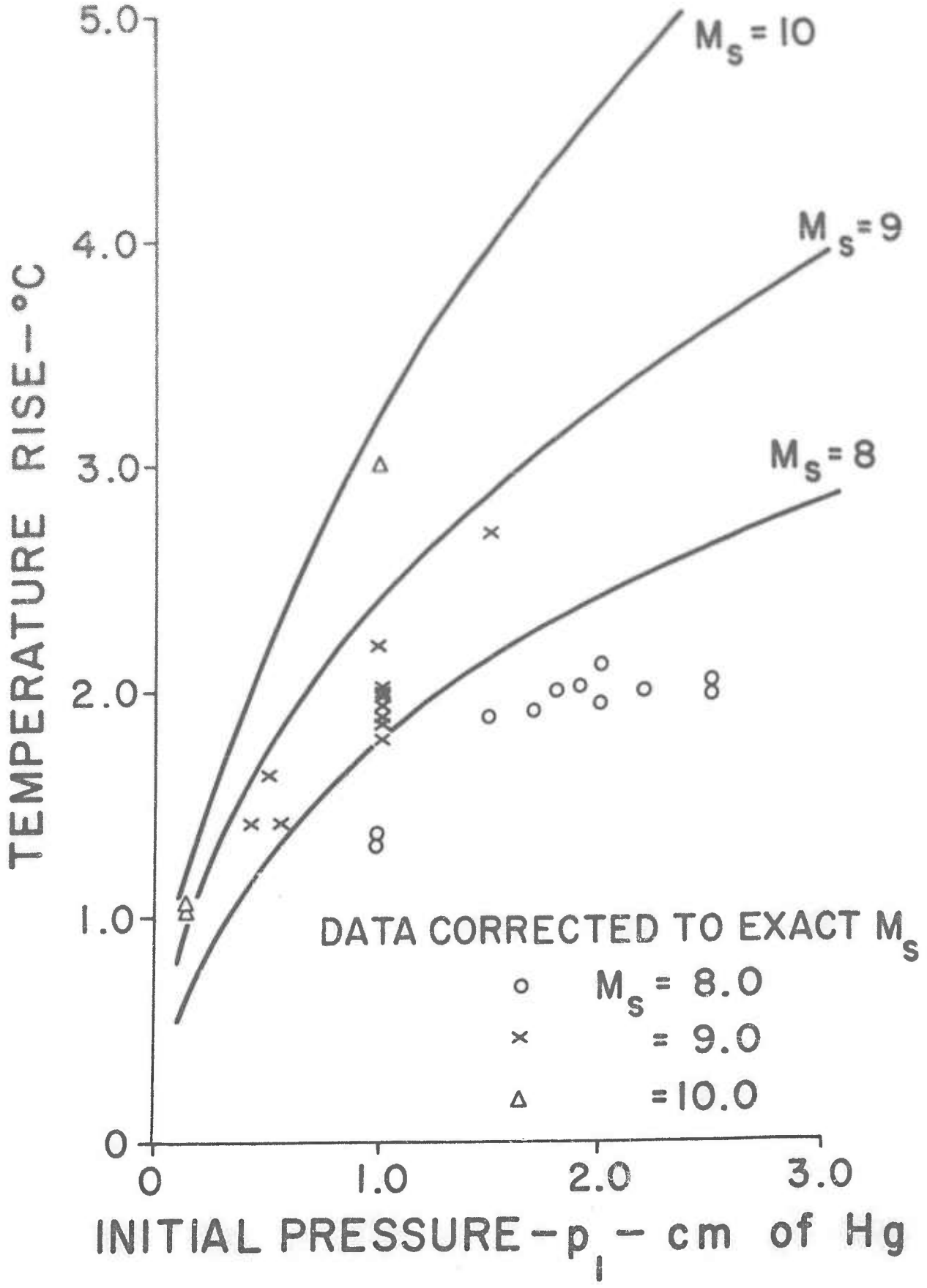

Fig. 4. Laminar boundary layer heat transfer measurements on the side wall of a square shock tube compared to theory[16].

PRESSURE HISTORIES

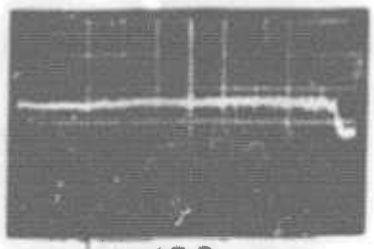

100 μsec

τ/2 = 660 μsec

P_1 = 40 cm

M_s = 7.90 → 6.50

P_2/P_1 = 76 → 50

L = 55 ft

100 μsec

τ/2 = 522 μsec

P_1 = 10 cm

M_s = 9.60 → 7.60

P_2/P_1 = 117 → 71

L = 55 ft

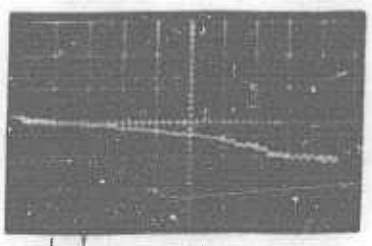

100 μsec

τ/2 = 226 μsec

P_1 = 1 cm

M_s = 14.3 → 12.0

P_2/P_1 = 267 → 184

L = 55 ft

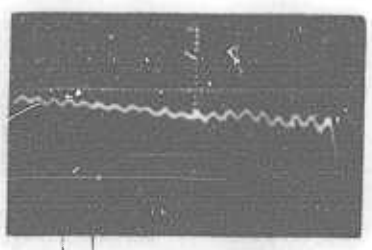

50 μsec

τ/2 = 275 μsec

P_1 = 0.5 cm

M_s = 12.5 → 10.1

P_2/P_1 = 200 → 131

L = 55 ft

Fig. 5. Typical static pressure histories behind strong moving shock waves. Attenuation is given by Mach number and corresponding pressure ratio ranges.

PRESSURE OSCILLOGRAM

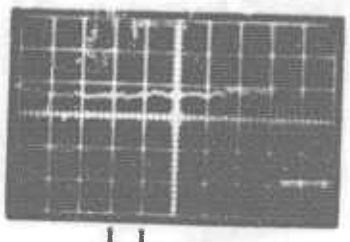

ARL TRANSDUCER

Fig. 6. Oscillogram from homemade (ARL) pressure transducers showing details of rise time and ringing.

PRESSURE AND DENSITY HISTORIES

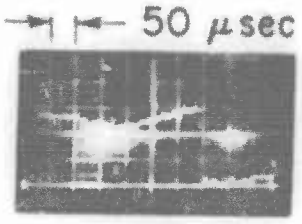

A
X-RAY
DENSITY HISTORY

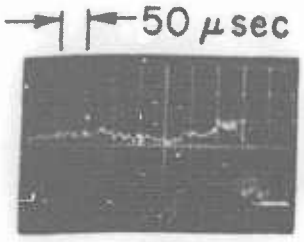

B
SLM
PRESSURE TRANSDUCERS

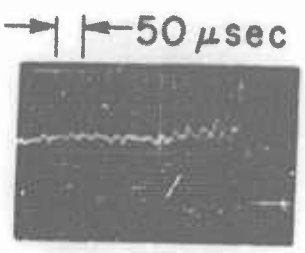

C
ARL

Fig. 7. Oscillograms from simultaneous pressure and density measurements behind an attenuating shock wave.

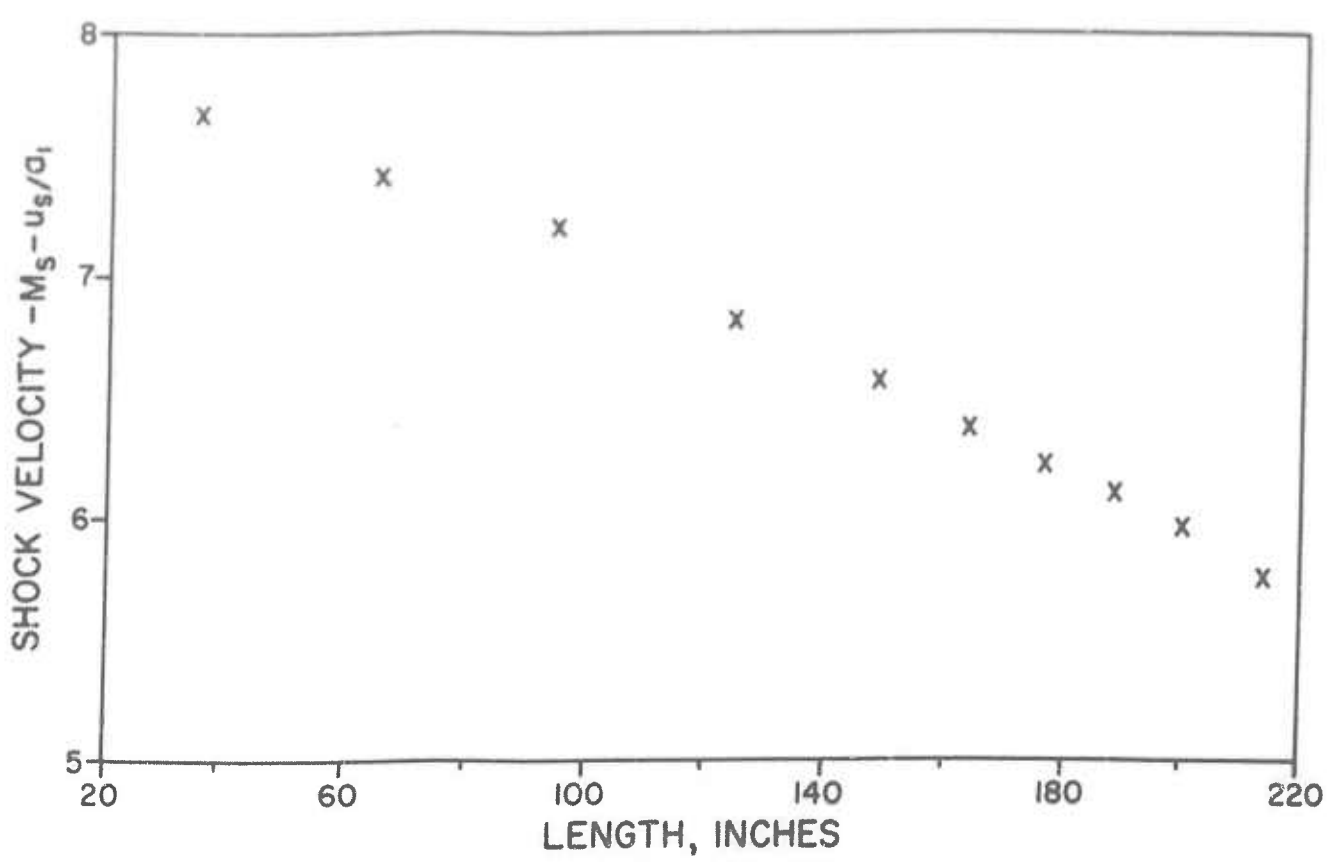

Fig. 8. Incident shock velocity history measurements for attenuating shock wave under consideration (Fig. 7).

FLOW CONDITIONS ON MOLLIER DIAGRAM

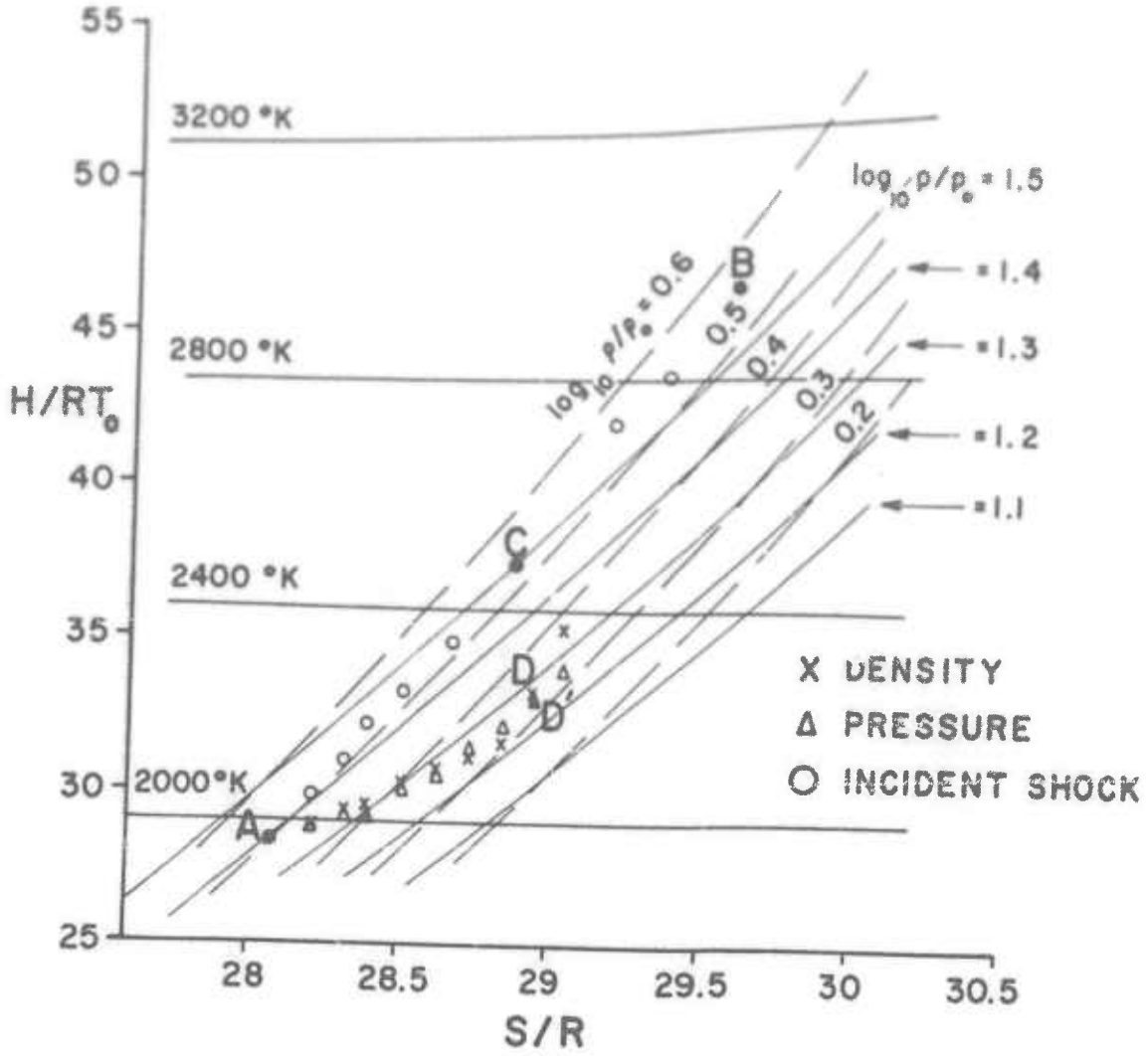

Fig. 9. Schematic Mollier diagram representation of the gas conditions with data from pressure and density measurements (Figs. 7 and 8) superimposed.

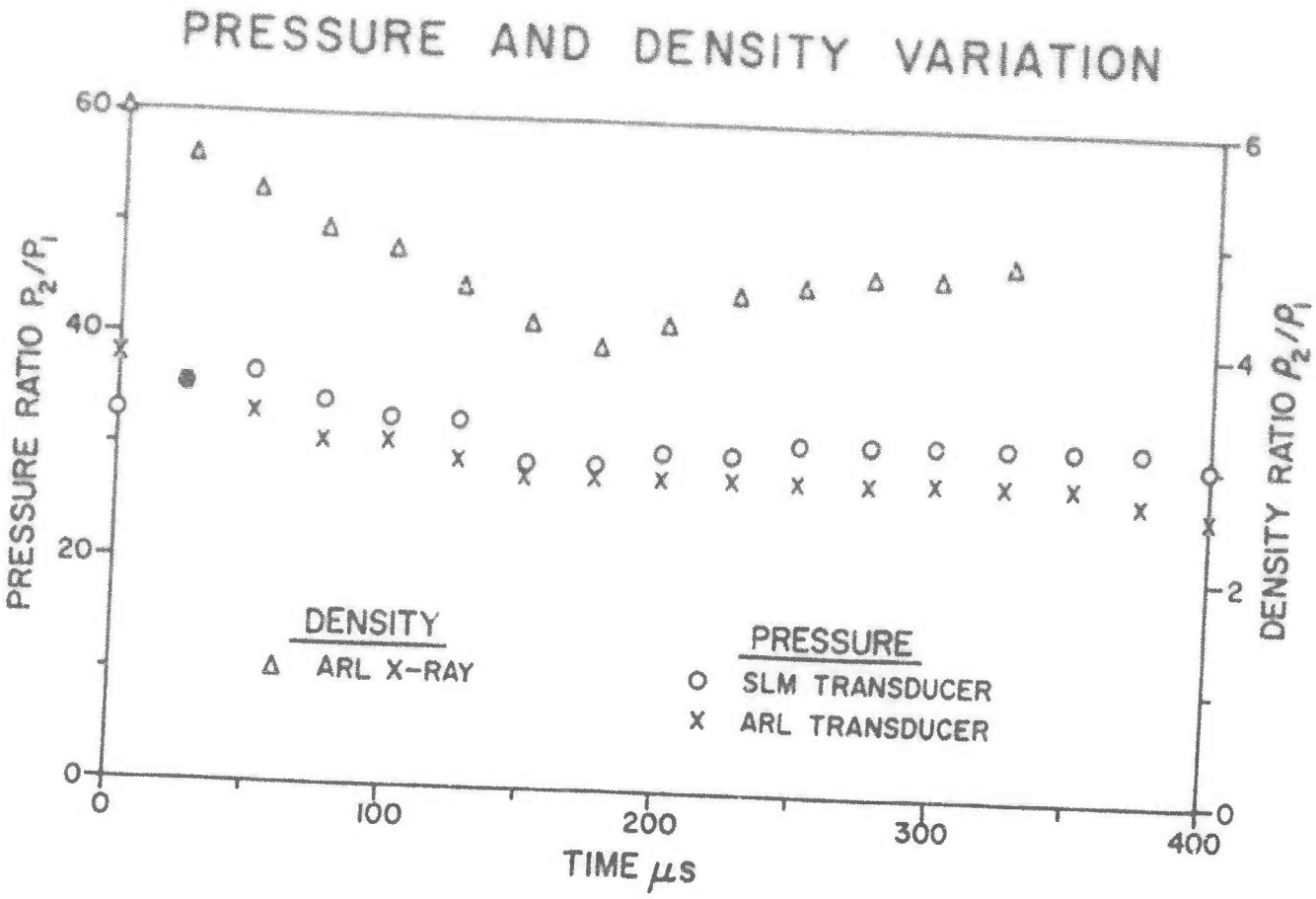

Fig. 10. Pressure and density variations from oscillograms in Fig. 7.

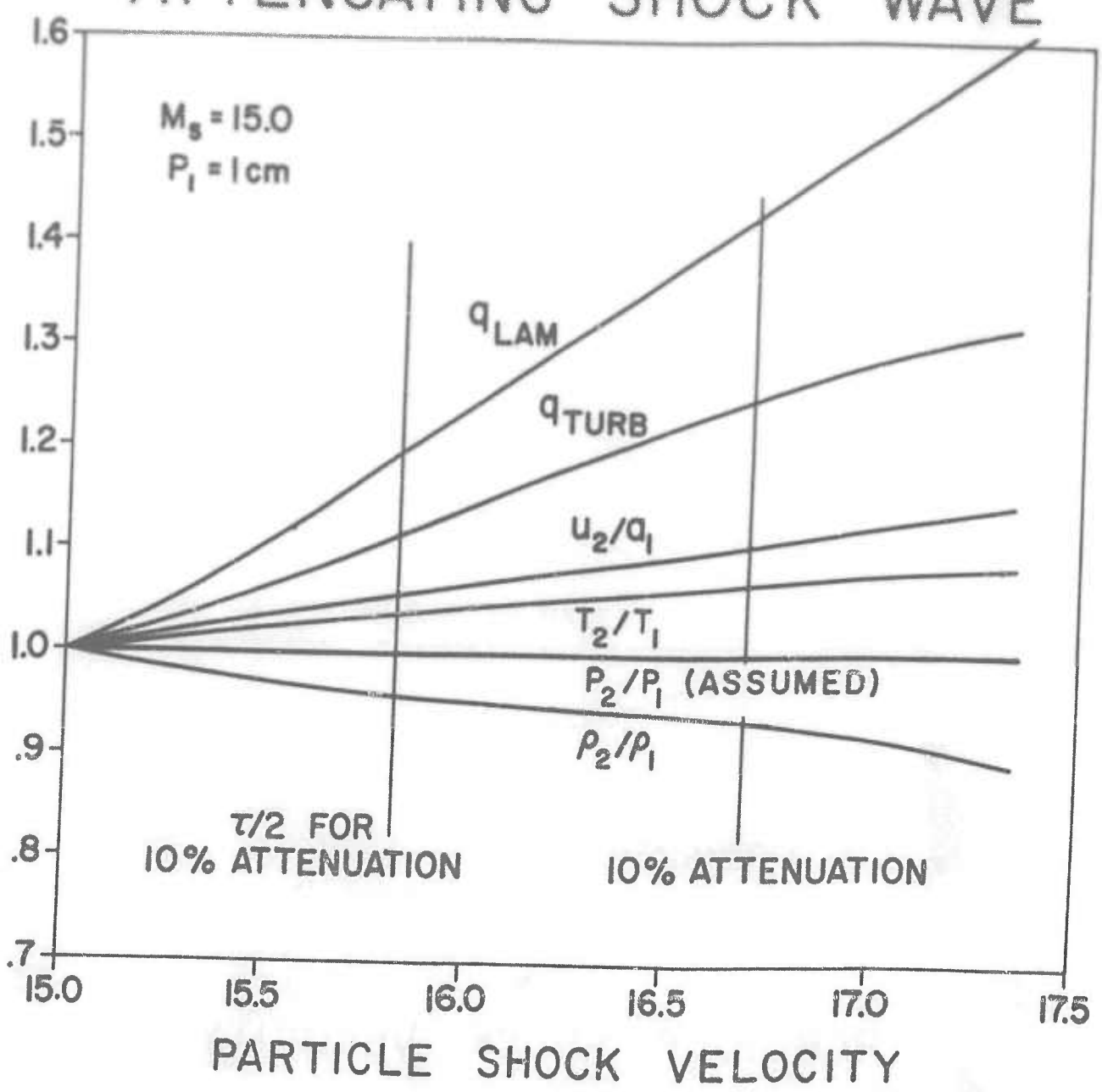

Fig. 11. Variations in the physical properties of the flow behind a typical attenuating strong shock wave at low initial density.

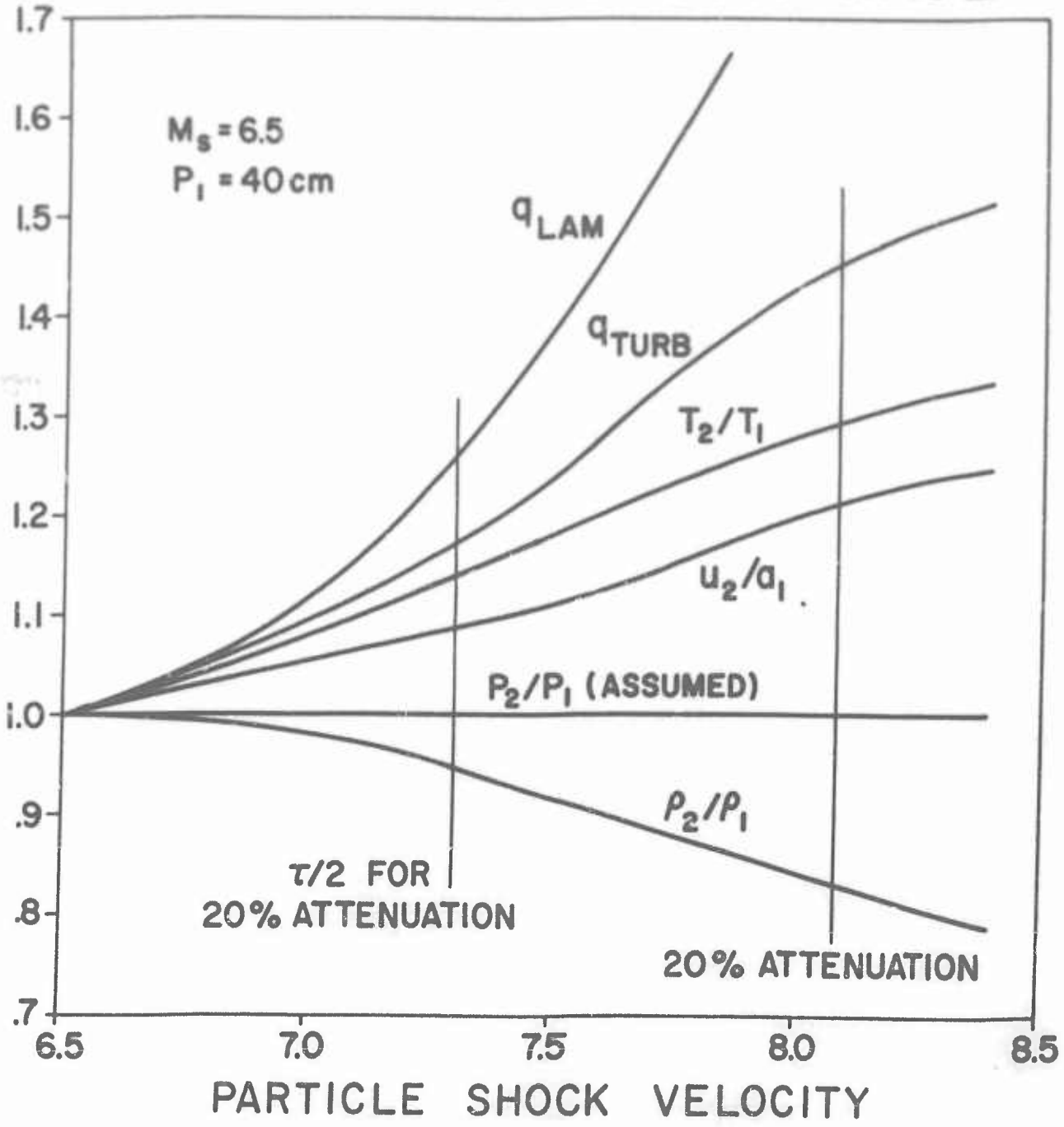

Fig. 12. Variation in the physical properties of the flow behind a typical attenuating moderate strength shock wave at high initial density.

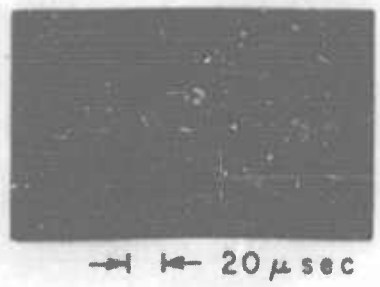

STAGNATION POINT - LAMINAR

45° ON HEMISPHERE-CYLINDER
TURBULENT ($\tau/2 \approx 600\mu$sec)

Fig. 13. Heat transfer measurements by the calorimeter technique. (A steady slope implies a constant rate). Note the rise of both the slopes with time.

RADIATION HISTORY

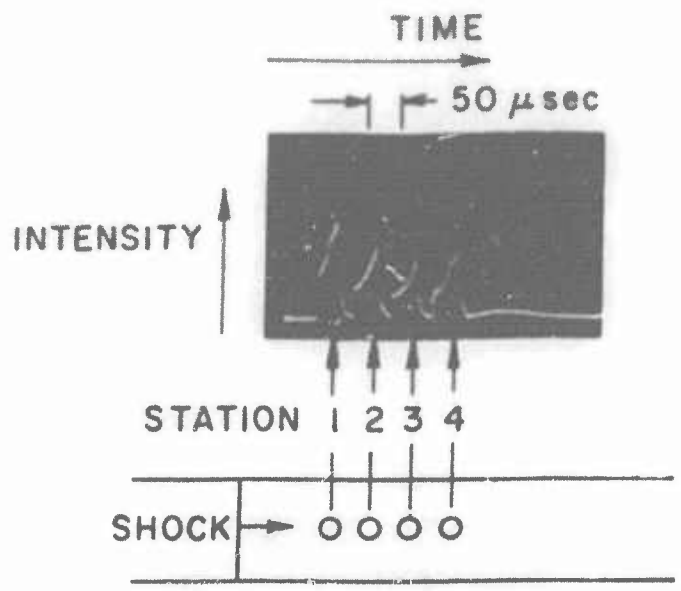

Fig. 14. Radiation from shock compressed air behind an attenuating strong shock. Slits at four stations observe the radiation history as the hot gas flows by. Note the increasing trend at each station with time but the decreasing trend from station to station.

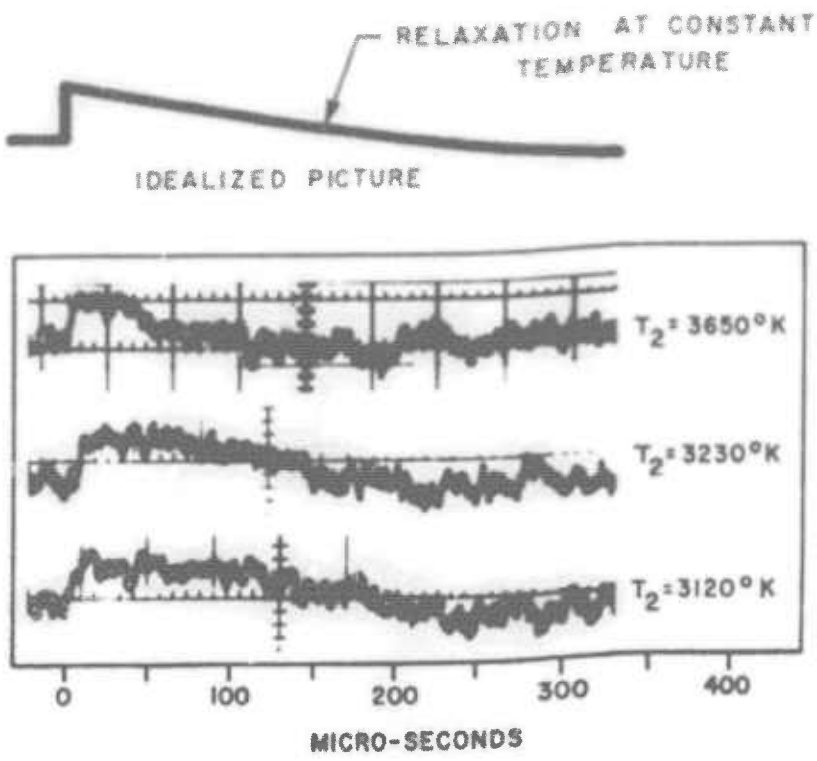

Fig. 15. Vacuum ultraviolet measurement of oxygen dissociation time in an oxygen argon mixture. Note the level portion in each picture which gets longer as the temperature decreases. This apparent "incubation time" was explained to be due to the lower temperature immediately behind the shock wave down stream due to attenuation. Effectively each particle relaxes according to its own temperature history and consequently the relaxation process is faster the further away the particle is from the incident shock wave.

UNCLASSIFIED

AD 201239

Armed Services Technical Information Agency
ARLINGTON HALL STATION
ARLINGTON 12 VIRGINIA

FOR
MICRO-CARD
CONTROL ONLY

4 OF 6

NOTICE: WHEN GOVERNMENT OR OTHER DRAWINGS, SPECIFICATIONS OR OTHER DATA ARE USED FOR ANY PURPOSE OTHER THAN IN CONNECTION WITH A DEFINITELY RELATED GOVERNMENT PROCUREMENT OPERATION, THE U. S. GOVERNMENT THEREBY INCURS NO RESPONSIBILITY, NOR ANY OBLIGATION WHATSOEVER; AND THE FACT THAT THE GOVERNMENT MAY HAVE FORMULATED, FURNISHED, OR IN ANY WAY SUPPLIED THE SAID DRAWINGS, SPECIFICATIONS, OR OTHER DATA IS NOT TO BE REGARDED BY IMPLICATION OR OTHERWISE AS IN ANY MANNER LICENSING THE HOLDER OR ANY OTHER PERSON OR CORPORATION, OR CONVEYING ANY RIGHTS OR PERMISSION TO MANUFACTURE, USE OR SELL ANY PATENTED INVENTION THAT MAY IN ANY WAY BE RELATED THERETO.

UNCLASSIFIED

SHOCK DETACHMENT DISTANCE

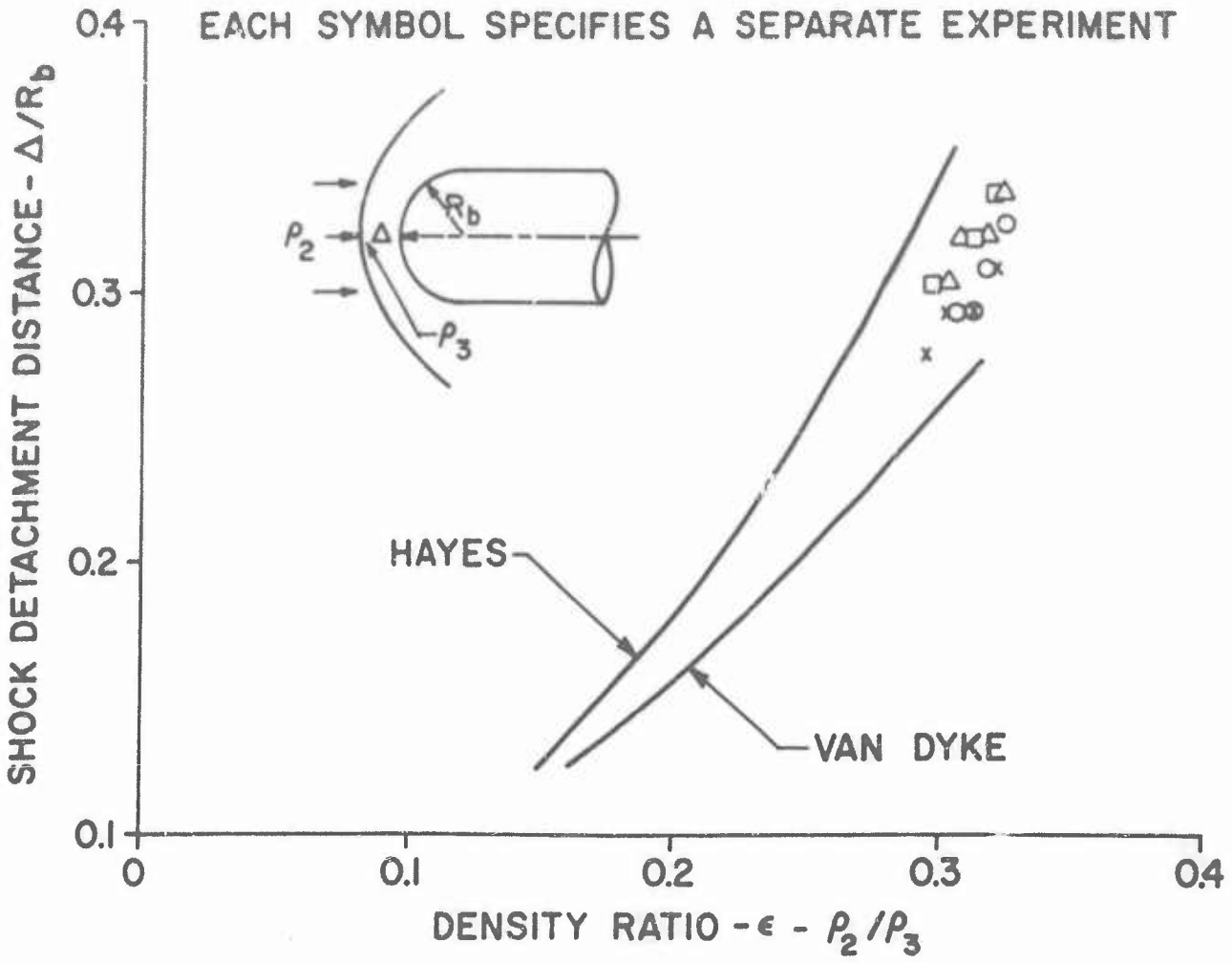

Figure 16 Shock velocity history predicted from Mirels[4] compared to typical data.

GENERATION OF PRESSURE WAVE FORMS THROUGH THE DETONATION OF EXPLOSIVE CHARGES

Dr. T. H. Schiffman, D. Anderson, G. Tzantzos
Armour Research Foundation

I. INTRODUCTION

This study investigates the general behavior of shock waves generated through the detonation of high explosive charges. The analysis in particular is concerned with one dimensional flow, that is shock waves propagating down a unit cross-sectional area channel. It is also limited to shock waves with shock front overpressures, (i.e., pressures immediately behind the shock front) of ten atmospheres or below. With these limits and restrictions it is seen that this study confines itself to shock waves which may feasibly be generated in a shock tube.

The analysis is similar to that previously made for calculating total energy yields for atomic bombs.[1,2*] However, in this case, because of the limits and restrictions placed on the study the end result is different and yields far more information. The analysis leads to shock strength-scaled distance and shock strength-scaled time decay curves, where shock strength is defined as the shock front overpressure to ambient pressure ratio. It also yields, under the assumptions made considerable insight into the behavior of the gas flow variables behind an explosive generated shock.

The laws of conservation of mass, momentum, energy governing the flow are all employed and satisfied in carrying out and completing the analysis.

With these results an approximate method is developed for generating various desired pressure pulses.

II. DISCUSSION OF THE PROBLEM

A sketch of a typical distance-time curve for a shock wave propagating from a zero origin is presented in Fig. 1. The figure shows the shock front distance R as a function of t, time, and also a typical particle position r_1 as a function of time. This figure will be referred to periodically throughout the analysis for a better understanding of the presentation.

The Space Density Distribution

The study begins with the assumption of a density distribution, namely

$$\rho(r) = \rho_s \left[\frac{r_1(t)}{R(t)}\right]^{q(t)} \qquad (1)$$

*For all numbered references see bibliography.

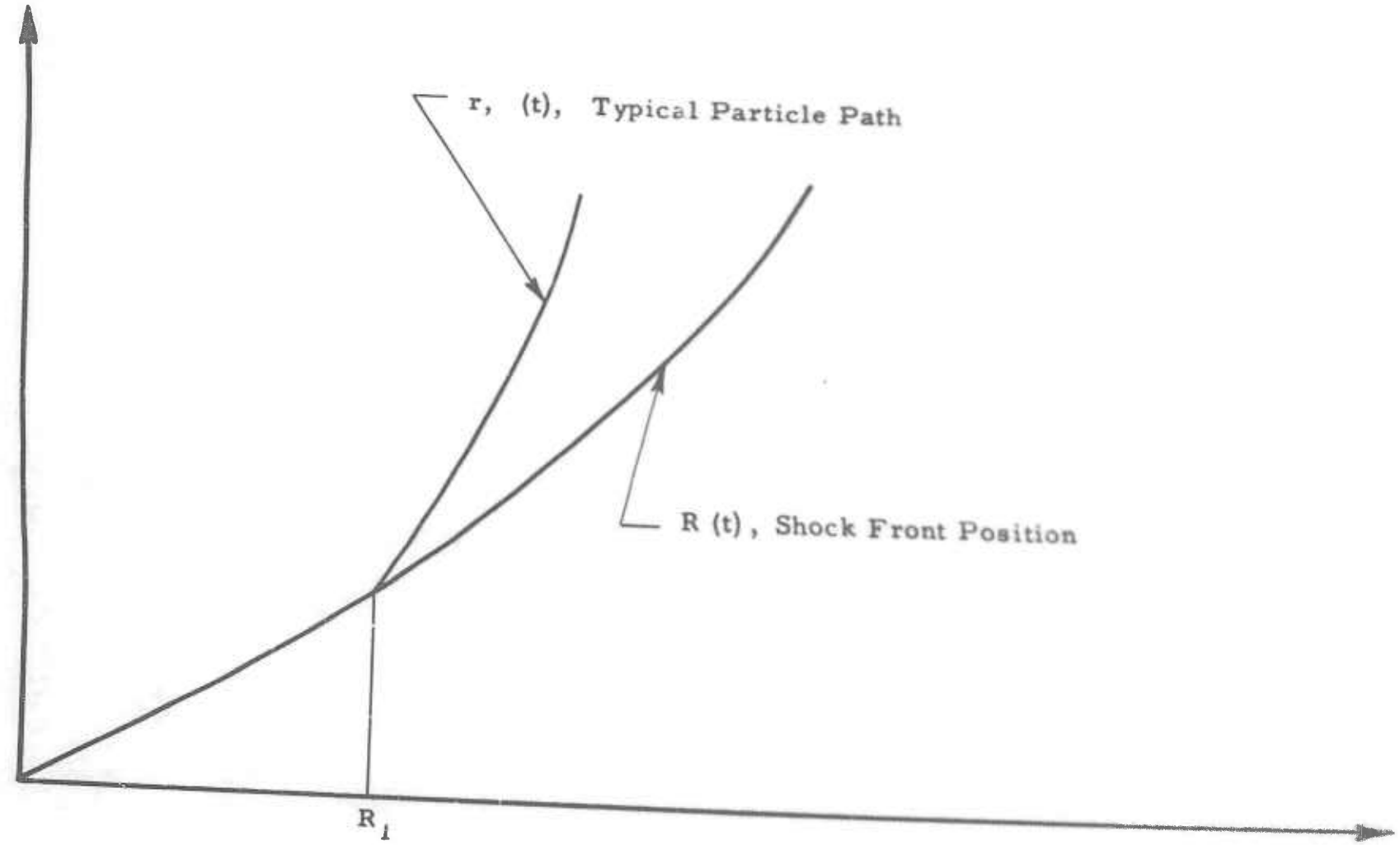

Fig. 1 Sketch of a Typical Distance Time History of a Moving Shock Wave

where ρ is the gas density behind the shock at a distance r_1 from the origin, ρ_s is the gas density at the shock front distance R, and q is a function of shock front conditions to be determined by considering conservation of mass. At a fixed time, t, Eq. 1 depicts the special density distribution behind the shock.

Justification for such an assumption on the density distribution are: (1) it is known that the density is some monotonically decreasing function with the distance behind the shock front, (2) the observed density distribution is closely approximated by this power law, and (3) it yields, as will be shown, results which are in agreement with experimentally gathered data. The fact this assumption requires that the density go to zero at the origin is in all probability its main error. However, in reality the density very nearly goes to zero at this point for shock front overpressures of two atmospheres or above. The difference is negligible. For weaker shocks the assumption is still good but not as accurate.

The value of q will now be determined by considering the conservation of mass law from the origin out to the shock front distance R. This states

$$\int_0^R \rho \, dr = \rho_0 R$$

for a constant time, where ρ_0 is the ambient gas density. Substituting the value of ρ from Eq. 1 into the above integral and integrating results in

$$\frac{\rho_s R}{q+1} = \rho_0 R$$

Solving this equation for q gives

$$q = \frac{\rho_s}{\rho_0} - 1 = \eta_s - 1 \qquad (2)$$

where η_s is the ratio of densities across the shock front.

Space Particle Velocity Distribution

Conservation of mass is again employed, but this time the mass from the origin to a particular particle path is considered (see particle path $r_1(t)$ in Fig. 1). This gives the integral equation

$$\int_0^{r_1} \rho \, dr = \rho_0 R_1$$

where R_1 is the particle distance before the shock engulfs it. Using Eq. 1 and integrating gives

$$\frac{\rho_s (\frac{r}{R})^q r_1}{q+1} = \frac{\rho r_1}{q+1} = \rho_o R_1$$

where Eq. 1 is again used after integration.

Next the substantial derivative,

$$\frac{D}{Dt} = \frac{\partial}{\partial t} + u \frac{\partial}{\partial r}$$

where u is the particle velocity and is equal to dr/dt, of the above integration result is formed. This gives after simplification

$$\frac{D\rho}{Dt} + \frac{\rho u}{r} - \frac{\rho}{q+1} \frac{d(q+1)}{dt} = 0$$

The one dimensional conservation of mass equation

$$\frac{D\rho}{Dt} + \rho \frac{\partial u}{\partial r} = 0$$

is combined with the above equation to give

$$\frac{\partial u}{\partial r} = \frac{u}{r} - \frac{1}{q+1} \frac{d(q+1)}{dt}$$

The solution is readily obtained with the substitution $u = ry$ and integrating with respect to r at a fixed time. The solution is

$$\frac{u}{r} = -\frac{1}{q+1} \frac{d(q+1)}{dt} \ln r + A(t)$$

where A(t) is the constant of integration which may be function of time. At the shock front the solution becomes

$$\frac{u_s}{R} = -\frac{1}{q+1} \frac{d(q+1)}{dt} \ln R + A(t)$$

where u_s is the particle velocity at the shock front. From this equation the value of A(t) is evaluated, and the final particle velocity distribution may be expressed as

$$u = u_s (\frac{r}{R}) \left[1 - \alpha (t) \ln (\frac{r}{R})\right] \qquad (3)$$

where

$$\alpha = \frac{R}{u_s} \frac{1}{q+1} \frac{d(q+1)}{dt}$$

This value of α may be simplified considerably as follows

$$\alpha = \frac{R}{u_s} \frac{1}{q+1} \frac{d(q+1)}{dt} = \frac{R}{u_s} \frac{1}{\eta_s} \frac{d\eta_s}{dR} \frac{dR}{dt}$$

$$= \frac{U}{u_s} \frac{R}{\eta_s} \frac{d\eta_s}{dR} = \frac{\eta_s}{\eta_s - 1} \cdot \frac{R}{\eta_s} \frac{d\eta_s}{dR}$$

$$= \frac{d \ln (\eta_s - 1)}{d \ln R}$$

where

$$U = \frac{dR}{dt} \text{ (shock propagation velocity)}$$

and

$$\frac{U}{u_s} = \frac{\eta_s}{\eta_s - 1}$$

from the Rankine-Hugoniot relation[6] obtained from the conservation of mass across the shock front.

Space Pressure Wave Form

The conservation of momentum equation states

$$\frac{\partial P}{\partial r} = - \rho \frac{Du}{Dt}$$

where P is the absolute pressure.

The space pressure wave form may now be found by considering the following integral at a fixed time.

$$P = \int \frac{\partial P}{\partial r} \, dr = - \int \rho \frac{Du}{Dt} \, dr$$

The quantities in the integrand on the right may be found either directly or derived from Eqs. 1 and 3.

In forming the substantial derivative Du/Dt all of the quantities appearing in the expression for particle velocity, Eq. 3, are functions of time. The derivative is thus formed and combined with the density expression to give the above integrand. The integrand contains such expressions as

$$\frac{dr}{dt}, \frac{du_s}{dt}, \frac{dR}{dt}, \text{ and } \frac{d\alpha}{dt}$$

which are all rewritten as follows.

$$\frac{dr}{dt} = u = u_s \left(\frac{r}{R}\right)\left[1 - \alpha \ln \left(\frac{r}{R}\right)\right]$$

$$\frac{dR}{dt} = U$$

$$\frac{du_s}{dt} = U \frac{du_s}{dR} = \frac{U}{R} \frac{d \ln u_s}{d \ln R}$$

$$\frac{d\alpha}{dt} = U \frac{d\alpha}{dR} = \frac{\alpha U}{R} \frac{d \ln \alpha}{d \ln R}$$

With the integrand expressed as a function of r the integration is performed and the constant of integration is evaluated at the shock front. The resulting pressure wave is

$$\frac{P(r) - P_o}{P_s(R) - P_o} = 1 - K + \left(\frac{r}{R}\right)^{\eta_s + 1}\left[K + L \ln \left(\frac{r}{R}\right) + M \left\{\ln \left(\frac{r}{R}\right)\right\}^2\right] \qquad (4)$$

where P_o is the absolute ambient pressure, and P_s is the absolute pressure immediately behind the shock front. The quantities K, L, and M are parameters dependent on shock front conditions only. Their values are

$$K = \frac{1}{\eta_s + 1}\left[1 - \left(1 + \frac{\alpha}{\eta_s + 1}\right)\eta_s \beta + \frac{\alpha}{\eta_s + 1}(1 - \eta_s \beta - 2\eta_s) + \left(\frac{\eta_s - 1}{\eta_s + 1}\alpha\right)^2\right]$$

$$L = \frac{\alpha}{\eta_s + 1}\left[\eta_s (\beta + \beta) + \frac{(\eta_s - 1)^2}{\eta_s + 1}\alpha + \eta_s - 2\right]$$

$$M = -\frac{\eta_s - 1}{\eta_s + 1}\alpha^2$$

where

$$\beta = \frac{d \ln u_s}{d \ln R}$$

and

$$\beta = \frac{d \ln \alpha}{d \ln R}$$

The Total Shock Energy Yield

The total shock energy yield, W, manifests itself in two forms: (1) the kinetic energy, E_K, given by

$$E_K = \int_o^R (1/2)\rho u^2 \, dr$$

and (2) the internal energy increment, E_I, given by

$$E_I = \int_0^R \epsilon P dr - \epsilon_o \rho_o \int_0^R dr$$

For ideal gases the internal energy is known to be a function of state only, and hence the internal energy per unit volume can be written as ϵ PV, where ϵ is at most a function of state, and not of process. Here V represents specific volume. For a stream tube of unit cross section, the specific volume is numerically equal to the length of the tube enclosing a unit mass of fluid. Hence, the above expression represents the change in total internal energy of the fluid from the origin to the shock front. It can be shown from thermodynamic considerations that $\epsilon = 1/\gamma - 1$, whether or not γ, the ratio of specific heats of the fluid, is a constant.

Over the range of pressures considered in the present analysis, γ is known to be substantially constant at the value 1.4; then $\epsilon = \epsilon_o = 5/2$.

Using the values of ρ and u given by Eqs. 1 and 3 respectively, the integral for kinetic energy may be evaluated readily. It gives

$$E_K = \frac{1}{2} \rho_s u_s^2 \frac{R}{\eta_s + 2} \left[1 + \frac{2\alpha}{\eta_s + 2} (1 + \frac{\alpha}{\eta_s + 2}\right]$$

Likewise, employing Eq. 4 the integral for the internal energy increment is found to be

$$E_I = \frac{5}{2} (P_s - P_o) R \left[1 - K + \frac{K}{\eta_s + 2} - \frac{L}{(\eta_s + 2)} 2 + \frac{2M}{(\eta_s + 2)} 3\right]$$

adding the two expressions and using the conservation of momentum across the shock front to simplify the equation results in

$$W = E_K + E_I = \frac{1}{2} (P_s - P_o) R \left[\frac{\eta_s - 1}{\eta_s + 2} \left\{1 + \frac{2\alpha}{\eta_s + 2} (1 + \frac{\alpha}{\eta_s + 2})\right\}\right.$$
$$\left. + 5 \left\{1 - K + \frac{K}{\eta_s + 2} - \frac{L}{(\eta_s + 2)} 2 + \frac{2}{(\eta_s + 2)}) 3\right\}\right] \qquad (5)$$

Equation 5, as will be shown, is a second-order differential equation. It must be revised in form in order to be solved. First the following are defined

$$\xi \text{ (shock strength)} = \frac{P_s}{P_o}$$

$$\lambda \text{ (scaled distance)} = \frac{P_o R}{W}$$

and

$$X(\xi, R) = \frac{d \ln (\xi - 1)}{d \ln R}$$

Using the first and last definitions, and employing the Rankine-Hugoniot relations between ρ, u, and P at the shock front, it is found that

$$\alpha = \frac{d \ln (\eta_s - 1)}{d \ln R} + \frac{7X}{\xi + 6}$$

$$\beta = \frac{d \ln u_s}{d \ln R} = \frac{3\xi + 4}{6\xi + 1} X$$

and

$$\phi = \frac{d \ln \alpha}{d \ln R} = \frac{d \ln X}{d \ln (\xi - 1)} - \frac{\xi - 1}{\xi + 6} X$$

Now with the help of the Rankine-Hugoniot relations again, and the above values for α, β, and ϕ, Eq. 5 becomes

$$\frac{1}{\lambda} = \frac{5(\xi - 1)}{2(8\xi + 13)} \left[(8\xi + 6) + \frac{24\xi^2 + 169\xi + 52}{8\xi + 13} X - \frac{7(24\xi^2 - 125\xi - 46)}{(8\xi + 13)^2} X^2 + \frac{7(6\xi + 1)}{8\xi + 13} X^2 \frac{d \ln X}{d \ln (\xi - 1)} \right]$$

Which is of second order and may now be broken up into two first-order equations as follows.

$$\frac{d\lambda}{d\xi} = \frac{\lambda}{X(\xi - 1)}$$

and

$$\frac{dX}{d\xi} = \frac{\frac{1}{\lambda} \frac{2(8\xi + 13)^2}{5(\xi - 1)} - (8\xi + 6)(8\xi + 13) - (24\xi^2 + 169\xi + 52) X}{7(6\xi + 1)(\xi - 1) X}$$

$$+ \frac{\frac{7(24\xi^2 = 125\xi - 46)}{8\xi + 13}}{7(6\xi + 1)(\xi - 1) X}.$$

These two differential equations were integrated numerically on the IBM 650 computer using the Bell Telephone Laboratory L1 interpretive routine and the R.C.A. Laboratory routine for the solution of differential equations.[3,4] The results of the integration are shown in Fig. 2.

Development of a Time-of-Arrival Curve

Until now the analysis has been independent of time, which has thus far appeared only as a parameter. Now, by further considerations, a shock strength-scaled time curve will be constructed.

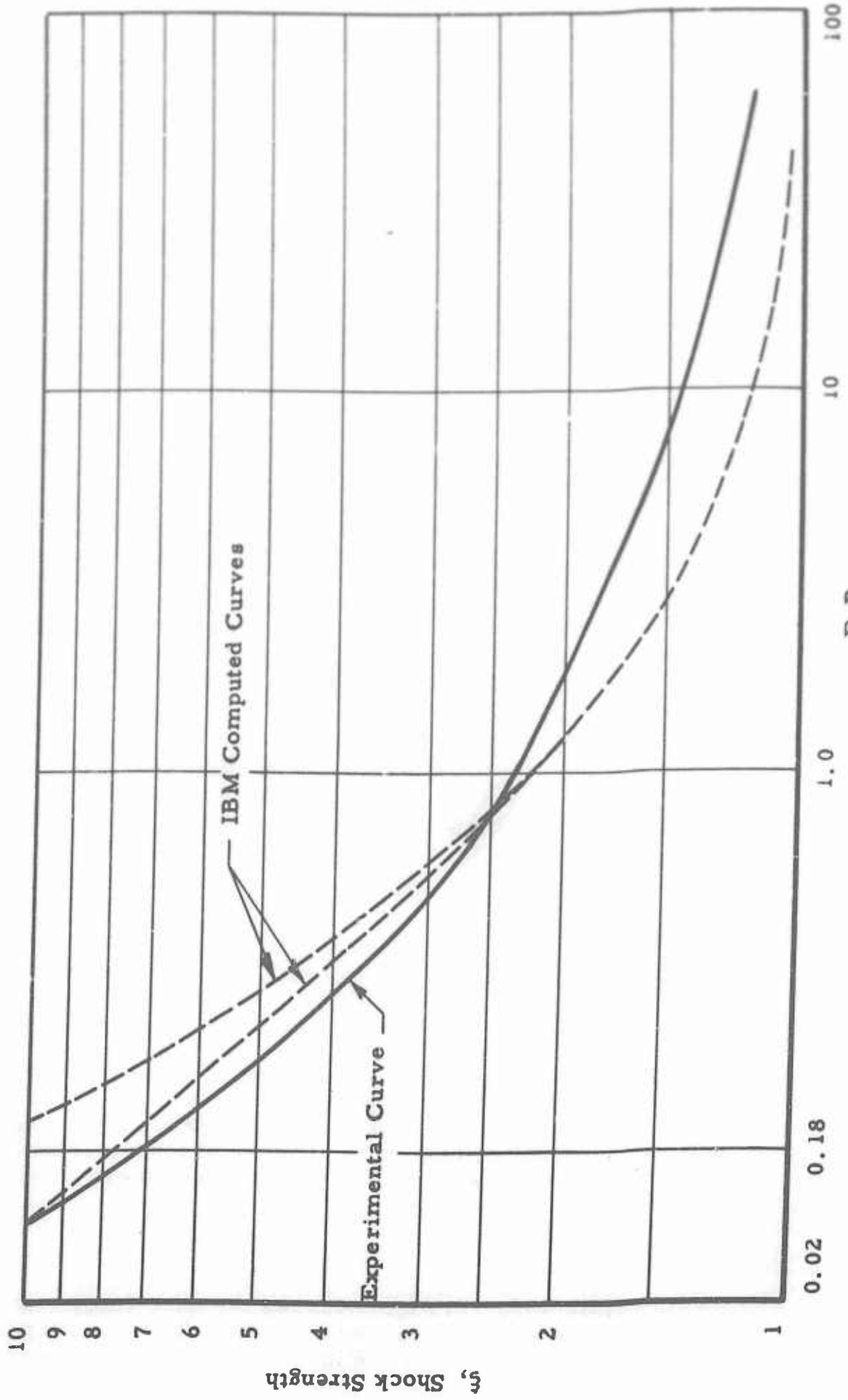

Fig. 2 Scaled Distance, λ, Versus Shock Strength, ξ

The Rankine-Hugoniot expression for shock velocity

$$U = c\left[\frac{6\xi + 1}{7}\right]^{1/2}$$

is used with

$$ct = c\int_0^R \frac{dR}{U},$$

which is numerically integrated to determine the time of arrival; c is the sound speed in the region immediately in front of the shock. Figure 3 is a plot of U/c versus ξ. The time corresponding to $\xi = 10$ is assumed to be $t = t_1$.

$\frac{P_o c\,(t-t_1)}{W}$ is now plotted versus λ, shown in Fig. 4. This curve is extrapolated back to where $\lambda = 0$ to find a value for t_1.

With this value of t_1, ξ versus $\frac{P_o ct}{W}$ is plotted and is shown in Fig. 5. The addition of this time-of-arrival curve makes it possible to find, if given values for any two of the following, ξ, R, t, or W, the remaining two.

III. SINGLE CHARGE RESULTS APPLIED TO MULTIPLE CHARGE SYSTEM FOR GENERATING DESIRED PRESSURE PULSES

In retrospect the results obtained in this study specifically are; (1) a shock strength-scaled distance decay curve, (2) a shock strength-scaled time decay curve, and (3) a complete description as to the behavior of the gas flow variables behind an explosive generated shock front, that is, under the power law density assumption.

Shock Strength-Scaled Distance Curve

The first of these results as shown in Fig. 2 is considered in good agreement with experimentally gathered data. That the theoretical and the experimental curves do tend to separate for the lower range of shock strengths is more than likely due to the fact that the assumed density distribution is less accurate for low values of shock strength. These two curves do agree quite well, however, for shock strengths above two. This result enables one to calculate the conditions necessary to generate a desired shock wave. For example, if the distance and shock strength of a desired wave are given, the size of the charge necessary to generate the wave may be easily calculated.

Shock Strength-Scaled Time Curve

This curve, as shown in Fig. 5, shows the time decay history of an explosive generated shock wave. It serves somewhat the same purpose as the shock strength-scaled distance curve. With the addition of this curve it

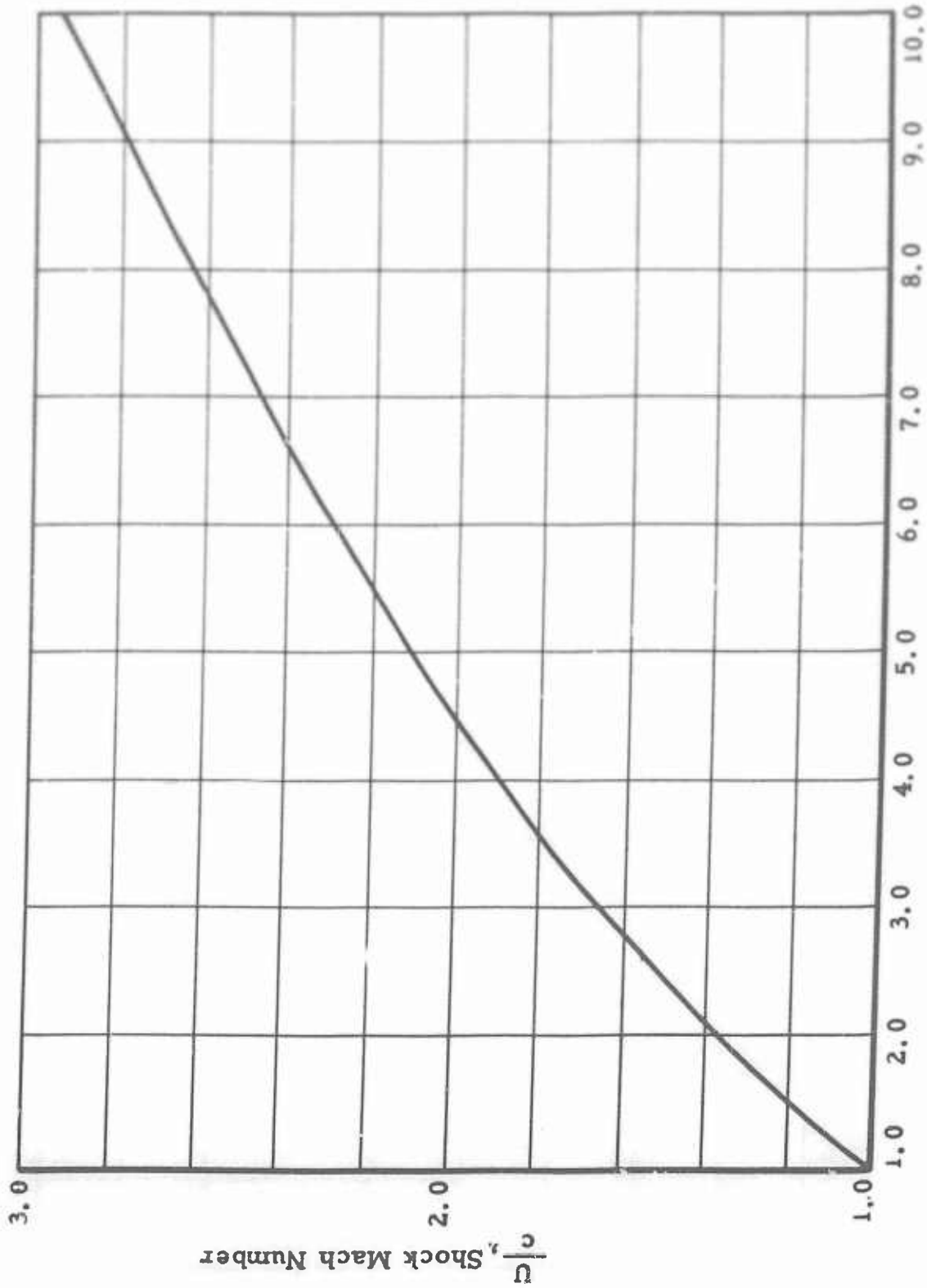

Fig. 3 Shock Mach Number Versus Shock Strength, ξ

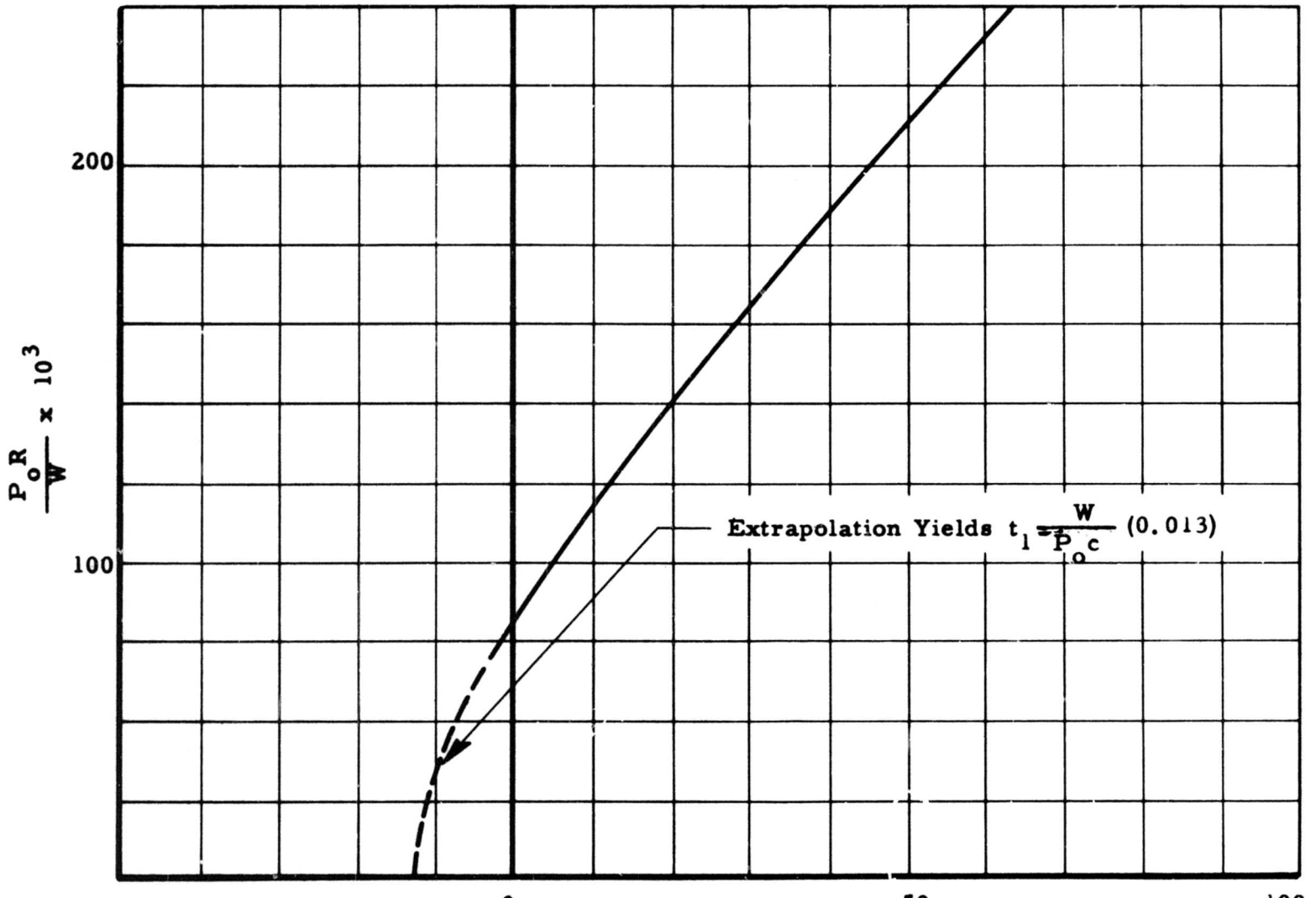

Fig. 4 Scaled Distance Versus Scaled Time $\frac{P_o c\,(t - t_1)}{W} \times 10^3$

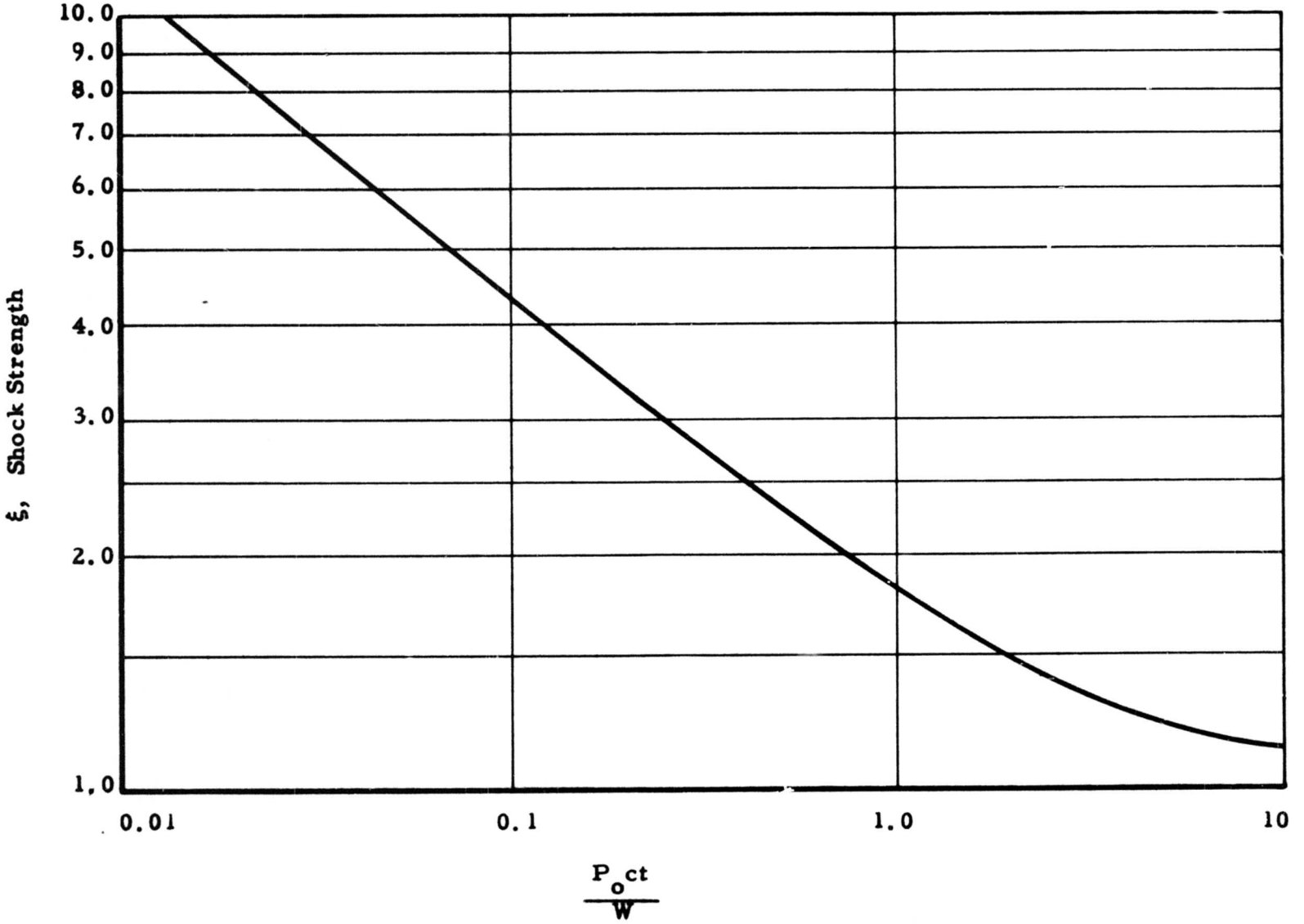

Fig. 5 Scaled Time Versus Shock Strength, ξ

is now possible to calculate the time of arrival of any given shock. This time decay history also makes it possible to calculate numerically the density, particle velocity, and pressure time distributions behind an explosive generated shock wave. With time distributions a direct comparison may be made with experimentally gathered data.

Approximate Method Employed for Multiple Charge Problem

In order that a solution for a second charge may be found, the conditions set up by the first charge must be considered. It is therefore assumed that the first shock sets up a new set of average ambient conditions given by the expressions

$$\overline{P} = \frac{\int_o^R P \, dr}{\int_o^R dr},$$

and

$$\overline{u} = \frac{\int_o^R u \, dr}{\int_o^R dr}$$

These are easily computed using the pressure and particle velocity wave form solutions from the single charge. The results are

$$\overline{P} = \left\{ (\xi - 1) \left[1 - K + \frac{K}{\eta_s + 2} - \frac{L}{(\eta_s + 2)^2} + \frac{2M}{(\eta_s + 2)^3} \right] + 1 \right\} P_o$$

$$\overline{u} = \left(\frac{\alpha + 2}{4}\right) u_s.$$

A new average sound speed $\overline{c}$ is defined by $\overline{c} = c_o \left(\frac{\overline{P}}{P_o}\right)^{1/2}$

The two charge problems may now be solved. Suppose a ξ_1 is desired at a distance R_1, and is to be followed by a ξ_2 at a distance R_2; the charge weights W_1, W_2 and the time delay between the detonation of the two charges may be found as follows:

ξ_1, R_1 imply
- W_1 (from λ versus ξ plot, Fig. 2)
- t_1 (from $\frac{P_o c t}{W}$ versus ξ plot, Fig. 5)
- $\overline{P}$ and $\overline{u}$, (from above equations)

ξ_2 implies $\begin{cases} \frac{R_c^*}{W_c} \text{ (from } \lambda \text{ versus } \xi \text{ plot)} \\ \frac{t_2}{W_2} \text{ (from } \frac{P_o ct}{W} \text{ versus } \xi \text{ plot)} \end{cases}$

*some distance R corresponding to a shock of strength ξ_2 moving into a still gas, but not equal to R_2 as the gas in front of second shock is in motion.

Using the above information and noting that

$$R_2 = R_c + \bar{u}\ t_2$$
$$= (\frac{R_c}{W_2})\ W_2 + \bar{u}\ (\frac{t_2}{W_2})\ W_2$$

Solving for W_2 the second charge weight gives

$$W_2 = \frac{R_2}{(\frac{R_c}{W_2}) + \bar{u}\ (\frac{t_2}{W_2})} \tag{6}$$

from which

$$t_2 = W_2\ (\frac{t_2}{W_2})$$

This gives the time delay between detonations

$$\Delta t = t_1 - t_2 \tag{7}$$

These are the necessary parameters for generating the desired wave form.

It will now be shown that this method may be expanded into a solution for an arbitrary number of charges. The assumption is made as before that each successive shock sets up a new set of ambient conditions. For the n^{th} shock these conditions are:

$$\bar{P}_n = \left\{ (\xi - 1) \left[1 - K + \frac{K}{\eta_s + 2} - \frac{L}{(\eta_s + 2)^2} + \frac{2M}{(\eta_s + 2)^3} \right] + 1 \right\} \bar{P}_{n-1}, \tag{8}$$

$$\bar{u}_n = (\frac{\alpha + 2}{4})\ (u_s)_n + \bar{u}_{n-1},$$

and

$$\bar{c} = (\frac{\bar{P}}{P_o})^{1/2}\ c_o \tag{10}$$

where the parameters ξ, η_s, K, L, M, and α are all determined by the n^{th} shock.

The procedure consists of treating ξ_1, R_1 and ξ_2, R_2 as described above, thus obtaining the complete solution for generating waves one and two. Next wave two and wave three are considered. The procedure is the same with the exception of the computation of $\overline{P}$, $\overline{u}$, and c. They are computed using Eqs. 8, 9, and 10. Likewise, any number of charges may be treated in this manner. In the following chapter the three desired wave forms are constructed using this procedure. The form of the solution will be more explicitly defined as these individual cases are treated.

Reliability of the Approximate Solution

There are several errors introduced by the use of this approximation solution, however each error is in itself compensating or has a corresponding compensating error. The errors are:

(1) An average $\overline{u}$ is used instead of its actual value at a particular point.

(2) An average $\overline{P}$ is used instead of its actual value at a particular point.

(3) The above are computed by assuming the shock, which sets up the new ambient conditions, is at its desired strength and position.

(a) This results in a lower $\overline{P}$ than is actually seen by the shock wave following, and thus giving the new shock wave a higher shock velocity than it actually has.

(b) It also results in a lower $\overline{u}$ than is actually the case.

It is apparent that (1) and (2), being averages, are nearly self-compensating, but they are not entirely self-compensating because they are average values over the entire shock wave where as the new shock travels only a fraction of this distance.

This implies the $\overline{P}$ and $\overline{u}$ computed are too high, giving the new shock wave a lower computed velocity than it actually has, but the correspondingly high $\overline{u}$ compensates. Similarly (3a) and (3b) compensate for each other. Although the errors introduced by this approximation method compensate for each other, there is no guarantee that the balance is perfect.

IV. SOLUTIONS TO THE THREE DESIRED WAVE FORMS

It is now possible to find the charge weights and their times of detonation in order to produce a series of desired shock waves at a corresponding series of desired distances. However, in the three cases to be solved, shock strengths and time durations are given, as opposed to shock strengths

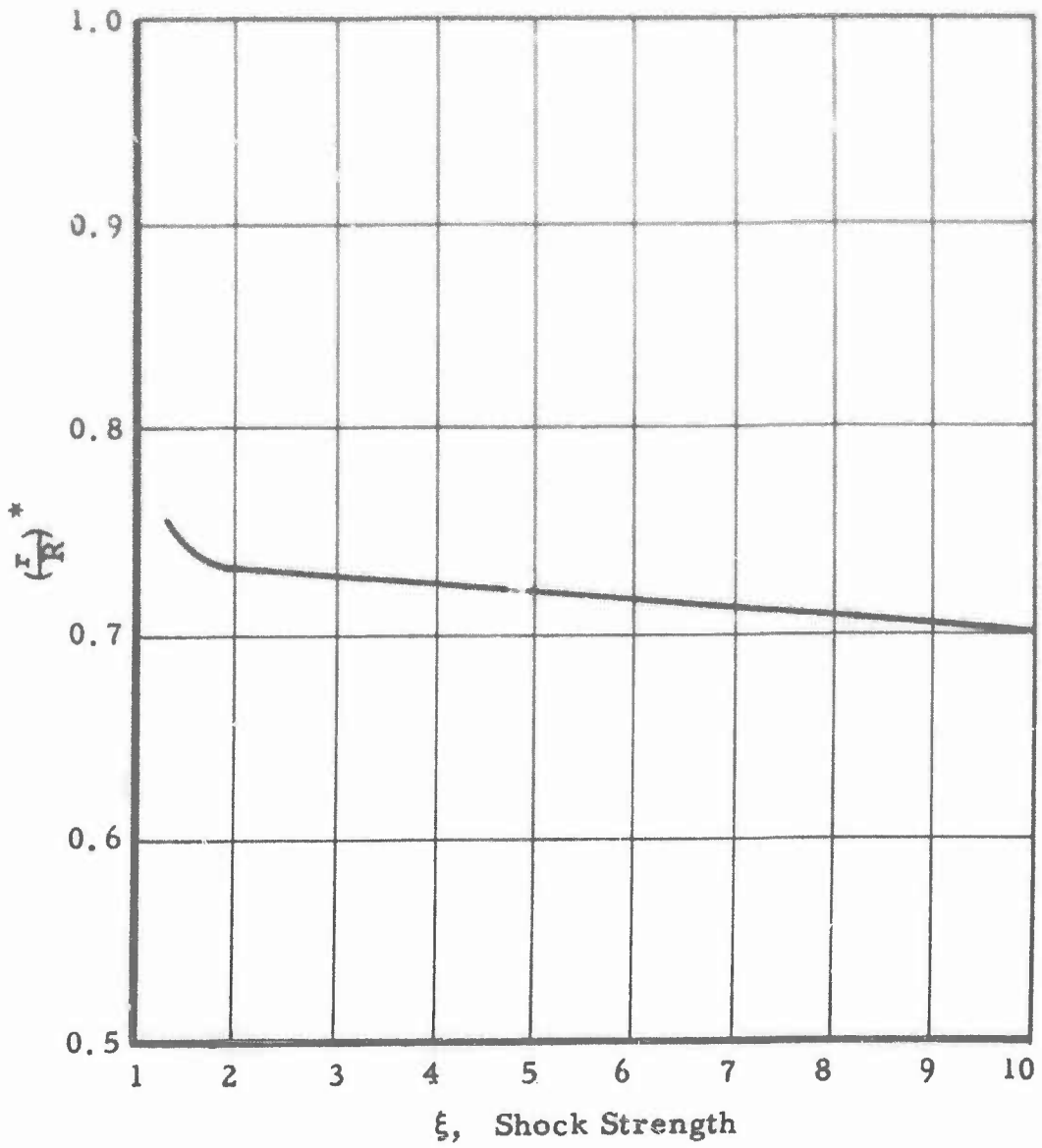

Fig. 6 $(\frac{r}{R})^*$ Versus Shock Strength, ξ

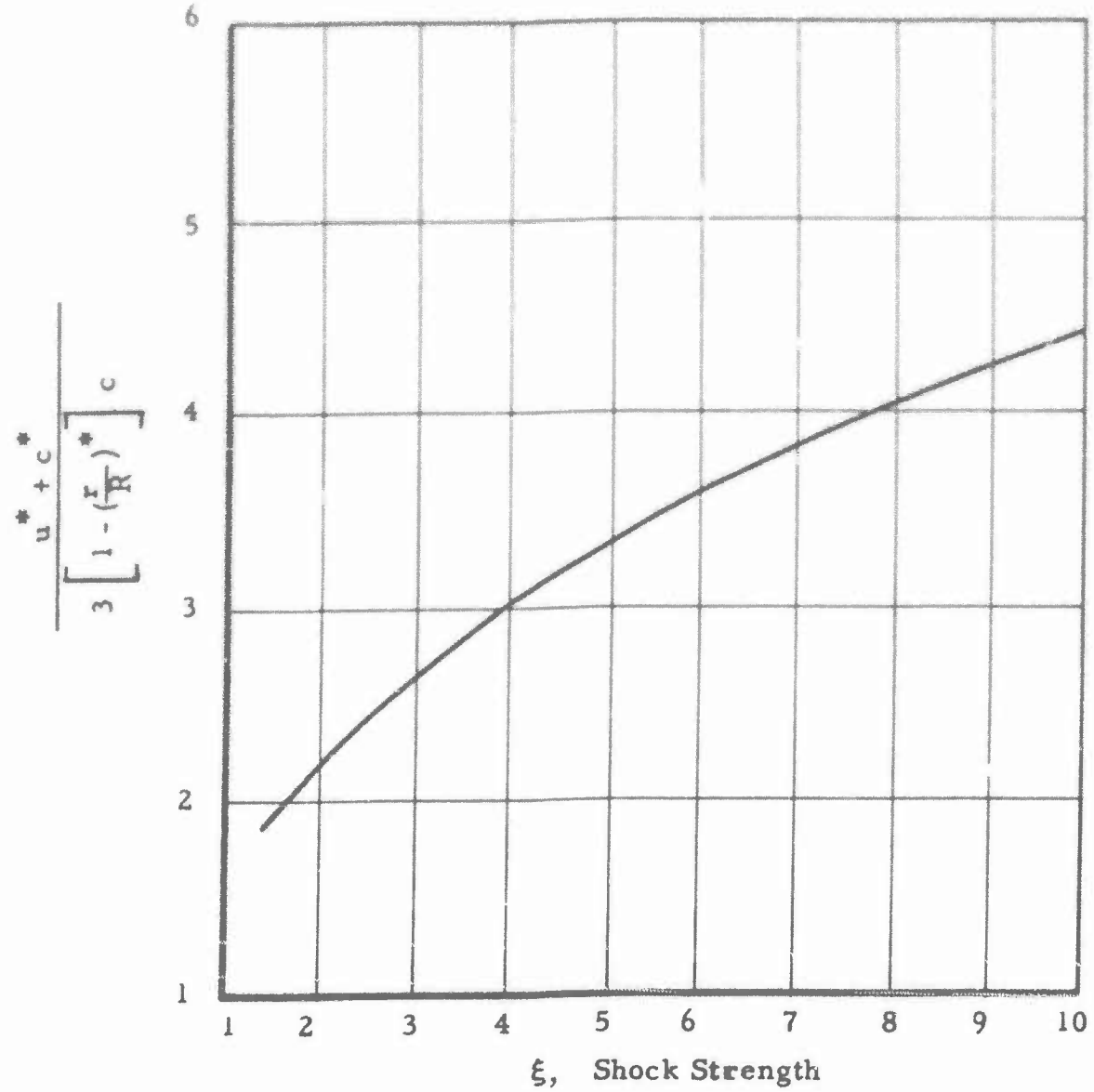

Fig. 7 $\frac{u^* + c^*}{3\left[1 - (\frac{r}{R})^*\right]c}$ Versus Shock Strength, ξ

and distances. This makes it necessary to determine the relationship between ξ, R, and t_o, duration.

The conventional form taken for pressure-time variations in work with high explosives has been

$$P(t) - P_o = (P_s - P_o)\, e^{-t/t_o}\,(1-t/t_o),$$

in which t_o is the duration of the positive pressure phase. It is seen that this wave form decays in overpressure to one-half of the peak overpressure in about one-third of the positive phase duration. The conventional "duration" for a wave propagating in a constant area channel (shock tube) is thus calculated in the present report as three times the decay time to half the peak overpressure.

Now using Eq. 4, it is possible to fine a value of (r/R), say $(r/R)^*$, which corresponds to $P-P_o/P_s-P_o = 0.5$, for any given shock strength. These values, $(r/R)^*$, have been computed and are presented as a function of shock strength in Fig. 6. Values of particle velocity, where $(r/R) = (r/R)^*$ are not computed from Eq. 3 for a range of shock strengths. For the same range of shock strengths the sound velocity say c*, is computed at the half overpressure point relative to still air. With this information the following equation relates the previously defined duration to distances:

$$\left(\frac{u^* + c^*}{3}\right) t_o = \left[1 - \left(\frac{r}{R}\right)^*\right] R$$

or solving for R gives

$$R = \frac{(u^* + c^*)\, t_o}{3\left[1 - \left(\frac{r}{R}\right)^*\right]} \qquad (11)$$

The ratio of the coefficient of t_o to c, sound speed, is plotted as a function of shock strength in Fig. 7. This curve may now be used in computing a distance, given a shock strength, a duration, and the ambient conditions.

Solution for the Double Peaked Wave Form

The simplest of the three wave forms to be constructed is the double peaked wave form. It will therefore be treated first. The particular pressure time form desired is shown in Fig. 8.

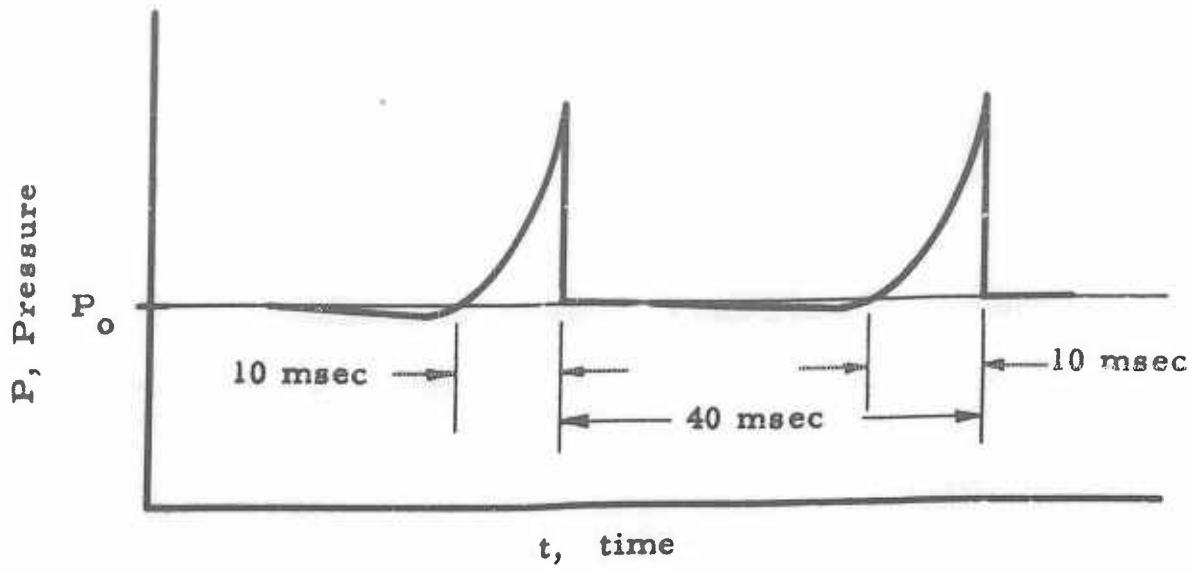

Fig. 8 DOUBLE PEAKED WAVE FORM

Wave one is first considered. It is noted that a shock strength, ξ, of 2 with a duration of 10 milliseconds is desired. Figure 7 gives

$$\frac{u^* + c^*}{3\left[1 - \left(\frac{r}{R}\right)^*\right]} \frac{1}{c_o} = 2.21$$

for $\xi = 2$, which gives

$$R = 2.21\, c_o\, t_o$$

$$= (2.21)(117 \text{ ft/sec})(0.01 \text{ sec})$$

$$= 25 \text{ ft}$$

Figure 2, ζ versus λ, gives

$$\lambda = 1.25/\text{ft}^2$$

for $\xi = 2$, and taking the value of R from above gives

$$\frac{\lambda}{R} = \frac{P_o}{W} = 0.05/\text{ft}^3$$

$$W_1 = \frac{(14.7 \text{ lb/in.})^2\, (144 \text{ in.}^2/\text{ft}^2)}{0.05/\text{ft}^3} = 42,336 \text{ ft-lb.}$$

Figure 5 gives a time of arrival for the first shock wave. For $\xi = 2$

$$\frac{P_o\, c\, t_1}{W} = 0.7/\text{ft}^2$$

$$t_1 = \frac{0.7/\text{ft}^2}{\frac{P_o}{W}\, c} = \frac{(0.7/\text{ft}^2)\ 10^3 \text{ msec/sec}}{(0.05/\text{ft}^3)\,(1117 \text{ ft/sec})} = 12.5 \text{ msec}$$

With the time of arrival known, the position of shock wave one may be found at the time the second wave is at the 25-foot distance (40 milliseconds later).

$$\frac{P_o\, c\, (t_1 + 40)}{W_1} = 2.94/\text{ft}^2$$

which corresponds to a $\xi = 1.2$ and a distance $R = 156$.

The problem is now in the form in which the approximate method may be applied. The charge weight for the first shock has already been found, which leaves only the second charge weight and the time differential between detonations to be found.

The values of $\overline{P}$, $\overline{u}$, and $\overline{c}$ for $\xi = 1.2$ are, from Eqs. 8, 9 and 10

$$\overline{P} = 1.05\ P_o$$

$$\overline{u} = 0.04\ c$$

$$\overline{c} = 1.025\ c_o$$

This implies that the second wave with a $\xi_2 = 2$ relative to P_o has for purposes of computation a $\xi = 2.00/1.95 = 1.90$. From Figs. 2 and 5, $\xi = 1.90$ implies

$$\frac{R_c}{W_2} = \frac{1.43/ft^2}{\overline{P}} = 6.43 \times 10^{-4}/lb$$

and

$$\frac{t_2}{W_2} = \frac{0.9\ ft^2}{\overline{P}\ \overline{c}} = 3.63 \times 10^{-7}\ sec/ft\text{-}lb$$

Putting these values into Eq. 6 gives

$$W_2 = 3.79 \times 10^4\ ft/lb$$

and therefore

$$t_2 = (W_2\ (\frac{t_2}{W_2}) = 13.75\ msec.$$

By Eq. 7

$$\Delta t = t_1 - t_2 = (12.5 + 40) - 13.75 = 38.75\ msec.$$

To summarize then, the desired wave form in Fig. 8 may be generated at a distance of 25 feet using

$$W_1 = 4.23 \times 10^4\ ft\text{-}lb$$

and

$$W_2 = 3.79 \times 10^4\ ft\text{-}lb$$

with a time spacing of detonation equal to 38.75 milliseconds. These are the parameters for a unit cross-sectional area channel.

The 50-Millisecond Buildup, Finite Rise Time Wave Form

The next shock wave to be considered is the finite rise time wave form which builds up slowing to peak in about 50 milliseconds, and then decays to zero in another 50 milliseconds. This wave will be approximated by a series of six smaller shock waves, as shown in Fig. 9.

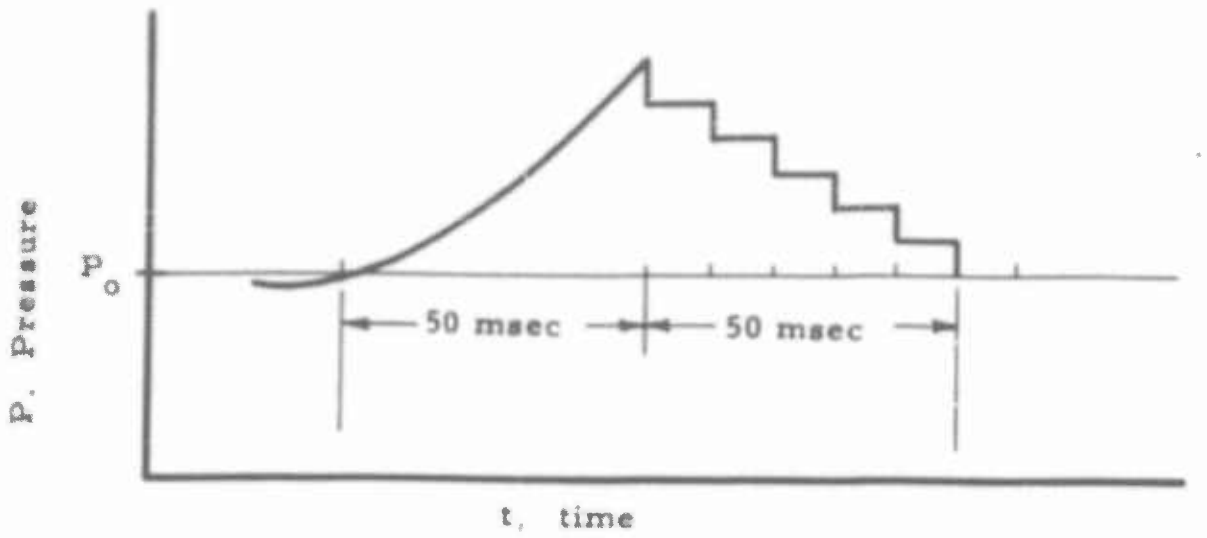

Fig. 9 THE 50-MILLISECOND BUILDUP, FINITE RISE TIME WAVE FORM

The first step in determining the parameters which will generate this finite rise time wave is to determine the distance at which a duration of 50 milliseconds occurs for a shock strength of two. Using Fig. 9

$$R = (2.205)(1117)(0.05) = 123 \text{ ft}$$

For wave one ξ_1, = 1.167, which gives

$$\lambda_1 = 10/\text{ft}^2$$

from Fig. 2. At R = 123

$$\frac{\lambda_1}{R} = \frac{P_o}{W_1} = 0.0813/\text{ft}^3$$

and at atmospheric conditions

$$W_1 = 2.61 \times 10^4 \text{ ft/lb.}$$

Figure 5 gives

$$\frac{P_o c_o t_1}{W_1} + 6.2/\text{ft}^2$$

from which

$$t_1 = 68.3 \text{ msec.}$$

When wave two arrives at the 123-foot distance, wave one has traveled another ten milliseconds. It has therefore decayed to the following derived shock strength

$$\frac{P_o c_o (t_1 + 10)}{W_1} = 7.11/\text{ft}^2 \quad \text{which implies} \quad \xi_1 = 1.145$$

This new ξ_1 gives the new ambient conditions for the second wave. They are

$$\bar{P} = 1.04\ P_o$$

$$\bar{u}_1 = 0.029\ c_o$$

$$\bar{c}_1 = 1.02\ c_o$$

Relative to the new ambient pressure the shock strength of wave number two is

$$\xi_2 = \frac{1.33}{1.04} = 1.28.$$

Now for ξ_2, Figs. 2 and 11 give respectively

$$\frac{\bar{P}_1 R_o}{W_2} = 5.5/ft^2$$

$$\frac{\bar{P}_1 \bar{c}_1 t_2}{W_2} = 3.7/ft^2$$

Using the values of $\bar{P}$ and $\bar{c}$ in the above yields

$$\frac{R_c}{W_2} = 2.5 \times 10^{-3}/lb$$

$$\frac{t_o}{W_2} = 1.48 \times 10^{-6}\ sec/ft\text{-}lb$$

Equation 6 now gives

$$W_2 = 4.82 \times 10^4\ ft\text{-}lb$$

and

$$t_2 = W_2 \left(\frac{t_2}{W_2}\right) = 70.3,\ xo \text{ by Eq. } 7$$

$$\Delta t_1 = (t_1 + 10) - t_2 = 8\ msec.$$

Next, wave three is considered, with wave two setting up the new ambient conditions. Wave two travels for an additional 10 milliseconds before wave three is at the 123-foot distance so that it decays in shock strength. Its new shock strength is, from Fig. 5,

$$\frac{\bar{P}_1 \bar{c}_1 (t_2 + 10)}{W_2} = 4.22/ft^2$$

which implies $\xi_2 = 1.245$. Again from Fig. 5 the new set of ambient conditions is

$$\bar{P}_2 = 1.06\ \bar{P}_1 = 1.10\ P_o$$

$$\bar{u}_2 = 0.048\ \bar{c}_1 + \bar{u}_1 = 0.078\ c_o$$

$$\bar{c}_2 = 1.048\ c_o$$

Relative to the new conditions, the shock strength of wave three is

$$\xi_3 = \frac{1.50}{1.10} = 1.365$$

For ξ_3, Figs. 2 and 5 yield

$$\frac{\bar{P}_2 R_c}{W_3} = 4.1/\text{ft}^2 \quad \text{and} \quad \frac{\bar{P}_2 \bar{c}_2 t_3}{W_3} = 2.75/\text{ft}^2$$

from which

$$\frac{R_c}{W_3} = 1.76 \times 10^{-3}/\text{lb}$$

and

$$\frac{t_3}{W_3} = 1.000 \times 10^{-6}\ \text{sec/ft-lb}$$

Equation 6 gives

$$W_3 = 6.66 \times 10^4\ \text{ft-lb}$$

and it follows that

$$t_3 = W_3 \left(\frac{t_3}{W_3}\right) = 66.6\ \text{msec}$$

so by Eq. 7

$$\Delta t_2 = (t_2 + 10) - t_3 = 13.7\ \text{msec.}$$

By repeating this procedure, the remaining charge weights may be found, and also their times of detonation. The results are:

$W_4 = 7.52 \times 10^4$ ft-lb $\qquad \Delta t_3 = 15.8$ msec

$W_5 = 8.43 \times 10^4$ ft-lb $\qquad \Delta t_4 = 13.4$ msec

$W_6 = 8.83 \times 10^4$ ft-lb $\qquad \Delta t_5 = 14.2$ msec

This completes the analysis for the 50-millisecond buildup, finite rise time wave form.

The 5-Millisecond Buildup, Finite Rise Time Wave Form

The final wave considered is another finite rise time type. However, in this case the buildup time to the peak overpressure is much more rapid, 5 milliseconds to peak overpressure and then 45 milliseconds for decay to zero overpressure. The wave is generated by a series of three smaller waves as shown in Fig. 10.

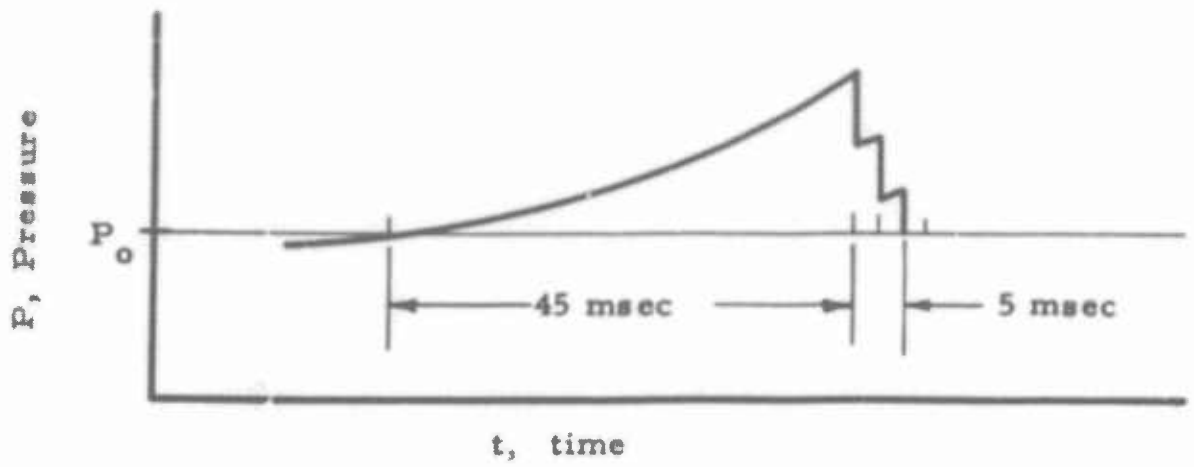

Fig. 10 THE 5-MILLISECOND BUILDUP, FINITE RISE TIME WAVE FORM

The distance at which a shock strength of two has a duration of 45 milliseconds (from Fig. 7) is

$$R = (2.205)(1117)(0.045) = 110.8 \text{ ft}$$

Figures 2 and 5 give, for wave number one, $\xi_1 = 1.33$, respectively

$$\lambda_1 = 4.65/\text{ft}^2$$

$$\frac{P_o c_o t_1}{W_1} = 3.10/\text{ft}^2$$

At R = 110.8 feet

$$\frac{\lambda_1}{R} = \frac{P_o}{W_1} = 0.0420/\text{ft}^3$$

and at atmospheric conditions

$$W_1 = 5.04 \times 10^4 \text{ ft-lb}$$

The time of arrival at R = 110.8 feet for wave one is

$$t = \frac{3.10/\text{ft}}{\frac{P_o}{W_1} c_o} = 66.1 \text{ msec.}$$

Wave one progresses for 2.5 milliseconds farther before wave two arrives at the 110.8-foot position. Its shock strength then decays, and the new value (from Fig. 5)

$$\frac{P_o c_o (t_1 + 2.5)}{W} = 3.22/\text{ft}$$

is $\xi_1 = 1.32$.

This new ξ_1 gives the new ambient conditions for the second wave,

$$\bar{P} = 1.083 P_o$$

$$\bar{u} = 0.06 c_o$$

$$\bar{c} = 1.041 c_o$$

Relative to these ambient conditions the shock strength of wave two is

$$\xi_2 = \frac{1.67}{1.083} = 1.54$$

For ξ_2, Figs. 2 and 5 give, respectively

$$\frac{\bar{P}_1 R_c}{W_2} = 2.63/\text{lb}$$

$$\frac{\bar{P}_1 \bar{c}_1 t_2}{W_2} = 1.68/\text{ft}$$

and knowing $\bar{P}_1$ and $\bar{c}_1$ results in

$$\frac{R_c}{W_2} = 1.147 \times 10^{-3}/\text{lb}$$

$$\frac{t_2}{W_2} = 0.628 \cdot 10^{-6} \text{ sec/ft-lb}$$

Equation 6 now gives

$$W_2 = 9.32 \times 10^4 \text{ ft-lb}$$

and

$$t_2 = W_2 \left(\frac{t_2}{W_2}\right) = 58.5$$

The time differential of detonation is, from Eq. 7

$$\Delta t_1 = (t_1 + 2.5) - t_2 = 10.1 \text{ msec}$$

Next wave three is considered with wave two setting up the new ambient conditions. Wave two travels for an additional 2-1/2 milliseconds before wave three arrives at the 110.8-foot distance. Its decayed shock strength is, from Fig. 5

$$\frac{\bar{P}_1 \bar{c}_1 (t + 2.5)}{W_2} = 1.75/\text{ft}$$

which implies $\xi = 1.525$. From Eqs. 8, 9 and 10 the new ambient conditions are

$$\bar{P}_2 = 1.143 \bar{P}_1 = 1.24 P_o$$

$$\bar{u}_2 = 0.096 \bar{c}_1 + \bar{u}_1 = 0.16 c_o$$

$$\bar{c}_2 = 1.114 c_o$$

Relative to these conditions, wave three has a shock strength of

$$\xi_3 = \frac{2.00}{1.24} = 1.61$$

For this value of ξ, Figs. 2 and 5 give

$$\frac{\bar{P}_2 R_c}{W_3} = 2.275/\text{ft}$$

$$\frac{\bar{P}_2 \bar{c}_2 t_3}{W_3} = 1.43/\text{ft}$$

Substituting the value of $\bar{P}_2$ and $\bar{c}_2$ into the above equations give

$$\frac{R_c}{W_3} = 0.886 \times 10^{-3}/\text{lb}$$

$$\frac{t_3}{W_3} = 0.437 \times 10^{-6} \text{ sec/ft-lb}$$

Equation 6 now gives

$$W_3 = 11.73 \times 10^4 \text{ ft-lb}$$

and

$$t_3 = W_3 \left(\frac{t_3}{W_3}\right) = 51.4 \text{ msec}$$

The t between the second and third detonations, by Eq. 6, is

$$\Delta t_2 = (t_2 + 2.5) - t_3 = 9.6 \text{ msec.}$$

This completes the analysis for the third desired wave.

In the following section the results of these calculations will be summarized and abulated.

Tabulated Results

In order that the results may be tabulated in a practical form, the charge weights are converted into feet of double-strength Primacord, the explosive used to generated blast waves in the Air Force's Shock Tube Laboratory at Gary, Indiana. Furthermore, the lengths are calculated for both a 6-foot diameter channel and a 2-foot diameter channel, which corresponds to the diameter sizes of the tubes at Gary. These parameters are indicated in Table I.

Suggestions on Experimental Set Up for Multiple Charges

The experimental procedure would involve arranging the charges, Primacord, in concentric circles. They have to be separated sufficiently to avoid sympathetic detonation, which in the case of Primacord is very rare even at distances of about one inch. The blasting caps used to detonate the Primacord might have to be shielded in some way as they are very sensitive, however, the separation of the charges is probably sufficient so that the only precaution necessary is insuring the mechanical integrity of the second charge until the time of its detonation. The time delay between charge detonations could be accomplished with instrumentation already in existence which is designed to take pulses, and at prescribed time intervals discharge pulses. These pulses then would detonate each charge at the proper time.

Table I

CONDITIONS NECESSARY TO GENERATE THE THREE DESIRED WAVE FORMS

Wave Type*	Distance at Which Desired Wave Occurs (ft)	Charge Number	Time Detonated after Preceding Detonation (msec)	Length of Double-Strength Primacord (ft)	
				6-ft tube	2-ft tube
1	25	1	0	43.0	4.77
		2	38.75	38.4	4.28
2	123	1	0	26.5	2.94
		2	8.0	49.0	5.45
		3	13.7	67.5	7.52
		4	15.8	76.2	8.48
		5	13.4	84.6	9.42
		6	14.2	89.6	9.96
3	110.8	1	0	51.2	5.70
		2	10.1	94.4	10.5
		3	9.6	119.2	13.3

*1 - double peaked wave
2 - finite rise time, slow buildup wave
3 - finite rise time, rapid buildup wave

3

BIBLIOGRAPHY

1. F. B. Porzel, Los Alamos Scientific Laboratory, Title Classified, LA-1664, May, 1954, pp. 24-48, (Secret-Restricted Data).

2. Armour Research Foundation, "Surface Effects on Blast Loading" May, 1956, (Secret-Restricted Data).

3. V. M. Wolontis, "A Complete Floating Decimal Interpretive System for the IBM 650 Magnetic Drawn Calculator", Bell Telephone Labs., Inc., IBM Technical Newsletter No. 11, March, 1956.

4. Radio Corporation of America, "An Interpretive Subroutine for the Solution of Systems of First Order Ordinary Differential Equations on the 650 Calculator".

5. Armour Research Foundation, "Memorandum Report on Calibration of Shock Tubes", Report No. 47 of Contract No. AF33(616)-2644, February, 1957.

6. A. H. Shapiro, "The Dynamics and Thermodynamics of Compressible Fluid Flow", Volume 1, 1953.

PROBLEMS IN THE USE OF PIEZO-GAGES FOR SHOCK TUBE INSTRUMENTATION

G. A. Coulter
Ballistic Research Laboratories

I. INTRODUCTION

This paper discusses the problem of correlating the pressures as calculated from a piezo-gage velocity system with the measured pressures obtained from previously calibrated pressure gages.

The problem to be discussed concerns the 24 inch O.D. shock tube at the BRL Shock Tube Facilities. Strong diaphragms are needed to separate the high pressure compression chamber from the low pressure test section before firing. Figure 1 shows a ruptured diaphragm of 2 SO aluminum, 0.020 inch thick. This is the firing end of the 36 foot compression chamber. Notice the alignment pins and the diaphragm break. The break was a pie-shaped break but was twisted during the later stages of the firing.

Figure 2 shows the test section located about a 100 feet from the firing section. This section is about 20 inches square to allow easy mounting of the models. Notice in the foreground the circular velocity ports.

II. VELOCITY SYSTEM

A primary means of measuring the shock pressure is by means of a velocity system. Certain experiments, for example, in which the instrument section is filled with dust or fog, make the use of the usual light screens impractical. As a substitute, small piezo-gages have been installed as velocity pick-ups.

Small 1/2 inch gages utilizing barium titanate cylinders as sensing elements were built by Granath of BRL. These were used for both velocity probes in this instance and in other cases for pressure gages.

Figure 3 is an assembly drawing of the gage. The principle components are listed in the legend at the lower right hand corner. These are the barium titanate cylinder, a phenalin insert to center crystal, Armstrong A-2 cement to mount the crystal and a Mylar cover with A-2 sealing the assembly into the 1/2" - 20NF brass or stainless steel case. Two such gages spaced on a known baseline may be used to record the shock as it passes the gage positions. The time interval as measured by a Potter Chronograph used with the baseline will allow the average velocity to be calculated. The velocity, and hence the shock pressure may be calculated from the known initial conditions of the gas in the shock tube.

The problems of rise time or crossing time for the gages must be considered. The usual crossing time for the subsonic flow in the 24 inch shock tube is somewhere between 15 and 30 μ-sec. for a gage, depending

upon crystal size and variation in shock strength. An error in time measurement can occur if the pulse amplifiers do not have exactly equal characteristics. This assumes already matched gages with respect to output.

A way of monitoring the pulse amplifiers is suggested by the use of a piezo-gage calibrator. The one pictured in Fig. 4 is patterned after a particle accelerator built by NOL (1956). The gage receives from the calibrator a pressure step function with a rise time of 3 to 5 milliseconds.

Figure 4-A is a cross-section view of the air tank with the valve. The center portion is the air reservoir. This supply volume is about 2000 times that of the valve and passageway volume. The heat transfer to the gage in calibrating is therefore very small. The air in calibration moves from the large chamber, through the small push valve, through the little passageway, and then to the piezo-gage face. The calibration is made from this pressure pulse.

The gains of the velocity pulse amplifiers may be preset by applying a known pressure pulse to each of the amplifiers in turn. The gain can be then preset just to trigger the chronograph. If this level is above the vibration noise level of the gages, then any shock pressure above this preset value should give correct time intervals. When this method was used, the velocity calculated pressures were still found to disagree with measurements from statically calibrated gages.

III. STUDY OF PRESSURE-TIME RECORDS

A clue to this discrepancy may be found in the diaphragm break at the compression chamber. Figure 5 shows pressure-time records from a piezo-gage for both a shock wave and the step calibration. The solid trace is from the shock wave and the broken line is from the piezo-gage calibrator. Note the rounding of the trace after the initial rise. Emrich and Wheeler (Ref. 2) show similar traces which they attribute to the boundary layer formation in the shock tube. Either or both reasons may cause the rounding.

The particular record shown in Fig. 5 varies from +6% to - 1% from the initial value at the front which agrees with the velocity system. The problem is worse for different diaphragm breaks. If the pressure from the statically calibrated gage is calculated very carefully and compared with the initial rise only, agreement between the velocity system and the static gages is found to an accuracy of 1% to 1/2 % maximum error. This probelm is then resolved to one of careful data reduction accepting the fact of varying diaphragm breaks. Careful data reduction is very necessary.

IV. DRAG MEASUREMENTS

A correlated valocity system can then be used to give control in repetition of the shots from the shock tube. The pressure gage is needed if individual pressures as a function of time are required. This is necessary for the calculation of drag coefficients. Figure 6 shows a model of a cube mounted in position to record drag force with a strain gage force balance. Strain gages AB-11 are placed at both ends of the balance tube. The strain

gages are then sensitive to bending moments at the ends. These can be related to the normal force load applied to the model.

Figure 7 shows some coefficients for three different models mounted against the shock tube wall. This data is not corrected for the shock tube size. These curves appear different from the usual plots of wind tunnel data. However, if one recalls that shock pressure involves both Mach number and Reynolds number, then the curves appear more reasonable. These curves are actually cross plots of the families of curves, where coefficients are plotted as function of Reynolds number at a constant Mach number.

NOL has also recorded the coefficients for the cube with a different type force balance. This work was also done in the 24 inch BRL shock tube. The NOL curve was similar in shape but the numerical values appeared to be somewhat higher than the values in Figure 7. The two methods should, of course, give the same results. The difference may have been caused by basic calibration error or perhaps to the records being averaged at different times.

The coefficients are based on the relationship $C_D = \frac{F/A}{Q}$ where C_D is the coefficient of drag, F/A is the drag force per unit area normal to the flow, and Q is the flow parameter $1/2\ \rho u^2$. ρ is the density of the gas with a velocity u.

Some effort has been expended in attempting to measure the parameter Q. This has been tried in two ways at the Shock Tube Facilities. A small gage, 1/2 inch diameter, cigar shaped, and a few inches long was used. The sensing element again was a barium titanate cylinder. It was mounted such that the stagnation pressure reached the inside and the side-on pressure reached the outside of the cylinder. The gage thus acted as a differential gage to measure Q. The internal oscillation from the nose cavity caused low Q records to be unreadable. Larger values of Q could be measured.

A second method using a face-on flush mounted piezo-gage and a second side-on flush mounted gage was tried. This method has the advantage of lower noise than the previous method but it has the disadvantage of measuring the pressure at points relatively far removed. If the flow is not uniform, an error will result. More work is needed to accurately measure Q and hence to obtain more useful values of the drag coefficients.

V. FUTURE NEEDS FOR DRAG PROGRAM

The coefficients need to be found as functions separately of each of the parameters of Mach number and Reynolds number. This is not too easy to do with a large shock tube, but by choosing model sizes in combination with shock pressures some variation can be obtained. This will mean variation of initial gas conditions in the expansion chamber of the shock tube. It is anticipated that this will be tried in the future.

VI. SUMMARY AND CONCLUSIONS

To summarize, it is possible to correlate velocity calculated shock pressures with statically calibrated piezo-electric gages if one compares either ideal step shock waves, or if the measurement is made very carefully at the initial shock front. Drag coefficients can then be calculated from measurements obtained from the use of a force balance. Better measurements of the flow parameters are needed to allow more meaningful coefficients to be calculated.

REFERENCES

1. Bingham, Harry H., David K. Weimer, and Wayland, Griffith, "The Cylinder and Semi-Cylinder in Subsonic Flow", Princeton University, Department of Physics, TN II-13, July 1952.

2. Coulter, G. A. and W. T. Matthews, "Coefficients of Drag Measured with a Shock Tube Force Balance", Ballistic Research Laboratories, TN 1155, August 1957.

3. Emrich, Raymond J. and Donald B. Wheeler, Jr., "Wall Effects in Shock Tube Flow", The Physics of Fluids, Vol. 1, No. 1, January - February 1958.

4. Hoerner, Sighard F., "Aerodynamic Drag", Published by author, 148 Busteed, Midland Park, New Jersey, 1951.

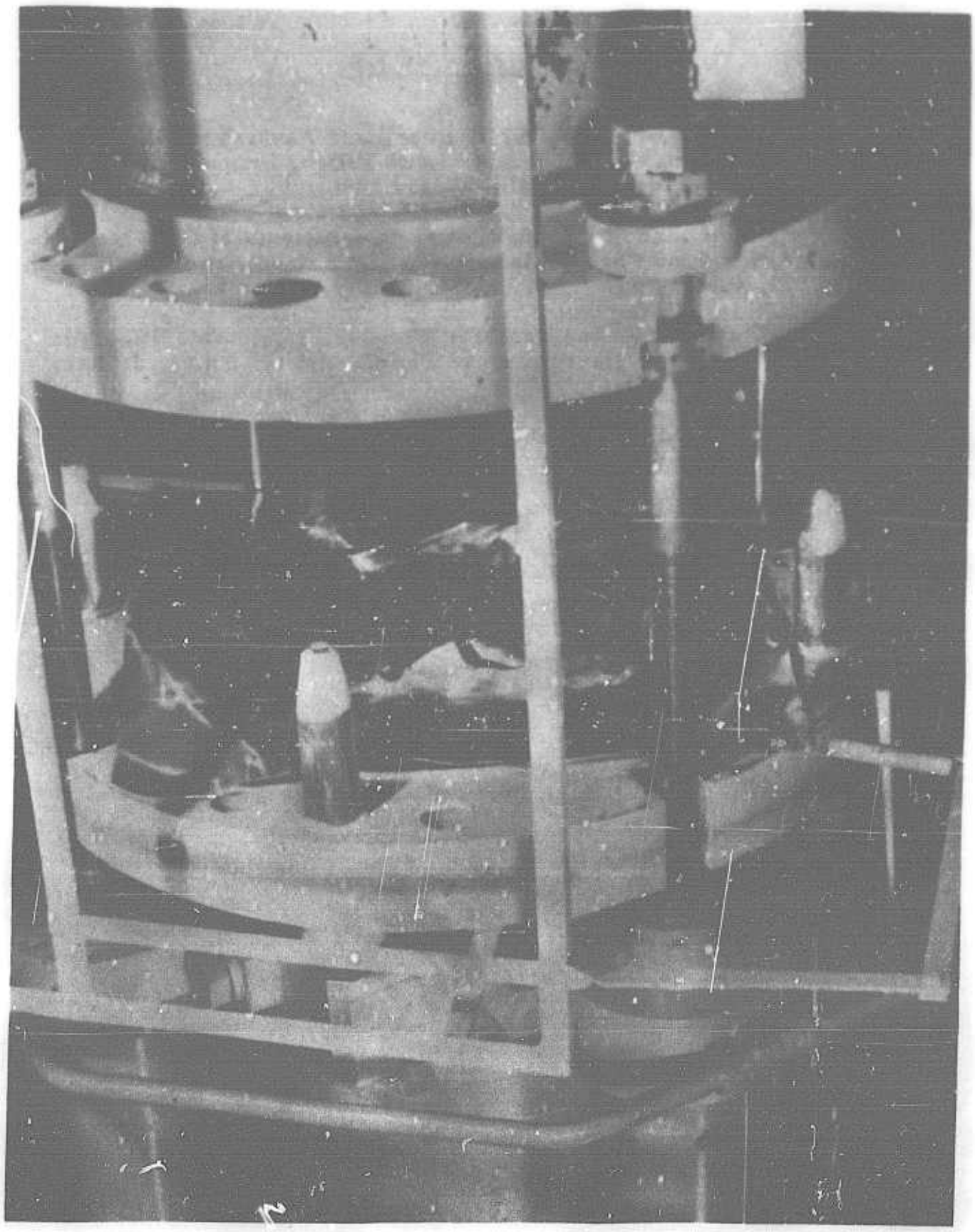

Figure 1 Compression Chamber 24" O.D. Shock Tube

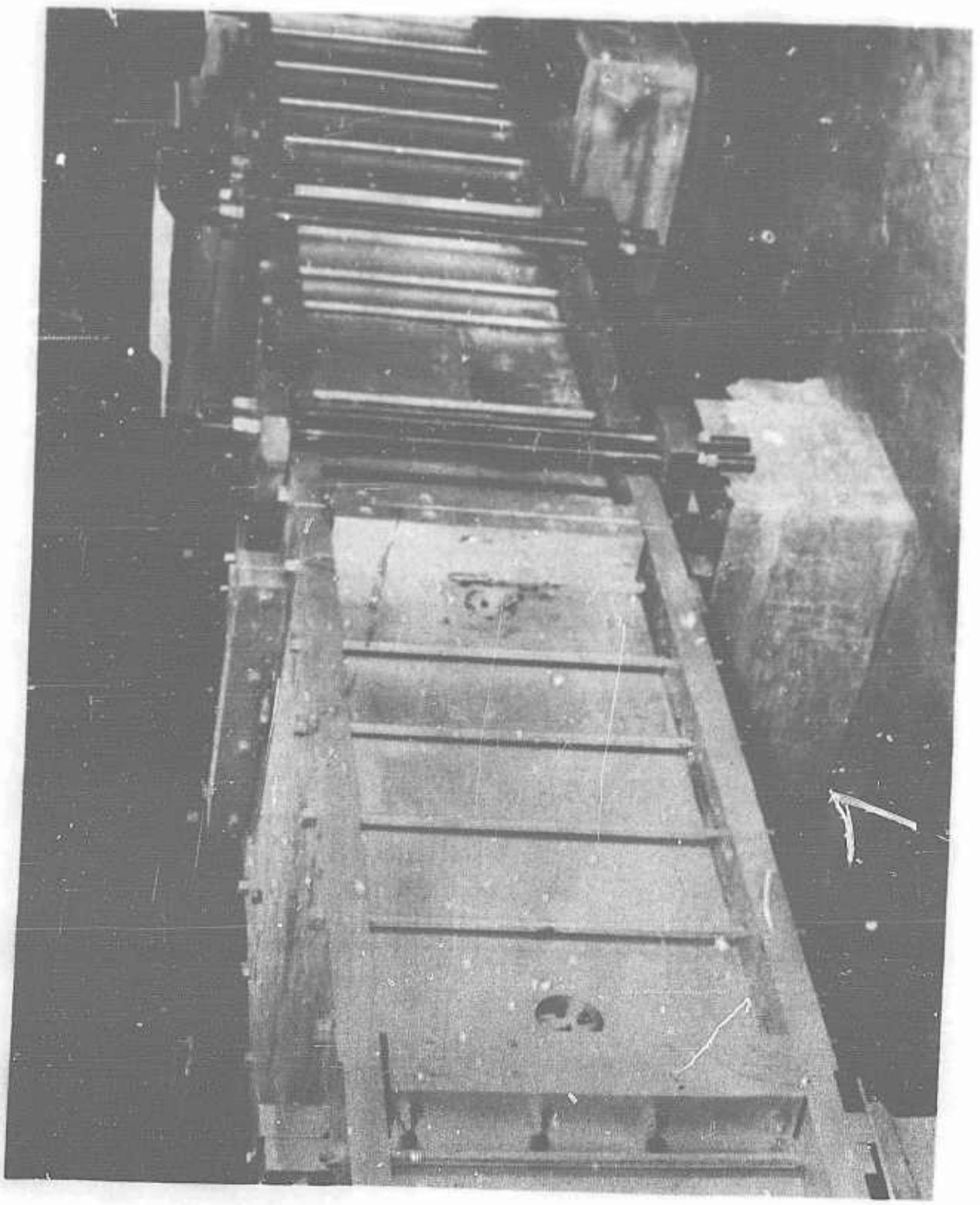

Figure 2 20" Square Test Section

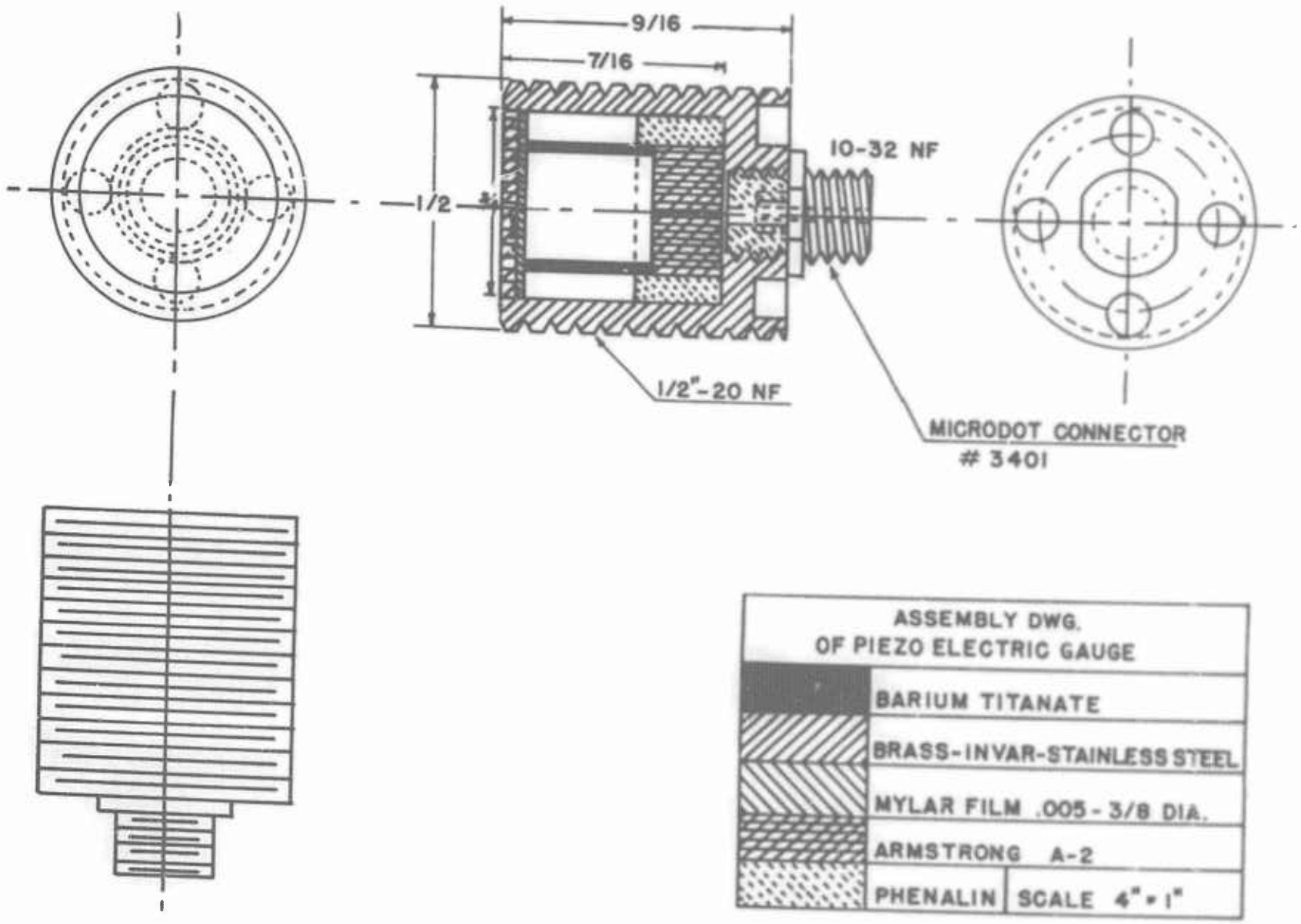

Figure 3 Diagram of 1/2" - 20 Pressure Gage

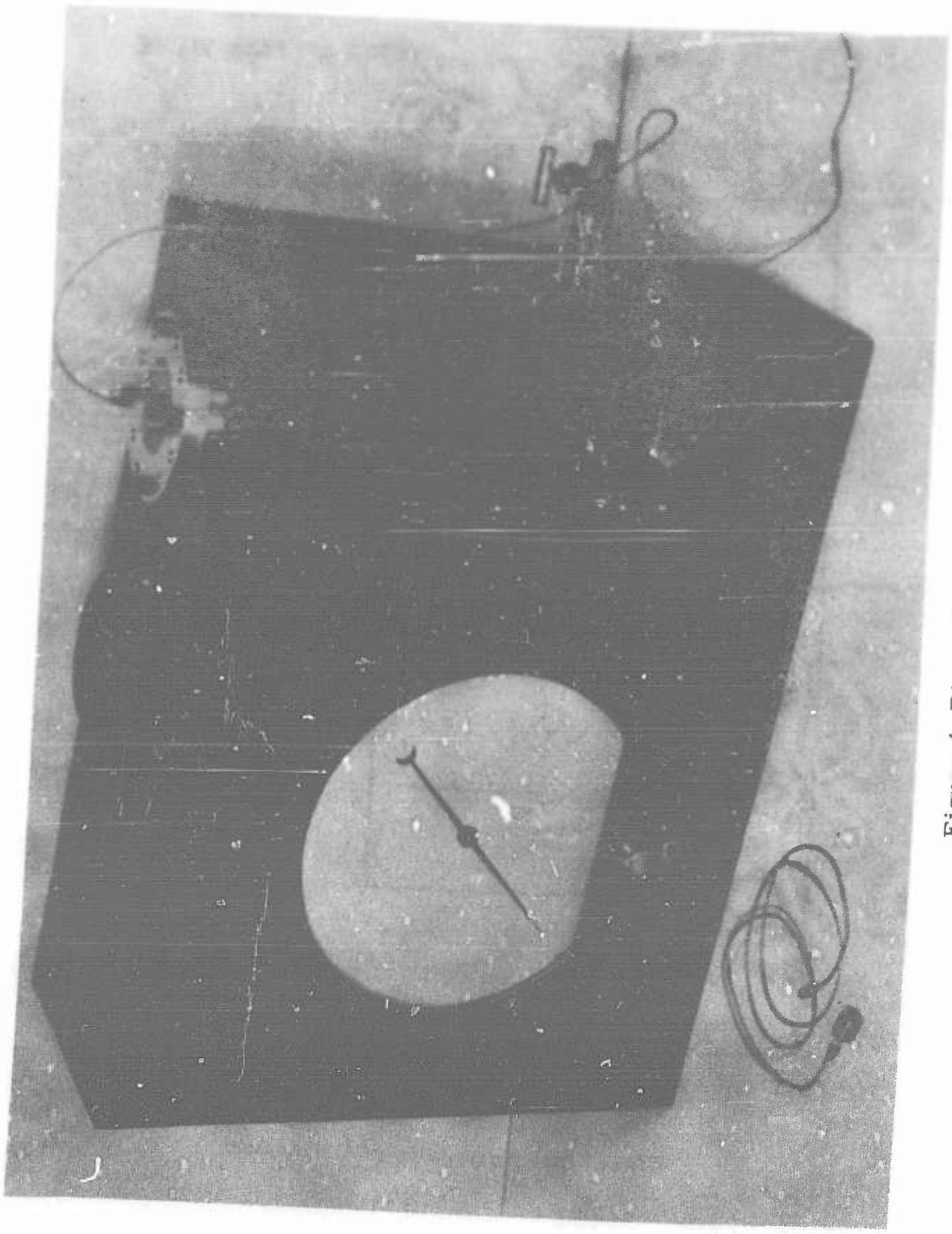

Figure 4 Piezo-Gage Calibrator

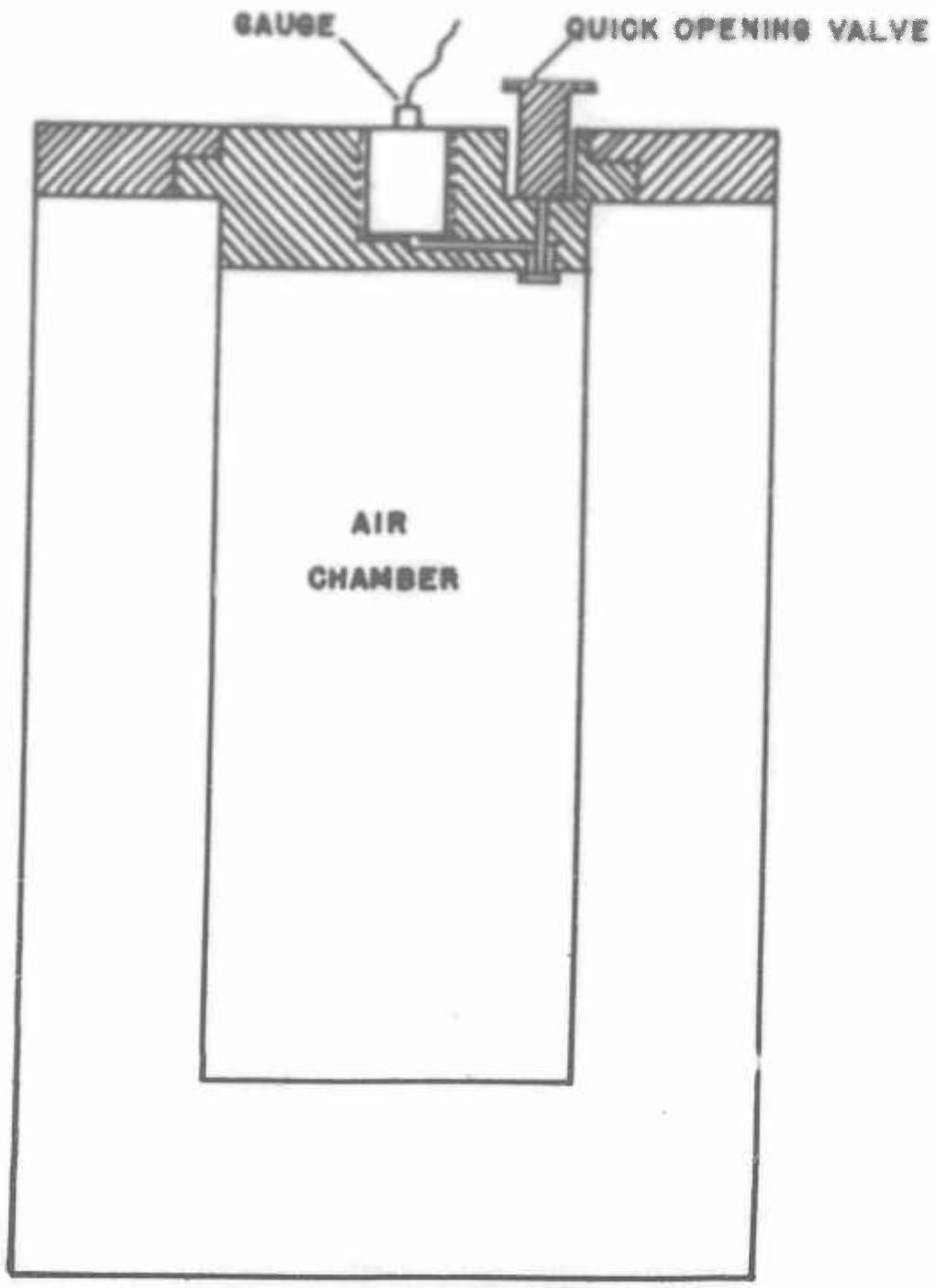

Figure 4a Schematic of Calibrator

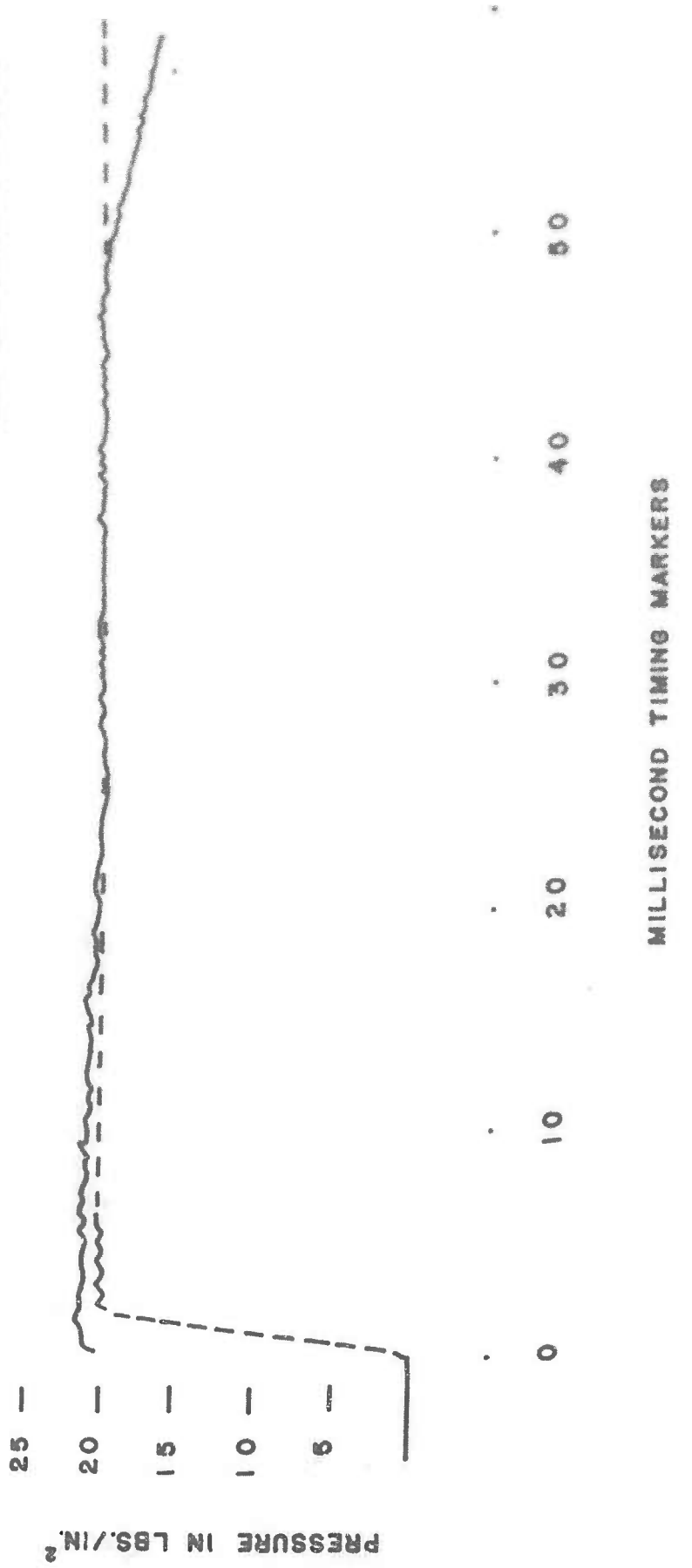

Figure 5 Pressure-time Curves for Pressure Gage

CROSS - SECTIONAL VIEW

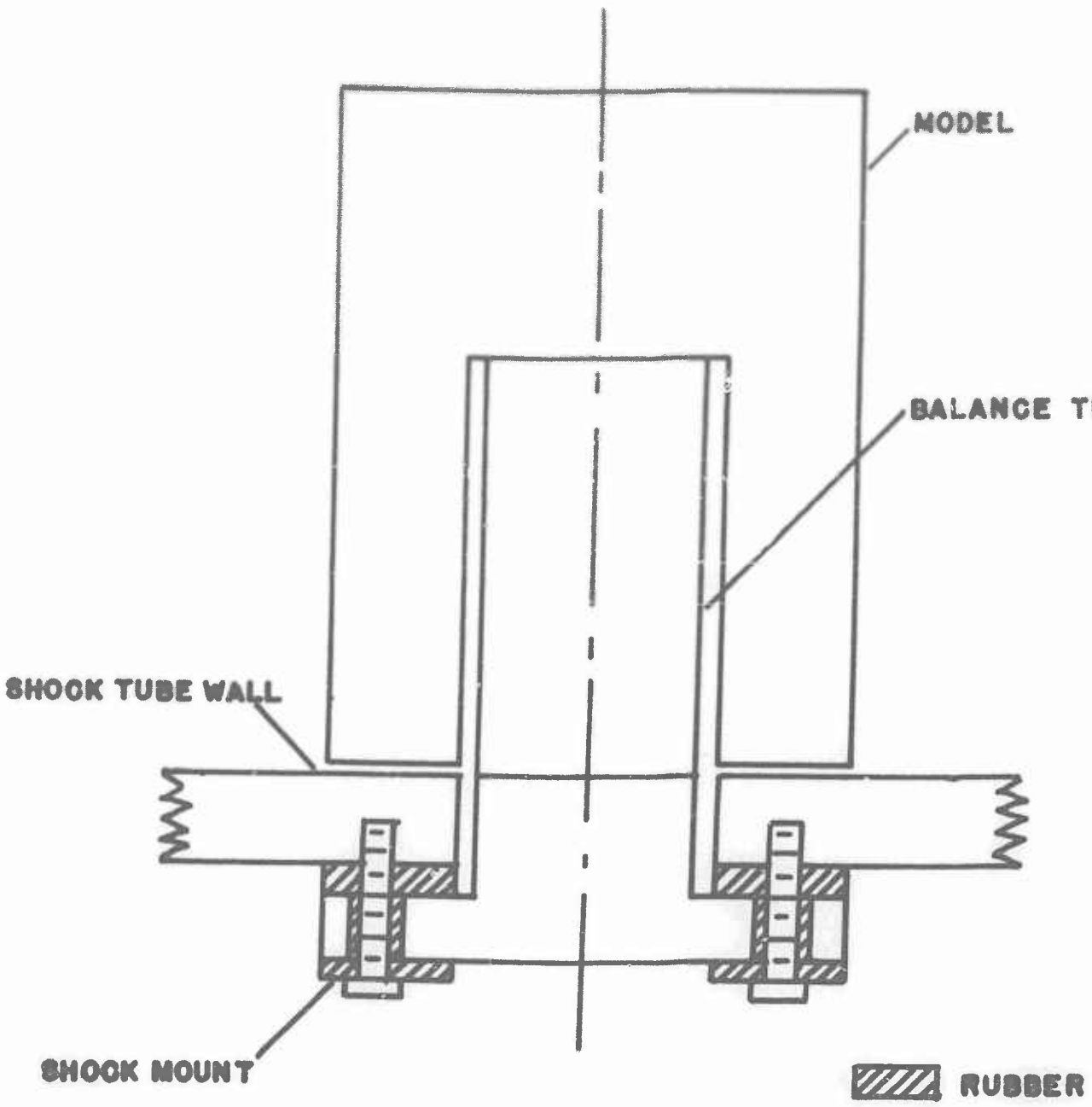

Figure 6 Mounted Model on Force Balance

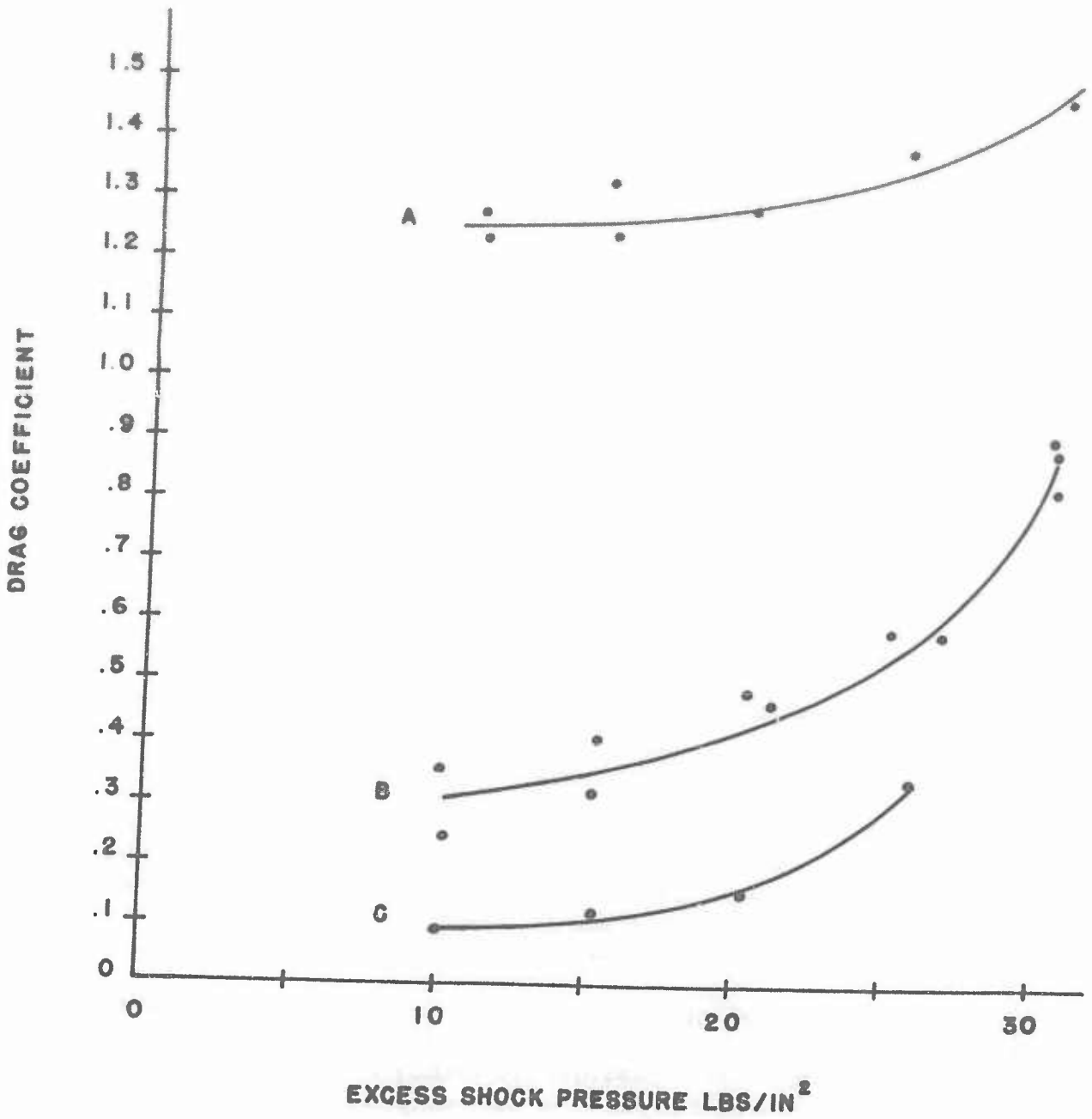

Figure 7 Curves of Drag Coefficients vs Peak Shock Pressure

DETERMINATION OF THE DYNAMIC RESPONSE CHARACTERISTICS OF PRESSURE MEASURING SYSTEMS UTILIZING SHOCK TUBE TESTING TECHNIQUES

Lt. William A. Russell, Jr.
Wright Air Development Center

INTRODUCTION

In recent aeronautical and propulsion research, the measurement of rapidly fluctuating pressures has become more essential and at the same time more difficult. They are more essential because air flow disturbances become much more pronounced with increase in Mach number. They are difficult because, in general, the pressures encountered fluctuate at varying and very high frequencies.

The Wright Air Development Center has been confronted with the problem of measuring the effects of shockwave overpressure on aircraft flying in the vicinity of nuclear detonations for more than a decade. Consequently WADC has constantly been desirous of obtaining improved frequency response from airborne pressure measuring systems for this purpose. Recent and anticipated increases in demands from airloads, missile, and anti-missile programs for more accurate pressure measurements have also provided a spur toward improving the state of the art in this field.

Realizing the need for better dynamic pressure measurements, there consequently is a need for a better means of evaluating the measurement system. The dynamic properties of an instrument or a system may be expressed as a plot of an instrument's response to a step-function input, or as a frequency response curve. The latter is commonly considered more useful and easier to interpret, however, it is difficult physically to obtain the necessary accurately-known sinusoidal input at high frequencies when it must be in the form of a pressure. Presently available means of producing sinusoidal excitation of pressure gages falls far short of the desired high frequencies, so that use of some manner of stroke pump to sinusoidally excite a system becomes unfeasible above some figure of around 100 cycles per second. Since the characteristics of most of the electronic components of a pressure measuring system will be expressed as frequency response curves, it makes it very desirable to have the dynamic response of the pressure pick-up expressed this way also for purposes of determining compatibility.

The shock tube offers a very convenient and inexpensive way to excite a pressure system with a step-function input. If a Fourier integral method is used to obtain the sinusoidal frequency response characteristics from the pressure systems response to this step transient pressure, then we have a method of obtaining frequency response curves for a "very fast-responding" dynamic pressure measuring system. The paper discusses the use of this approach at the Wright Air Development Center in shock tube testing of pressure gages and installations.

DISCUSSION

The use of a step-function pressure wave for the dynamic testing of pressure measuring systems requires the change from one known pressure level to a second known level in a time sufficiently short to shock excite the gage or system under test. The pressure level must be maintained for a sufficient time to obtain a steady record of the system's response. The shock tube meets these requirements very well for the testing of very "fast-responding" gages and systems i.e. well damped gages of high natural frequency. The length of the square pressure wave is a function of the speed of sound in the driver gas used and the physical characteristics of the shock tube. Conversely, the length of testing time needed is a function of the response of the pressure system to be tested. The method of analysis to be used by WADC dictates that the step-function pressure must be of sufficient duration to allow the transducer or gage to damp out completely (for an underdamped system) or rise to the value of the step-function pressure wave (if the system is over damped). The flat topped portion of the pressure wave in the case of the WADC tests was of about 8.5 milliseconds duration. With either slower-responding or highly under damped systems, this could prove to be an insufficient duration time.

The shock wave excitation method used has the following desirable characteristics for transducer or pressure measuring system testing: (1) it is very easy to repeat the same pressures and a very accurate calibration can be run on the shock tube; (2) the method of generating the wave is inexpensive and relatively easy to master; (3) the step-function pressure wave has a very fast rise time, equivalent to 1 or 2 microseconds over the face of a small transducer mounted perpendicular to the passage of the shock front; (4) the amplitude of the square wave is constant within several percent throughout the testing time; (5) evacuation and cooling of the down stream end of the tube permits altitude simulation; and (6) all the frequencies are contained in the square wave, necessitating only one excitation of the system under investigation.

The WADC tests were initiated to investigate the dynamic characteristics of the transducer and mounting components of a pressure measuring system to assure their compatibility with the rest of a pressure measuring system. It has been found that the sensing device has often been the limiting element within a high response system. This may be due to the requirements for a recessed installation involving some length of tubing leading to the gage. This present investigation is collecting data concerning the characteristics of the gage and various recessed mounting factors to give an insight into some of the design problems that will face the engineer when he must choose the various parts of a pressure measuring system.

The first step in the WADC program was to test various high frequency response pressure transducers mounted flush to the wall of the shock tube. After the characteristics of these gages were known, one was chosen to be mounted in the ends of tubes of various lengths and diameters. For each length of tubing, several different diameters were tested. The tubes were made from heavy bar stock which has a high natural period, thus eliminating tube ringing from the data. Knowing the characteristics of the flush mounted

transducer, the assumption was made that any major deviations by the recessed mounting would be due to the acoustics of the tube between the gage and the shock tube. As stated before, the fact that the testing time was, in this case less than 9 milliseconds, limited the tube length investigations to tubes under 6 inches in length. Beyond this, the frequency response was lowered so much that the system would not damp out in 8.5 milliseconds square wave duration. The recording of the data was accomplished by feeding the transducer output into a triggering oscilloscope and photographing the trace.

The Fourier integral method was used to determine the dynamic response characteristics from the recorded traces of the response of the system to the step-function pressure wave. The mathematical development of this method and its application to the present problem may be found in a report published by the Cornell Aeronautical Laboratory, Flight Research Department. A Fourier Integral Method for Obtaining the Sinusoidal Frequency Response from a Unit Step Transient. Report No. FRM-30, Revised 9 March 1949.

Simply stated, the Fourier Analysis provides the means for calculating the output characteristics, magnitude and phase, of a given system relative to an input of specified sinusoidal frequency. The only data required is the transient response of the system to a step input signal. This transient response or time record of the response is then mathematically operated on using Fourier Transfer theorems to obtain the desired information.

This method is independent of the order of the system under investigation and any frequency or random frequencies may be analyzed in any sequence. This is of particular importance where the system to be investigated includes components with various inherent damping and natural frequencies qualities and where the only requirement is to establish the response of the system for a given frequency range.

The required computations can be accomplished by hand, but they are rather laborious and time consuming. The computations, however, are well suited for automatic computing machine work. Practical use of the method demands an electronic computer where a wide frequency range and(or) a number of different systems are to be investigated.

The accuracy of the results is primarily dependent on the accuracy of the unit step input provided by the test procedure and on data reduction procedures. Appendix "A" gives a summary of the mathematical steps and a flow chart used in the computer program for the reduction of the data.

Appendix "B" shows the trace of a system's response, the computer program answers, and the response curves obtained for a particular system.

CONCLUSION

The present test program, which should be completed within the next month, will define the effects of various tube lengths and diameters on the frequency response, magnitude and phase, of the dynamic pressure measuring

system. The development of the previously described testing techniques, however, has a broader intention than the determination of pressure gage and mounting characteristics. It is believed that components of various existing and proposed measuring systems might be modified and tested in this manner to obtain the ultimate performance from the system as a whole. Eventually, certain codes of compatibility or suitability will be established with respect to the various components of a system. This would, in itself, effect a considerable advance in the field of pressure measurement.

Programs are planned to accumulate knowledge of techniques for sensing short duration pressure impulses at high-frequencies with good accuracy, in connection with detonation effects of nuclear weapons at very high altitudes.

It is believed that methods of measuring pressure must be greatly extended in frequency response in order to meet problems that are already present. Shock tube testing techniques will be used by WADC to attempt to achieve these needs.

APPENDIX A

SUMMARY OF MATHEMATICAL STEPS AND FLOW CHART USED IN COMPUTER PROGRAM FOR REDUCTION OF DATA

REPORT ON RESPONSE FUNCTIONS OF VARIOUS TRANSDUCERS AT DIFFERENT FREQUENCIES

The Datatron, Model 205 was programmed to evaluate ϕ, the LAG ANGLE, and A_o/A_i, the response ratio, for different values of f, the frequency. f was varied at intervals of 1, 10, 100, 1000, etc. for the ranges 1-10, 10-100, 100-1000 etc. respectively. The final frequency used was f = 50,000 Cps.; however, the programs will handle f up to approximately 100,000 Cps.

$$\phi = \tan^{-1} A/B$$

$$\frac{A_o}{A_i} = \frac{1}{\Gamma}\sqrt{A^2 + B^2}$$

where 1 is assumed equal to X_{ss}, the Steady state value

$$A = \omega C_o(\omega) - X_{ss} \operatorname{Sin} \omega T$$

$$B = \omega S_o(\omega) + X_{ss} \operatorname{Cos} \omega T$$

where $t \rightarrow T$ as $X(t) \rightarrow X_{ss}$

$$\omega = 2\pi f$$

$$C_o(\omega) = \int_o^T X(t) \operatorname{Cos} \omega t \, dt$$

$$S_o(\omega) = \int_o^T X(t) \operatorname{Sin} \omega t \, dt$$

X(t), the ordinates of the response curve were read at equal intervals of time, in counts on a Telerecordax. The number of counts varied with the magnification used to read the film, but was never less than 600 Cts/Cm. The Δt was chosen such that all peaks and troughs would be read, and was equal to 25μ Sec. or less.

Both integrals were evaluated by Simpson's rule

$$\int_o^X f(x)\,dx = \frac{\Delta X}{3}\left\{f(X_o) + 4f(X_1) + 2f(X_2) + \ldots + f(X_n)\right\}$$

where n is always even.

To simplify computation X (t) was multipled by Simpson coefficients, in the initial loading process. The values of X_{ss} and X_o were determined from a plot of the readings and all values modified by the formula:

$$X(t) = \frac{X_{read} - X_o}{Cts/Cm}$$

X_{ss} is chosen such that the No. of pts. is odd.

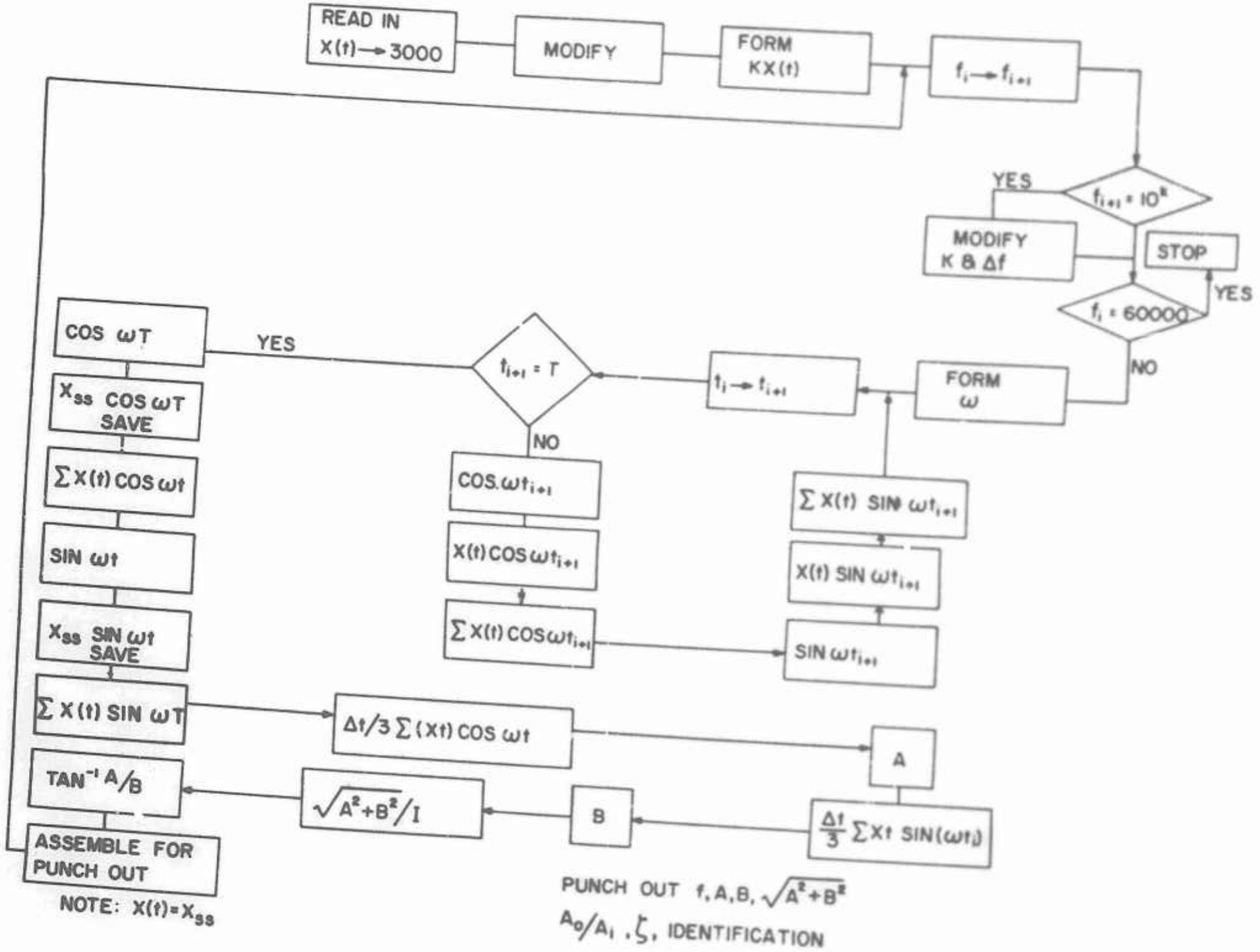
READ IN X(t)→3000
MODIFY
FORM KX(t)
$t_i \rightarrow t_{i+1}$
YES
$t_{i+1} = 10^R$
MODIFY K & Δf
STOP
t_i = 60000
YES
NO
COS ωT
YES
$t_{i+1} = T$
$t_i \rightarrow t_{i+1}$
FORM ω
X_{ss} COS ωT SAVE
Σ X(t) COS ωt
SIN ωt
X_{ss} SIN ωt SAVE
Σ X(t) SIN ωT
NO
COS ωt$_{i+1}$
X(t) COS ωt$_{i+1}$
Σ X(t) COS ωt$_{i+1}$
Σ X(t) SIN ωt$_{i+1}$
X(t) SIN ωt$_{i+1}$
SIN ωt$_{i+1}$
Δt/3 Σ (Xt) COS ωt
A
TAN^{-1} A/B
$\sqrt{A^2+B^2}/I$
B
$\frac{\Delta t}{3}$ Σ Xt SIN(ωt$_i$)
ASSEMBLE FOR PUNCH OUT
NOTE: X(t)=X_{ss}
PUNCH OUT f, A, B, $\sqrt{A^2+B^2}$
A_o/A_i , ζ, IDENTIFICATION

APPENDIX B

PROGRAM RESPONSE DATA

PHOTOGRAPH OF OSCILLOGRAPH TRACE

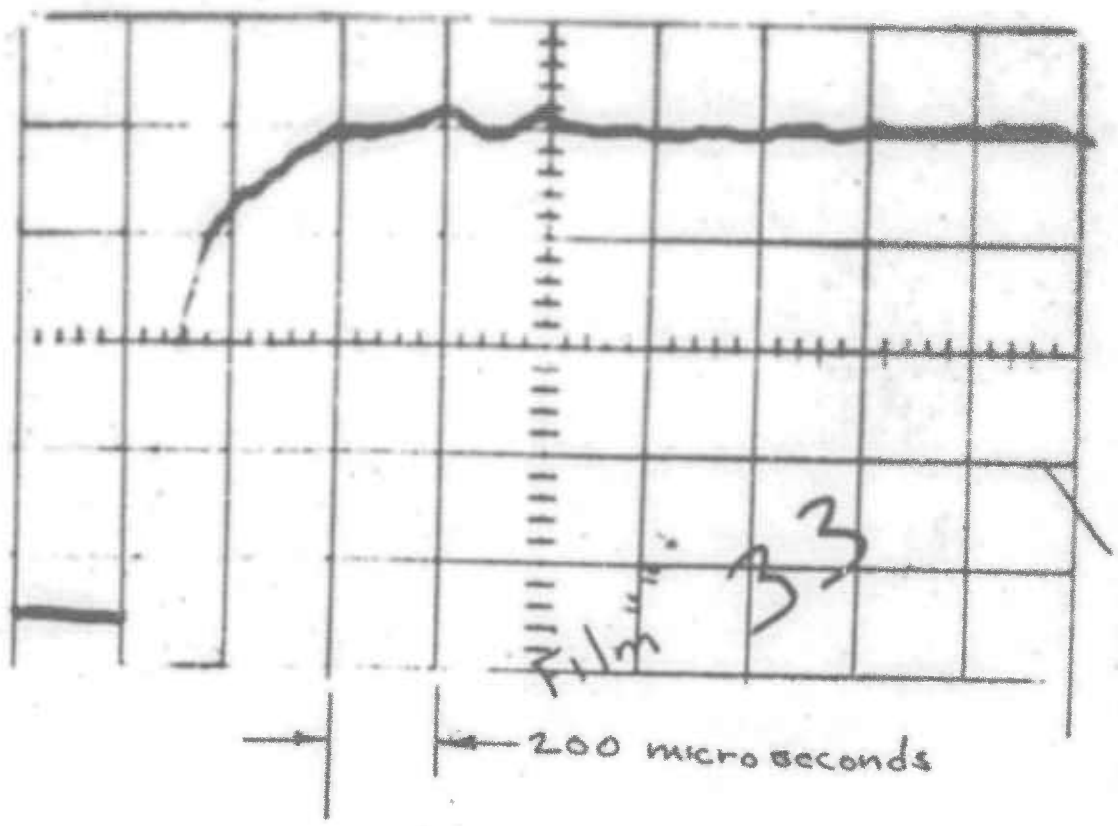

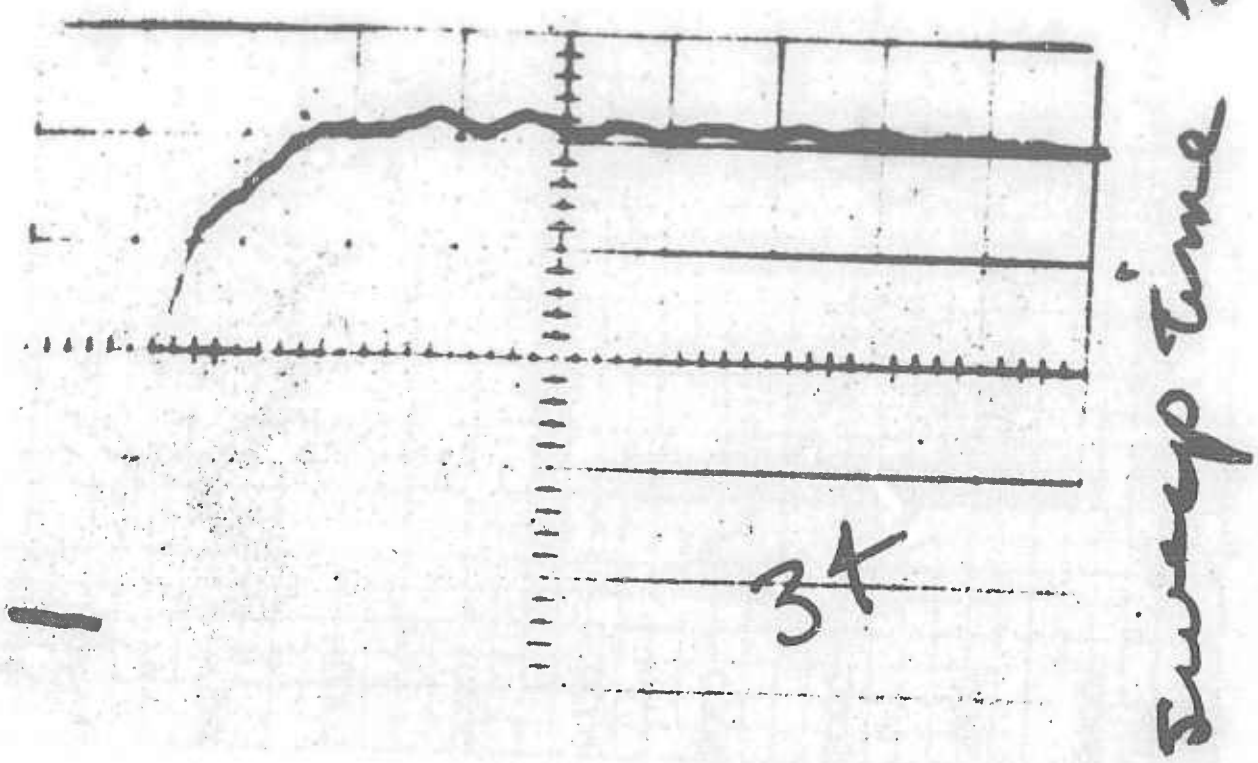

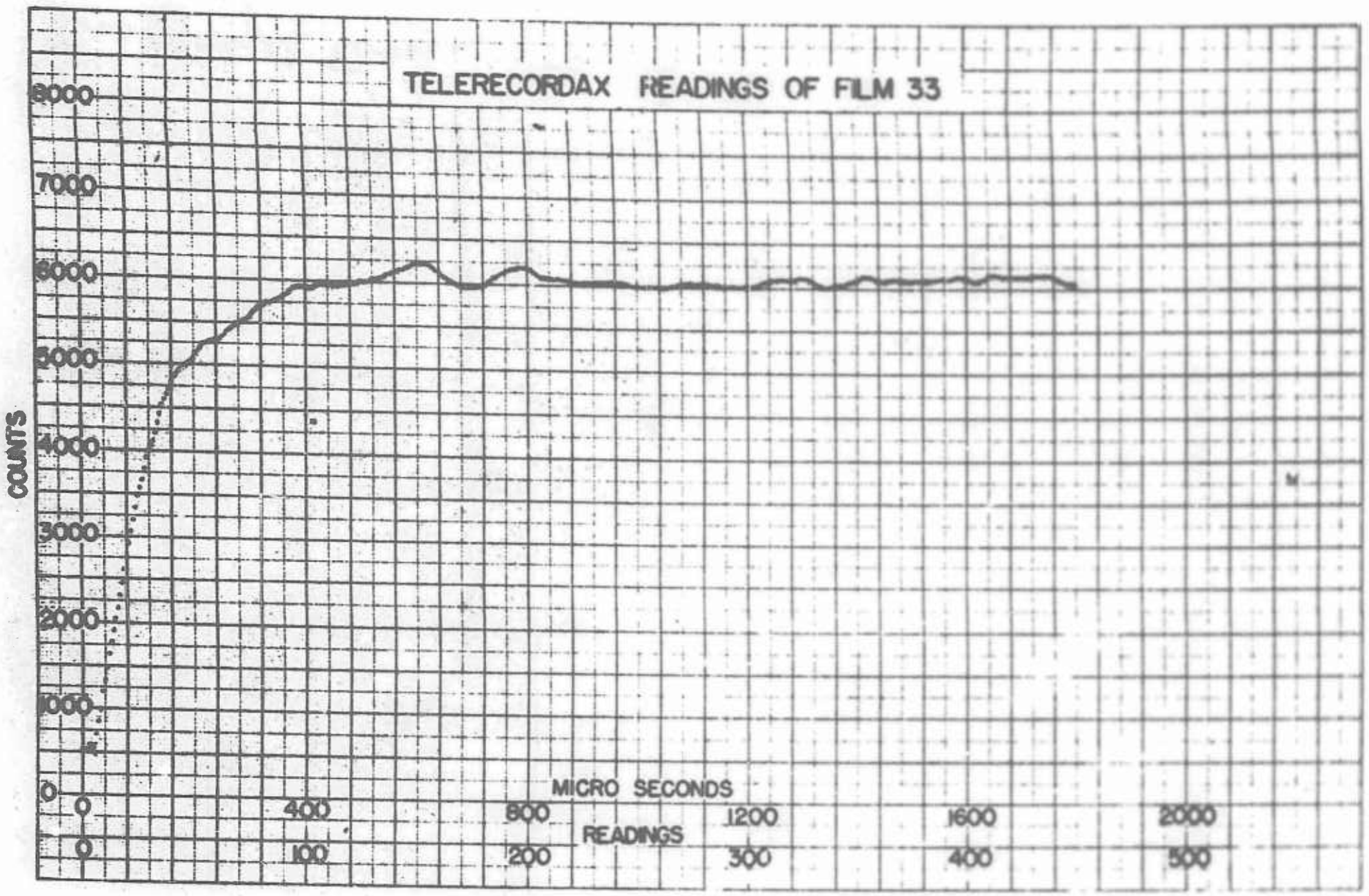
TELERECORDAX READINGS OF FILM 33
COUNTS
8000
7000
6000
5000
4000
3000
2000
1000
0
0
400
800
1200
1600
2000
MICRO SECONDS
0
100
200
300
400
500
READINGS

COMPUTER ANSWERS --FRAME 33

f CPS	A	B	$\sqrt{A^2+B^2}$	A_0/A_1	ϕ RADIANS	IDENTIFICATION FILM
1	50M	.86862	86862	1.000004	6.282609681	3310000480
2	99M	86862	86862	1.000004	6.282045569	3310000480
3	149M	86860	86860	1.000027	6.281469905	3310000480
4	198M	86862	86862	1.000004	6.280905854	3310000480
5	247M	86864	86864	.999981	6.280341791	3310000480
6	301M	86862	86862	1.000004	6.279720056	3310000480
7	350M	86858	86858	1.000050	6.279155765	3310000480
8	397M	86862	86862	1.000004	6.278614873	3310000480
9	444M	86866	86867	999947	6.278074034	3310000480
10	499M	86862	86863	999993	6.277440689	3310000480
20	995M	86869	86874	999966	6.271731786	3310000480
30	1485M	86873	86885	999739	6.266093064	3310000480
40	2011M	86880	86903	999532	6.260048585	3310000480
50	2508M	86857	86893	999647	6.254318898	3310000480
60	3018M	86863	86915	999394	6.248454931	3310000480
70	3560M	86870	86942	999084	6.242887474	3310000480
80	4082M	86902	86997	998452	6.236247384	3310000480
90	4592M	86901	87022	998165	6.230398697	3310000480
100	5108M	86878	87028	998097	6.224457856	3310000480
200	10881M	86508	87189	996254	6.158062145	3310000480
300	1657 M	84751	86355	1.005875	6.090106973	3310000480
400	21421M	81612	84376	1.029468	6.026501585	3310000480
500	25194M	78467	82412	1.054001	5.972505100	3310000480
600	.28131M	.76745	.81738	1.062692	5.931841988	3310000480
700	.32229M	.75299	.81906	1.060513	5.878764877	3310000480
800	.37597M	.71789	.81038	1.071872	5.800745917	3310000480

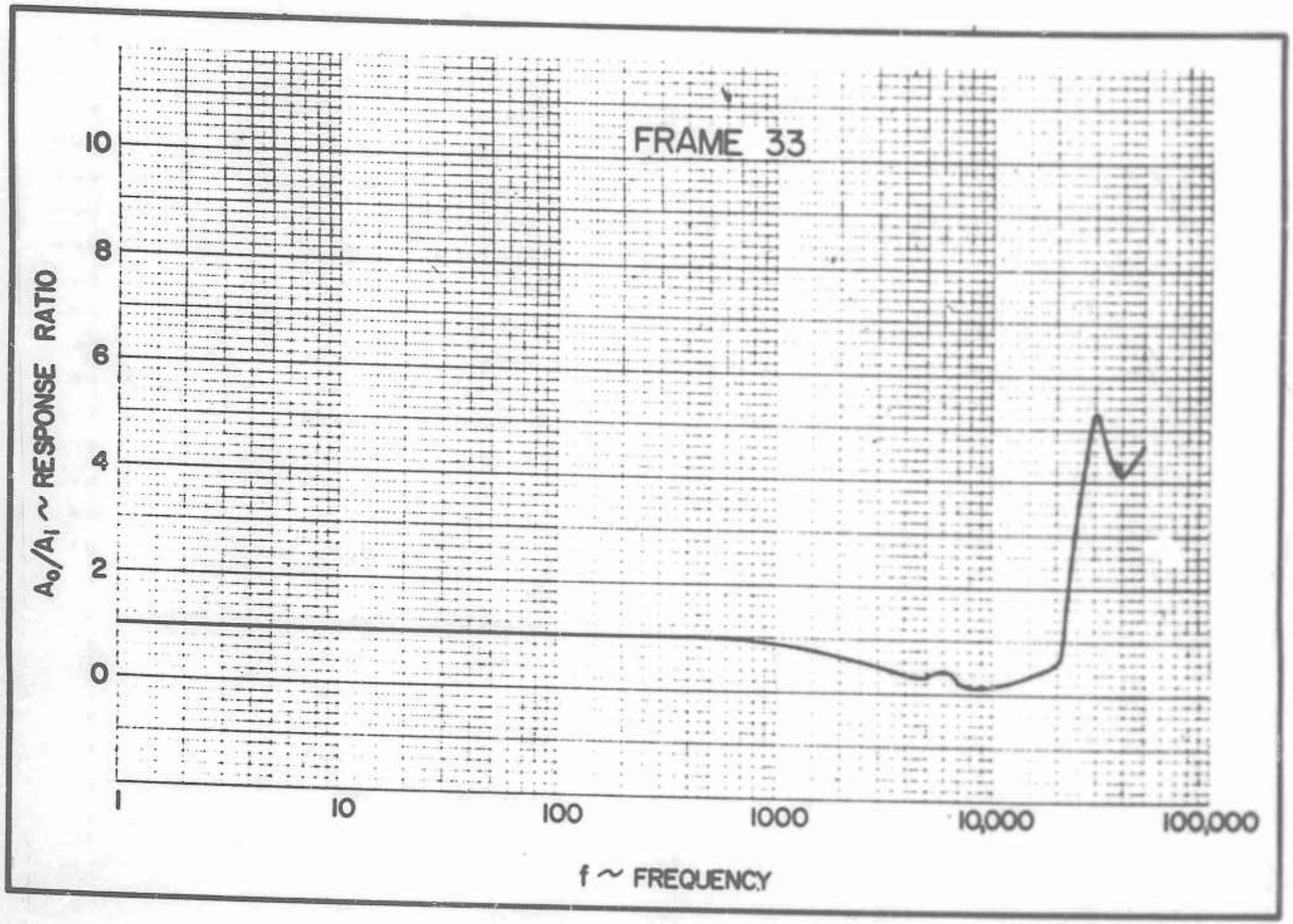
FRAME 33
10
8
6
4
2
0
A₀/A₁ ~ RESPONSE RATIO
1
10
100
1000
10,000
100,000
f ~ FREQUENCY

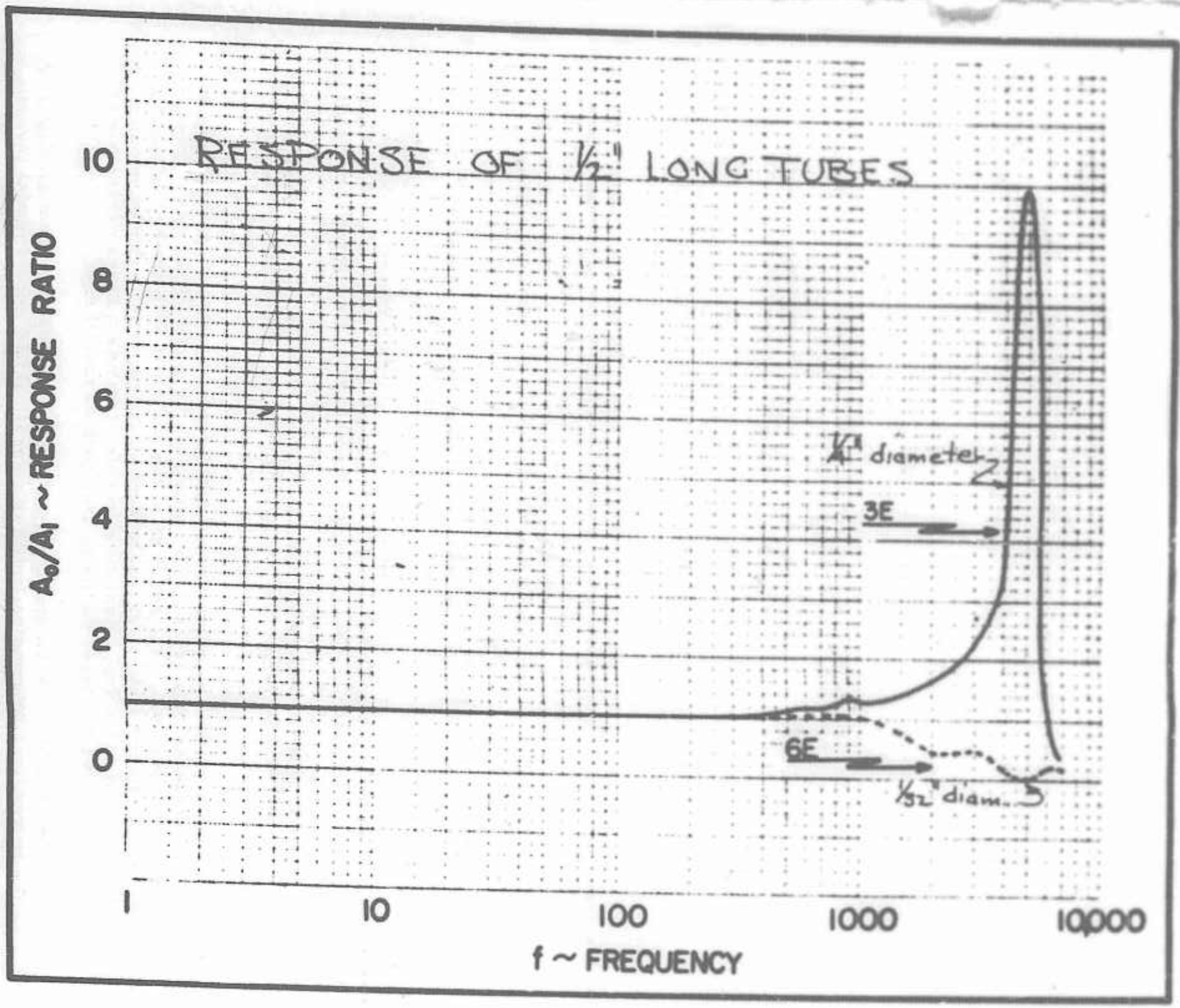
RESPONSE OF ½" LONG TUBES
10
8
6
4
2
0
A₀/Aᵢ ~ RESPONSE RATIO
¼" diameter
3E
6E
1/32" diam.
1
10
100
1000
10000
f ~ FREQUENCY

UNCLASSIFIED

AD 211239

Armed Services Technical Information Agency

ARLINGTON HALL STATION
ARLINGTON 12 VIRGINIA

FOR
MICRO-CARD
CONTROL ONLY

5 OF 6

NOTICE: WHEN GOVERNMENT OR OTHER DRAWINGS, SPECIFICATIONS OR OTHER DATA ARE USED FOR ANY PURPOSE OTHER THAN IN CONNECTION WITH A DEFINITELY RELATED GOVERNMENT PROCUREMENT OPERATION, THE U. S. GOVERNMENT THEREBY INCURS NO RESPONSIBILITY, NOR ANY OBLIGATION WHATSOEVER; AND THE FACT THAT THE GOVERNMENT MAY HAVE FORMULATED, FURNISHED, OR IN ANY WAY SUPPLIED THE SAID DRAWINGS, SPECIFICATIONS, OR OTHER DATA IS NOT TO BE REGARDED BY IMPLICATION OR OTHERWISE AS IN ANY MANNER LICENSING THE HOLDER OR ANY OTHER PERSON OR CORPORATION, OR CONVEYING ANY RIGHTS OR PERMISSION TO MANUFACTURE, USE OR SELL ANY PATENTED INVENTION THAT MAY IN ANY WAY BE RELATED THERETO.

UNCLASSIFIED

HIGH TEMPERATURE EFFECTS IN SHOCK STRUCTURE

Hari K. Sen and Arnold W. Guess
Geophysics Research Directorate, AFCRC

I. INTRODUCTION

The purpose of this paper is to motivate discussion rather than to give definite conclusions. In view of the extensive developments in the subject matter of the paper, we shall not attempt to be exhaustive. We will only mention some effects of high temperature on the structure of a shock front, that appeared interesting to us and have been engaging our attention for some time. Further, stress will be laid on physical theory, as it is hoped that other papers in the Symposium will cover some of the experimental aspects.

Even a casual student of hydrodynamics would discern three stages in its development: (1) classical hydrodynamics of the incompressible liquid, (2) aerodynamics of a compressible gas, and (3) high temperature gas dynamics. The last is the phase of development occasioned by the circumstances of the present age, e.g., extreme hypersonic flight. Of this last phase, von Karman says[1], "The air dissociates at these temperatures and we have an extremely complicated problem of aerothermochemistry eventually involving also magnetoaerodynamics if ionized particles are present. It is certainly a problem that constitutes a challenge to the best brains working in these domains of modern aerophysics".

One of the most important effects of high temperature on gas dynamics is the accentuation of the molecular against a continuum treatment.[2] New parameters of length and time are added to those of old. The relaxation time covers not only collisional processes, but also rotation, vibration and dissociation of the molecular,[3] chemical reaction rates,[4] and finally ionization.[5] To the collisonal mean free path as a standard of length are added other quantities (under proper conditions), e.g., the mean free path scaled by the inverse of the Pradtl number (when the gas is ionized)[6], the Debye length (when there is charge separation)[7], and the gyro-radius (in the presence of a magnetic field)[8].

In the propagation of an intense shock wave, another important effect of high temperature manifests itself, which has been one of the prime interests of the authors, viz., the coupling of the radiation with the hydrodynamic field. The radiation field is characterized by the pressure, energy density and transport of radiation. Radiative transfer imports a fresh parameter of length into shock structure: the mean free path of radiation.

The possibility of obtaining electromagnetic radiation from an electron plasma is a further interesting field for theoretical and experimental investigation. A plasma in a shock tube may play an important role as a generator of sub-millimeter waves - the no man's land between the limits of infrared

and electronic techniques[9]. Such an investigation will also throw light on theories of the generation of solar radio noise in shock fronts[10].

II. IONIZATION AND SHOCK STRUCTURE

Apart from the effect of ionization relaxation on extending the width of the shock front ionization in itself broadens the shock front on account of two causes. The first[11] is the long range of the Coulomb forces, that makes the viscosity go as a higher power of the temperature[12] (viz., 2.5) than for a non-ionized gas. The increased viscosity extends the region of influence of the shock wave.

Figure 1 shows the width of shock for a plasma (macroscopically neutral, ionized gas) in terms of the mean free path with the shock as a unit of length[11]. h_o is a measure of the ratio of the magnetic to the internal energy per unit mass. We shall restrict our consideration to the case $h_o = o$ (Curves I and II) (plasma without a superposed magnetic field).

Figure I can be compared with corresponding computations for air.[13] We see that ionization considerably increases the width of the shock front.

Curve II is based on the Navier-Stokes equations. As these do not hold for strong shocks,[14] where the physical va .ables change appreciably within a mean free path, the Mott-Smith interpolation formula[32] is used for high Mach numbers (Curve I). Curves I and II join smoothly at $M \approx 1.3$. For stronger shocks, Curve I lies above II, indicating that the Navier-Stokes equations give a sort of lower limit to the shock thickness. However, the Mott-Smith analysis gives a finite[15] to the shock thickness as the Mach number $M \longrightarrow \infty$, whereas the Navier-Stokes equations give an infinite limit.[13]

The second factor that is responsible for the broadening of the shock front in a plasma is the low value of the Prandtl number[6],

$$P = \mu C_p / \lambda \qquad (2.1)$$

where μ and λ are respectively the coefficients of viscosity and thermal conductivity, and C_p is the specific heat at constant pressure. The reason for the diminution of the Prandtl number for a plasma is the following:

The plasma is a mixture of two particles viz., ions and electrons, that have very different masses. The momentum (viscosity) is carried principally by the heavier particles, i.e. the ions, whereas the thermal energy (conductivity is carried mostly by the more mobile electrons. For completely ionized atomic hydrogen, for example, we have[16]

$$\mu = 0.96 \mu_i, \quad \lambda = 14 \lambda_i, \qquad (2.2)$$

where the suffix i refers to the proton.

Thus, the Prandtl number, $P = \frac{0.96}{14} \cdot \frac{\mu_i C_p}{\lambda_i}$ (2.3)

We may take the Prandtl number for the proton[17]

$$\frac{\mu_i C_p}{\lambda_i} = \frac{2}{3} . \tag{2.4}$$

Hence, we have the Prandtl number for a proton-electron plasma $\simeq$ 1/20, as against the value 2/3 for a pure gas.

We wish to make two remarks in this connection. Charge separation in a plasma will produce an electrostatic field which will reduce the thermal conductivity by a factor of the order of one-half.[18] This will increase the Prandtl number for a proton-electron plasma to a value $\simeq$ 1/10.

Further, we have so far assumed ionization equilibrium. So long as ionization equilibrium is not attained, it appears that the ions will be at a higher temperature than the electrons in the shock front.[19] The electrons also will have a lower temperature gradient. Both these effects will tend further to increase the Prandtl number toward its original one-particle value.

Both Marshall's[6] and the authors' computations* indicate that the diminution of the Prandtl number by an order of magnitude will considerably increase the width of the shock front in a plasma. This increment in the shock width will extend the range of validity of the Navier-Stokes equations towards higher Mach numbers. In view of the considerable uncertainties over the respective spheres of applicability of the Navier-Stokes equations and the higher order kinetic theory approximations, both in theory and in experiment,[20] it would be worth while to devise an experiment to measure the shock width in a plasma.

III. RADIATION EFFECTS ON SHOCK-WAVE STRUCTURE

The usual hydrodynamic equations, modified by the inclusion of radiation pressure and energy density, lead to the extended Rankine-Hugoniot conditions first obtained by Sachs[21] from pure conservation laws. Radiation pressure and energy density become appreciable at a temperature of a few million degrees in air of atmospheric density, and must be considered along with material gas pressure and internal energy. This effect is well known to the astrophysicist, and forms an integral part of the theory of stellar structure.[22]

The pressure and energy density of radiation can be included formally in the analysis by considering the total (material gas + radiation) pressure and energy and an "effective" ratio of specific heats of gas and radiation, which is a function of the material ratio of specific heats (γ) and the ratio of radiation gas to pressure. It is interesting to note that the velocity of sound is changed in such a composite medium (material + radiation).

*See Table I in Sec. III.

At lower temperatures where radiation pressure and energy density are no longer appreciable, radiation may still exert its influence through a third characteristic, viz., radiative transport of energy. The over-all effect of radiative transfer, in a diffusion approximation, can be taken as a diminution of the Prandtl number and makes the shock front wider than when viscosity and heat conduction alone are considered.[23] The radiative contribution to the width of the shock is found to depend primarily on the ratio of the mean free path of radiation to that of the material particles. It is conceivable that in a rarefied atmosphere (extremely high altitudes) the mean free path of radiation and, consequently, the shock width may be so great as virtually to nullify the shock.

We shall develop first the equations for a shock wave with the inclusion of the effects of radiation in local thermodynamic equilibrium. The shock is taken as plane, steady and propagating non-relativistically along the x-axis. The flow is make time independent by referring to a coordinate system moving with the shock front. The suffixes 0 and 1 are used to denote the physical variables (velocity u, material gas pressure p, density ρ, and temperature T) in front and in back of the shock, respectively. The following equations then describe the flow.

The equation of conservation of mass is

$$\rho_u = \rho_o u_o = m, \text{ say.} \tag{3.1}$$

The Stokes-Navier equation is

$$m\frac{du}{dx} = -\frac{d}{dx}\left(p + \frac{a}{3}T^4\right) + \frac{4}{3}\frac{d}{dx}\left(\mu\frac{du}{dx}\right). \tag{3.2}$$

The equation of conservation of energy is

$$m\frac{d}{dx}\left(D + \frac{aT^4}{\rho}\right) = \frac{d}{dx}\left(k\frac{dT}{dx}\right) - \left(p + \frac{a}{3}T^4\right)\frac{du}{dx} + \frac{4}{3}\mu\left(\frac{du}{dx}\right)^2 - \frac{dF}{dx}, \tag{3.3}$$

$\frac{a}{3}T^4$ and $\frac{aT^4}{\rho}$ are the radiation pressure, and radiation energy per unit mass; and are added to the material pressure, p, and the internal energy, E, respectively. μ and k are the coefficients of viscosity and heat conductivity, respectively. F is the radiation flux and a is the radiation constant.

Equations (3.2) and (3.3) may be integrated to give

$$mu - mC = -\left(p + \frac{a}{3}T^4\right) + \frac{4}{3}\mu\frac{du}{dx}, \tag{3.4}$$

and

$$m\left(E + \frac{aT^4}{\rho}\right) = k\frac{dT}{dx} + \frac{m}{2}u^2 - mCu - F - C_1, \tag{3.5}$$

where C and C_1 are constants of integration.

The Rankine-Hugoniot conditions are obtained by assuming uniform conditions in front and in back of the shock. Application of (3.4) and (3.5) gives, respectively,

$$(p_o + \frac{a}{3} T_o^4) + m u_o = mC = (p_1 + \frac{a}{3} T_1^4) + m u_1 \tag{3.6}$$

and

$$m(E_o + \frac{aT_o^4}{\rho_o}) - \frac{m}{2} u_o^2 + mCu_o + F_o = -C_1 = m(E_1 + \frac{aT_1^4}{\rho_1}) - \frac{m}{2} u_1^2 + mCu_1 + F_1. \tag{3.7}$$

The term $(F_1 - F_o)$ in equation (3.7) represents the "radiation escape" (assumed to be small compared to the radiation energy). Equation (3.1) gives

$$\rho_o u_o = m = \rho_1 u_1. \tag{3.8}$$

Equations (3.6), (3.7) and (3.8) are equivalent (except for the term, $F_1 - F_o$) to the radiation Rankine-Hugoniot equations obtained by R. G. Sachs[21].

The Mach number of the shock may be defined in the usual manner, $M_o = |u_o|/c_o$ where c_o is the velocity of sound in the medium in front of the shock. However, in the present situation,

$$c_o^2 = \left[\frac{\partial(p_o + \frac{a}{3} T_o^4)}{\partial \rho_o}\right]_S \tag{3.9}$$

the subscript S indicating that the differentiation is to be performed for constant entrophy (S). Assuming the material gas to be perfect with ratio of specific heats γ, the equation for sound velocity becomes[23]

$$c_o^2 = \frac{p_o}{\rho_o}\left[\frac{\gamma + 20(\gamma - 1) + 16(\gamma - 1)\eta^2}{1 + 12(\gamma - 1)\eta}\right], \tag{3.10}$$

where

$\eta = \frac{a}{3} T_o^4 / p_o$ = radiation pressure/material gas pressure.

As $\eta \to o$, $c_o^2 \to \gamma p_o/\rho_o$ which is the usual expression for the material gas. As $\eta \to \infty$, $c_o^2 \to 4/3 (\frac{a}{3} T_o^4)/\rho_o$ (if $\gamma > 1$), showing that radiation behaves like a perfect gas with $\gamma_{rad} = 4/3$. In fact, equation (3.10) can expressed as $c_o^2 = \Gamma P_o/\rho_o$, where Γ is an "effective" ratio of specific heats for material gas and radiation, and P_o is the total (radiation plus gas) pressure. The situation is similar to what obtains in magneto-gas-dynamics.[24]

In the remainder of this section, we will briefly review the analysis and computations for the actual shock structure for a simple model.[23] Take the diffusion approximation for radiation flux,

$$F = -\frac{4a\,c\,T^3}{3\rho\kappa}\,\frac{dT}{dx}\,, \tag{3.11}$$

and the perfect gas law

$$p = R\rho T, \qquad E = C_v T. \tag{3.12}$$

Then equations (3.4) and (3.5) may be combined to give

$$\frac{dT}{du} = \frac{4\mu}{3k}\,\frac{m(C_v T + a\,T^4\,u/m) - mu^2/_2 + mC\,u + C_1}{(RmT/u + aT^4/_3) + m\,u - mC}\cdot g \tag{3.13}$$

where

$$g = \frac{1}{1 + \frac{4\,ac\,u}{3\kappa\,mk}\,T^3} = \frac{1}{1 + \frac{4P}{\delta}\cdot\frac{\gamma-1}{\gamma}\cdot\frac{c}{\bar{c}_o}\cdot\frac{p_{Ro}}{p_o}\cdot\frac{\lambda_{Ro}}{\lambda_o}\,U^{\alpha+1}\,\pi^{3-\beta-\eta}}, \tag{3.14}$$

and is called the radiation broadening factor. Here, c is the velocity of light, κ is Rosseland mean absorption coefficient, δ is a constant, P is the Prandtl number, $\bar{c}_o$ is the mean particle velocity and p_{Ro} and λ_{Ro} are the radiation pressure and (radiation) mean free path in front of the shock. Also $U = u/u_o$, $\pi = T/T_o$; and n, β and α are the exponents of temperature and density variation in k and κ.

In the denominator of the radiation broadening factor, $g(\pi, U)$, appears the fraction, $\frac{c}{\bar{c}_o}\cdot\frac{p_{Ro}}{p_o}\cdot\frac{\lambda_{Ro}}{\lambda_o}$, which is essentially a measure of radiation effects to particle effects. $c/\bar{c}_o$ is always quite large while p_{Ro}/p_o will be quite small. λ_{Ro}/λ_o (ratio of radiation mean free path to particle mean free path) will be small when radiation transport effects are negligible, but will grow when radiative transport of energy becomes important compared with thermal conduction. The radiation broadening factor $g(\pi, U)$ approaches unity for the pure material gas, but when radiative transport effects are important, $g(\pi, U)$ is temperature and velocity dependent and may become quite small.

In order to gain a general idea of the shock structure we have taken

$$g(\pi, U) = \frac{1}{1 + U^2\,\pi^4}$$

as the form of the radiation broadening factor for computational purposes. The values $\gamma = 5/3$, $\eta = 2.5$, $\alpha = 1$ and $\beta = 3.5$ were taken, representing a Kramers opacity law in an electron-ion plasma. Equation (3.13) was solved numerically with the neglect of radiation pressure and energy density, and subsequently equation (3.4) was solved. Results are given in Fig. 2 in

which the actual shock structure is plotted in terms of the mean free particle path in front of the shock for a Mach number of 2 and a Prandtl number of 3/4. The effect of radiative transfer is to considerably broaden the shock-wave.

Finally, in Table I are presented the results of the computation for the width of the shock. The suffix R refers to inclusion of the radiation broadening factor.

Table I. Width of shock (t) in terms of mean free particle path (λ). The suffix zero refers to front of shock, and R to radiation.

Prandtl No.	M_o	t_o	t_{oR}	t_λ	$t_{\lambda R}$	$t_{\lambda R}/t$
0.75	1.5	9.5	27.3	8.3	23.7	2.9
	2	8.5	31.4	5.9	21.7	3.7
	2.5	9.7	40.8	5.0	20.9	4.2
	4	14.7	87.8	2.6	15.7	6.0
0.075	1.5	43.7	75.1	37.9	65.2	1.7

The last three columns of Table I are perhaps the most interesting. They show that, both with and without radiation, the shock width (in terms of mean free path within the shock front) decreases with increasing Mach number. However, the proportional increase in shock width due to radiation increases with increasing Mach number.

IV. RADIATION EFFECTS ON RANKINE-HUGONIOT CONDITIONS

The complete Rankine-Hugoniot conditions, with the inclusion of all radiation effects were presented in Section III. Sachs has examined the effect of radiation pressure and energy density; we will examine here the effect of "radiation escape". Radiation transfer and radiation escape can be important even when radiation pressure and energy density are negligible. This situation will be examined in two extreme limits: those of small and of large radiation escape. Finally, strong shocks in air will be considered with an approximating function for the radiation flux.

In the present situation, the Rankine-Hugoniot conditions (from equations (3.8), (3.6) and (3.7) are:

$$\rho_o u_o = m = \rho_1 u_1 \tag{4.1}$$

$$m u_o + p_o = mC = m u_1 + p_1 \tag{4.2}$$

and

$$m E_o - \frac{m u_o^2}{2} + m C u_o = -C_1 = m E_1 - \frac{m u_1^2}{2} + m C u_1 + F_E, \tag{4.3}$$

with the neglect of radiation pressure and energy density.*

$F_E = F_1 - F_o$ is the radiation flux escaping to great distances in front of the shock wave. The perfect gas laws: $p = R\rho T$, $E = C_v T$, and the dimensionless parameters: $\pi_1 = T_1/T_o$, $U_1 = u_1/u_o$, $M_o^2 = u_o^2/c_o^2 = u_o^2/\gamma RT$, will be used. Equations (4.1) and (4.2) may then be solved to give

$$\pi_1 = U_1 (\gamma M_o^2 + 1) - \gamma M_o^2 U_1^2. \tag{4.4}$$

Eliminating π_1 between equations (4.4) and (4.3) gives

$$U_1^2 \frac{\gamma+1}{2} - U_1 (\gamma + \frac{1}{M_o^2}) + \frac{\gamma-1}{2} - \frac{F_E (\gamma - 1)}{m u_o^2} + \frac{1}{M_o^2} = 0, \tag{4.5}$$

of which the physically acceptable root is

$$U_1 = \frac{\gamma + 1/M_o^2 - \sqrt{(1-1/M_o^2)^2 + 2 F_E (\gamma^2 - 1)/m u_o^2}}{\gamma + 1}. \tag{4.6}$$

The other root leads to $U_1 > 1$, or a rarefaction wave. Equations (4.4) and (4.6) are the exact expressions for the temperature and velocity prarmeters behind the shock when "radiation escape" is included. Note, from equation (4.6), that there is always a decrease in flow velocity (and therefore an increase in compression) behind the shock when "radiation escape" is included.

In the limit of small radiation flux escape (i.e., specifically for $2F_E/mu_o^2 \ll \frac{(M_o^2 - 1)^2}{M_o^4 (\gamma^2 - 1)}$, equation (4.6) becomes

$$U_1 = \frac{\gamma - 1}{\gamma + 1} + \frac{2}{M_o^2 (\gamma + 1)} - \frac{F_E (\gamma - 1)}{m u_o^2} \cdot \frac{M_o^2}{M_o^2 - 1}, \tag{4.7}$$

if we use the first order term in the square root expansion. If U_{1H} is defined as the pure hydrodynamic velocity parameters (no radiation escape), then

$$U_{1H} = \frac{\gamma - 1}{\gamma + 1} + \frac{2}{M_o^2 (\gamma + 1)}. \tag{4.8}$$

The difference between equations (4.7) and (4.8) is then

$$U_{1H} - U_1 \simeq \frac{F_E (\gamma - 1)}{m u_o^2}. \tag{4.9}$$

*Under these circumstances, the assumption of local thermodynamic equilibrium is no longer necessary.

In like manner, the pure hydrodynamic temperature parameter (no radiation escape) may be defined as

$$\pi_{1H} = U_{1H}(\gamma M_o^2 + 1) - \gamma M_o^2 U_{1H}^2. \tag{4.10}$$

Equations (4.10), (4.4), (4.7) and (4.8) may be combined to give

$$\pi_{1H} - \pi_1 \simeq \frac{F_E \gamma M_o^2 (\gamma - 1)(3 - \gamma)}{m u_o^2 (\gamma + 1)} \tag{4.11}$$

Equations (4.9) and (4.11) represent the difference between the pure hydrodynamic case and the radiation escape case for the velocity and temperature parameters. They are approximate expressions for $F_E/m u_o^2 \ll$ and $M_o^2 \gg 1$. Comparison of equation 4.9 with equation (4.11) indicates that the decrease in velocity discontinuity at the shock front depends only on the ratio $F_E/m u_o^2$. On the other hand, the decrease in temperature discontinuity depends on γM_o^2 times this ratio. Hence for strong shocks with small radiation escape, the flow will not appreciably be affected while the temperature will be decreased by a large amount from its usual hydrodynamic value. In this case, the compression ratio also will be relatively unaffected as follows from equation (4.1).

The absolute upper limit for the magnitude of the radiation flux escape occurs when the shock becomes "isothermal", i.e., when the radiation escaping through the shock front reduces the temperature behind it to such an extent that there is essentially no temperature jump across the front. The actual realization of an isothermal shock is not possible, but the situation may be approached if the opacity of the gas is quite small. The usual hydrodynamic shock may be termed an "adiabatic" shock.

The condition for the shock to be isothermal is,

$$\pi_1 = 1. \tag{4.12}$$

Equation (4.4) may then be solved to give the physically acceptable root for such a shock wave,

$$U_1 = RT_o/u_o^2. \tag{4.13}$$

Substituting this value of U_1 into equation (4.5) gives a radiation flux escape of

$$F_E = \frac{m u_o^2}{2}\left[1 - \frac{R^2 T_o^2}{u_o^4}\right] \tag{4.14}$$

This value of F_E is the absolute maximum of flux transport to great distances in any situation. Note that this flux is always less than the kinetic energy flow term, $m u_o^2/2$. For extremely strong shocks, almost the entire

kinetic energy is converted into radiation flux. Further, the mass compression ratio, $\rho_1/\rho_o = 1/U_1 = u_o^2/RT_o$ (from equation (4.13)) becomes large for large Mach numbers. The Mach number for an isothermal shock is defined by $M_o^2 = u_o^2/RT_o$.

For strong shocks in air, radiation flux escape may have a significant effect on the Rankine-Hugoniot conditions. The strong shock conditions are: $T_1 >> T_o$, $p_1 >> p_o$ and $E_1 >> E_o$ (however, $\rho_1 \simeq \rho_o$). The Rankine-Hugoniot conditions (from equations (3.6) and (3.7) are then:

$$mu_o = (p_1 + \frac{a}{3} T_1^4) + mu_1 \tag{4.15}$$

and

$$\frac{m}{2} u_o^2 = m (E_1 + \frac{aT_1^4}{\rho_1}) + \frac{m}{2} u_1^2 + p_1 u_1 + \frac{a}{3} T_1^4 u_1 + F_E, \tag{4.16}$$

where

$$m = \rho_o u_o = \rho_1 u_1.$$

We will take

$$F_E = \frac{a c T_1^4}{4 \left[1 + T_1/2 \times 10^4\right]^{2.65}}. \tag{4.17}$$

which approximates the radiation flux escape, F_E, by black body radiation with a sharp cutoff at 1860 A (depletion of ultraviolet).

Equations (4.15) and (4.16) may be put into the forms

$$U_o^2 = \frac{A^2}{A - 1} (\frac{p_1}{\rho_1} + \frac{a}{3} \frac{T_1^4}{\rho_1}) \tag{4.18}$$

and

$$A = \frac{2 E_1 \rho_1 + p_1 + \frac{7aT_1^4}{3}}{p_1 + \frac{a}{3} T_1^4 - 2F_E/u_o}, \tag{4.19}$$

where

$$A = \rho_1/\rho_o = \text{compression ratio.} \tag{4.20}$$

Using a table of thermodynamic properties of air, equations (4.18), (4.19) and (4.20) may be solved by iteration for a specified ambient density (ρ_o) and temperature behind shock (T_1). Some sample results are given in Table II.

Table II. Thermodynamic parameters for strong radiative shocks in air. h is the altitude above sea level that ρ_o corresponds to.

ρ_o(gm/cm^3)	h(ft)	T(°K)	A	u_o(cm/sec)	F_E(ergs/cm^{2}sec)	M_o
1.10×10^{-3}	4×10^3	10^4	11.65	7.27×10^5	1.94×10^{11}	21.7
		1.3×10^4	12.37	9.51×10^5	4.30×10^{11}	28.4
		10^3	9.83	4.14×10^6	4.91×10^{13}	123
		10^6	7.44	1.84×10^7	1.69×10^{15}	550
3.11×10^{-4}	4×10^4	10^4	12.82	8.00×10^5	1.94×10^{11}	27.1
		1.1×10^4	13.11	8.85×10^5	2.60×10^{11}	30.0
		10^5	10.01	4.51×10^6	4.91×10^{13}	153
		10^6	7.82	1.97×10^7	1.69×10^{15}	668
1.67×10^{-3}	10^5	10^4	15.18	9.50×10^5	1.94×10^{11}	31.0
		10^5	11.40	5.50×10^6	4.91×10^{13}	180
		10^6	8.13	2.46×10^7	1.69×10^{15}	804
1.26×10^{-6}	1.6×10^5	10^4	20.11	1.11×10^6	1.94×10^{11}	33.0
		1.5×10^4	21.02	1.59×10^6	6.51×10^{11}	47.2
		10^5	16.33	7.00×10^6	4.91×10^{13}	208
		10^6	7.39	5.21×10^7	1.69×10^5	1550
4.11×10^{-8}	2.5×10^5	10^4	84.64	2.27×10^6	1.94×10^{11}	80.8
		1.2×10^4	88.59	2.74×10^6	3.38×10^{11}	97.6
		10^5	64.31	1.45×10^7	4.91×10^{13}	517
		10^6	7.04	2.68×10^8	1.69×10^5	955

With this model, it is seen that the compression ratio ($A = \rho_1/\rho_o$) becomes larger for low ambient densities. The maximum value of A obtained by computation for each ambient density, is included in Table II. Also, note that the compression ratio approaches the value seven for high temperatures in each density case. This is a result of the increasing importance of radiation pressure.

The effect of "radiation escape" on the Rankine-Hugoniot conditions is thus found to be a lowering of the temperature jump across the shock and an increase in the compression ratio. This result may have interesting astrophysical applications, e.g. in the interpretation of double spectral lines in

Cepheids,[25] and large density fluctuations in interstellar gas clouds.[26] Further, the large compression brought about by sufficiently fast radiation escape makes shock amplification of a magnetic field in a highly conducting plasma an interesting possibility. Ordinarily, such amplification is limited by the finite compression ($(\gamma + 1)/(\gamma - 1)$) across the shock front.[27] Such amplification, if possible, would have useful applications in laboratory and cosmic physics.

V. ELECTROMAGNETIC RADIATION FROM AN ELECTRON PLASMA

The question under what conditions an electron plasma can radiate electromagnetic energy that can escape out of the plasma atmosphere is an interesting but as yet unsolved problem. The problem, when solved, would have important applications as a laboratory source of sub-millimeter waves and in astrophysical theories of the generation of solar radio noise. High enough ion densities can be obtained in shock tubes[9] for plasma wave lengths of 50μ to 500μ. Ionization relaxation may widen the shock fronts in a plasma to the order of a few microns.[28] There is thus good possibility for the matching of the plasma wave length with the shock width, which would favor the generation of sub-millimeter waves.

The sun during disturbed periods sends out bursts[29] of microwave noise in the meter wavelengths, that interpreted in terms of Planckian temperature amounts to a very high order of magnitude (10^8 - 10^{13} °K). This has led several workers to suggest a non-equilibrium process for the origin of these bursts. An important mechanism that has been extensively discussed in the literature is space-charge wave amplification in moving plasmas.[30] Denisse and Rocard[10] attributed the bursts to the excitation of electronic oscillations by shock fronts propagating in the solar atmosphere, that may very well be regarded as a highly ionized plasma. These shock waves could arise by several means, such as corpuscles shot out during solar flares that give rise to magnetic storms and aurorae, ejection of spicules, prominence motion, etc.

Denisse and Rocard showed that the electron velocity distribution in the shock front propagating in a plasma would not remain Maxwellian, but would develop a secondary hump at a velocity exceeding the mean thermal electron motion. The latter is the criterion stated by Landau[31] for space charge wave amplification in moving, interacting plasmas. Hence, they concluded that electronic oscillations would be excited by the fast moving electrons in the secondary hump, and applied their theory to explain the observed fine structure of solar radio noise.

Denisse and Rocard, however, used the Enskog-Chapman approximation in their analysis. Wang Chang[14] had pointed out that the Enskog-Chapman method, on account of its slow convergence, was applicable only to very weak shocks. Mott-Smith[32] had indicated a promising method to find the velocity distribution for a strong shock. He remarked, "A considerable number of the Maxwellian molecules of the bounding supersonic and subsonic streams penetrate into the shock." He therefore assumed the required velocity distribution function to be a sum of two Maxwellian terms with temperatures and mean velocities corresponding to the subsonic and supersonic streams. Sen[10] applied

the Mott-Smith interpolation formula to extend the Denisse-Rocard conclusions to strong shocks as well, and obtained frequency bandwidths of amplifications that decreased with the shock strength. It was believed that the discontinuity at the shock front would favor conversion of space charge wave energy into electromagnetic radiation.

There is, however, a difficulty in the above method of approach, that requires clarification, viz., the wide disparity in the plasma wavelength ($\sim$ meter) and the shock width (mean free path $\sim$ kilometer) in the solar atmosphere. It appears to the authors that the difficulty may be resolved by a result obtained by Cowling[33] in a very early paper, in which he discussed the influence of diffusion on the propagation of shock waves through a gas-mixture.

The differences of pressure (and temperature) in a shock wave give rise to diffusion. The direction of the diffusion is such that the heavier particles move towards the higher pressure (and temperature) regions. The effects are small when the masses of the components of the mixture are not appreciably different. But when there is a large mass ratio, diffusion effects are quite comparable with those of viscosity and thermal conduction in shock propagation. Cowling makes the following remarks in his paper, that are relevant to our case: "There is observational evidence of the existence of velocities comparable with the velocity of sound in stellar atmospheres; in the resulting shock waves the mutual diffusion of ions and electrons would be important".

Cowling considered a gas-mixture of hydrogen and oxygen molecules. In a plasma, a separation of the ions from the electrons will polarize the medium and create and electrostatic field which will work against the charge separation. Denisse and Rocard[10] estimated that the electric polarization would be a very effective means of limiting the diffusion effects in the solar atmosphere. They however conceded that the polarization could be important in an atmosphere more concentrated than the solar.*

Experiments at Los Alamos[28] indicated the existence of a positive electric potential in strong gaseous shock fronts, the strength of the potential increasing rapidly with the shock strength. Bond,[28] by a theoretical analysis based on ionization relaxation, obtained results in qualitative agreement with these experiments. The ionization starts from atom-atom collisions and subsequently builds up rapidly behind the shock by electron-atom collisions. This creates an electron density gradient in the gas, that makes the electrons diffuse out to the front. The ions, on account of their greater mass, do not share in this diffusion. The consequent charge separation and electric field soon prevents the electron diffusion.

---

*The authors have made a self-consistent field analysis of the electric field due to diffusion in a shock front. The analysis points to certain interesting considerations as to whether the Debye length should be the limiting distance for charge separation in a plasma shock. As the computations are not yet complete, the results are not reported in this paper.

Bond found the charge density due to the diffusion of electrons toward the shock front to be relatively small and to occur in a distance roughly of the order of the Debye length. Hence, a positive potential difference and a large electric field was established in the shock front. Bond used his analysis to estimate the time required to reach ionization equilibrium behind a strong shock wave in argon. Petschek[19] reconsidered the problem, taking account of the fact that in ionization by electron-atom collisions, the electrons have inelastic collisions that cool them to a lower temperature than the atoms. He performed diffusion potential measurements and obtained the electron density gradient from the electric field. This was found to be in agreement with the values obtained from measurements of the intensity of the continuum radiation from the gas.

The possiblity of obtaining electron density gradients and electric fields within a Debye distance in a shock front in a plasma makes the conditions for space charge wave amplification in shock waves in the solar atmosphere much more favorable. The Debye length, h, is given by[7]

$$h = (kT/4\pi n_e e^2)^{1/2} = 6.90\ (T/n_e)^{1/2}, \qquad (5.1)$$

where k is the Boltzmann constant, T temperature, n_e electron density and e charge of electron (e. s. units).

Setting coronal values $T = 10^6 \cdot K$, $n_e = 10^8\ cm^{-3}$ in (5.0), we have $h \simeq 1$ cm. The wavelength of the solar radio noise in space is $\lambda \simeq 1$ m. If we take the plasma wavelength to be given by

$$\lambda_p = v/\nu, \qquad (5.2)$$

where v is the velocity of the exciting corpuscles $\simeq 500$ km/s and ν = frequency of outburst $\simeq 100$ mc/s, we have $\lambda_p \simeq 1$ cm. Thus there is close match between the plasma wavelength and the Debye distance within which obtain the electron density gradient and the electric field. It can be shown that this condition is most favorable to space charge wave amplification.

One remarkable fact is that the kinetic energy available in the moving solar material is many orders of magnitude ($\simeq 10^4$) greater than the solar radio noise flux.[34] It follows from this that a very small efficiency would suffice in the physical mechanism of conversion of space-charge wave into electromagnetic radiation energy. In other words, there need only be a very weak coupling between the longitudinal plasma and transverse electromagnetic waves. This coupling may be provided by a transverse magnetic field, or mass velocity, or nonlinear effects.

A small signal (sinusoidal oscillations) theory is clearly not sufficient to explain the abnormally high intensity of solar radio outbursts, and a non-linear treatment is essential. Such a theory received added interest from the discovery by Australian workers of the second harmonic component in solar noise,[35] which was comparable with the fundamental in intenstiy. Sen[36] developed a non-linear theory of space-charge waves in moving, interacting electron beams to explain these results. Figure 3 shows the considerable anharmonicity of the steady-state oscillation curves of the electric field.

Two interesting papers by Japanese workers may be mentioned in this connection. The first paper[37] extends the Bohm and Pines plasma oscillation theory to involve coupling between longitudinal and transverse oscillations. The coupling arises from quantum fluctuation of the electrons interacting with the electromagnetic field. The efficiency factor of conversion is comparable with the one quoted above. The second paper[38] describes the experimental detection of microwave noise (14 mc/s) radiated by the detonation of explosives. The noise is attributed to electric impulse generated by sudden acceleration of electrons, e.g., by ionization of recombination at shock front.

In a very recent paper, Sturrock[39] has considered the non-linear effects in electron plasmas by a perturbation method, and interpreted the effects as the result of collisions between plasmons. He finds that the exchange of energy between the longitudinal and transverse modes must be an incoherent, second-order effect. He has studied the incoherent interaction which is responsible for spectral decay, that is, the dissipation of organized large-scale into disorganized small-scale motion. To a certain stage of approximation, purely one-dimensional spectra do not exhibit any spectral decay. He gives the following interesting formula for the time T in which a spectrum, which is almost one-dimensional, approaches isotropy:

$$T = \frac{1}{2}\ \pi/\varepsilon\ D^2\ \omega_p, \qquad (5.3)$$

where ω_p is the (angular) frequency, D the depth of modulation (ratio of variation of electron density to mean electron density), and ε the angle of collimation (characterizing the initial anisotropy), of the plasma oscillations.

Sturrock explains the anomalous rapid decay of the plasma oscillations in Merrill and Webb's experiment by relation (5.3). We shall apply (5.3) to the solar atmosphere. If we use the diffraction formula for ε, viz., $\varepsilon = \lambda p/d$, where λp is the plasma wavelength and d the diameter of the source of oscillations, and estimate λp to be given by $2\pi/\lambda p = \omega_p / v$, where v is the velocity of the moving electron beam, we may transform (5.3) into

$$T = d/v D^2. \qquad (5.4)$$

For the motion of a typical prominence,[40] we may take d = 6000 km, v = 500 km/sec and D = 0.3 (30% modulation). Then formula (5.4) gives T = 2 min. This is of the order of the lifetime of a typical solar outburst.

REFERENCES

1. Proceedings of the Symposium on "High Temperature - a Tool for the Future", Stanford Research Institute, University of California, 1956, p. 142.

2. J. M. Burgers, "Selected Topics from the Theory of Gas Flow at High Temperatures", The Institute for Fluid Dynamics and Applied Mathematics, University of Maryland, Technical Note BN, - 83, Sept. 1956.

3. H. A. Bethe and E. Teller, "Deviations from Thermal Equilibrium in Shock Waves", Aberdeen Proving Grounds, B.R.L. Rept. No. X-117. Reprinted by U. of Michigan Eng. Res. Inst., 1945; E. Greene, G. Cowan and D.Hornig, "The Thickness of Shock Fronts in Argon and Nitrogen and Rotational Heat Capacity Lags", J. Chem. Phys. 19, 427 (1951); V. H. Blackman, "Vibrational Relaxation in O_2 and N_2, Princeton Univ. Technical Rept. 11-20, N6 ori - 10J, Task II NR - 061-020, 1955.

4. G. B. Kistiakowsky, H. T. Knight and N. E. Malin, "Gaseous detonations III and IV. Dissociation energies of nitrogen and carbon monoxide and the acetylene oxygen mixtures", J. Chem. Phys. 20, 876-883, 883-888 (1952); W. Griffith, D. Brickl and V. Blackman, "Structure of Shock Waves in Polyatomic Gases", Phys. Rev. 102, 1209, 1956.

5. E. L. Resler, S. C. Lin and A. Kantrowitz, "The production of high temperature gases in shock tubes", J. App. Phys. 23, 1390-1399 (1952); H. E. Petschek, P. H. Rose, H. Glick, Ann Kane, and A. Kantrowitz, "Spectroscopic Studies of Highly Ionized Argon Produced by Shock Waves", Jour. Applied Physics, 26, 83 (1955); S.C. Lin, E.L. Resler, and A. Kantrowitz, "Electrical Conductivity of Highly Ionized Argon Produced by Shock Waves", Jour. Applied Physics 26, 95 (1955).

6. W. Marshall, "The Structure of Magnetohydrodynamic Shock Waves", Proc. Roy. Soc. A 233, 367-376 (1956).

7. L. Spitzer, Jr., "Physics of Fully Ionized Gases", Interscience Publishers Incs., New York, 1956, pp. 16 and 72.

8. T. G. Cowling, "Magnetohydrodynamics", Interscience Publishers Inc., New York, 1957, p. 99.

9. Eugene B. Turner, "The Production of Very High Temperatures in the Shock Tube with an Application to the Study of Spectral Line Broadening", AFOSR TN-56-150, Eng. Res. Inst., Univ. of Michigan, May 1956, p. 10.

10. J. F. Denisse and Y. Rocard, "Excitation of electronic oscillations in a Shock Wave. Radioastronomical Applications", J. de Phys. et le Rad. 12 (10), 58 (1951); Hari K. Sen, "Space Charge Wave Amplification in a Shock Front and the Fine Structure of Solar Radio Noise", Austr. J. Phys. 7, 30 (1954).

11. H. K. Sen, "Structure of a Magnetohydrodynamic Shock Wave in a Plasma of Infinite Conductivity", Phys. Rev. 102, 5 (1956).

12. S. Chapman and T. G. Cowling, "The Mathematical Theory of Nonuniform Gases", (Cambridge University Press, Cambridge, (1953), Second Edition, p. 218, Sec. 12.1 (ii).

13. M. Morduchow and P. A. Libby, "Complete solution of the one-dimensional flow equations in a viscous, heat conducting compressible gas", J. Aeronaut. Sci. 16, 674 (1949).

14. C. S. Wang Chang, "On the Theory of the Thickness of Weak Shock Waves" Univ. of Michigan, Dept. Engng. Report UMH-3-F APL/ JHU CM-503, Feb. 1948.

15. Ref. 11, eq. (46).

16. S. Chapman, "The Viscosity and Thermal Conductivity of a Completely Ionized Gas", Ap. J. 120, 151 (1954).

17. Ref. 12, p. 235.

18. L. Spitzer and R. Harm, Phys. Rev. 89, 977 (1953).

19. H. Petschek and S. Byron, "Approach to equilibrium ionization behind strong shock waves in argon", Ann. Phys. 1, 270 (1957).

20. L. Talbot and F. S. Sherman, "Structure of Weak Shock Waves in a Monatomic Gas", Tech. Rept. No. HE-150-137, U. of Calif., Berkeley Calif., May 13, 1956; D. Gilbarg and D. Paolucci, "Structure of Shock Waves in the Continuum Theory of Fluids", J. Rational Mechanics and Analysis, Vol. 2, No. 4, 1953.

21. R. G. Sachs, Phys. Rev. 69, 514 (1946).

22. S. Chandrasekhar, "An Introduction to the Study of Stellar Structure", University of Chicago Press, Chicago, 1939, Chap. V.

23. H. K. Sen and A. W. Guess, "Radiation Effects in Shock Wave Structure", Phys. Rev. 108, 560 (1957).

24. R. Lüst, Z. Naturforsch. 8a, 282 (1953).

25. Helmut A. Abt, Ap. J. Suppl. 3 (Vol. 1), 63 (1954); C. Whitney, Ann. D. Astrophys. 19, 34, 142 (1956); M. P. Savedof, "Shock Waves in Cepheid Atmospheres", Proc. NSF Conference on Stellar Atmospheres, Indiana Univ., 1954; F. D. Kahn, "The acceleration of interstellar clouds", B. A. N. XII (No. 456), 187 (1954).

26. S. A. Kaplan, "On the formation of interstellar gas clouds", paper presented at Third Symposium on Cosmical Gas Dynamics, 1957, at Cambridge, Mass.

27. H. L. Helfer, "Magnetohydrodynamic Shock Waves", Ap. J. 117, 177 (1953).

28. J. W. Bond, Jr., "Electric Potential in a Gaseous Shock Front", Special Defense Projects Dept., General Electric, Philadelphia, Pa. July 1, 1956.

29. J. L. Pawsey, Proc. Inst. Electr. Engrs. 97 (III), 305 (1950).

30. A. V. Haeff, Phys. Rev. 75, 1547 (1949).

31. L. Landau, J. Phys, Moscow 10, 25 (1946).

32. H. M. Mott-Smith, Phys. Rev. 82, 885 (1951).

33. T. G. Cowling, "The Influence of Diffusion on the Propagation of Shock Waves", Phil. Mag. 33, 61 (1942).

34. H. K. Sen, Austr. J. Phys. 6 (1), 67 (1953).

35. Wild, Murray and Rowe, Nature 172, 533 (1953).

36. H. K. Sen. Phys. Rev. 97, 849 (1955).

37. S. Hayakawa and N. Hokkyo, "Electromagnetic radiation from electron plasma", Progr. Theor. Phys. 15 (3), March 1956.

38. T. Takakura, "Radio noise radiated on the detonation of explosive", Publ. Astron. Soc. Jap. 7 (4), 1955.

39. P. A. Sturrock, "Non-linear effects in electron plasmas", Proc. Roy. Soc. A. 242, 277 (1957).

40. "The Sun", Edited by G. P. Kuiper, Univ. of Chicago Press, 1953, p. 395.

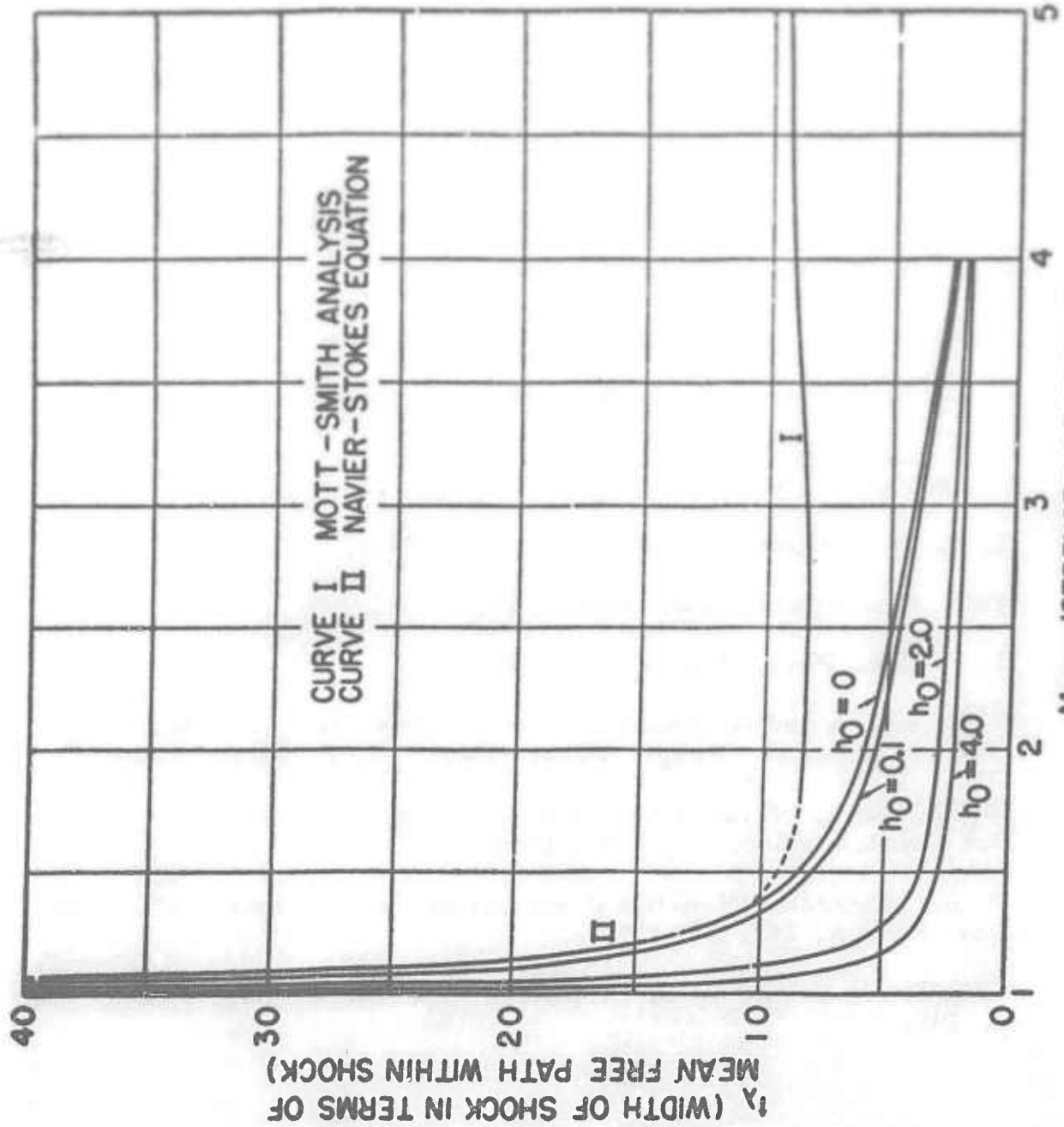

FIG. 1. Width of shock for an ionized gas in terms of mean free path within shock.

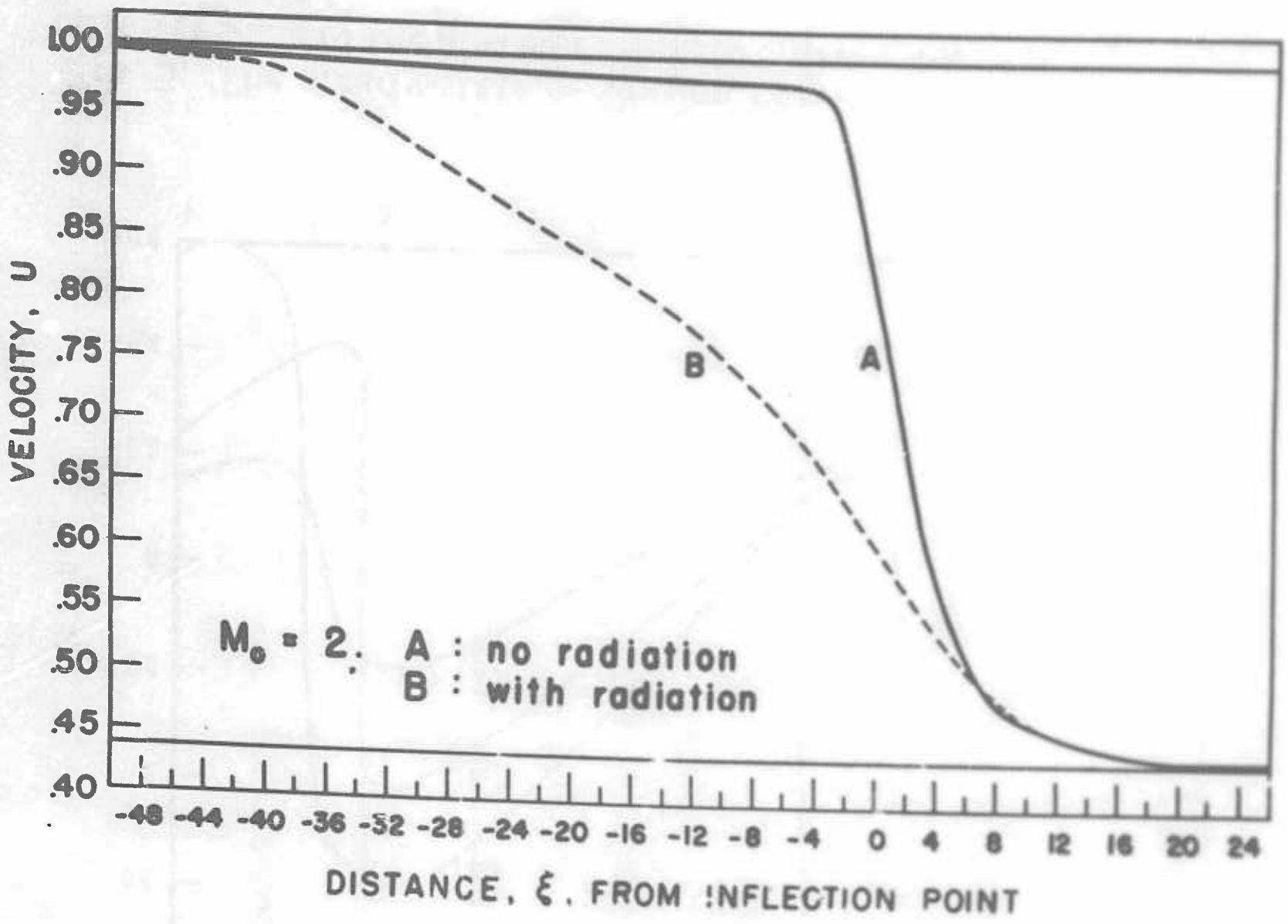

Fig. 2 VARIATION OF VELOCITY WITHIN THE SHOCK

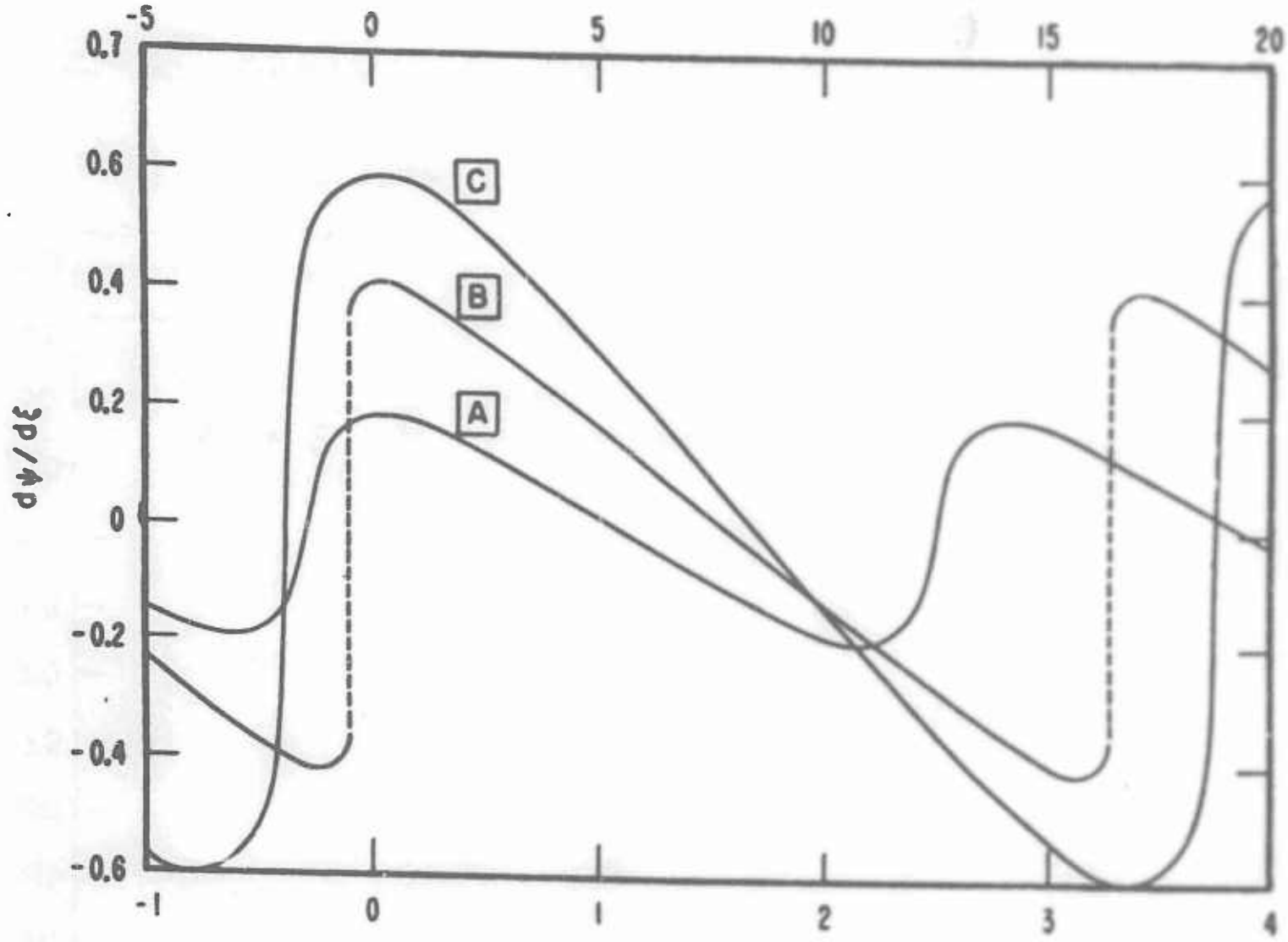

FIG. 3. The steady-state oscillation curves of the electric field. The lower scale of the abscissa refers to Curves *A* and *B*, the upper refers to Curve *C*.

SHOCK WAVE CALCULATIONS FOR HIGH TEMPERATURE GASES

J. D. Teare
Avco Research Laboratory

I. INTRODUCTION

Flight speeds in excess of 25,000 feet per second within the Earth's atmosphere are liable to be encountered before manned space flight becomes commonplace, and many questions remain to be answered about the behavior of the gas behind shock waves on bodies traveling at such speeds. The radiation from the gas, its electrical properties, and the heat transfer to the body surface are all of interest, and all three can be affected by chemical kinetic effects when the flow times become comparable with the chemical relaxation times. A great deal must be learned before such effects become calculable, and much of the work at the Avco Research Laboratory is directed towards furthering the understanding of the chemical physics of hypersonic flight.

Some of the phenomena observed in air are very complicated, and in attempts to clarify the situation many shock tube experiments have been carried out in other gas mixtures. In the efficient operation of a shock tube facility engaged in this type of work, it has been found a great asset to be able to calculate readily the shock tube conditions for any gas mixture. There are additional problems in the interpretation of the experimental observations obtained during the interval between the arrival of the shock wave and the establishment of equilibrium conditions, and the calculation procedures to be described have been of assistance in, for example, the determination of rate constants in chemical kinetics experiments.

Thus the purpose of the present paper is threefold: To describe two calculation methods which have been used, to outline the extent of the accumultated results and to point out the application to experimental chemical kinetics.

A brief introductory discussion of the behavior of high temperature gas is presented with apologies to those thoroughly familiar with this subject.

II. "REAL GAS" EFFECTS

In many compressible flow applications the gas temperature remains fairly low and variations in specific heat are negligible. In such a case the well-known Rankine-Hugoniot relationships describe the flow across a shock wave, and all fluid property ratios can be expressed analytically in terms of a single variable, usually chosen to be the Mach number in the incident flow. For example,

$$\frac{\rho_2}{\rho_1} = \frac{\gamma + 1}{\gamma - 1 + 2/M^2}$$

For air, with $\gamma = 7/5$, the density ratio approaches the value six as the Mach number approaches infinity.

As the temperature of the shock-heated gas rises, other effects come into play, as discussed by Bethe and Teller[1]. For a diatomic gas, molecular vibration increases the heat capacities, and thus reduces γ. If no other effects were to take precedence, the value of γ would decrease towards 9/7 as the shock strength increased, and the density ratio would approach a limiting value of eight.

Temperature and density ratios for air for both the above cases are shown versus Mach number as the dashed curves in Figure 1. In both cases the curves are independent of the absolute level of density, but the amount of energy absorbed in molecular vibration is a function of temperature, which implies that the vibrational equilibrium curves are dependent on temperature level, and thus on T_1.

However, in general this dependence on T_1 is completely overshadowed by dissociation and ionization effects which are strongly dependent on density. When the temperature of the gas becomes high enough for dissociation or ionization to occur, the energy per unit mass of gas becomes a function of both temperature and density. For argon-free air, for example, the variation of the equilibrium fluid properties for T and ρ is shown in Table I.

Table I

PROPERTIES OF ARGON FREE AIR DATA
OF HILSENRATH AND BECKETT[2]
$\rho_o = 1.288 \times 10^{-3}$ gm/cm^3

T°K	273	2000	5000	10,000
$\rho/\rho_o = 1$	E/R 2.5	2.982	5.169	11.230
	pV/RT 1.0	1.0000	1.1456	1.7601
$\rho/\rho_o = 10^{-2}$	E/RT 2.5	2.996	6.427	14.888
	pV/RT 1.0	1.0005	1.2387	2.0501
$\rho/\rho_o = 10^{-4}$	E/RT 2.5	3.144	11.940	22.662
	pV/RT 1.0	1.0055	1.4872	2.4845
$\rho/\rho_o = 10^{-6}$	E/RT 2.5	4.432	22.656	46.055
	pV/RT 1.0	1.0490	1.9628	3.7901

The excitation of the "inert"[1] degrees of freedom of the gas particles introduces the further complication of chemical relaxation. The translational and rotational modes equilibrate after very few collisions between the particles, but the vibrational and dissociation processes take much longer. For example, in oxygen at 3500°K the vibrational and dissociation

modes require respectively 10^3 and 10^6 collision to reach equilibrium. Thus air passing through a strong shock wave will be instantaneously heated to the temperature appropriate to $\gamma = 1.4$, and the subsequent "relaxation" to the equilibrium conditions may take several microseconds.

Complete description of the gas conditions behind strong shock waves thus requires knowledge both of the equilibrium situation and of any non-equilibrium phenomena in the relaxation region. The next two sections will be confined to equilibrium calculations, but some discussion of relaxation in oxygen-argon mixtures will be given in § 5.

III. EQUILIBRIUM CALCULATIONS FOR ARGON-FREE AIR

From continuity, momentum and energy considerations we may obtain relationships for one-dimensional flow through a normal shock wave in the form

$$E_b - E_a = \tfrac{1}{2}(p_b + p_a)\left(\frac{1}{\rho_a} - \frac{1}{\rho_b}\right) \tag{1}$$

$$U_a^2 = \frac{p_b - p_a}{\rho_a(1 - \rho_a/\rho_b)} \tag{2}$$

and

$$U_b = U_a \rho_a / \rho_b \tag{3}$$

where the subscripts a and b denote, respectively, conditions upstream and downstream of the shock, and where the velocities are measured relative to the shock front.

When E_b and P_b are known functions of T_b and ρ_b, Eq. (1) can be used to determine ρ_b if T_b and E_a, p_a, ρ_a, are all specified. Once ρ_b is determined, the values of U_a and U_b follow from Eqs. (2) and (3).

For argon-free air the equilibrium values of E and p have been tabulated by Hilsenrath and Beckett,[2] for temperatures up to 15000 °K and for a wide range of density.

Using the tables, it is possible to specify a value of T_b, assume a value of ρ_b, interpolate for the appropriate E_b and p_b, and then iterate on ρ_b until Eq. (1) is satisfied. Then from Eq. (2) we may determine the shock speed necessary to produce the specified temperature T_b. The results of such a procedure are illustrated by the solid curves of Fig. 1, for a normal shock moving into air at 300 °K and at various pressures. In this coordinate system $U_s = U_a$ and $U_2 = U_s(1 - \rho_a/\rho_b)$.

The same procedure may be applied to a reflected shock, as shown in Fig. 2. Here, however, we are not free to specify T_b, but must determine both T_b and ρ_b such that $U_b = U_{sr}$ and $U_a = U_2 + U_{sr}$. This involves a double iteration and double interpolation procedure.

Similar considerations apply to the case of the standing normal shock in front of a model in a shock tube. Oblique shocks, however, are less complicated, since it is merely necessary to solve Eq. (1) for the density ratio across the shock appropriate to a specified temperature ratio. The shock angle and flow deflection necessary to produce that temperature ratio are then determined from the kinematic relationships.

Feldman and the Avco Research Laboratory computer group applied these calculation procedures to the tables of Hilsenrath and Beckett to produce the compilation of charts in Ref. 3. Shocks are calculated for flight conditions up to 250,000 ft altitude and up to 26,000 ft/sec, and for shock tube conditions with initial pressures ranging from 0.001 cm Hg to one atmosphere. Also included is a Mollier diagram with interpolated lines of constant p and constant pV/RT, and with sound speed contours obtained from Logan and Treanor.(4)

IV. OTHER EQUILIBRIUM CALCULATIONS

The above methods may be applied to any gas for which tabulations of equilibrium fluid properties are available. For any oxygen-nitrogen mixture such tabulations could undoubtedly be constructed from the same statistical mechanics sources used in Ref. 2. However, when equilibrium calculations are required for many oxygen-nitrogen mixtures, both with and without noble gas diluents, it is worthwhile pausing to examine the possibility of bypassing the tabulation procedure.

This can be done by incorporating the actual equilibrium relationships into the shock wave equations in the following manner.

For the i^{th} species in a gas mixture we may write

$$n_i = VQ_i \exp(\mu_i/kT)$$

where n_i is the number of particles in the volume V, μ_i is the chemical potential, and Q_i is a function of temperature T only, VQ_i being the partition function for the species (see, for example, Ref. 5).

Then $n_i = VQ_i\lambda_i$ where $\lambda_i = \exp(\mu_i/kT)$. Now for equilibrium of the reaction $N_2 \rightleftharpoons N + N$ we must have $\mu_{N_2} = 2\mu_N$, or $\lambda_{N_2} = \lambda_N^2$. Similarly, for equilibrium of $N_2 \rightleftharpoons N_2^+ + e$, we require $\mu_{N_2} = \mu_{N_2^+} + \mu_e$ or $\lambda_{N_2^+} = \lambda_N^2 \div \lambda_e$, and so on.

It is thus clear that the chemical potentials of all the species present in an oxygen-nitrogen-argon mixture can be represented in terms of four fundamental variables λ_e, λ_b, λ_N and λ_A, as in Table II.

Table II

$\lambda_{o_2} = \lambda_o^2$	$\lambda_{o_2}^+ = \lambda_o^2 \div \lambda_e$	$\lambda_{o_2}^- = \lambda_o^2 \lambda_e$
$\lambda_{N_2} = \lambda_N^2$	$\lambda_{N_2}^+ = \lambda_N^2 \div \lambda_e$	$\lambda_A^+ = \lambda_A \div \lambda_e$
$\lambda_N^+ = \lambda_N \div \lambda_e$	$\lambda_o^+ = \lambda_o \div \lambda_e$	$\lambda_o^- = \lambda_o \lambda_e$
$\lambda_{NO} = \lambda_N \lambda_O$	$\lambda_{NO}^+ = \lambda_N \lambda_O \div \lambda_e$	

All the thermodynamic properties can now be expressed compactly as follows:

$$\rho V = \Sigma n_i m_i$$

$$pV = kT \Sigma n_i$$

$$e = \Sigma n_i \epsilon_i$$

$$e + pV - Ts = \Sigma n_i \mu_i$$

where

$$\epsilon_i = \frac{kT^2}{Q_i} \frac{dQ_i}{dT} .$$

Equation (1) thus becomes

$$\frac{(\Sigma n_i \epsilon_i)_b}{\rho_b V} - E_a = \frac{1}{2 \rho_b V} \left\{ kT_b \Sigma n_i + p_a V \right\} \left\{ 1 - \frac{\rho_a}{\rho_b} \right\} . \qquad (4)$$

If Q_i and $\frac{dQ_i}{dT}$ are tabulated functions of T, then for a specified value of T_b Eq. (4) invoives five unknowns, ρ_b, λ_e, λ_o, λ_N and λ_A.

The conservation of the various species yields the following:

$$n_A + n_A^+ = \text{Total argon present}$$

i.e., $$\lambda_A \left\{ Q_A + Q_A^+ / \lambda_e \right\} = \text{Total argon per unit volume} \qquad (5)$$

Similarly

$$\lambda_N^2 \left\{ Q_{N_2} + \frac{Q_{N_2}^+}{\lambda_e} \right\} + \lambda_N \left\{ Q_N + \lambda_o Q_{NO} + \frac{Q_N^+}{\lambda_e} + \frac{\lambda_o Q_{NO}^+}{\lambda_e} \right\}$$

$$= \text{Total nitrogen per unit volume} \qquad (6)$$

$$\lambda_o^2 \left\{ Q_{o_2} + \frac{Q_{o_2}^+}{\lambda_e} + \lambda_e Q_{o_2}^- \right\} + \lambda_o \left\{ Q_o + \lambda_N Q_{NO} + \frac{Q_o^+}{\lambda_e} + \lambda_e Q_o^- + \frac{\lambda_N Q_{No}^+}{\lambda_e} \right\}$$

$$= \text{Total oxygen per unit volume} \qquad (7)$$

and for the electrons

$$\lambda_e Q_e + \lambda_e \lambda_o Q_o^- + \lambda_e \lambda_o^2 Q_{o_2}^- = \frac{1}{\lambda_e} \left\{ \lambda_N Q_N^+ + \lambda_o Q_o^+ + \lambda_A Q_A^+ + \lambda_N^2 Q_{N_2}^+ + \lambda_o^2 Q_{o_2}^+ \right\} \qquad (8)$$

giving four more relationships between the five variables. The complete determination of the conditions behind a shock wave which produces an arbitrary temperature T in an arbitrary $O_2 - N_2 - A$ mixture thus evolves from the solution of five non-linear algebraic equations.

The prime advantage of the above method, apart from an added flexibility to be discussed later, is in the fact that all the fluid properties and particle concentrations behind the shock wave can be immediately obtained once the algebraic equations have been solved. For moving and oblique shocks, the solution of the algebraic equations replaces the iterative interpolation in the tables of fluid properties, while for reflected and standing shocks the double interpolation in replaced by a single interpolation in the tables of Q_i and dQ_i/dT.

This procedure, initiated by M. M. Litvak and described in an Avco Research Laboratory internal report, was programmed for an IBM 650 computer by W. M. Wolf.* A prerequisite for the shock wave calculations was the computation of the partition functions and their derivatives, initiated by Wolf and expanded by C. L. Keeler. The resultant Q_i and dQ_i/dT values have subsequently been compared with the tabulations of Logan and Treanor[4] with excellent agreement.

Specific adaptations of the above method have proved extremely useful in permitting the rapid determination of equilibrium conditions for various gas mixtures of interest in shock tube experiments. A broad survey of an area can be readily undertaken and detailed investigation confined to the regions of experimental promise. Some of the results are presented in Ref. 6.

The method has also been used in a modified form to produce tabulations of E and p as functions of T and ρ for pure nitrogen. These tabulations were then handled by the method of § 3 to yield the shock tube charts of Ref. 7. In addition, equilibrium calculations for argon-free air have been carried out in the range 1000 °K through 2000 °K for the purpose of obtaining the electron concentrations in this range.[8]

---

*William M. Wolf Company, Boston, Mass.

V. APPLICATION TO NON-EQUILIBRIUM CONDITIONS

The method of § 4 offers some immediate advantages, for example, in that the effect of vibrational lag of a particular species can be studied by merely modifying the partition functions to exclude the vibrational states of the molecule. Equally simple is the "freezing" of the dissociation of a species or the enforcement of a specified amount of dissociation by "gerrymandering" of the equilibrium relationships implicit in Eqs. (5), (6), (7) and (8). These techniques have contributed to the interpretation of the relaxation experiments of Camac and Petty in air[9] and other gas mixtures[10].

The present discussion will be confined to the less complicated of these, the relaxation in an oxygen-argon mixture. Curves are shown for a mixture of 95% argon, 5% oxygen, at an initial pressure 0.5 cm Hg. Computation of the shock conditions for various specified amounts of dissociation α in this mixture leads to the temperature and density plots of Fig. 3. The "frozen vibration" case is also shown. The plots indicate that a shock traveling at 2.4 mm/μsec would instantaneously raise the temperature to 5300°K. The subsequent vibrational and dissociative relaxation would steadily lower the temperature towards the equilibrium value of 4200°K, while the density ratio would increase from 3.77 towards 5.15. The rate for the dissociation process could be evaluated if it were possible to observe the time-history of the decrease of O_2 concentration. Camac has obtained such relaxation histories by monitoring the absorption of ultra-violet light at 1470 Å by the oxygen molecules in the ground vibrational state. The absorption as a function of α and shock speed is shown in Fig. 4, a schematic view of the experimental set-up in Fig. 5, and a typical time-history of the absorption in Fig. 6.

The experiment is arranged so that the undisturbed gas mixture transmits about two-thirds of the incident light. When the shock passes the window, the increased molecule density due to the shock compression decreases the transmission. Then the absorption steadily decreases as the molecules dissociate.

With the aid of Fig. 4 the oscillogram can thus be interpreted as an α-t curve, and the dissociative rate can be obtained. In regions where the equilibrium dissociation is high, the vibrational relaxation occurs too rapidly to be observed, but at lower shock speeds an increased transmission occurs as the depopulation of the ground vibrational state proceeds.

Similar procedures aid in the interpretation of other non-equilibrium phenomena observed in shock tube experiments. The flexibility of the method outlined in § 4 has proved highly advantageous in this connection.

VI. CONCLUSIONS

Two methods of calculating the gas properties behind strong shock waves have been described. Their usefulness in both equilibrium and non-equilibrium situations has been evaluated.

Symbols

e	energy of gas in volume V
E	energy per unit mass
k	Boltzmann's constant = 1.3804×10^{-16} ergs/°K
m	mass of particle
M	Mach number
n	number of particles in volume V
p	pressure
Q	(partition function) $\div$ V
s	entropy of gas in volume V
T	temperature, °K
U	velocity
U_s	velocity of incident shock wave relative to shock-tube
U_{sr}	velocity of reflected shock wave relative to shock tube
V	volume
α	fraction of 0_2 dissociated
ϵ	energy per particle
γ	ratio of specific heats
λ	exp (μ/kT)
μ	chemical potential
ρ	density

Subscripts

a	upstream of shock wave
b	downstream of shock wave
i	i^{th} species
1	initial conditions in shock tube
2	behind incident shock in shock tube
4	behind reflected shock in shock tube

REFERENCES

1. Bethe, H.A. and Teller, E., Deviations from Thermal Equilibrium in Shock Waves. BRL Report No. X-117, Aberdeen Proving Ground, Maryland, 1945.

2. Hilsenrath, J. and Beckett, C. W., Tables of Thermodynamic Properties of Argon-free Air to 15,000°K. Arnold Engineering Development Center Report No. AEDC-TN-56-12, Sept., 1956.

3. Feldman, S., Hypersonic Gas Dynamic Charts for Equilibrium Air. Avco Research Laboratory, January, 1957.

4. Logan, J. G. Jr. and Treanor, C.E., Thermodynamic Properties of Air between 3000°K and 10,000°K. Cornell Aeronautical Laboratory Report No. BE-1007-A-3, January, 1957.

5. Mayer, J.E. and Mayer, M.G., Statistical Mechanics. John Wiley & Sons, Inc., New York, 1940.

6. Teare, J.D., Shock Tube Calculations for High Temperature Gas Mixtures. Avco Research Laboratory Research Report No. 18, (in preparation).

7. Hypersonic Gas Dynamic Charts for Nitrogen. Avco Research Laboratory Research Note No. 85, (in preparation).

8. Thermodynamic Properties of Air between 1000°K and 2000°K, with electron concentrations. Avco Research Laboratory, unpublished.

9. Camac, M., Camm, J., Keck, J.C., and Petty, C.C., Relaxation Phenomena in Air between 3000 and 8000°K, Avco Research Laboratory Research Report 22, Mar., 1958.

10. Camac, M., Camm, J., Feldman, S., Keck, J. and Petty, C., Chemical Relaxation in Air, Oxygen and Nitrogen. IAS Preprint No. 802, January, 1958.

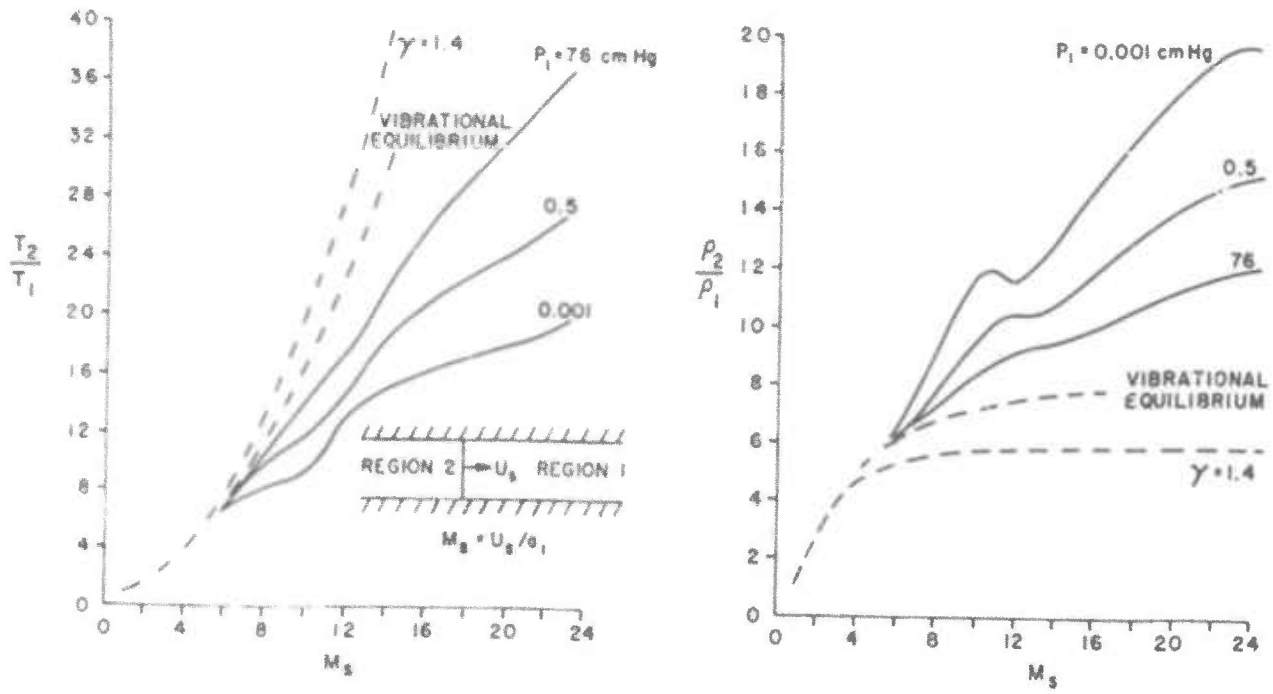

Figure 1 Moving Normal Shock in Equilibrium Air, $T_1 = 300^{\circ}K$.

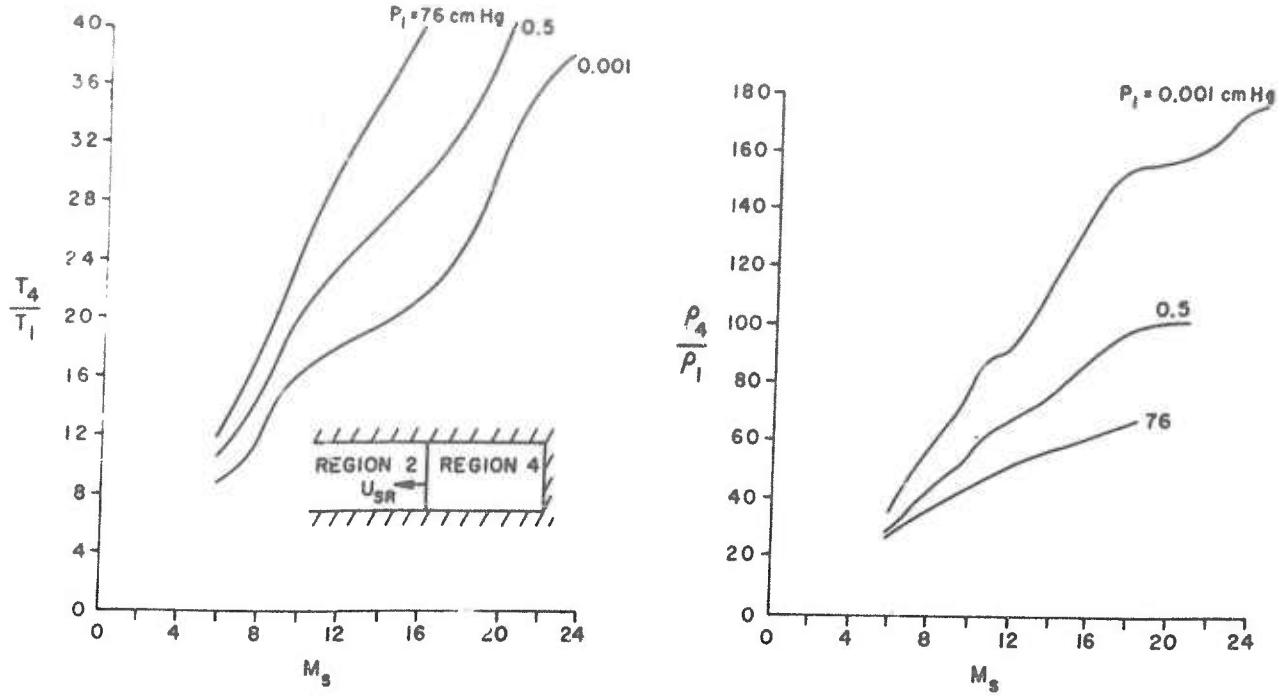

Figure 2 Reflected Normal Shock in Equilibrium Air, $T_1 = 300^{\circ}K$.

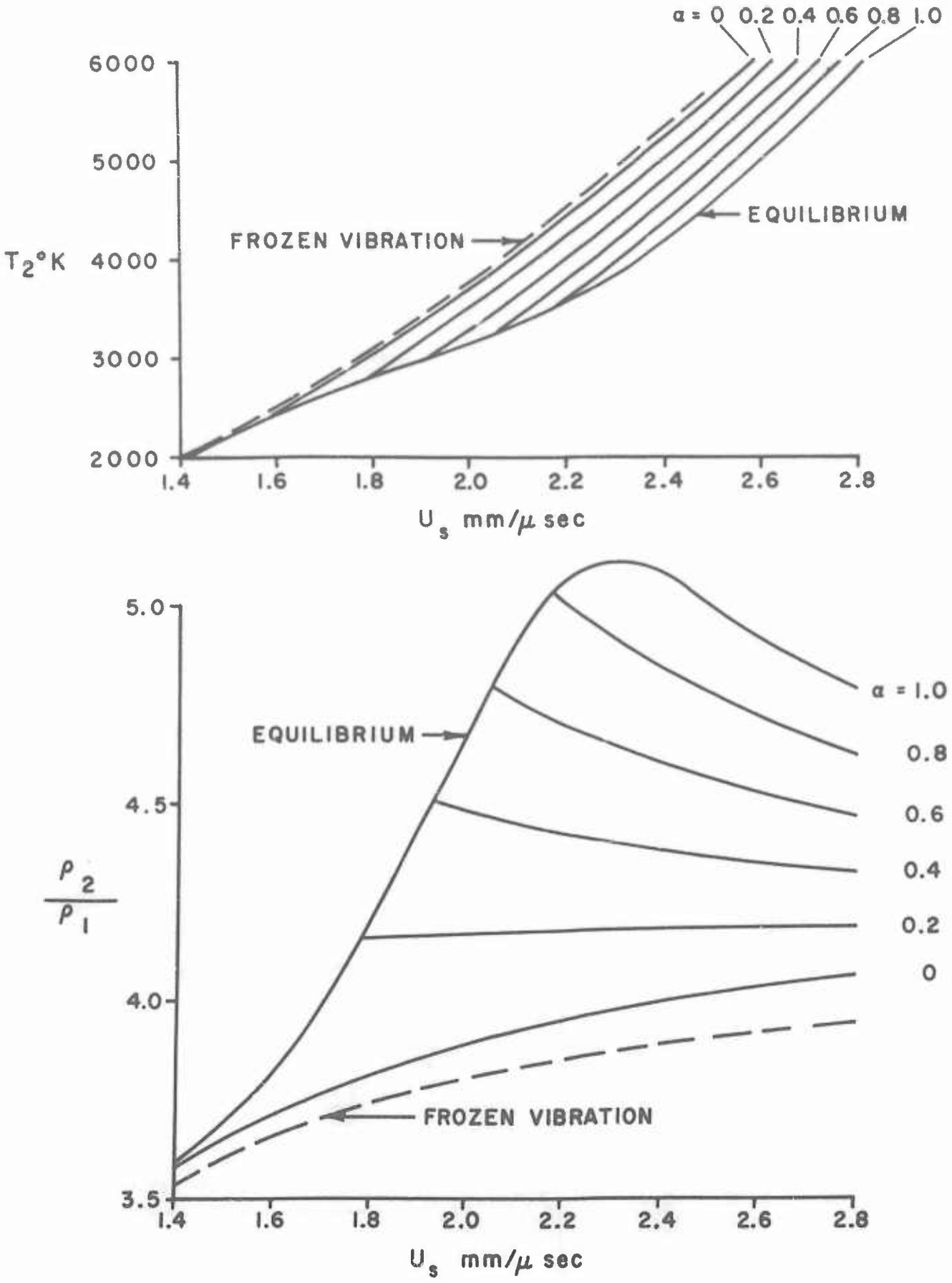

Figure 3 Moving Normal Shock in 5% Oxygen, 95% Argon.
P_1 = 0.5 cm. Hg., T_1 = 294°K.
α = fraction of O_2 dissociated.

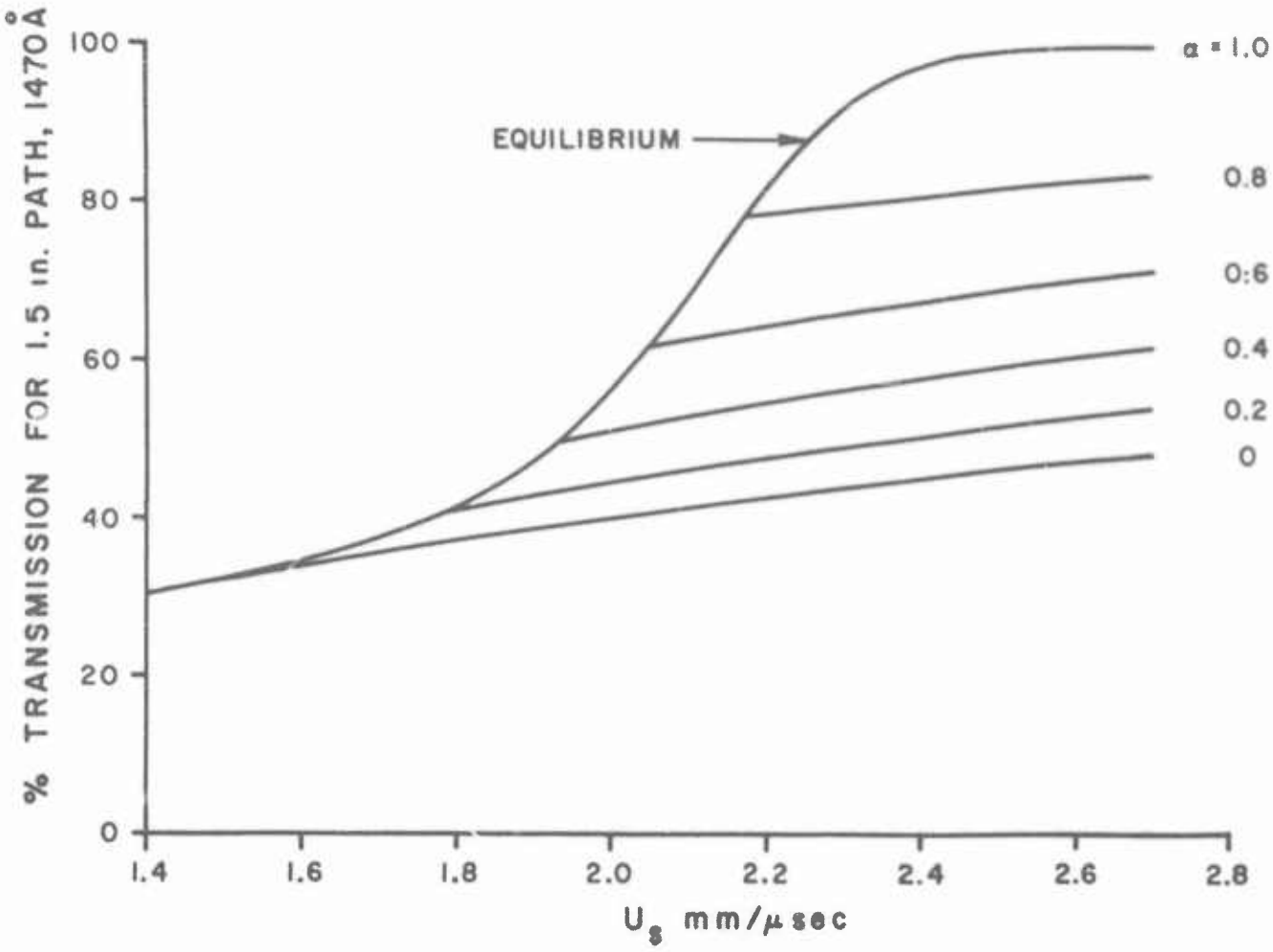

Figure 4 U. V. Transmission behind Moving Normal Shock in 5% Oxygen, 95% Argon.
P_1 = 0.5 cm. Hg., T_1 = 294°K. α = fraction of O_2 dissociated.

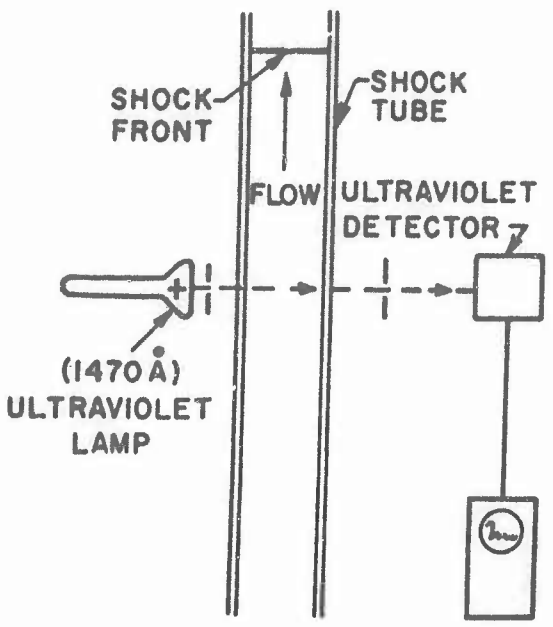

Figure 5 Apparatus for the Measurement of Molecular Oxygen Concentration.

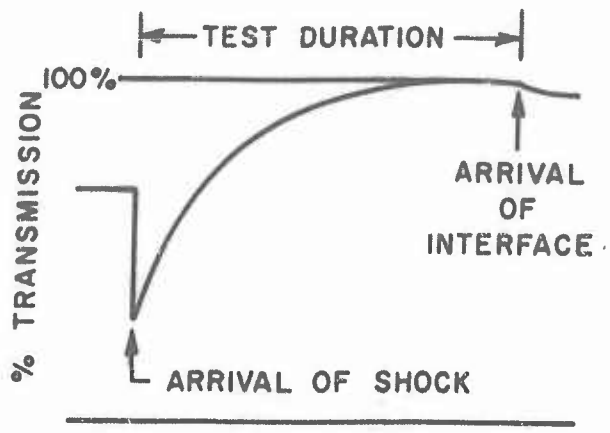

Figure 6 Schematic Oscillogram

HEAT TRANSFER MEASUREMENTS ON A HEMISPHERE-CYLINDER IN THE LOCKHEED THREE-INCH SHOCK TUBE

By R. W. Rutowski and D. Weimer
Lockheed Aircraft Corporation

INTRODUCTION

The three-inch shock tube at the Lockheed Research Laboratories, Palo Alto, was placed into operation during the fall of 1957. In this paper we will describe one phase of the shock tube work there and give some preliminary results. The shock tube is 44 feet in length, including an 8-foot driver section and a dump chamber. The walls vary from 1" to 1-5/8" in thickness, providing a yield strength of over 50,000 psi for most of the components. The shock tube is designed for use of combusting as well as inert gases in the compression chamber; however, operations to data have not utilized combustible mixtures. Most of the tests have used helium, at 2,000 psi and less, as the driving gas. Figure 1 is a view of the compression chamber; Fig. 2 shows the expansion chamber, dump tank, and control station.

Some of the first work with this tube has been concerned with the obtaining of heat transfer measurements on models. The uniform flow of Region 2, shown in Fig. 3, is utilized to simulate, on these models, temperatures and densities that missiles re-entering the atmosphere would experience at and near their stagnation points.

INSTRUMENTATION

Shock wave velocity measurement is accomplished by use of platinum films mounted in the shock tube wall at regular intervals. The response of the film is also used to trigger the oscilloscopes. Rott and Hartunian[1] Bromberg,[2] and others have discussed the response of such a thin film to the passage of a shock wave. They show that the heat transfer rate into the surface of an infinitely thin film varies inversely as the square root of the time after passage of the shock wave. Using a LaPlace transform, one finds that this heat transfer rate corresponds to a step increase in temperature at $t = 0$, (time of passage of the shock wave) with the film remaining at this new temperature for the duration of uniform flow. It can also be shown that the small, but finite, thickness of a sputtered film introduces a time lag of considerably less than a microsecond in this step response.

These platinum films, about 0.05 cm wide and 0.50 cm long, with a resistance of 50 to 100 ohms, are sputtered onto aluminum oxide plugs, which are mounted in the shock tube wall. Figure 4 shows the response of one such film, mounted with its longitudinal axis at right angles to the flow, to the passage of a shock wave. Oscilloscope settings were 2 mv/cm and 20 μ sec/cm. The width of the film is such that about 1/2 microsecond is required for a shock wave to pass over it. The later fluctuations are believed due to flow disturbance about the flat plug. Velocity of the shock wave is measured in terms of the time interval between pulses from two such films mounted about one foot apart. These films have been found excellent for this purpose, being durable and subject to almost no ambiguous signals.

Models were constructed of a metal base which is coated with a layer of flame-sprayed aluminum oxide about 0.025" thick. Copper wires were embedded in the coating so that their terminals would be at appropriate positions on the surface for application of resistance thermometer gages. The surface was ground to an RMS roughness of 30 to 50 micro-inches. This procedure allowed the construction of models of arbitrary shape and provided a surface which would not deteriorate under such high temperature operations associated with film applications as sputtering, baking or soldering. Figure 5 shows one of the models mounted on its sting, and the shock tube end plate.

For the heat transfer measurements, platinum strips, about 0.003 cm thick, 0.050 cm wide and 0.5 cm long, were used as sensors, acting as resistance thermometers. These are soldered directly to the copper wire terminals exposed on the model surface. Several such films can be seen in Figure 5.

If we consider the film as a thermal R-C element and apply the concept of a diffusion depth, $\delta = \sqrt{kt/c\rho}$ we can distinguish two distinct types of films. If this depth, for the time considered, is very much greater than the film thickness, then the film is considered "thin" and almost immediately takes on the temperature of the backing material. Whereas, if the diffusion depth is of the order of magnitude or less than the film thickness, then the film is called "thick", and, as a first approximation, it can be considered a calorimeter. If the film is in intimate contact with the backing surface, as in the case of the sputtered film, there is no thermal resistance at the interface; however, when the film lies on this surface without bonding, the thermal resistance of the interface appears to be such that little heat is lost during the test period. Assuming that no heat is lost, we write for the rate of heat flow per unit area into the film:

$$q = \rho \frac{cp\ell}{dt} \frac{dT}{dt}$$

where ℓ is the film thickness.

The change in temperature of the film is obtained from its change in resistance which, in turn, is determined by measuring the change in voltage across the film with a steady current flowing through it. Neglecting higher order terms, we write:

$$\Delta R = R_o \alpha \Delta T$$

and

$$\Delta E = I_o \Delta R$$

so

$$\frac{\Delta T}{\Delta t} = \frac{\Delta R}{R \alpha \Delta t} = \frac{1}{I_o R_o \alpha} \cdot \frac{\Delta E}{\Delta t}$$

and, finally,

$$q = \rho \frac{c_p}{I_o R_o \alpha} \frac{\Delta E}{\Delta t} .$$

Thus, the heat transfer rate is given by the slope of the voltage-time curve. Figure 6 is a typical oscilloscope record of the change in voltage with respect to time during a test run. Oscilloscope sensitivity is set at 1 mv/cm with a sweep speed of 50 microsec/cm, and current through the film is 0.50 amps. The instant the shock wave hits the film is marked by the discontinuous change in slope of the trace. The trace continues with generally uniform slope during the flow of Region 2. In this particular test the uniform flow appeared to continue for about 300 microsec.

As a further check on the uniformity of the flow, some optical studies were made of the flow using the 1 1/4" diameter windows installed in the shock tube at the model position. The thin films in the wall were again used to trigger the flash equipment. Figure 7, an example of the type of pictures taken, is a shadowgraph of the shock wave a few microseconds after it hit the nose of the model. The high temperature, radiating region between the nose and the reflected shock can be seen. The disturbance on the window is due to turbulence in the recessed region at the window in the cylindrical tube. Although shadowgrams gave sharp indications of shock wave position up to the instant shown, they were useless for any later time as the radiating gas at the stagnation point completely fogged the film. The study was continued taking single fringe interferograms which, in effect, masked out most of the undesired radiation. Pictures were taken of the flow at various intervals after the arrival of the shock at the model. Figure 8 shows the results. Although each picture was taken of a separate test run, the densities and shock Mach number were reproduced each time as nearly as possible. It is evident that the flow was quite uniform for a period of about 300 microseconds. For those shots, when the diaphragm failed to open completely, the situation at the model indicates a lower velocity flow.

RESULTS

Measurements were made of the stagnation point heat transfer rate, using the thick film technique described above, on a hemisphere of radius 0.47". The measurements were adjusted to correspond to heat transfer rates on 0.25" radius hemisphere for direct comparison with published curves of heat transfer rates predicted by Fay and Riddell.[3] The initial data, represented by the circles on Fig. 9, appeared self-consistent but were higher than the predicted values. A change in the procedure of determining the resistance of the film from that of computing the resistance based on the material resistivity and film size, to that of directly measuring the resistance of the film in place on the model, resulted in an adjustment of the data which placed them and the theory in good agreement.

The heat transfer rates at other points on this hemisphere were also measured. Two different types of flow were observed. In one case the heat transfer rates decreased as angular displacement from the stagnation point increased, in agreement with Lees' theory.[4] However, as the Reynolds number of the flow was increased, particularly by increasing its density, heat transfer measurements markedly higher than those predicted by Lees' theory were obtained. These higher rates first were observed sporadically at individual gages, but became general at displacements from the stagnation point of 45° and more when the initial test section pressure, P_1, was 100 mm.

The two classes of heat transfer observations were sufficiently distinct to lead us to hypothesize that a turbulent boundary layer was being developed, probably triggered at a relatively low Reynolds number by the platinum films. Theories for heat transfer in turbulent boundary layer are on considerably more tenuous ground than are the theories for laminar boundary layers. They are based on a phenomenological approach, and usually depend on experimental data to evaluate constants, etc. Several theories for turbulent heat transfer now exist for hypersonic flow. Most have in common the integral of the boundary layer energy equation, and the evaluation of the heat transfer rate, q_w, in terms of the shear stress at the wall, τ_w, by use of the Reynolds analogy. One such theory is that of Bromberg, described by Phillips.[5]

Figure 10 shows the heat transfer data obtained at 45° on the hemisphere and compares them with Lee's laminar theory and Bromberg's turbulent theory.

It seems clear from these preliminary measurements that the nature of the test data changes with changing flow parameters, however, further work will be necessary in order to arrive at definitive conclusions on boundary layer transition and its relationship to such flow parameters as Reynolds number.

REFERENCES

1. Rott, N., and Hartunian, R., "On the Heat Transfer to the Walls of a Shock Tube," Cornell University Graduate School of Aero. Eng., Nov., 1955.

2. Bromberg, R., "Use of the Shock Tube Wall Boundary Layer in Heat Transfer Studies," Jet Propulsion, 26, 737, 1956.

3. Fay, J. A., and Riddell, F. R., "Theory of Stagnation Point Heat Transfer in Dissociated Air," Jour. of Amer. Sciences, 25, 73, 1958.

4. Lees, L., "Laminar Heat Transfer over Blunt-Nosed Bodies at Hypersonic Flight Speeds," Jet Propulsion, 26, 259, 1956.

5. Phillips, R. L., "A Summary of Several Techniques Used in the Analysis of High Enthalpy Level, High Cooling Ratio Turbulent Boundary Layers on Blunt Bodies of Revolution," 16 September 1957, Report No. GM-TM-194, Ramo-Wooldrige Corporation.

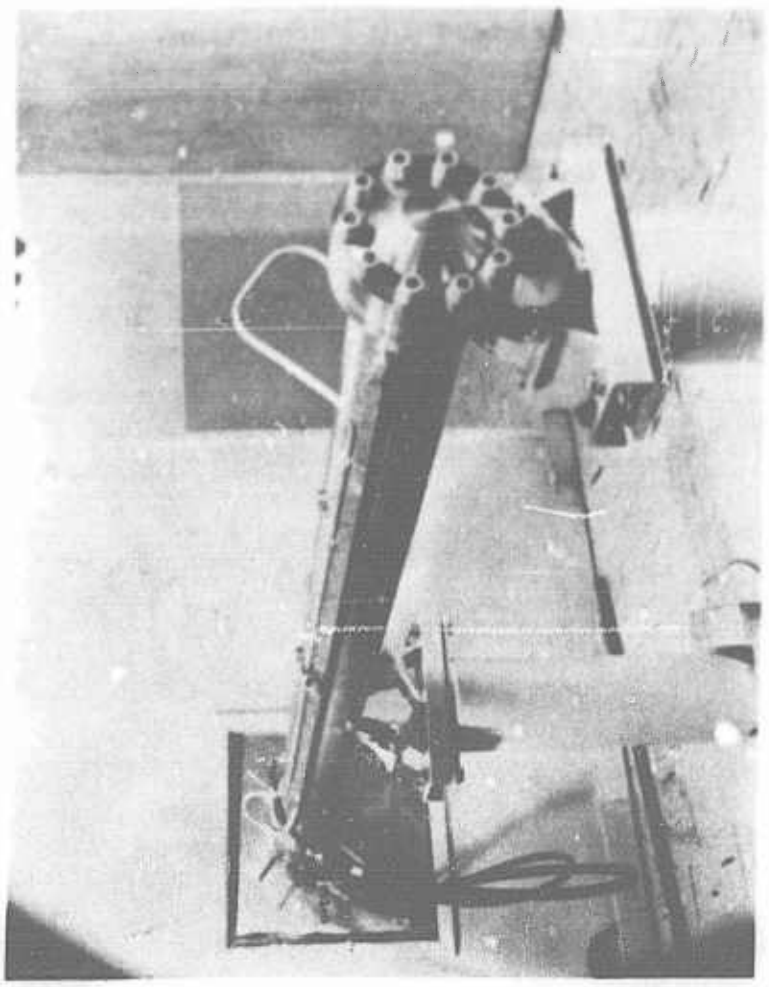

Figure 1 View of Driver Section

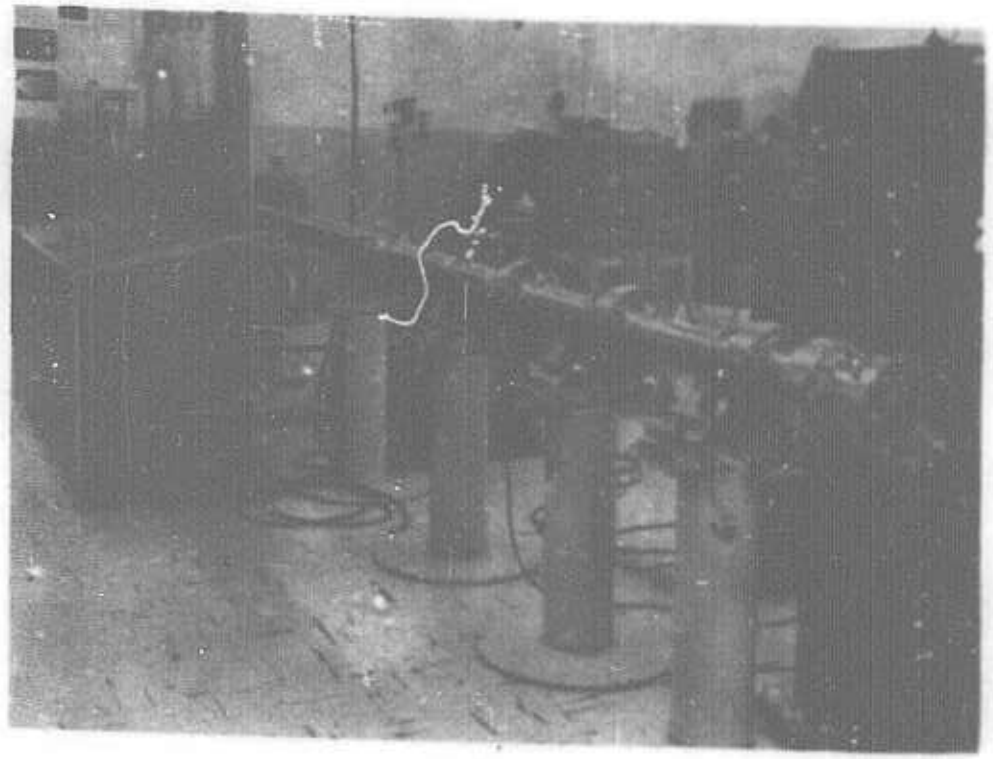

Figure 2 View Expansion Chamber

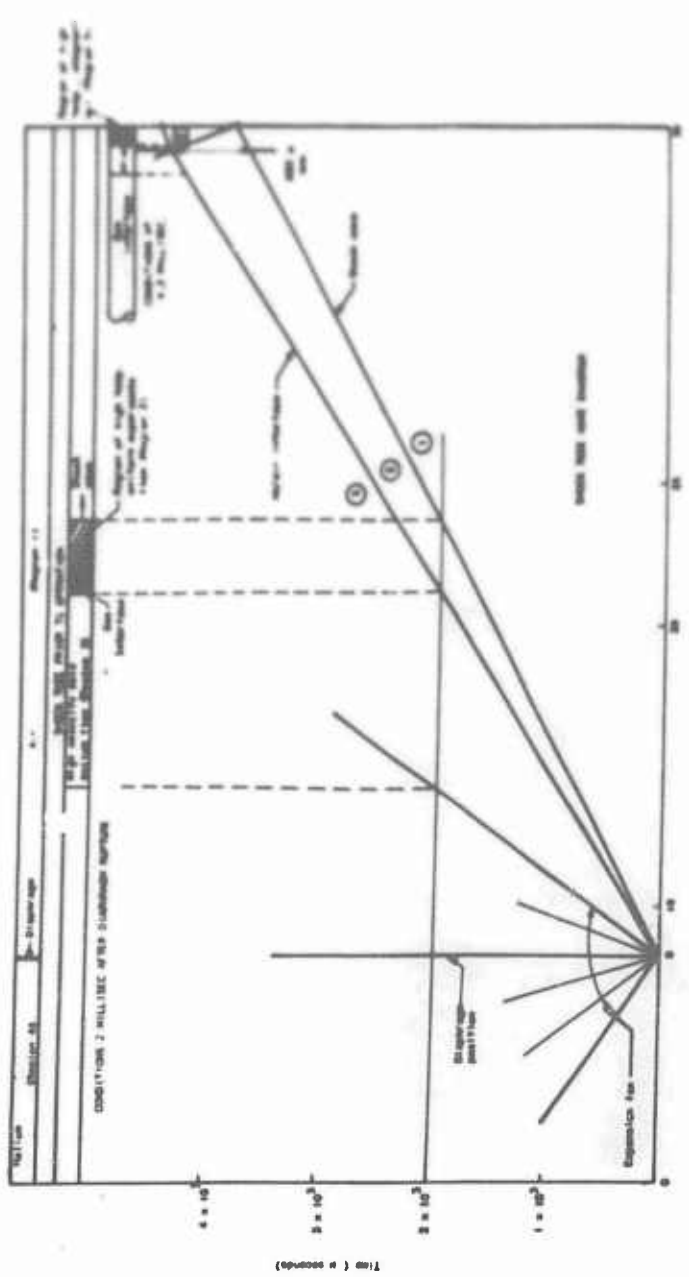

Figure 3 Typical Wave Diagram for Shock Tube

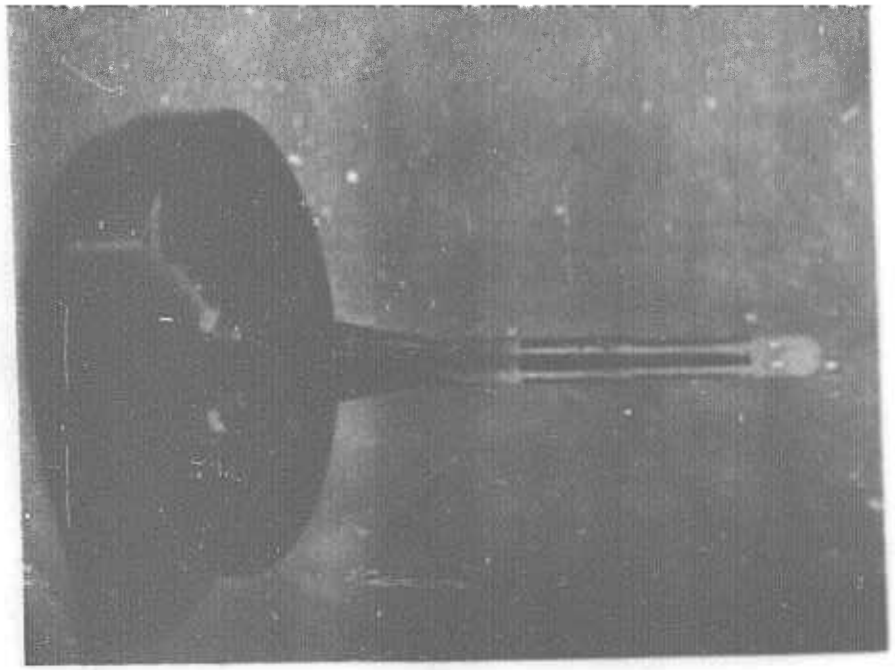

Figure 5 View of Heat Trans for Model and Shock Tube End Plate

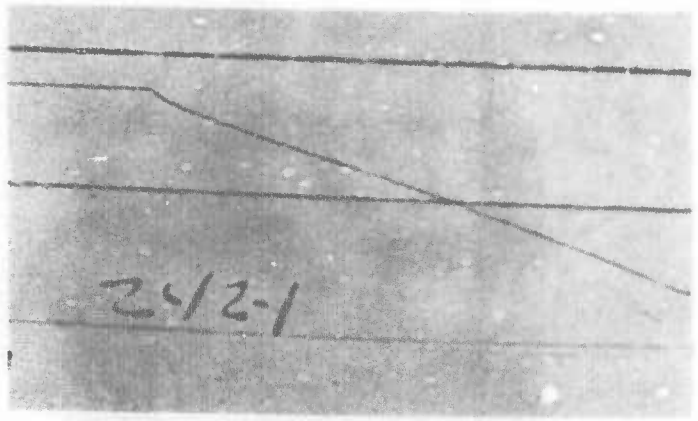

Figure 6 Typical Response of Heat Transfer Gage

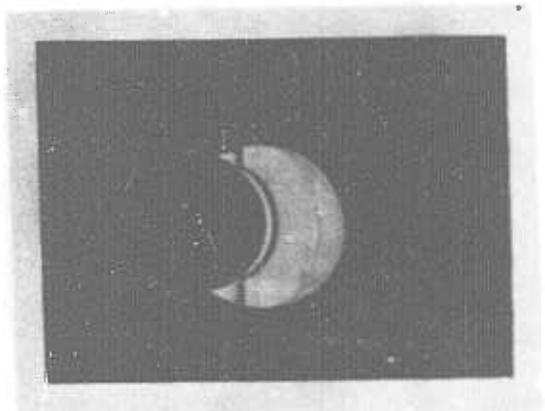

Figure 7 Shadowgraph of Shock Wave Hitting Model

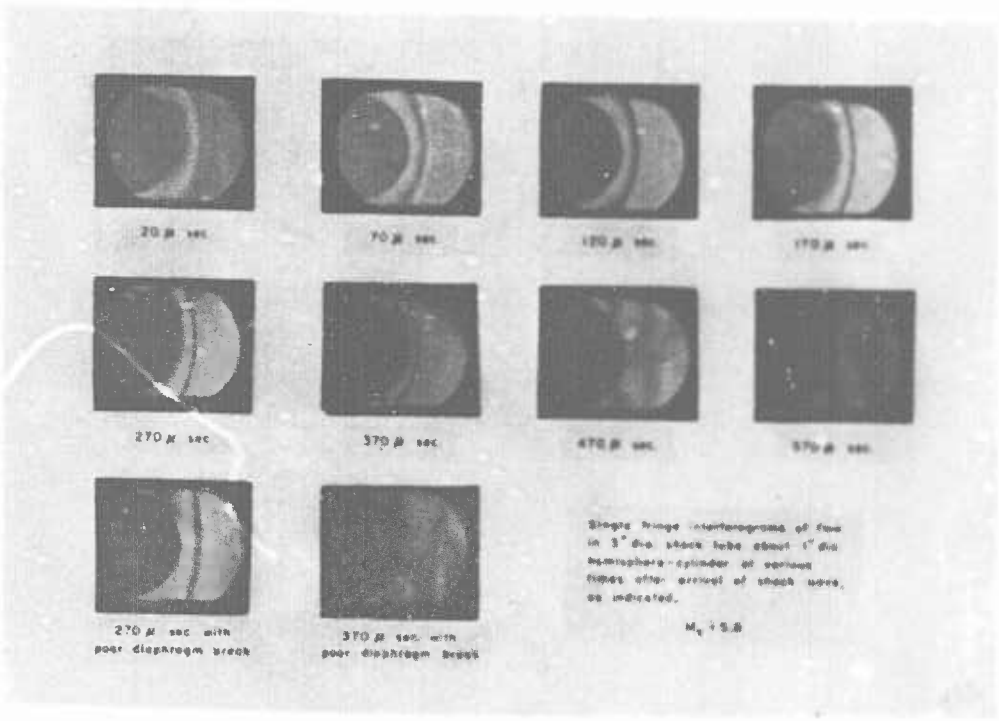
270 μ sec with
poor diaphragm break
370 μ sec with
poor diaphragm break

Figure 8

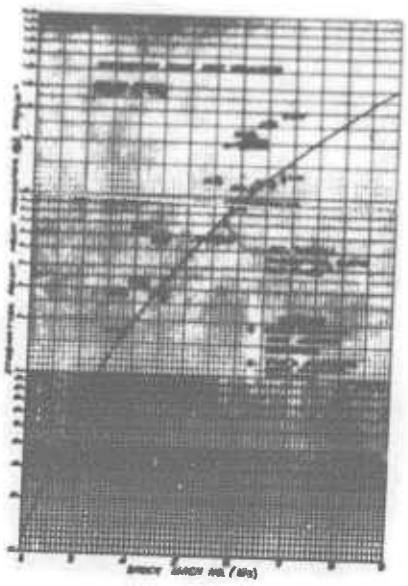

Figure 9

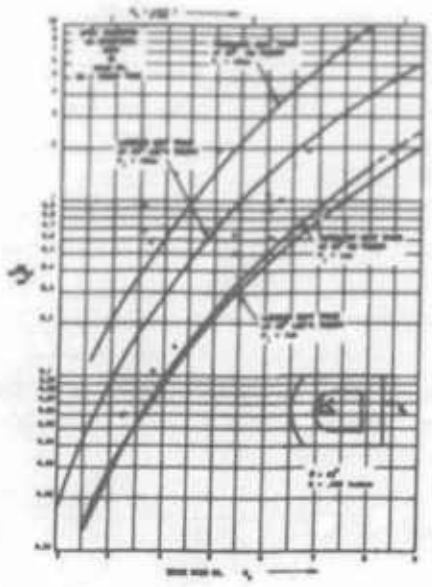

Figure 10 Comparison of Heat Transfer Data with Laminar and Turbulent Theories

A PARTICULAR APPLICATION OF A CONVENTIONAL SHOCK TUBE FOR THE STUDY OF TRANSIENT IGNITION AND COMBUSTION IN SUBSONIC FLOW*

D. Bitondo, N. Thomas, D. Perper
Aerophysics Development Corporation

I. GENERAL DESCRIPTION AND REQUIREMENT

The present research arose out of the development program of a certain type of wave engine called the Multi-jet. This engine is essentially a pulse-jet with controlled valving at the inlet and exhaust of the combustion tubes.

Figure 1 shows a perspective view of the multi-jet. The combustion tubes are arranged in an annulus and are opened and closed by rotating the inlet and outlet valves. The cycle consists of four phases: scavenge, pulse compression, combustion, and exhaust, as shown in Fig. 2. During the scavenge and pulse compression phases when the fuel-air mixture moves through the tube, due to the fact that the tubes are un-cooled and are allowed to reach wall temperatures of the order of 1800°F, ignition occurs along the surface of the tube. During the burning phase, the flame which is occuring at the boundaries of the tube now proceeds radially inwards completing the combustion of the fuel-air mixture. Although the wave diagrams for the flow in the tube can be constructed by known procedures, their construction is dependent upon the knowledge of the rate of heat release in the tube and its distribution along the tube axis. At this stage it became apparent that some useful information would be gained by studying a simplified model of the conditions in the tube which could be examined in more detail both experimentally and if possible analytically.

II. DESCRIPTION OF SHOCK TUBE

This simplified model was a short test section of a square shock tube with glass side walls in the test section for observation and whose lower surface consisted of an electrically heated nichrome strip. Figure 3 shows a sketch of the shock tube and the time displacement diagram of the conditions occurring in the shock tube. Normally, the expansion chamber is opened to the atmosphere. In the shock tube a section about 6' long immediately downstream of the compression chamber was filled with an inflammable mixture and was isolated from the rest of the tube by a slide valve on one end and the diaphragm at the other end. The slide valve was immediately opened before bursting the diaphragm and thus a "slug" of flammable gas was accelerated

*This work was supported by the Combustion Dynamics Division of the Air Force Office of Scientific Research, Air Research and Development Command under Contract AF 18(600)-1509 and the initial results have been reported in AF OSR-TN-57-454 (Sept 1957).

downstream at subsonic speeds behind the shock. Optical observations of the ignition and combustion process were made through glass side walls using a Schlieren system with a high voltage spark gap to obtain snapshot photographs or a Fastax camera and a steady light source for high speed motion pictures. Tests were conducted with ethelyne and propane fuels.

Figure 3 illustrates the sequence of events that follow the puncture of the diaphragm separating the high and low pressure chambers. As the shock passes any given cross-section in the tube the gaseous particles there are set into motion at a velocity U_2. After the shock wave has reached the front face of the fuel-air mixture at the slide valve, the entire fuel-air "slug" is moving at a velocity U_2 towards the test section containing the "hot wall". The velocity U_2 is readily computed from shock tube theory using the experimentally obtained shock wave velocity. The stay time of the fuel-air mixture within the test section varies from approximately 60 milliseconds down to 10 milliseconds depending on the flow velocity. The compression chamber is made sufficiently long to prevent the reflected expansion wave from arriving in the test section before the fuel-air mixture has completely passed through the test section. A length of tube is added beyond the test section to prevent the reflected wave formed when the shock wave passes through the open end of the tube from arriving at the test section before the phenomena has been completely photographed.

During this program we too had difficulty in the selection of proper diaphragm material. It was associated with the fact that we could not find a material weak enough to provide the proper bursting characteristics for the low pressures that were necessary for the low flow velocities used in some of our tests. With a material 0.0005" thick, compression chamber pressures down to about 10 inches of mercury gage could be used. The lower limit of U_2 with this pressure was about a Mach number of 0.09 or about 100 ft/sec. Below 10 inches of mercury, bursting consistency was poor and the spread in the shock velocities corresponding to a given diaphragm pressure ratio was considerable.

Figure 4 shows the variation of Mach number of the principal shock and of the flow behind the shock wave plotted against diaphragm pressure ratios. Normally, we operated between diaphragm pressure ratios of about 1-1/2 to about 4. The shock tube consisted of standard 1-1/4" square pipe. The test section was built up to provide a floor that could be electrically heated and observed through windows which provided a clear view from the floor to the ceiling of the test section. The "hot wall" consisted of a 1" wide, 12" long, electrically heated nichrome strip 0.010" thick. The floor is recessed for a bed of fire brick. A sketch of the test section and the power supply is shown in Figure 5. Slots were cut at either end of the floor and the nichrome strip was passed through these slots. When the strip was electrically heated to high temperatures, buckling of the strip was prevented by means of tension produced by weights attached to one end of the strip. The power supply is also shown in Fig. 5. Temperatures of the nichrome strip were measured by means of an optical pyrometer. Maximum temperatures obtainable with the present installation is about 1,060°C.

Figure 6 shows a photograph of the test section. The hot wall or the nichrome strip is located along the floor of the test section. Weights are hung on the insulated terminal on one side; windows consist of ordinary plate glass.

Figure 7 shows the arrangement of the principal components of the shock tube. 1 is the test section, 2 the slide valve, 3 are the photo screens used for shock wave velocity measurements, 4 is a chronograph and time delay circuit, 5 is the location of the diaphragm, and 6 the diaphragm breaker.

Figure 8 shows the general arrangement of the Schlieren system and the shock tube. A high voltage confined spark gap was used to obtain the snapshot pictures of the events occurring in the test section, these pictures were obtained on a 4 × 5 photographic plate. Recently, a Mercury arc vapor lamp was added as a steady light source and is used in conjunction with a high speed Fastax camera. With the Fastax camera the complete sequence of events could be photographed during a test run. Speeds up to 16,000 frames per second were used to obtain the sequence of events. The length of tube inserted between the section containing the fuel-air mixture and the test section containing the "hot wall", provided a buffer zone of air to prevent pre-ignition of the fuel-air mixture upon the opening of the slide valve and before the diaphragm is punctured.

III. OBSERVATIONS AND TEST RESULTS

Before the Fastax camera was used in this installation, snapshot pictures were taken during each test run. One snapshot per run was obtained. The time delay used to trigger the light source was varied for each run. In this way, a sequence of events could be obtained. However, each event occurred in a separate run and the accuracy with which the sequence of events could be obtained depended on how well the events could be repeated between test runs. Actually, it was not too difficult to obtain the correct sequence of events. However, during certain tests, such as those resulting in "predetonation" flames (described later), events occurred so rapidly that it was impossible to obtain the correct timed sequence and determine such parameters as flame velocity. Such a sequence of snapshot photographs are shown in Figure 9. The first picture shows a shock wave within the test section at 4.7 milliseconds. From about 10 milliseconds to 25 milliseconds, only the thermal boundary layer could be detected. At about 27 milliseconds a turbulence spot was seen to occur at the outer edges of the thermal boundary layer. At 29 milliseconds the first appearance of flames could be definitely seen propagating through the free stream. From then on the events occurred so rapidly that sequence snapshots for different test runs gave the last series of pictures. The flame very rapidly bursts out of the boundary layer and travels completely across the test section. For these pictures the knife-edge was placed horizontally so as to cut off the upper half of the image at the focal point of the second mirror.

Figure 10 shows another series of photographs where the horizontal placement of the knife-edge was such to cut off the lower half of the image at the focal point. These photographs produced the clearest details of the

processes occurring within the boundary layer. As you can see, again it was very difficult to obtain the correct sequence of events by means of our snapshot photographs. However, for the time delays that were preset to trigger and spark the position of the front of the fuel-air mixture could be calculated and is indicated by the smaller arrow. It will be noticed that at a given time and position a flame occurs within the boundary layer as is shown by the density gradients indicated. Although the flame is occurring within the boundary layer, no visible change on the outer edge of the thermal boundary layer is seen until the flame front which appears to be travelling with the front of the fuel-air mixture reaches a point further downstream from the ignition point within the boundary layer. Then the characteristic breakout of turbulence is noticed and a few milliseconds later the flame has completely traversed the whole of the test section.

In order to obtain better detail of the processes, occurring within the test section, photographs were taken using glass slides as the photographic plates. Figure 11 shows such a slide. This figure clearly shows the development of the flame within the boundary layer. The light portion indicates the thermal boundary layer and the flame front is clearly visible on the photograph. It was found later by means of Fastax high speed movies that the flame front after it breaks out of the boundary layer moved upstream and completely out of the test section. Figure 12 shows a plate that was obtained at a later time after ignition within the boundary layer. In this case the flame front has moved upstream and is now traversing the free stream flow in the test section.

Figure 13 is a reproduction of a short length of a strip of Fastax movie film taken at approximately 12,000 frames per second. The time interval between each frame is of the order of 87 microseconds. At the top we see the thermal boundary layer relatively undisturbed. In a very short time the characteristic breakout of the flame is seen as shown by the change in turbulence. This breakout first appears at the downstream end of the test section and slowly proceeds forward as shown by the sequence in the first strip. Finally, the flame encompasses the complete test section and is seen to move in an upstream direction until near the end of the second strip the combustion is completed within the test section and the flame is seen to move upstream. We were able to further blow up the series of 7 frames from the mid portion of the first strip of film and this is shown in Fig. 14. Here more details can be seen of the breakout of the flame from the boundary layer. Not only do these photographs provide the correct sequence of events, but show a remarkable clarity of the processes occurring during each frame. They in fact, confirmed our conclusion that we were able to draw from our previous series of snapshot photographs.

The complete Fastax film from which the previous two slides were obtained shows the following sequence of events. The first motion that you will observe will be the shock wave traversing the test section. The shock wave is not too clear due to the fact that the knife-edge is set at a direction perpendicular to the density gradient of the shock front. The motion immediately behind the shock wave is that of the air originally in the spacer section upstream of the test section and downstream of the fuel-air mixture. In just a short time the flame will break out of the boundary layer at the right hand

side of the frame. It will grow, traversing the test section perpendicularly to the air flow, then it will move upstream indicating that combustion has been completed within the test section. A few seconds later the flame will reappear within the test section and move from left to right with the free stream flow direction. This also finally sweeps out of the test section, and a few milliseconds later, a final burst of flame is observed and further motion of the gas indicates that now reflections of expansion waves and shock waves are occurring and causing the flow to oscillate and die down within the shock tube.

You will remember that there were three distinct flames appearing within the test section. The first is the usual flame that we expected due to the initial ignition of the fuel-air mixture as it travels along the hot strip. This ignition occurs within the boundary layer, as we have shown, finally breaking out of the boundary layer, traversing the test section in a direction perpendicular to the flow direction, and then moving upstream. There are two possible reasons why the flame moves upstream. First is due to the fact that the flame velocity is approaching and exceeding the normal free stream velocity. Second, due to the heat release within the flowing fuel-air mixture, a thermal choking can occur which will reduce the flow velocity and therefore allow the flame to travel in an upstream direction with respect to the shock tube wall. It can also be a combination of both effects. Tests with various fuel-air mixtures have shown that these "fast flames", the ones moving upstream in the test section, occur more readily with very rich fuel-air mixtures, that is, stoichiometric or higher fuel-air mixtures. They are also associated with a loud explosion and several times have crached our observation windows. Flow velocities in the particular example that was shown in Fig. 13 are of the order of 186 ft/sec.

The second flame can be due to the following considerations. The initial flame which travels upstream, traverses the "slug" of fuel-air mixture and reaches the tail of the fuel-air mixture. At this point, its forward progress is stopped, however, burning may continue within the "slug" of fuel-air mixture. Due to the normal flow velocity in the tube, now the flame is swept back into the test section and this is the second flame that we observed in the Fastax sequence. The third flame at this point seems to be a pure accident. There seems to have been remaining in the vicinity of the test section, residual fuel which does not ignite in the vicinity of the hot strip. However, if you closely observe the events just before the ignition of the third flame, you will notice a piece of cellophane entering the test section which is ignited due to the hot strip. This burning particle seems to provide an ignition point which results in the ignition of the residual fuel within the test section.

IV. ANALYSIS OF TEST RESULTS

Now to describe the results that were obtained from the observations of the snapshots of the flame and the sequence from the Fastax movie film.

As the front face of the fuel-air mixture passes over the hot strip, it is being heated within the boundary layer as it progresses along the strip. At a given distance downstream from the leading edge of the hot strip, the

temperature in the boundary layer reaches a point where ignition temperature is reached. At this point a flame is observed to occur within the boundary layer. The flame remains within the boundary layer until finally, at a point further downstream, the flame front breaks out of the boundary layer. As soon as this breakout occurs, the flame within the boundary layer moves forward as well as moving perpendicularly across the test section. The velocity of flame propagation varies with the fuel-air ratio. For the rich mixtures, the flame travels very rapidly and traverses the whole of the test section and moves upstream. For the leaner mixtures, the flame breaks out of the boundary layer, however, its forward progress is limited and it finally is blown downstream. An ignition time delay, τ_b, can now be defined as to the length of time that is required for the appearance of a self-propagating flame in the test section. The time, $\tau = 0$, is taken as the time when the front face of the fuel-air mixture arrives at the leading edge of the hot strip. The time delay can then be broken into two parts, τ_1 and τ_2. First, τ_1 is the time required for the passage of the front face of the fuel-air mixture over the hot strip before ignition occurs within the boundary layer. τ_2 is the time during which a flame propagates in the boundary layer and breaks into the free stream. The ignition time delay was measured for a number of flow velocities, strip temperatures for two fuels, ethylene and propane, at various fuel-air ratios.

Figure 15 shows the variation of the ignition time delay plotted against the free stream flow velocity for ethylene and propane. In both cases, a stoichiometric fuel-air mixture was used. Due to the geometry of the tube, for given flow velocities, a limit is obtained for τ_b above which the fuel-air "slug" has completely passed the hot strip before any ignition is seen to occur. This is due to the finite length of the "slug" of fuel-air mixture. Another limitation of the present equipment is the finite length of the hot strip. In the case of propane, at stoichiometric fuel-air ratio and with a wall temperature of 1,025 °C, the upper velocity limit was observed to occur at the point where the "slug" has completely passed the hot strip. The variation of the ignition time delay with fuel-air mixture is shown in Fig. 16. For lean mixtures, the ignition time delay is increased. This variation ended at a certain lower value of the fuel-air ratio when bulk ignition would no longer occur, although burning across part of the test section was observed. Attempts to measure values of τ_b for fuel-air ratios above the stoichiometric value ran into difficulty in that ignition of a rich mixture produced flames of the predetonation type, sometimes damaging or blowing out the test section itself. It was decided, therefore, not to pursue the results for rich mixtures any further, at least not until a stronger test section could be obtained.

In the region where data can be obtained, the value of the ignition time delay was much less sensitive to velocity changes than it was to temperature changes as can be seen on the Fig. 17. This, presumably, was due to the fact that primary ignition occurs in the low velocity region of the boundary layer which is rather insensitive to changes in main stream velocity.

Ignition delay time may be correlated with the rate of combustion reaction if we assume that the reaction rate follows the Arrhenius law and that it is inversely proportional to τ_b. This assumption is crude but was adopted. From this relation it can be seen that the slope of the plot of $1/T$ against $1/\tau$ will give E the apparent activation energy of the reaction.

As seen on Fig. 18, the linear relation was obtained, however, the activation energies were an order of magnitude higher than that expected for the fuels tested. One of the reasons that we may be obtaining a very large value for the activation energy is since this is a transient flow, the pre-existing boundary layer, whether of air or burnt gas, has to be displaced by fresh fuel-air mixture. Now at any given time, the dividing line between the fresh fuel-air misture and the air will run obliquely across the boundary layer following the velocity profile. It will advance further downstream in the outermost portion and thus a photograph of the layer at any given time would shown a higher mean concentration of fuel in the outer cooler regions, and a lower one in the hotter inner region close to the wall. Molecular diffusion would tend to equalize the concentration and being temperature dependent, would respond to changes in the wall temperature. It is, therefore, probable that the rate controlling process is a combination of chemical reaction and inward diffusion into the hot sub-layer.

Let us define the distance over the hot strip from the leading edge to the point where ignition first occurs within the boundary layer as x'.

Measurements of x' and τ_b have been made under steady-flow conditions similar to ours.* The distance measured was shorter than ours. This can also be due to the same reason that affected the activation energy mentioned above.

However, x' may be determined by energy considerations, It is reasonable to assume that the input of thermal energy to the gas in the boundary layer upstream of the ignition point, is that required to raise this volume of gas to ignition temperature. At least, this will be so if the boundary layer is assumed to be quasi-steady, so that its profile immediately after passage of the shock over the length x' remains unchanged as long as the outside flow does not change significantly. This is true over the time intervals (< 0.05 sec) involved in our tests.

On this assumption, and knowing the temperature profile of the layer, one can calculate the amount of energy required to raise the layer to ignition temperature if its volume is known. But calculation of the volume involves knowledge of x'.

However, the "ignition energy" per unit of volume can be taken as constant for a given fuel-air mixture, regardless of the way in which the energy is introduced -- provided the energy is thermal. And this ignition energy may be calculated from the work on spark ignition of Lewis and Von Elbe.

Calculations carried out for propane give a value of 3 inches for x', as against an experimentally determined value of about 6 inches. This order-or-magnitude agreement is as good as can be expected.

---

*Unpublished work at Jet Propulsion Laboratory, California Institute of Technology and private communication from F. E. Marble and F. H. Wright.

V. SUMMARY OF RESULTS

We have thus seen how it is possible to observe the processes occurring during the transient ignition of fuel-air mixture passing over a "hot wall". Detailed observations can be made of the initial ignition with the boundary layer as well as to the ignition delay times or bulk ignition delay times where the flame becomes self-propagating within the main free stream. A further usefulness of this apparatus is due to the fact that only small quantities of fuel can be used and therefore, lends itself well to the testing of the new exotic fuels which are very difficult to obtain in quantity at present.

In the present investigation, the transient flow conditions associated with the ignition of a fuel-air mixture passing over a "hot wall" type of flame stabilizer was studied. The "hot wall" flame stabilizer can be substituted by other means of flame stabilization normally used, for instance, in jet engines. The transient ignition conditions could be studied for these flame holding devices. Such problems are of great magnitude with jet engines where the engine must be re-ignited after flame blowout. Under laboratory conditions, the problem associated with the transient ignition for these flame holders can be studied in detail in an apparatus similar to the one described here.

Other investigations involving the interaction of a shock wave with ignition and combustion flames can be carried out by means of the addition of a second compression chamber which can produce a shock wave following the primary shock wave and interacting with the ignition and combustion processes occurring in the test section. Referring to Fig. 3, the second compression chamber can be added at the right end, thus producing a shock wave which will travel upstream into the test section, or the second compression chamber can be mounted at the extreme left end, thus producing a shock wave which will enter the test section from a downstream direction. Referring to Fig. 11 again, the interaction of the shock wave with the thermal boundary layer upstream of the point where ignition occurs, may produce conditions where the combination of temperature gradient due to the "hot wall" and the pressure gradient due to the shock will provide early ignition. The interaction of the shock wave with the flame downstream of the ignition point may provide conditions the combination of which will produce detonations. The fact that we have already observed what we call "pre-detonation waves", although we feel these are not true detonation waves, we believe that by the addition of perhaps a realtively weak wave of pressure ratio of up to 5 that we can accelerate the process leading to a detonation wave.

Recently, interest has grown with regard to the conditions that occur within a solid propellant motor causing it to explosively detonate itself during the normal course of burning. It is felt that detonation of the propellant may be due to shock waves which may cause a shock pressure at the burning surface of the propellant causing acceleration in the burning velocity or causing erosion of the propellant producing many fine particles which will burn and produce a higher pressure which results in a stronger wave which in turn results in more erosion and finally, building up to pressures which rupture the rocket motor case. Studies of the erosion and the detonation of

a burning solid propellant due to the impingement of a shock wave could be made in a setup similar to the one described, however, in principle only - the tube itself probably should take the form of an oversize atomic cannon. Referring to Figure 5 the nichrome strip and the firebrick bed could be replaced by a slab of solid propellant in the test section. By means of an igniter material coating the top surface in which are imbedded fine wires, the slab could be electrically ignited to provide a burning surface along the wall of the test section. As soon as ignition has occurred a shock wave can be fired into the test section and the resulting conditions may be photographed and observed by means of high speed photography. The conditions being simulated would be those occurring within a rocket motor and the experiment can be controlled on a laboratory scale. A better analysis of the problem can be made and a better understanding of the conditions leading to self-detonation of a solid propellant can be obtained.

The following points can be cited as the main conclusions obtained thus far in the investigation.

1. Ignition in transient flows at a hot surface takes much longer than a continuous flow process because of the need to displace and mix the fuel mixture with an existing boundary layer of air or inert gas.

2. Primary ignition after fairly long delay occurs in the boundary layer. Inflammation is propagated through the main stream by a turbulent transfer process which is very fast relative to the primary ignition process.

3. The origin of the turbulence in the tube is not yet known. It may be flame generated or caused by peculiarities of the boundary layer flow.

4. Transition of turbulent combustion to fast pre-detonation flames is noted in rich fuel-air mixtures. In lean mixtures, on the other hand, inflammation will not propagate through the tube cross-section.

5. The over-all reaction leading to ignition appears to follow the Arrhenius law.

6. Finally, this experimental apparatus permits a means of simulating in the laboratory, the conditions existing during ignition and combustion in a transient flow applicable not only to non-stationary combustion devices but also for steady flow combustion devices.

REFERENCES

1. I. I. Glass, W. Martin and G. N. Patterson, UTIA Report No. 2, A Theoretical and Experimental Study of the Shock Tube.

2. D. R. Chapman and N. W. Rubesin, Journal Ae. Sc. 16, 546 (1949).

3. H. Mirels, Boundary Layer Behind Shock or Thin Expansion Wave Moving into Stationary Fluid, May, 1956, NACA TN 3712.

4. B. Lewis and G. Von Elbe, Combustion, Flame and Explosion in Gases, 'Academic Press', New York, 1951.

5. E. E. Zukoski, Jet Propulsion Lab Report 20-75 (1954). California Institute of Technology.

6. E. Schmidt, Proc. 4th Symposium on Combustion, Boston, 1952, Theory and Combustion and Detonation of Gases.

7. Y. B. Zeldovich, A.M.C. Translation, F-TS-1226-LA (1949).

8. R. S. Brokaw, Proc. 5th Symposium on Combustion, Pittsburg, 1954.

UNCLASSIFIED

AD 211239

Armed Services Technical Information Agency

ARLINGTON HALL STATION
ARLINGTON 12 VIRGINIA

FOR
MICRO-CARD
CONTROL ONLY

6 OF 6

NOTICE: WHEN GOVERNMENT OR OTHER DRAWINGS, SPECIFICATIONS OR OTHER DATA ARE USED FOR ANY PURPOSE OTHER THAN IN CONNECTION WITH A DEFINITELY RELATED GOVERNMENT PROCUREMENT OPERATION, THE U. S. GOVERNMENT THEREBY INCURS NO RESPONSIBILITY, NOR ANY OBLIGATION WHATSOEVER; AND THE FACT THAT THE GOVERNMENT MAY HAVE FORMULATED, FURNISHED, OR IN ANY WAY SUPPLIED THE SAID DRAWINGS, SPECIFICATIONS, OR OTHER DATA IS NOT TO BE REGARDED BY IMPLICATION OR OTHERWISE AS IN ANY MANNER LICENSING THE HOLDER OR ANY OTHER PERSON OR CORPORATION, OR CONVEYING ANY RIGHTS OR PERMISSION TO MANUFACTURE, USE OR SELL ANY PATENTED INVENTION THAT MAY IN ANY WAY BE RELATED THERETO.

UNCLASSIFIED

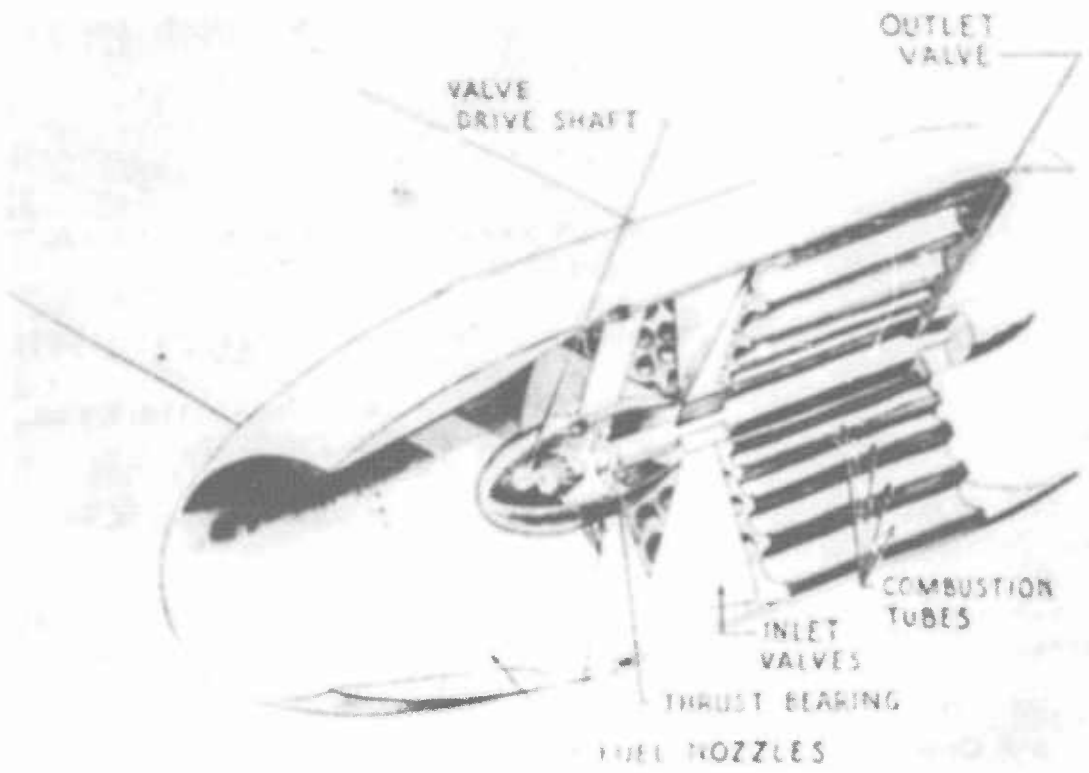

PERSPECTIVE VIEW OF THE MULTI - JET

Figure 1

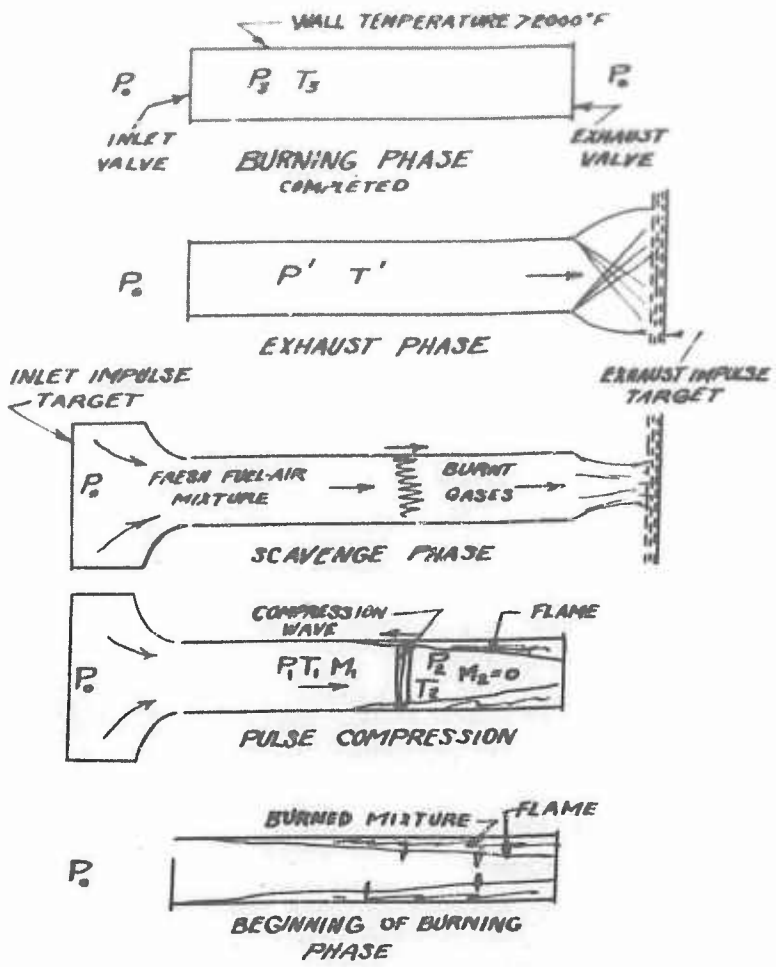

Figure 2

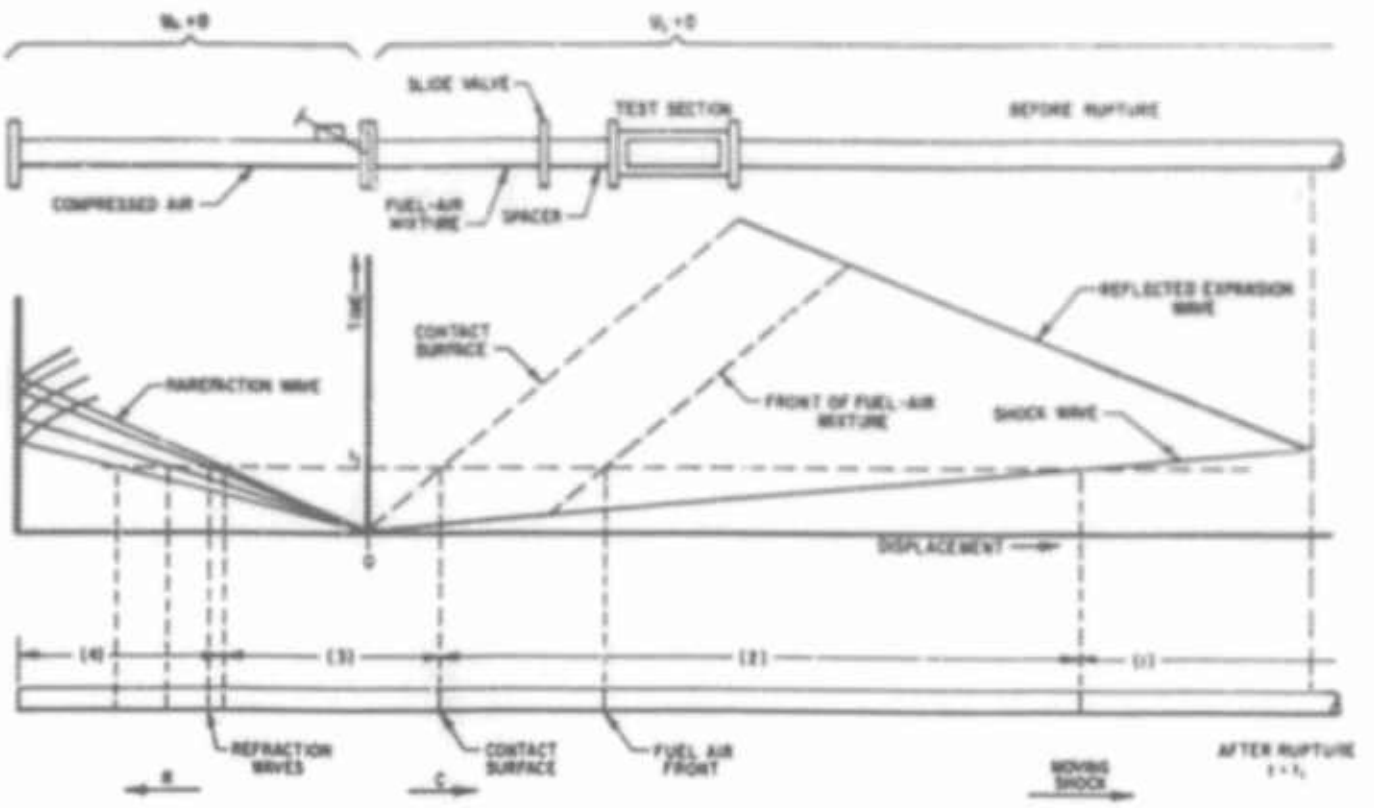

Figure 3

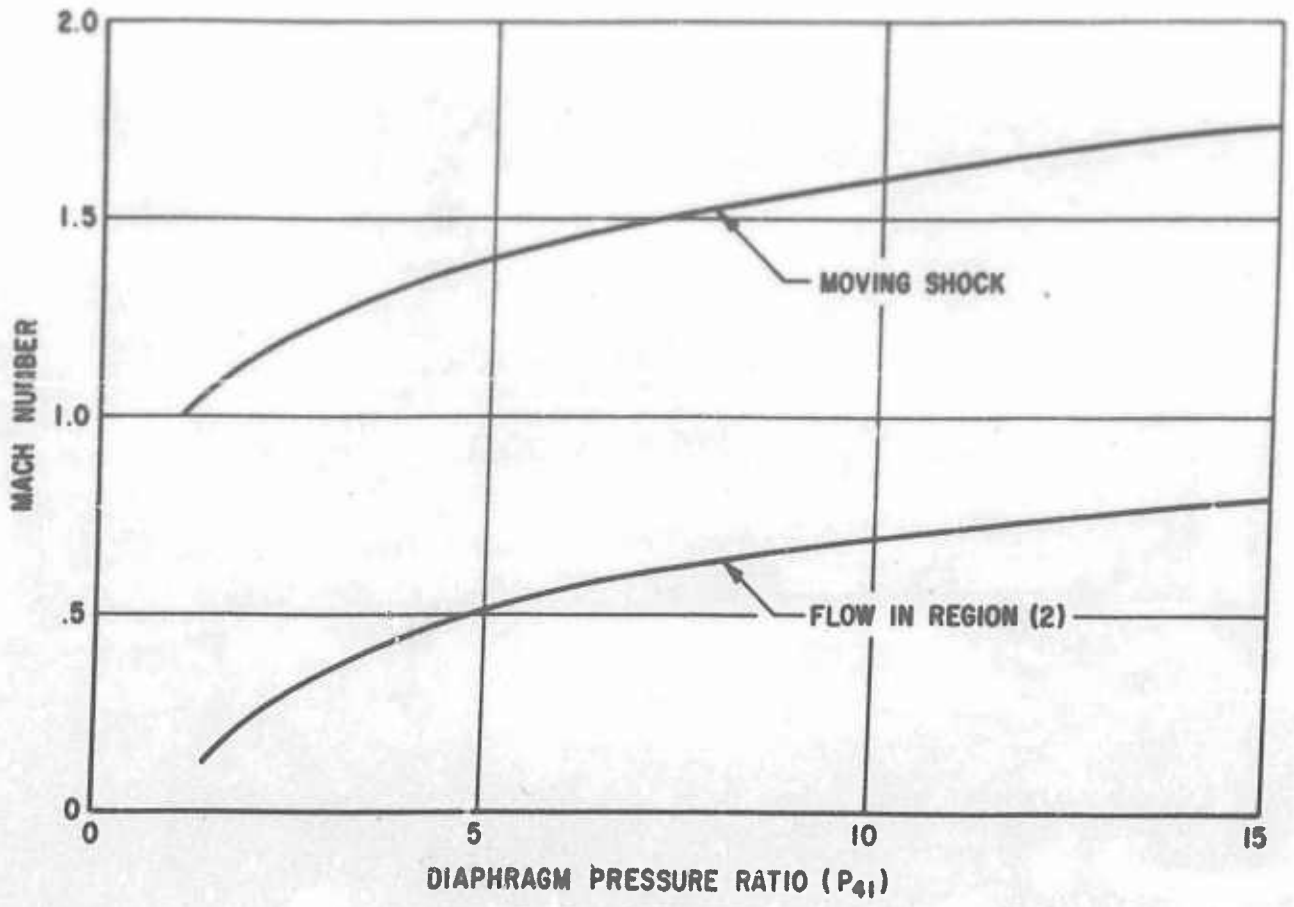

Figure 4

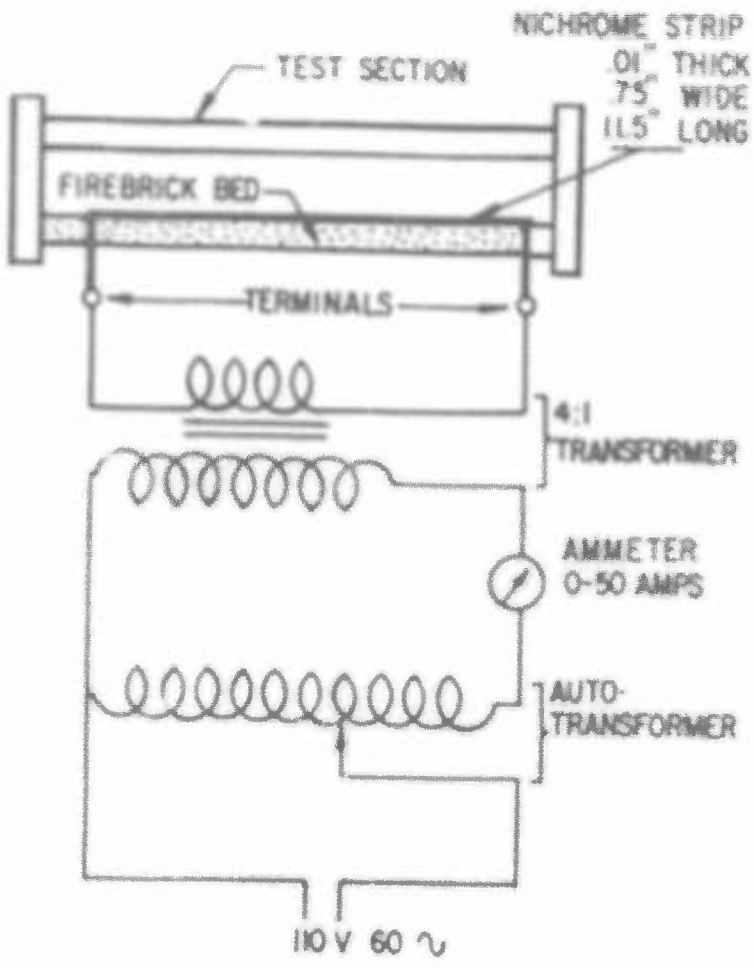

Figure 5

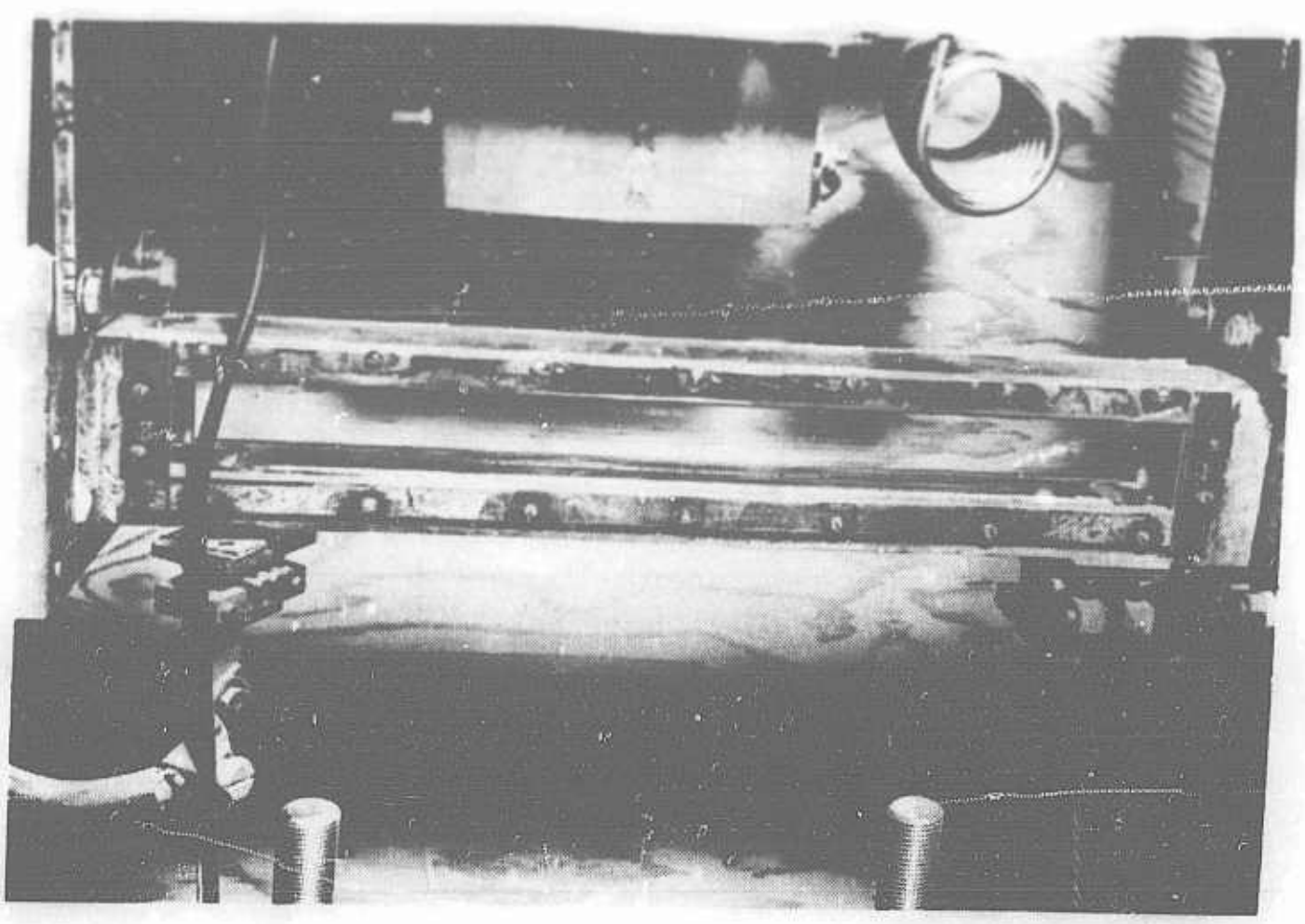

Figure 6

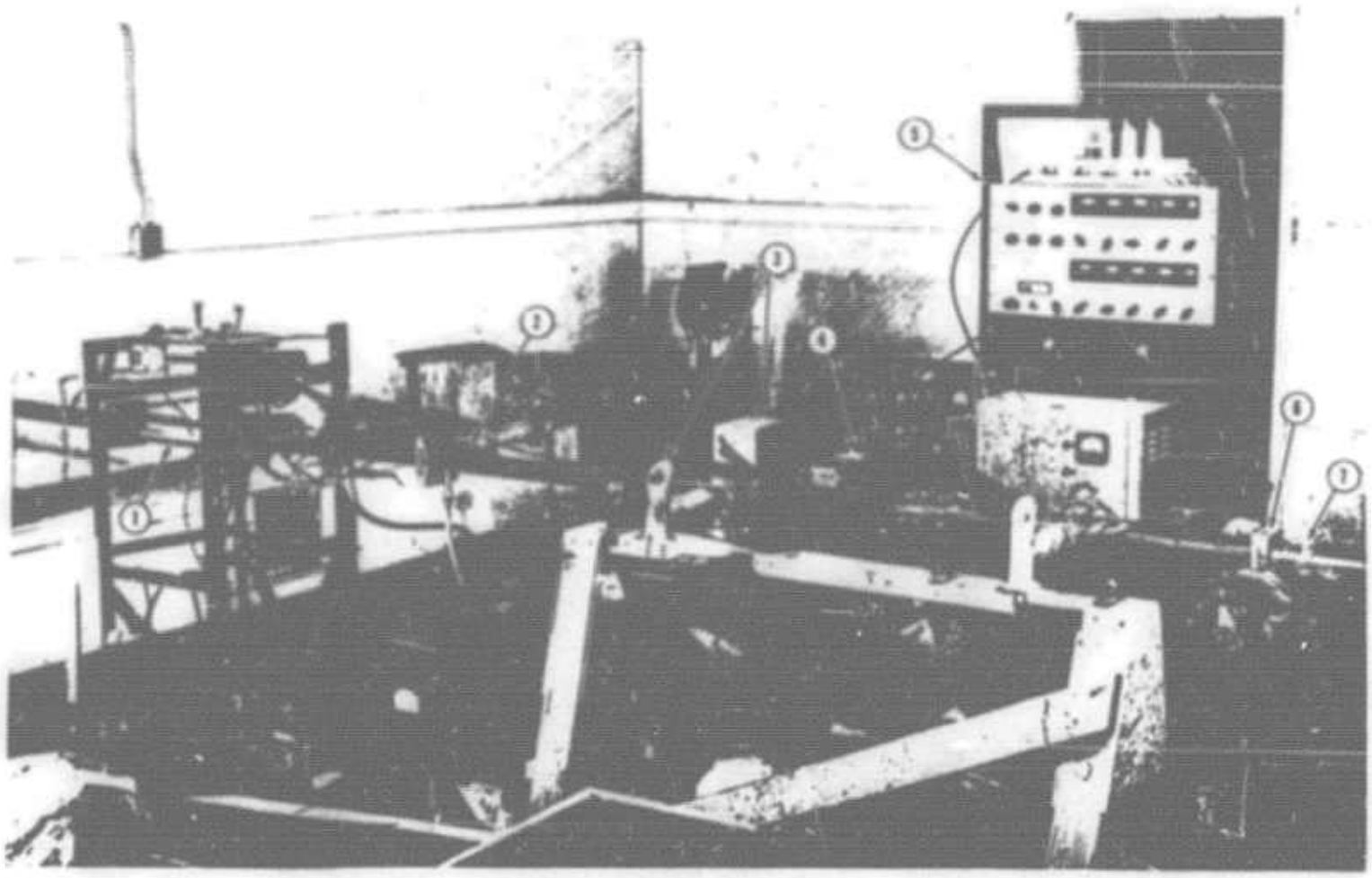

Figure 7

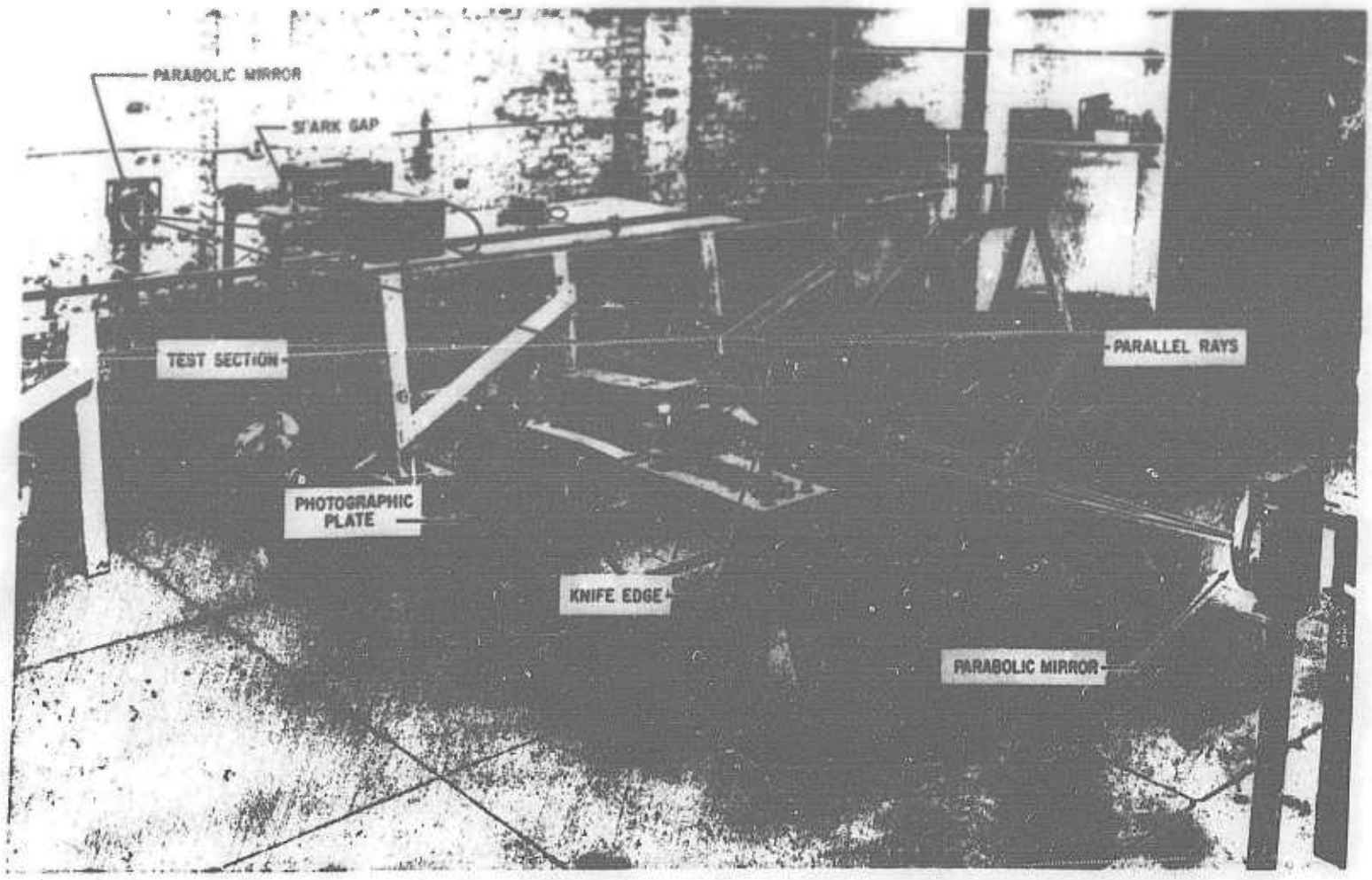

Figure 8

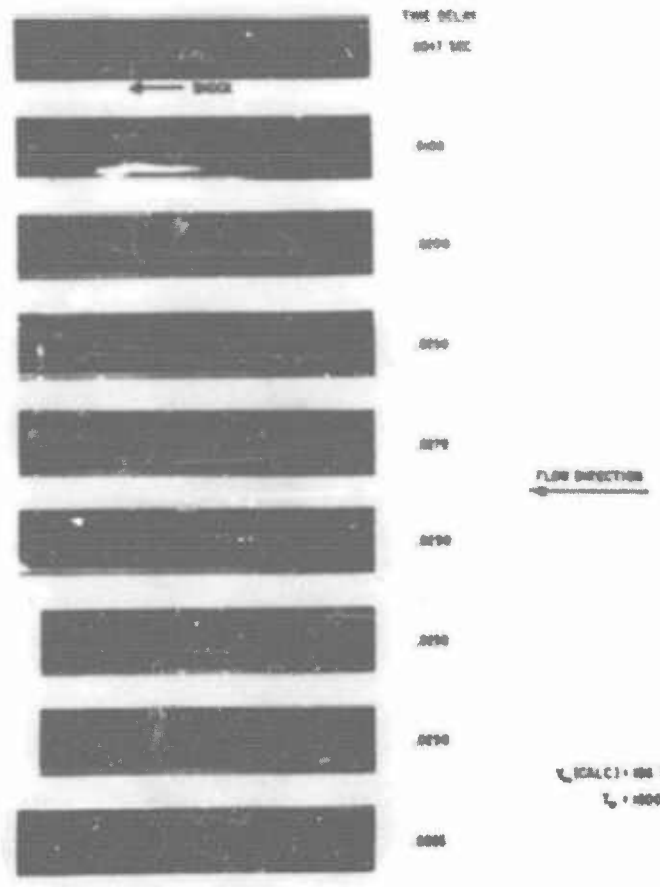

Fig. 13. Ignition Sequence

Figure 9

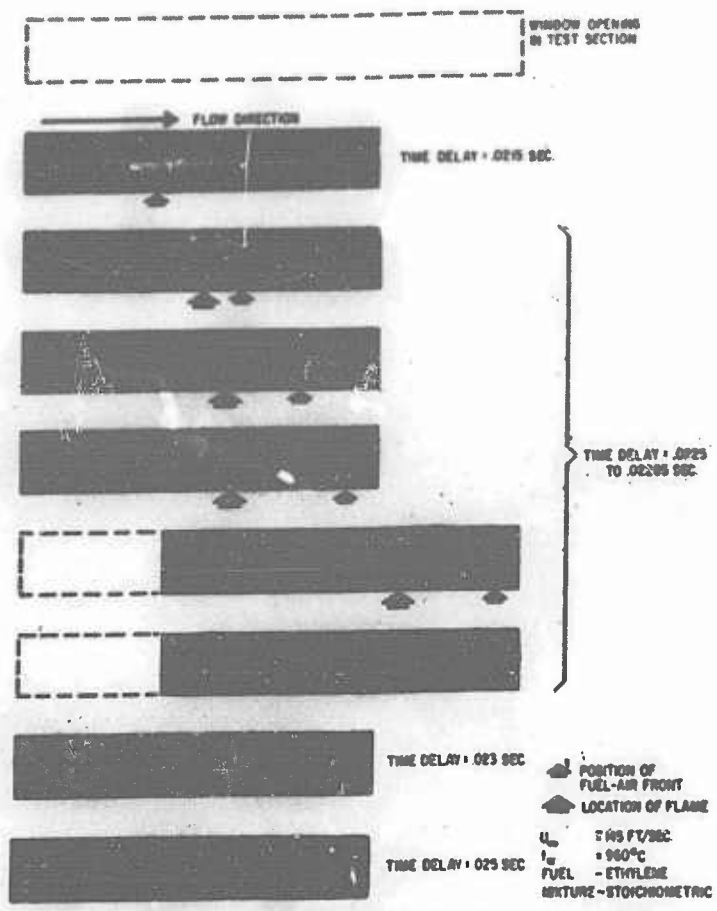

Fig. 14. Stages of Flame Breakout into Free St... (photographs)

Figure 10

Figure 11

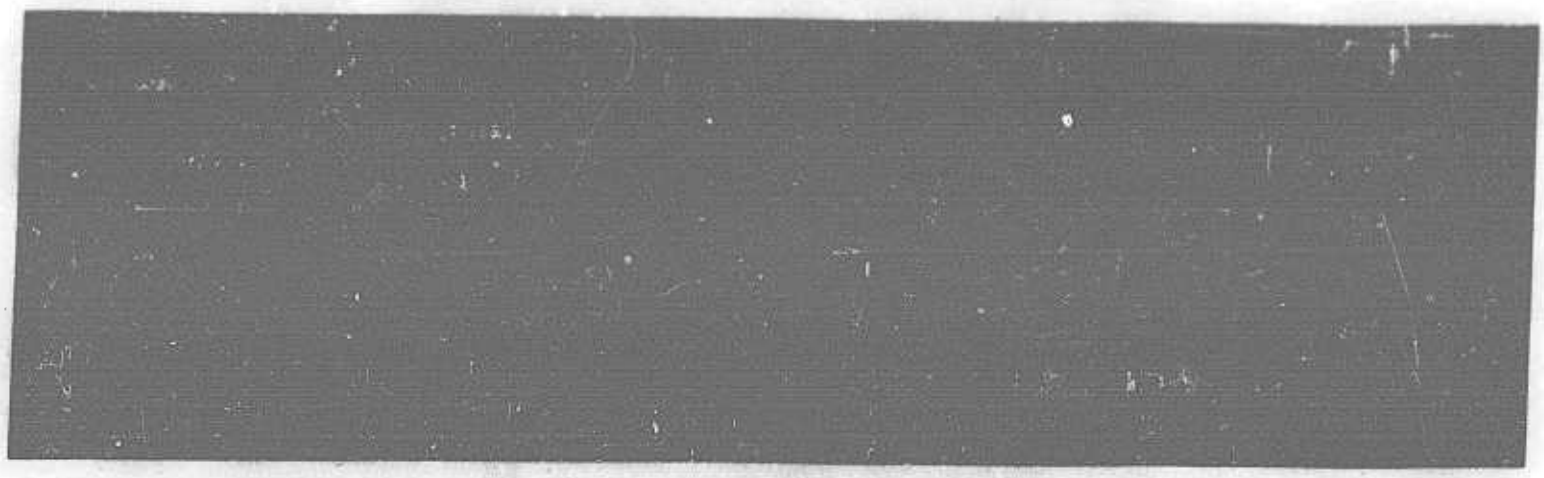

Figure 12

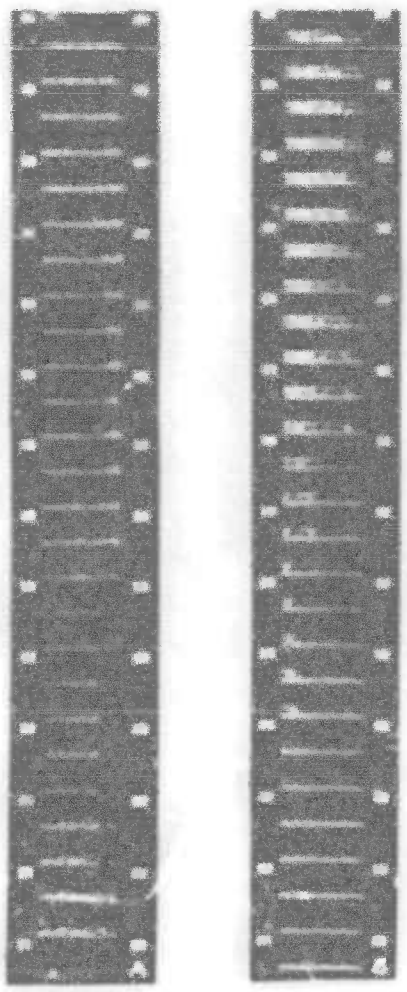

Figure 13

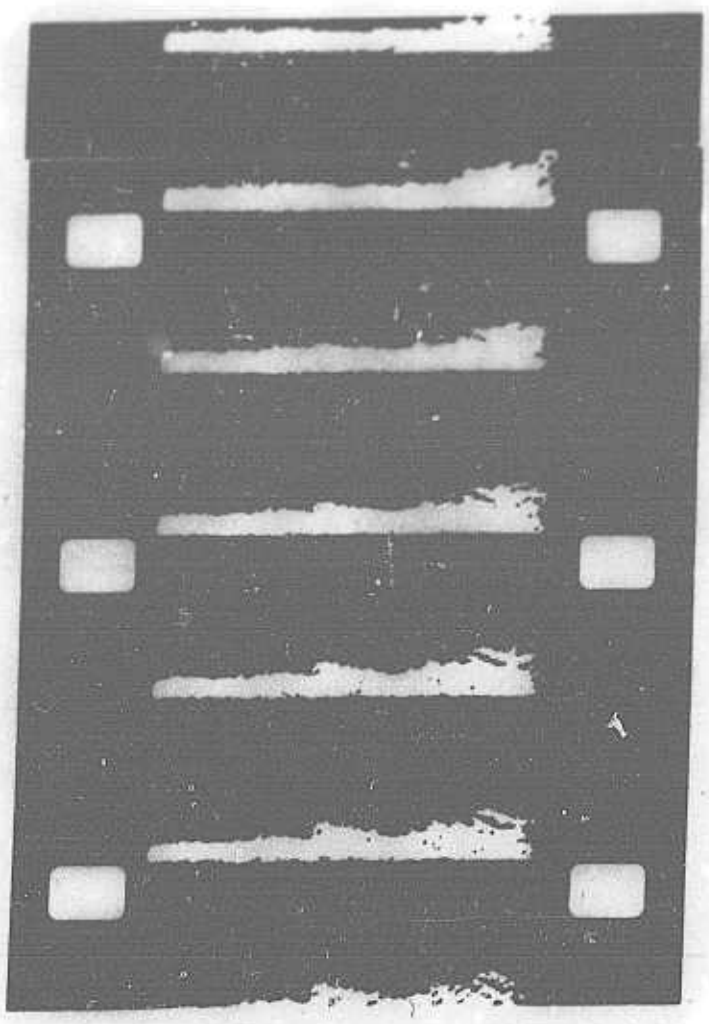

Figure 14

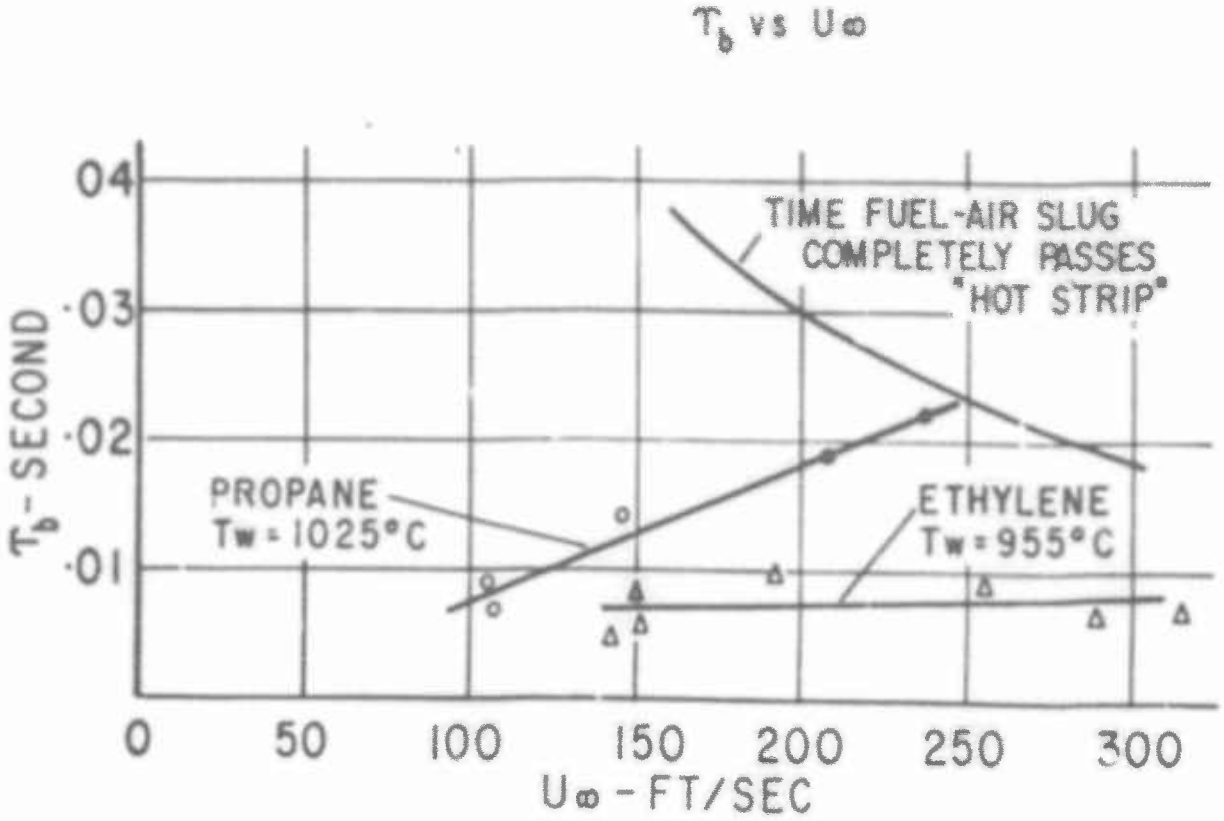

Figure 15

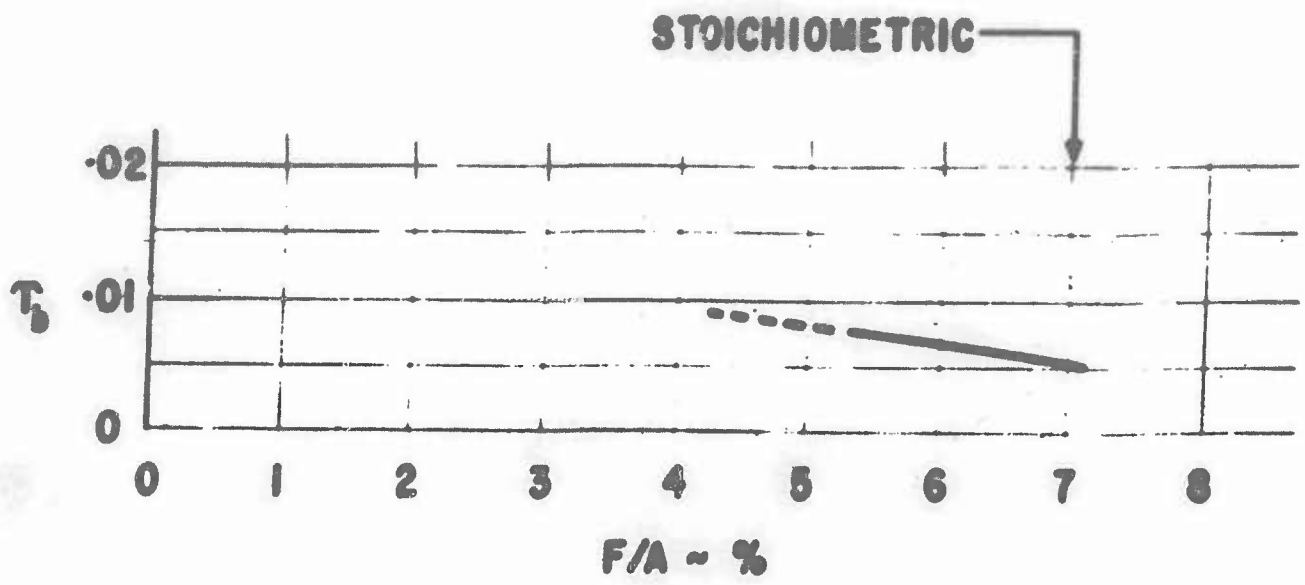

Figure 16

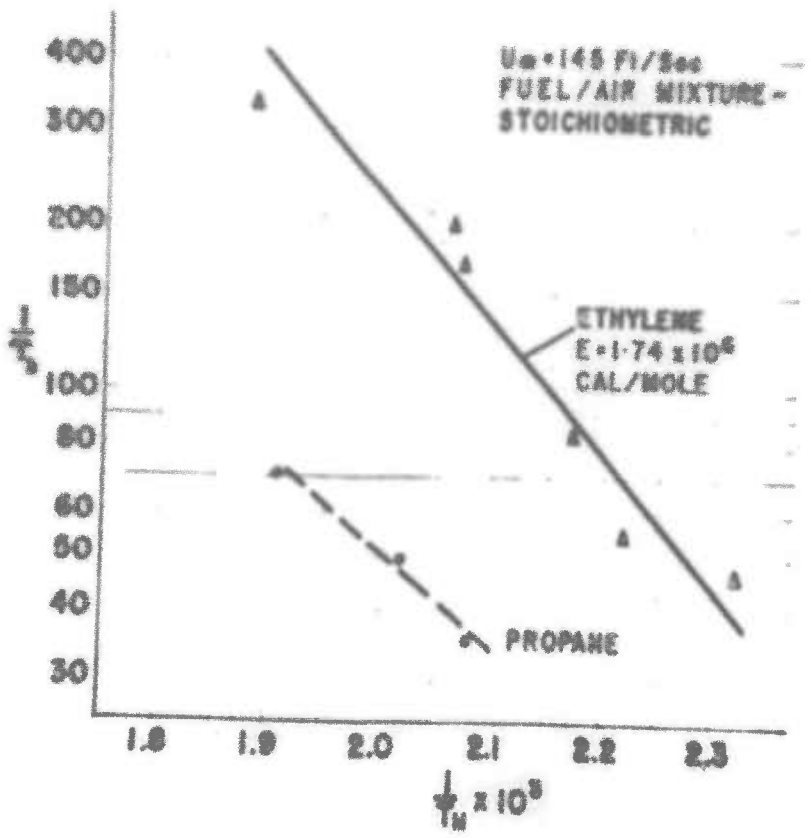
LOG $\frac{1}{t_b}$ VS $\frac{1}{T_M}$
400
300
200
150
100
80
60
50
40
30
$\frac{1}{t_b}$
Ua = 145 Ft/Sec
FUEL/AIR MIXTURE - STOICHIOMETRIC
ETHYLENE
E = 1·74 x 10⁶
CAL/MOLE
PROPANE
1.8
1.9
2.0
2.1
2.2
2.3
$\frac{1}{T_M} \times 10^3$

Figure 17

ONE-DIMENSIONAL SHOCK WAVES FROM AN AXIALLY SYMMETRIC ELECTRICAL DISCHARGE

J. Gauger and V. Vali
Lockheed Missile Systems Division
Palo Alto, California

A number of capacitor-discharge shock tubes have been described in the literature.[1,2] Some preliminary results on such a device capable of yielding plasma temperatures in the region from one to ten electron volts are presented here.

The funnel electrode system used for these experiments is shown in Fig. 1. Nickel was used for both electrodes to reduce contamination of the shocked gas.

The electrode system is similar to the Los Alamos "wine glass" configuration described by Scott[3] but differs in that the outer electrode was folded back along the teflon insulation to further minimize the external circuit inductance. With this arrangement, the entire system from capacitor through spark gap and the shock tube electrodes was coaxial and the inductance of the circuit was lowered to a total of 0.085 micro-henries. A 1.1 microfarad coaxially constructed capacitor with an inductance of 0.040 micro-henries was used in the energy storage system. The ring frequency of the system was 520 kc. The capacitor was charged each time to 30kv (500 joules) and discharged through a spark gap triggered by an induction coil. In each case the ambient pressure in the shock tube was pre-set.

Most of the position-time data were obtained through use of an image converter framing camera, with which a set of five pictures of the gas luminosity was obtained. The exposure time per frame could be varied from 0.020 microseconds to 0.5 microseconds, while the time between frames could be adjusted from 0.5 to 25 microseconds. A photo cell trigger which was positioned at the end of the shock tube was used to initiate the time sequence of the P.T.I.[4] camera. An example of the framing camera record is shown in Fig. 2.

Four sets of framing camera shots are pictured here. The first frame shows no shock luminosity since the frame is initiated only 50 milli-microseconds after a trigger pulse is applied. The light strips visible on each frame were regions covered by distance marker stripes painted on the glass shock tube. The pressure at which this particular data was obtained was one millimeter. The time between frames was approximately 5 micro-seconds and the exposure time per frame was 0.1 microseconds.

The image converter data were recorded on Polaroid transparencies to aid in the analysis of the position-time information and the exposure pulses fed to the image converter were also displayed on an oscilloscope for the timing information on each shock.

An example of the position-time data is shown in Fig. 3. Here the distance x is plotted in centimeters from a point located halfway between the electrodes. The error in determining the position of the luminosity front was at maximum 3 millimeters (the thickness of the distance marking stripes painted on the shock tube), while the maximum error in the time measurement was limited only by the reading of the records of the exposure pulse and was at most 0.05 mi roseconds. The image converter yielded four x, t points on each shot and four shots were taken for each pressure. The ambient pressure was varied from 0.040 mm to 10 mm in discrete steps. The data could be represented quite accurately for each pressure by a relationship of the form

$$t = ax^n \tag{1}$$

as indicated by the lines drawn through the data points.

If one uses strong shock theory[5] and assumes that all of the gas has been swept up and moves with the shock velocity, one can prove that

$$E = \frac{u^2}{2} \tag{2}$$

where E is the internal energy, $\frac{u^2}{2}$ is the kinetic energy per unit mass of the shocked gas. Further,

$$u = \frac{2}{\gamma' + 1}\,\dot{x} \tag{3}$$

where $\dot{x}$ is the shock velocity.

If one assumes that all the energy dumped into the gas goes into the shock, then

$$W = \int \left(\frac{u^2}{2} + E\right) \rho_d \tau \tag{4}$$

where W is the energy per unit area of the shock front and d_τ is a volume element.

One can integrate this expression easily if it is assumed that all the gas is picked up and moved with the shock front,

$$W = \rho_o u^2 x = \left(\frac{2}{\gamma' + 1}\right)^2 \rho_o \dot{x}^2 x \tag{5}$$

where γ' is the ratio of specific heats of the shocked gas.

Assuming constancy of γ' and W, i.e., no energy attenuation, then it is apparent that

$$\text{Const.} = \dot{x}^2 x \quad \text{or}$$

$$t = ax^{3/2} \tag{6}$$

For no energy loss, then, the exponent should be 3/2. If, however, energy loss through heat conduction and radiation is considered, then one cannot integrate equation 4 directly.

In Fig. 4, we have plotted the exponent n from the experimental data versus ambient pressure in the shock tube. One can see that at the lower pressures (40μ), we approach n = 1.5. We have computed the energy associated with the gas flow in the shock front by substituting in equation 5, the value of the shock velocity at a point derived from the experimental data, i.e.,

$$\text{where } t = ax^n,$$

$$k = \frac{1}{nax^{n-1}} \tag{7}$$

from which

$$W = \left(\frac{2}{\gamma' + 1}\right)^2 \rho_o \frac{1}{n^2 a^2 x^{2n-3}} \tag{8}$$

Since for these experiments the value γ' is close to one, then

$$W \propto \frac{\rho_o}{n^2 a^2 x^{2n-3}} \tag{9}$$

We have plotted W versus x computed from equation 9 in Fig. 5 for several pressures. If we use the entire cross-sectional area of the tube ($\sim$20 cm^2), it is quite apparent that the energy transfer from the capacitor to the gas is not too effecient ($\sim$10% for the higher pressures).

To obtain some idea of the temperature range in these experiments, we computed the temperature from the shock Mach number using the data presented in Gilmore[4] and velocity determined from the position-time data. The temperature as a function of position for several initial shock tube pressures is shown in Fig. 6. The value of γ', the ratio of specific heats in the shocked gas, was also determined from the Hugoniot of air to 24,000°K and was found to vary from about 1.10 to 1.15. Approximately 90% of the internal energy of the shocked gas goes into dissociation and ionization. The fluctuations of the temperature at the same ambient pressure reflect variations of γ'.

The measurements with the funnel system showed no evidence of secondary shocks formed by ringing of the capacitor system. Subsequent measurements using a streaking unit for the P.T.I. camera do show weak secondary shocks exist; however, most of the gas is driven out of the discharge region on the first half cycle of the discharge.

Observations of the electrodes, after several shots, has shown that the discharge occurs in the form of a current sheath. The discharge currents were sufficiently large ($\sim$50,000 amperes) for the pinch effect to become important. Again, observation of the electrode damage confirmed this.

To improve the energy transfer to the gas, the system was modified to eliminate the triggered spark gap. To produce a discharge, the shock tube was evacuated, the condenser charged to 30 kv and the discharge was initiated by admitting air slowly into the shock tube. With this arrangement, the downstream pressure lay between 20 and 100 microns at firing. The position-time data were recorded over 3 meters of shock tube by two methods: photocells recording the passage of the luminous front and by a microwave interferometer.[5] The data are compared in Fig. 7. At first the microwave points lead the photocell data in time, then for some distance both techniques yield points which follow the same curve. At later times microwave penetration of the shock front occurs when the ionization drops below an electron density of $10^{12}/cm^3$. The region where the microwave points occur in time ahead of the luminosity may be attributed to photo ionization of the gas ahead of the shock front. Again for these pressures the position-time data could be adequately fit to a curve of the form

$$t = ax^n \qquad \text{where } n = 3/2.$$

REFERENCES

1. Fowler, Goldstein, Clotfelter. Physical Review 52, 879 (1951).

2. A. C. Kolb, Physical Review 107, 345 (1957).

3. Shock Channeling
F. R. Scott, General Atomics
Lockheed Magnetohydrodynamics Symposium
December 16, 1957.

4. Precision Technology, Incorporated
Livermore, California.

5. Exact and Approximate Treatments of the One Dimensional Blast Wave, E. G. Harris, NRL Report 4858.

6. Equilibrium Composition and Thermodynamic Properties of Air to 24,000°K. F. R. Gilmore, Rand Corporation, RM 1543.

7. Private communication, T. E. Turner, Lockheed MSD, Palo Alto, California.

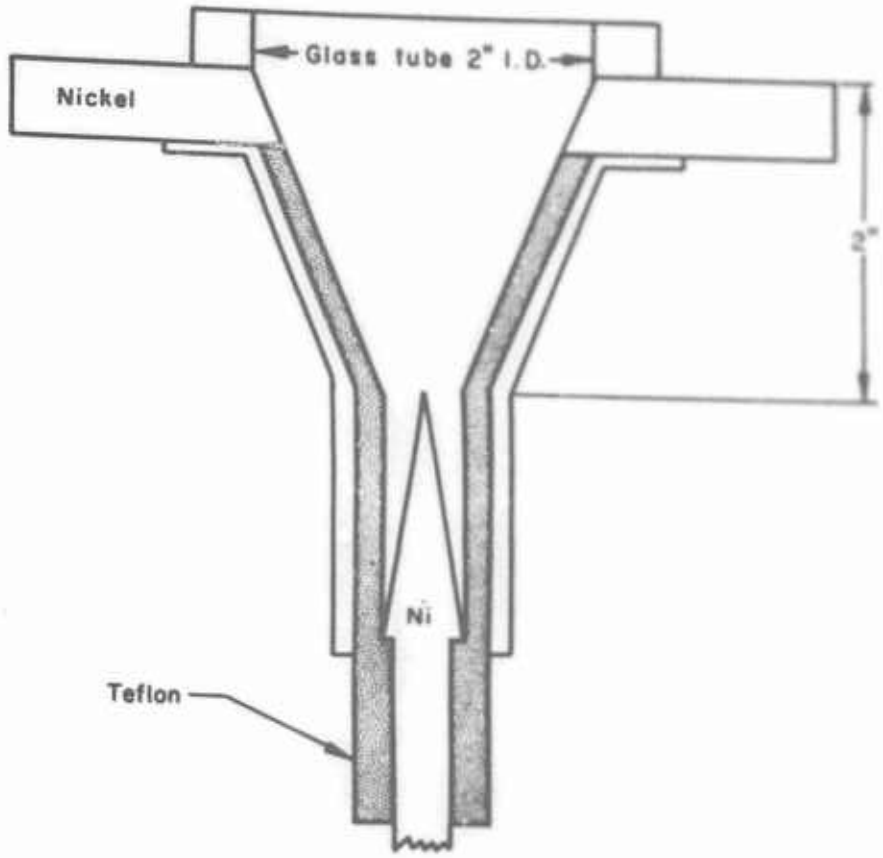

Center electrode Ni 1/2"dia. at base tapered to 1/16" at tip over 5 cm

Funnel electrode configuration

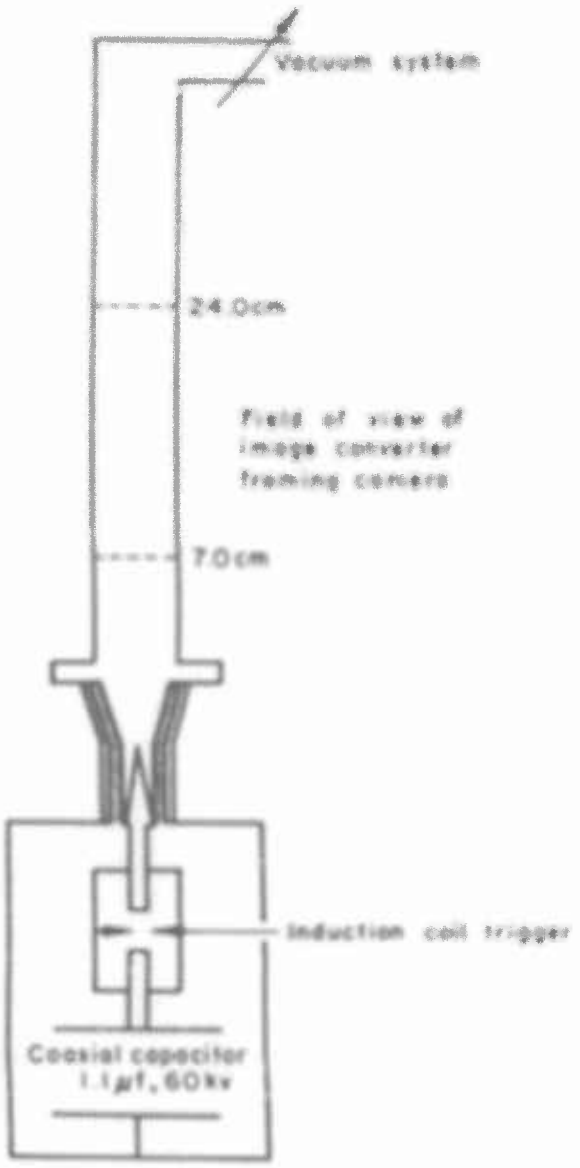

Ring frequency of system ~ 520 kc

Figure 1

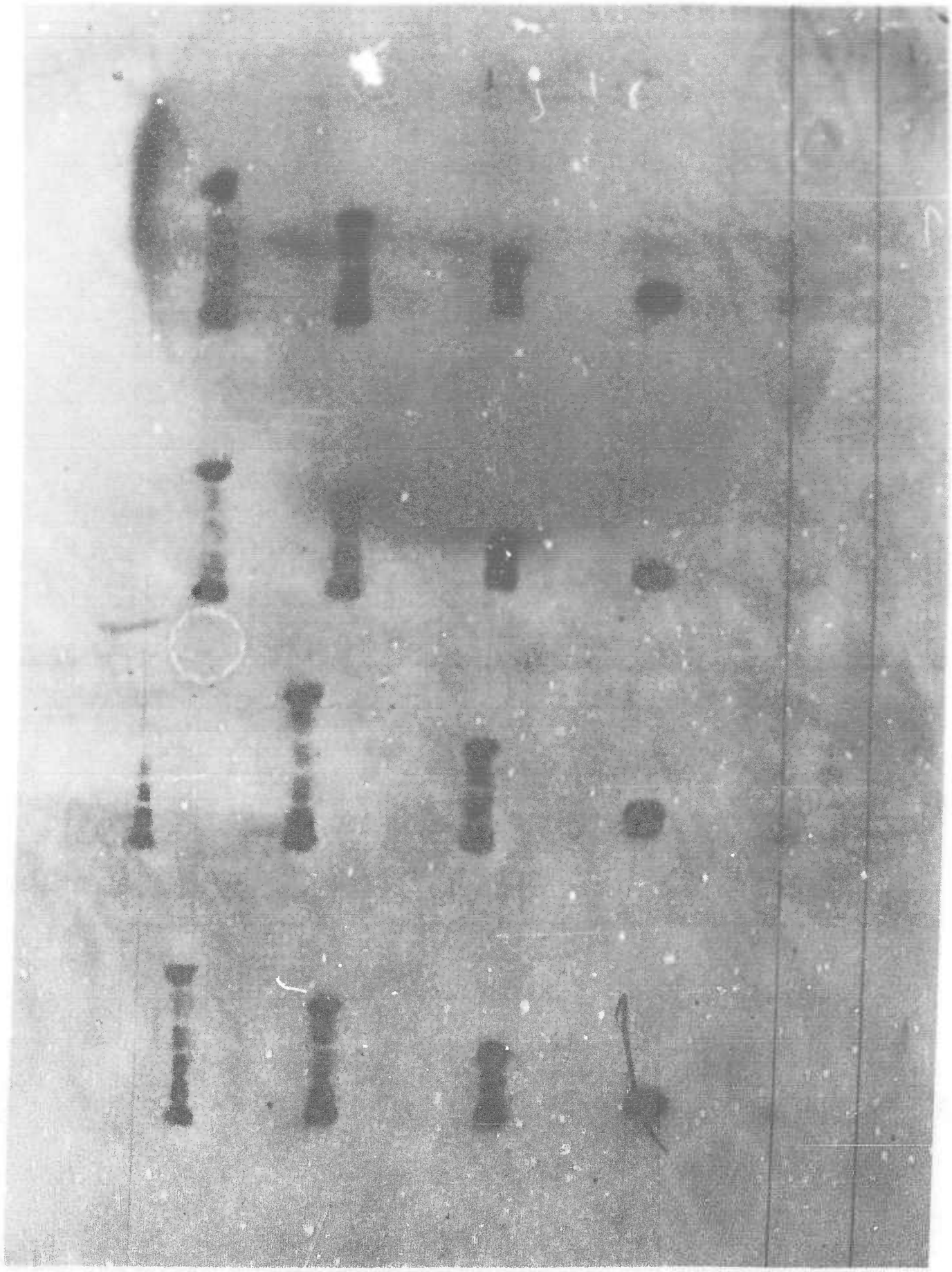

Figure 2

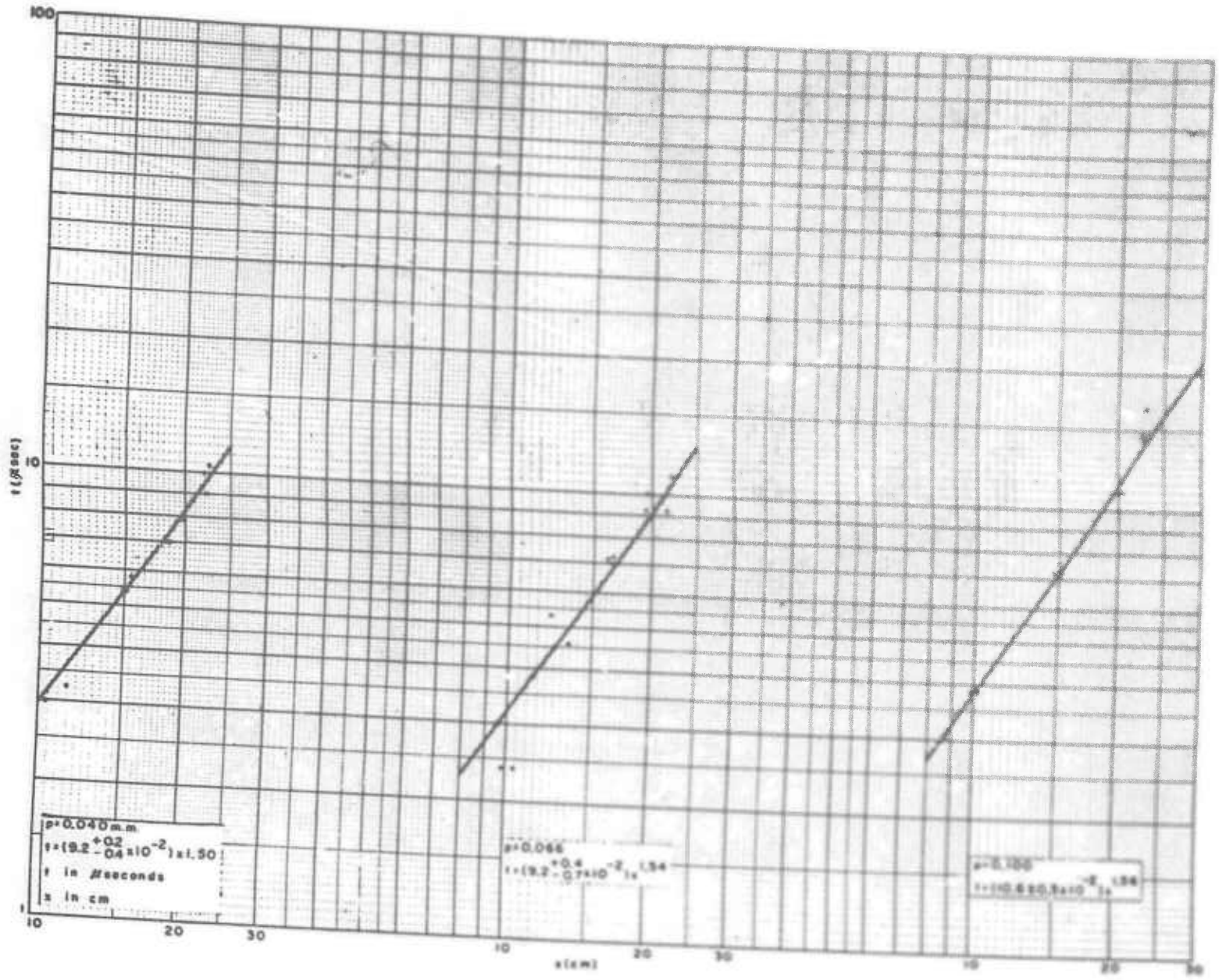
100
10
1
t (μsec)
p=0.040 m.m
t=(9.2 +0.2 -0.4 ×10⁻²) x^1.50
t in μseconds
x in cm
10
20
30
p=0.066
t=(9.2 +0.4 -0.7×10⁻²) x^1.54
10
20
30
x (cm)
10
20
30

Figure 3

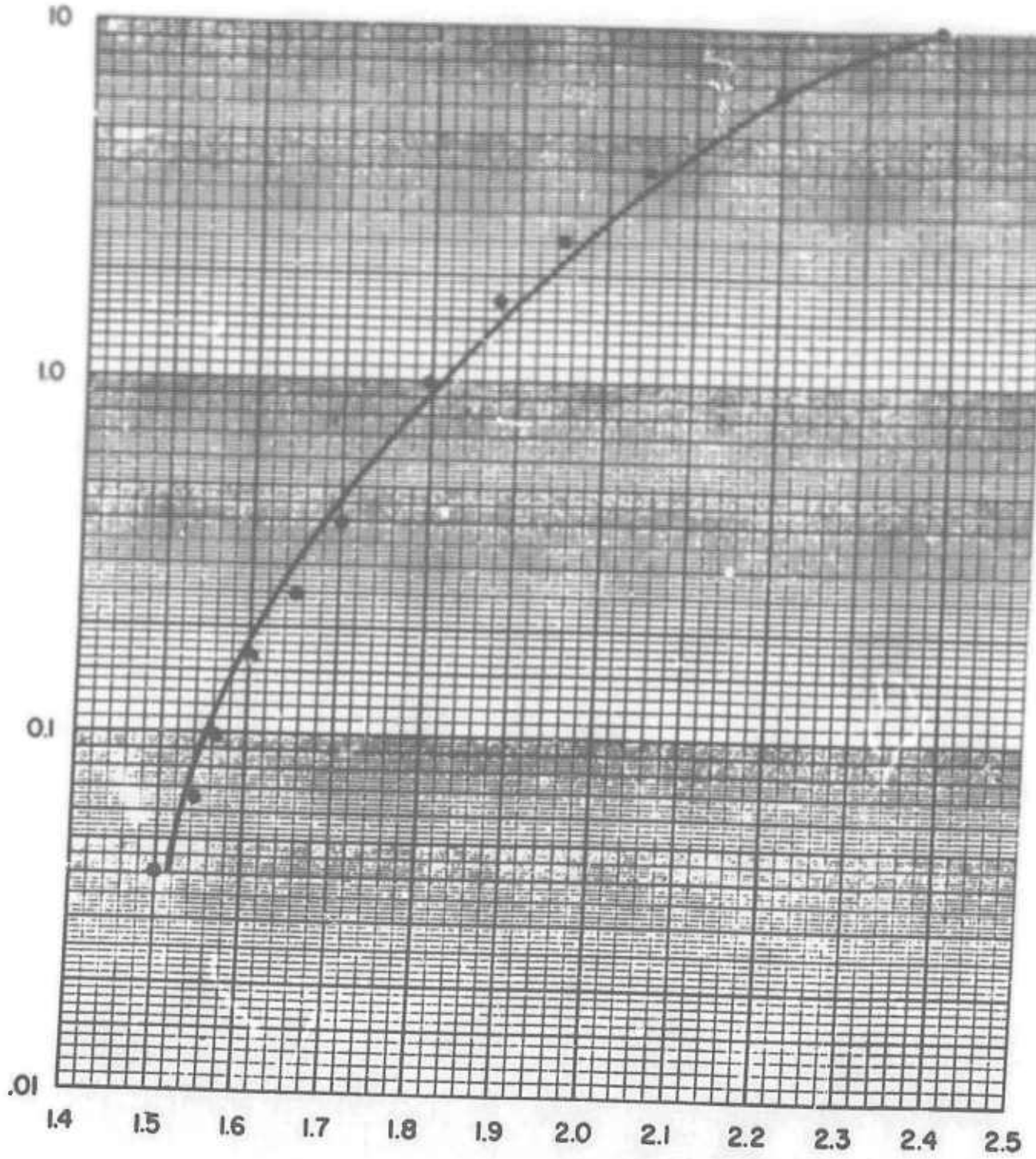

Figure 4

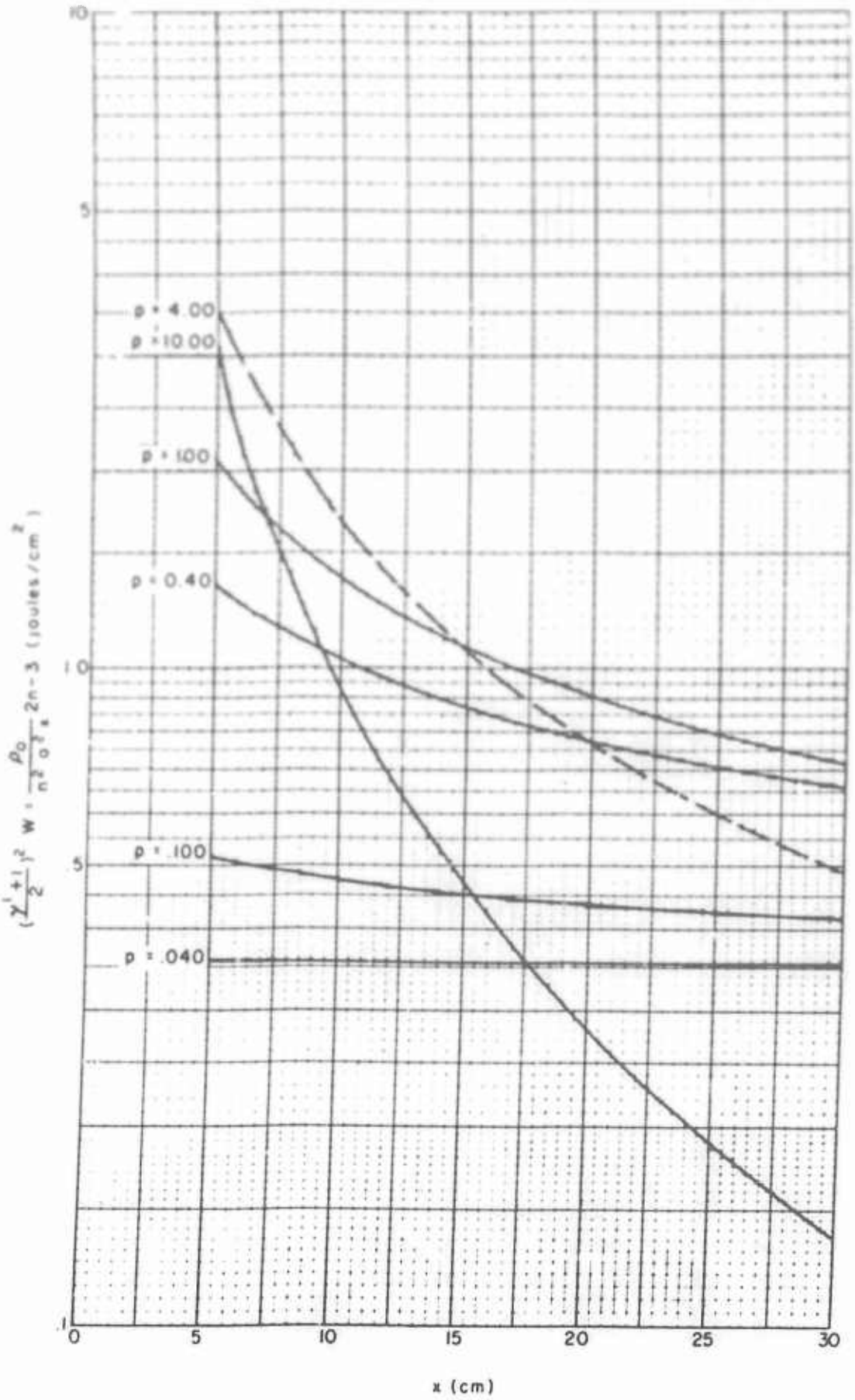
10
5
1.0
.5
.1
p = 4.00
p = 10.00
p = 1.00
p = 0.40
p = .100
p = .040
0
5
10
15
20
25
30
x (cm)
$(\frac{\gamma'+1}{2})^2 W = \frac{\rho_0}{n^2 a^2 \tau_e^2} 2n-3$ (joules/cm^2)

Figure 5

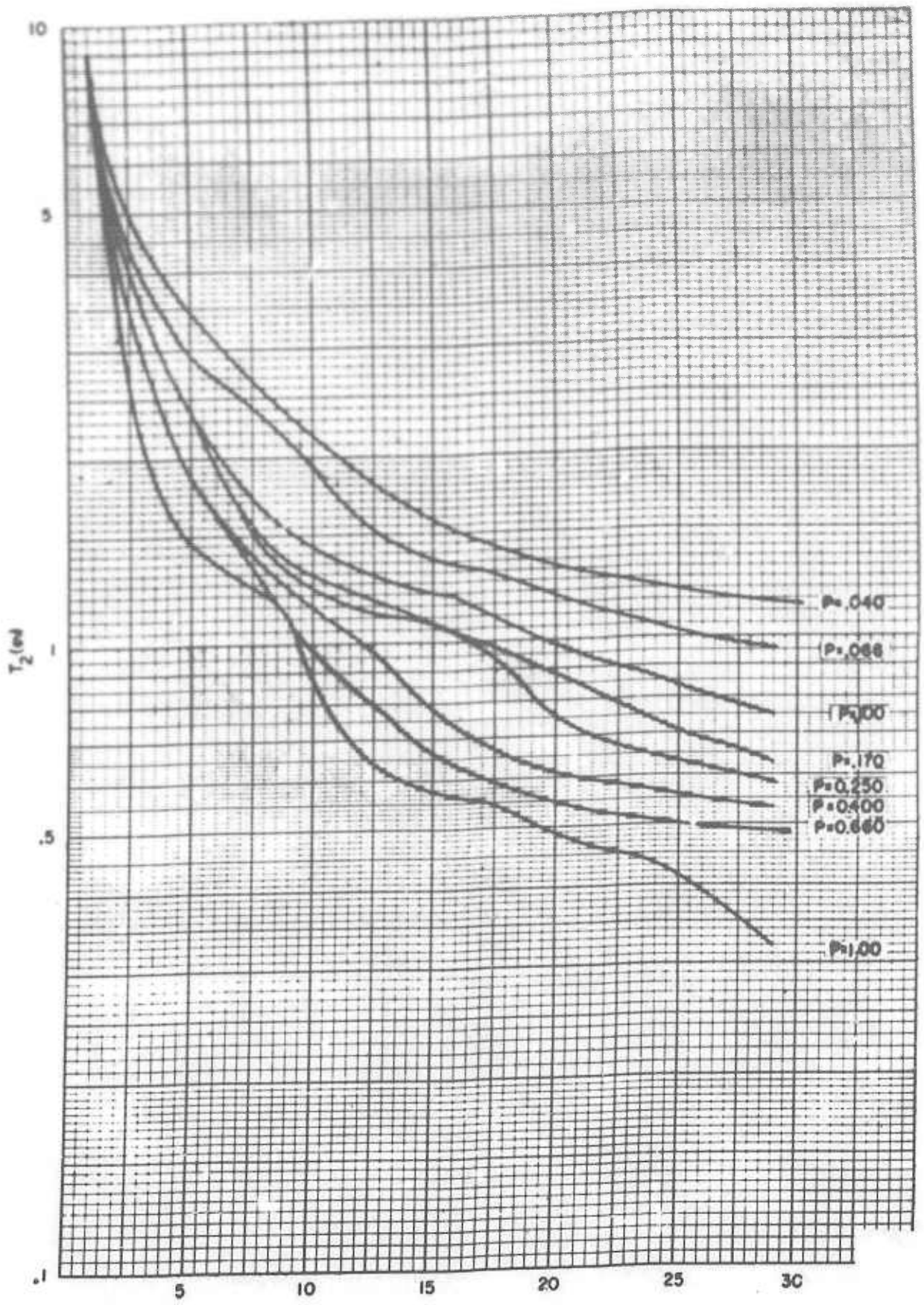
10
5
1
.5
.1
T_2 (s)
5
10
15
20
25
30
P=.040
P=.066
P=.100
P=.170
P=0.250
P=0.400
P=0.660
P=1.00

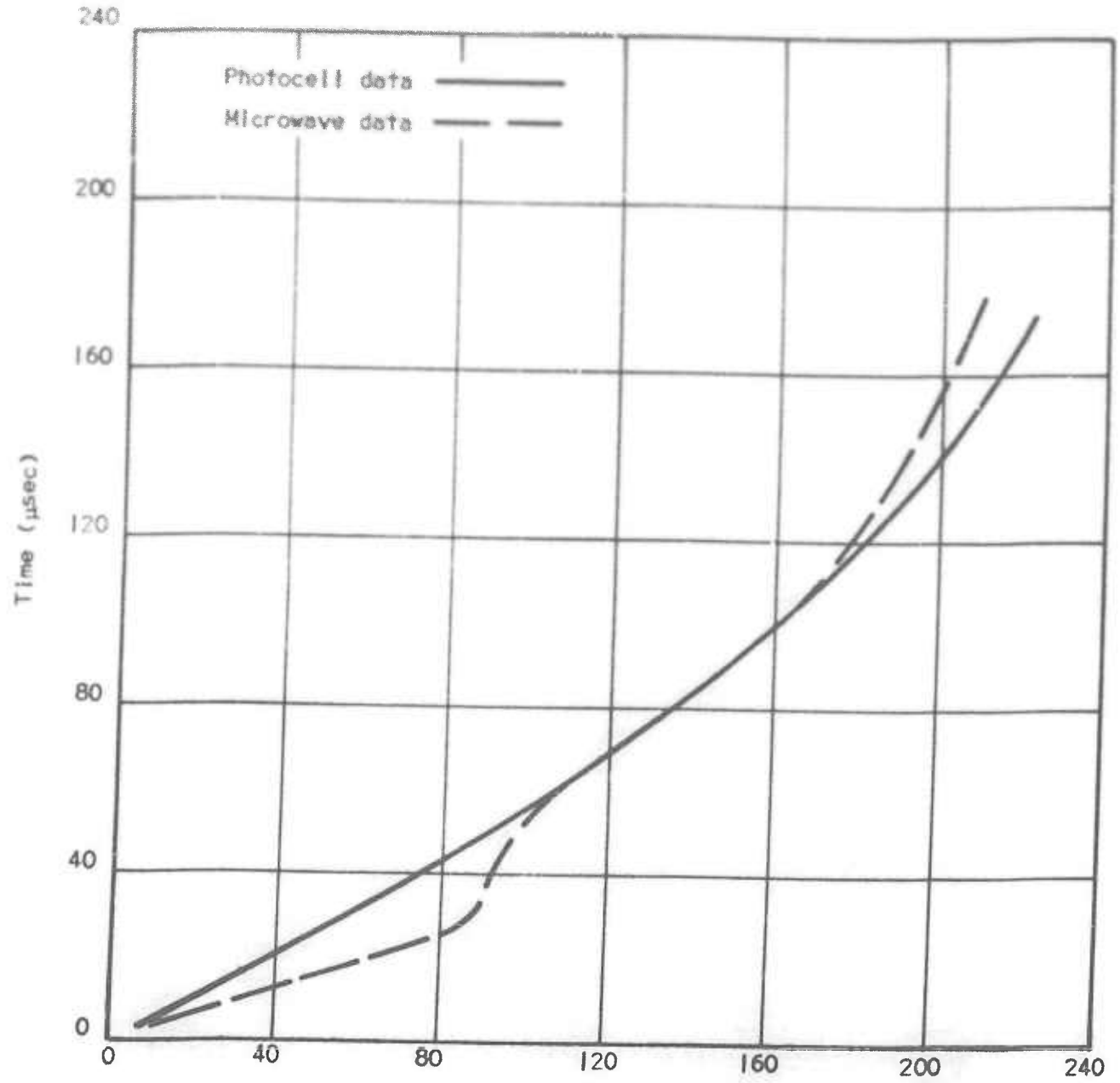
Photocell data
Microwave data
Time (μsec)
240
200
160
120
80
40
0
0
40
80
120
160
200
240
Distance (cm)

Figure 7

CLOSING REMARKS

Roman R. Birukoff
Structural Research Engineer
Air Force Special Weapons Center
Kirtland Air Force Base, New Mexico

Mr. Birukoff indicated that the interest in the Shock Tube Symposium apparently gained a momentum; this was evident in the increased number of attendants.

The attendance at this 2nd Shock Tube Symposium was double of the one held last year at MIT.

Before closing the meeting, in behalf of the Air Force Special Weapons Center, Mr. Birukoff thanked the participants, monitors: Mr. Eric H. Wang of AFSWC and Jack Kelso of AFSWP and all attendants for contributing their time and effort to the success of the 2nd Shock Tube Symposium.

UNCLASSIFIED

AD 211239

Armed Services Technical Information Agency

ARLINGTON HALL STATION
ARLINGTON 12 VIRGINIA

FOR
MICRO-CARD
CONTROL ONLY

6 OF 6

NOTICE: WHEN GOVERNMENT OR OTHER DRAWINGS, SPECIFICATIONS OR OTHER DATA ARE USED FOR ANY PURPOSE OTHER THAN IN CONNECTION WITH A DEFINITELY RELATED GOVERNMENT PROCUREMENT OPERATION, THE U. S. GOVERNMENT THEREBY INCURS NO RESPONSIBILITY, NOR ANY OBLIGATION WHATSOEVER; AND THE FACT THAT THE GOVERNMENT MAY HAVE FORMULATED, FURNISHED, OR IN ANY WAY SUPPLIED THE SAID DRAWINGS, SPECIFICATIONS, OR OTHER DATA IS NOT TO BE REGARDED BY IMPLICATION OR OTHERWISE AS IN ANY MANNER LICENSING THE HOLDER OR ANY OTHER PERSON OR CORPORATION, OR CONVEYING ANY RIGHTS OR PERMISSION TO MANUFACTURE, USE OR SELL ANY PATENTED INVENTION THAT MAY IN ANY WAY BE RELATED THERETO.

UNCLASSIFIED